

Microwave Imaging and Emerging Applications

Guest Editor: Paul M. Meaney





Microwave Imaging and Emerging Applications

International Journal of Biomedical Imaging

Microwave Imaging and Emerging Applications

Guest Editor: Paul M. Meaney



Copyright © 2012 Hindawi Publishing Corporation. All rights reserved.

This is a special issue published in "International Journal of Biomedical Imaging." All articles are open access articles distributed under the Creative Commons Attribution License, which permits unrestricted use, distribution, and reproduction in any medium, provided the original work is properly cited.

Editorial Board

Haim Azhari, Israel

K. Ty Bae, USA

Richard H. Bayford, UK

F. J. Beekman, The Netherlands

J. C. Chen, Taiwan

Anne Clough, USA

Carl Crawford, USA

Daniel Day, Australia

Eric Hoffman, USA

Jiang Hsieh, USA

M. Jiang, China

Marc Kachelrieß, Germany

Cornelia Laule, Canada

Seung W. Lee, Republic of Korea

A. K. Louis, Germany

Jayanta Mukherjee, India

Vasilis Ntziachristos, Germany

Scott Pohlman, USA

Erik L. Ritman, USA

Jay Rubinstein, USA

Peter Santago, USA

Lizhi Sun, USA

Kenji Suzuki, USA

Jie Tian, China

Michael W. Vannier, USA

Yue Wang, USA

Ge Wang, USA

Guo Wei Wei, USA

D. L. Wilson, USA

Sun K. Yoo, Republic of Korea

Habib Zaidi, Switzerland

Yantian Zhang, USA

Jun Zhao, China

Yibin Zheng, USA

Tiange Zhuang, China

Yu Zou, USA

Contents

Microwave Imaging and Emerging Applications, Paul M. Meaney
Volume 2012, Article ID 252093, 2 pages

On the Forward Scattering of Microwave Breast Imaging, Hoi-Shun Lui, Andreas Fhager,
and Mikael Persson
Volume 2012, Article ID 582037, 15 pages

A Prototype System for Measuring Microwave Frequency Reflections from the Breast, J. Bourqui,
J. M. Sill, and E. C. Fear
Volume 2012, Article ID 851234, 12 pages

Bone Dielectric Property Variation as a Function of Mineralization at Microwave Frequencies,
Paul M. Meaney, Tian Zhou, Douglas Goodwin, Amir Golnabi, Elia A. Attardo, and Keith D. Paulsen
Volume 2012, Article ID 649612, 9 pages

Surface Wave Multipath Signals in Near-Field Microwave Imaging, Paul M. Meaney, Fridon Shubitidze,
Margaret W. Fanning, Maciej Kmiec, Neil R. Epstein, and Keith D. Paulsen
Volume 2012, Article ID 697253, 11 pages

Three-Dimensional Near-Field Microwave Holography for Tissue Imaging, Reza K. Amineh,
Ali Khalatpour, Haohan Xu, Yona Baskharoun, and Natalia K. Nikolova
Volume 2012, Article ID 291494, 11 pages

Using X-Ray Mammograms to Assist in Microwave Breast Image Interpretation, Charlotte Curtis,
Richard Frayne, and Elise Fear
Volume 2012, Article ID 235380, 11 pages

Microwave Breast Imaging System Prototype with Integrated Numerical Characterization, Mark Haynes,
John Stang, and Mahta Moghaddam
Volume 2012, Article ID 706365, 18 pages

Measurement and Analysis of Microwave Frequency Signals Transmitted through the Breast,
Jeremie Bourqui, John Garrett, and Elise Fear
Volume 2012, Article ID 562563, 11 pages

Editorial

Microwave Imaging and Emerging Applications

Paul M. Meaney

Thayer School of Engineering, Dartmouth College, Hanover, NH 03755, USA

Correspondence should be addressed to Paul M. Meaney, paul.meaney@dartmouth.edu

Received 31 January 2012; Accepted 31 January 2012

Copyright © 2012 Paul M. Meaney. This is an open access article distributed under the Creative Commons Attribution License, which permits unrestricted use, distribution, and reproduction in any medium, provided the original work is properly cited.

Active microwave imaging for biomedical has been proposed, studied, and implemented to varying degrees by a plethora of worldwide institutions for the last 30 years. Much of the interest has been based on the fact that tissue dielectric properties embody important information about physiological state and function. Early efforts concentrated on techniques involving classic techniques such as diffraction imaging and the Born and Rytov approximations which ultimately proved too limited for the high degree of field scattering involved with electromagnetic fields. At a time of rapidly increasing computational power and speed, the electromagnetics field quickly adopted these capabilities for developing improved forward and inverse modeling tools. This was especially convenient in that hardware implementations could be rapidly simulated and validated without the considerable time and expense of fabrication and testing. The evolution of numerical capabilities has been considerable to the point where fully 3D software packages, both customized and commercial, can represent complex geometries in reasonable time frames with exquisite resolution.

Microwave imaging will always be a hybrid between numerical modeling and hardware. The two principle approaches today involve some form of tomography or 3D inversion and radar-based techniques. The former primarily utilizes transmission data, in combination with an inverse algorithm, produces maps of the interrogated dielectric properties. The algorithms fall under the category of classical parameter estimation problems and stem from a basic mathematical statement to minimize the differences between the measured and computed fields. A wide range of optimization problems have been implemented including, but not limited to, Gauss-Newton iterative schemes, genetic algorithms and backprojection techniques. These have often been 2D and 3D implementations and involved single and multifrequency modes. While this discipline has been dominated by

simulation experiments, several efforts have expanded to at least the level of phantom validation investigations and even more advanced clinical implementations for breast cancer imaging. As with any technology, these realizations have involved important design trade-offs with respect to signal attenuation and detection strength, operating frequency, resolution, antenna selection, mechanical versus electrical array scanning, and many others. Early results have been encouraging and in an important development it is clear that the technique can recover accurate property maps that, as earlier hypothesized, can discern objects at levels well below the $\lambda/2$, Rayleigh criteria.

Radar approaches have also progressed substantially over the last decade or two. While much of the earlier work remained in the simulation realm, more recent efforts have included credible translation to experimental and even clinical implementations. The different approaches have involved either forward or backscattered measurement data and have explored air-coupled, liquid-coupled and contacting antenna techniques. This concept has been applied initially for the detection of high-contrast targets such as breast cancer with more recent efforts exploring approaches to more broadly characterize abnormalities. The classical challenges in this case involve designing broadband antennas, beam coverage of the entire target and generating sufficient measurement signal strength. More specific issues relating to breast cancer imaging involve the high degree of scattering at the skin. Early clinical efforts have produced refined and interesting breast images, especially for lower density breasts.

The application of microwave imaging to the breast cancer detection problem has singularly motivated the wide-ranging worldwide efforts in this technology. Breast cancer is an important worldwide health problem afflicting primarily woman. Treatment outcomes have been shown to be progressively more positive when the cancers are detected earlier.

While conventional technologies such as X-ray mammography and MR do a good job of detecting and characterizing tumors, their effectiveness is particularly limited for more dense breasts. This has spurred the drive for investigating alternative approaches. As alluded to before, tissue dielectric properties can span a wide range of permittivity and conductivity values from very low values for fattier tissue to much higher values for high-water content tissues and a range of intermediate values depending on the composition. Initially the excitement for microwave breast imaging was based on the assumption that there was a very high property contrast between tumors and normal breast tissue and that these property differences would enable detection on a sub-centimeter scale. More recent studies have shown that the contrast is not necessarily as high and that the property variations are much more complex depending on the internal fibroglandular structure. However, this more nuanced understanding of the tissue properties provides real opportunities in the breast imaging area as the technology expands to roles in both breast cancer diagnosis and therapy monitoring. In fact, this opens up the opportunity for relating this recent data back to earlier, extensive studies by Ken Foster into the relationships between free and bound water with respect to tissue properties. These complex mechanisms have been hypothesized as prognostic indicators for cancer and may pave the way for dielectric properties becoming important biological markers.

As mentioned earlier, the earliest efforts in this arena were dominated by numerical modeling efforts. However, there is a realization within the community that for this technology to continue to be relevant, there needs to be concerted efforts to translate the various concepts into the clinic. This special issue is a step in that direction and demonstrates a maturing of the field. While there are some simulation studies within this collection, a good number of them deal directly with implementation challenges. Several in the radar area deal directly with acquiring *in vivo* measurements of a human breast. Another from the tomography techniques assesses the impact of surface waves to multipath contributions which can be an especially daunting problem in any radar, imaging, or communication system. These are healthy signs that the group understands that for it to continue to be relevant, it needs to steadily push these ideas into the clinic for real world validation. Simulations will always play an important role in this area, but the synergism with hardware implementations must be more heavily emphasized.

Beyond these classical motivations, this issue also highlights important points for the field as it moves forward. For instance, there is always room to explore new imaging techniques such as holographic approaches which may be particularly well suiting for the breast imaging situation. There are also clearly ways to improve on the overall approaches, especially when these methods can be combined with existing technologies such as proposed by the paper dealing with utilizing mammography in conjunction with radar approaches. Finally, while breast cancer imaging has dominated the landscape of microwave imaging for over a decade, we should not be blinded by other important health and commercial opportunities. The studies on bone

dielectric property variations with respect to mineral density set the stage for applying microwave imaging in the area of osteoporosis detection and bone health monitoring which is becoming a major health issue with our rapidly aging population. This is only one of a range of important health issues where microwave imaging could make a substantial impact.

Paul M. Meaney

Research Article

On the Forward Scattering of Microwave Breast Imaging

Hoi-Shun Lui,^{1,2} Andreas Fhager,^{1,2} and Mikael Persson^{1,2}

¹ Biomedical Electromagnetics Research Group, Division of Signal Processing and Biomedical Engineering, Department of Signals and Systems, Chalmers University of Technology, S 412 96 Gothenburg, Sweden

² Medtech West, Sahlgrenska University Hospital, SE413-45 Gothenburg, Sweden

Correspondence should be addressed to Hoi-Shun Lui, antony.lui@chalmers.se

Received 2 October 2011; Accepted 23 December 2011

Academic Editor: Elise Fear

Copyright © 2012 Hoi-Shun Lui et al. This is an open access article distributed under the Creative Commons Attribution License, which permits unrestricted use, distribution, and reproduction in any medium, provided the original work is properly cited.

Microwave imaging for breast cancer detection has been of significant interest for the last two decades. Recent studies focus on solving the imaging problem using an inverse scattering approach. Efforts have mainly been focused on the development of the inverse scattering algorithms, experimental setup, antenna design and clinical trials. However, the success of microwave breast imaging also heavily relies on the quality of the forward data such that the tumor inside the breast volume is well illuminated. In this work, a numerical study of the forward scattering data is conducted. The scattering behavior of simple breast models under different polarization states and aspect angles of illumination are considered. Numerical results have demonstrated that better data contrast could be obtained when the breast volume is illuminated using cross-polarized components in linear polarization basis or the copolarized components in the circular polarization basis.

1. Introduction

In the last two decades, extensive studies have been contributed to breast cancer detection using microwave-based technologies [1–25]. Compared to X-ray mammography that is widely used in hospital nowadays, microwave is a nonionizing radiation which is safer to subjects. Early studies [3–5] reported that there is a significant contrast between malignant tumor and healthy breast tissue which forms a strong foundation for the use of microwave-based techniques for breast cancer detection, although recent studies [26, 27] found that the contrast is much lower. This raises an issue of whether malignant tumor can be detected, especially when the relative permittivity of the tumor is close to that of the surrounding tissue.

In general, studies of microwave breast cancer detection can be divided mainly into two main groups, namely, the radar-based imaging approach (e.g., [1–12]) and the inverse scattering approach [13–20]. Radar-based imaging approach, first proposed by Hagness et al. [3–5], aims to identify the presence and location of strong scatterers due to the significant contrast between the tumor and the healthy breast tissue. This involves focusing on reflections from

the breast, that is, a coherent-sum process adapted from synthetic aperture radar techniques [4]. Throughout the years, numerous studies have been conducted from different research groups [6–12] and variations of the original radar-based technique, such as microwave imaging via space-time (MIST) beamforming [6, 7], tissue sensing adaptive radar (TSAR) [8, 9] have been proposed.

Here, we mainly focus on the inverse scattering approach [13–20]. The objective of inverse scattering is to reconstruct the unknown dielectric profiles of the breast volume. First, multistatic measurement from the breast volume is taken as reference. Based on numerical solutions of the Maxwell's equations (e.g., finite element method [13, 14], method of moment [15], finite-difference time-domain (FDTD) [16–18]), the entire volume can be spatially discretized into a number of variables with unknown dielectric properties. The corresponding forward problems with the same transmitter/receiver configuration are included and the computation can be done with an initial guess of the dielectric profiles of the breast volume. Given the reference data from the “actual” breast volume and the simulated data from the “assumed” breast volume, a cost function based on the differences between these two datasets is defined. The cost function

is then minimized in an iterative manner by changing the dielectric properties in the modeling domain using a gradient-based optimization algorithm. Assuming that the global minima is reached at the end of the optimization process, that is, the simulated data is almost the same or even identical to the reference data, the resulting dielectric profiles in the simulation domain is thus the resultant image provide that the global minima is reached.

The image reconstruction process is an ill-posed multidimensional optimization problem that the number of unknown variables ($\epsilon_r(x, y, z), \sigma(x, y, z)$) is determined in the image reconstruction stage. The number of unknown variables depends mainly on the physical size, the dielectric properties and geometry of the object, the required spatial resolution, and the frequency of interest (which is also a factor that determines the spatial discretization in the computation domain). Optimization of such a high-dimensional problem with thousands unknown variables is not trivial and chances for trapping into local minima could be high.

Furthermore, the uniqueness of the solution is also important. Given a set of measured-referenced data, there could be more than one distribution of dielectric profiles that can result in the same or similar measured data. As an example, if we consider some earlier studies in the literature [21] that compares the monostatic ultra wideband (UWB) response from the breast volumes with and without tumor, it is found that the differences between the copolarized components of the two cases is lower than that of the cross-polarized components. In other words, it is difficult to tell if there is any tumor by looking at the copolarized response, but the contrast is more apparent if the cross-polarized response is considered.

Polarization diversity has been widely used for radar imaging. The transmitters and receivers are located in the far-field region such that higher-order interactions between the object and the transmitters, as well as that of the object and the receivers, can be ignored. Coupling between transmitting and receiving antennas can be also ignored and thus the measured responses are purely object dependent. In microwave breast imaging scenario, the breast volume is surrounded by an antenna array in the near-field region. Mutual coupling between antenna elements as well as higher-order interactions between the breast volume and the antennas is significant. To reduce the reflection from the skin-air interface, the breast volume is usually immersed into some matching liquid. A possible exemption could be the case if the operation frequency is high enough such that the antenna is electromagnetically far from the breast and the conductivity of the matching liquid is relatively high such that higher-order interactions are attenuated. In microwave tomography, monopole antenna elements are used and thus only linear copolarized responses of the breast volume are considered in the image reconstruction process [15, 16].

In this paper, the forward scattering data of the two cases, that is, breast volume with and without tumor, under different polarization basis throughout the entire frequency bandwidth is investigated. The objective here is to investigate if better contrast of the forward data can be obtained such that the two cases are more distinguishable. With two

distinguishable sets of forward data, chances for the two inverse problems heading to the same solution in the optimization process could be reduced. To simplify the analysis, homogenous breast volume together with scattered far-field under different polarization basis is considered. We are aware that early efforts have been contributed to issues such as array configurations, development of image reconstructions and efficient forward solvers [25]. A summary of microwave inverse scattering can be found in [28]. We are also well aware that recent efforts have been contributed to experimental setups and clinical studies of microwave breast imaging, for instance the special session that was conducted in the IEEE Antenna and Propagation Society Conference in 2010 in Toronto [22]. This is also one of the major research topics in the research group in Chalmers. A dedicated, high-performance UWB time domain microwave breast imaging system is under development [23, 24]. The reasons behind such simplified models and setup considered in this work are given as follows.

First, we would like to see if the scattering problem itself under a different polarization basis resulted in forward data with better contrast that can be used for solving the inverse problem. Here, contrast means the differences of the forward data between the two cases: breast volume (i) with and (ii) without tumor. Chances for the two problems heading towards the same local minima could probably be reduced if the contrast is high. In electromagnetic scattering, any object can be treated as a polarization transformer that depolarizes the incoming electromagnetic wave. Boerner et al. [29] pointed out the importance of having full polarimetric data when the electromagnetic inverse problem is formulated. Ignoring the polarimetric properties of the scattering problem could lead to inconsistency formulation. Hence, it is important to study the forward scattering behavior of the breast volume numerically. Under this setup with solely breast volumes without any antenna array surrounding it, the scattered field is purely dependent to the breast volume. This allows us to get further understanding about the scattering data in microwave breast imaging problem under different polarization basis at different frequencies. Once we have a good idea about the scattering problem, specific antenna elements and array configurations can be designed. Second, polarization is well treated in the far-field region in frequency domain. Although the corresponding near-field components in the Cartesian coordinates can be computed, the concept of polarization in the near-field region is not well defined. As a result, plane wave incident and scattered far field are considered in this study.

The paper is outlined as follows. An overview of the research problem is given in Sections 2 and 3, followed by some numerical examples in Section 4. Discussions and conclusions will be reached towards the end of the paper.

2. Reviews of Microwave Breast Imaging

The microwave inverse scattering problem is illustrated in Figure 1. The object with unknown dielectric properties is surrounded by an array of antenna. Similar to X-ray

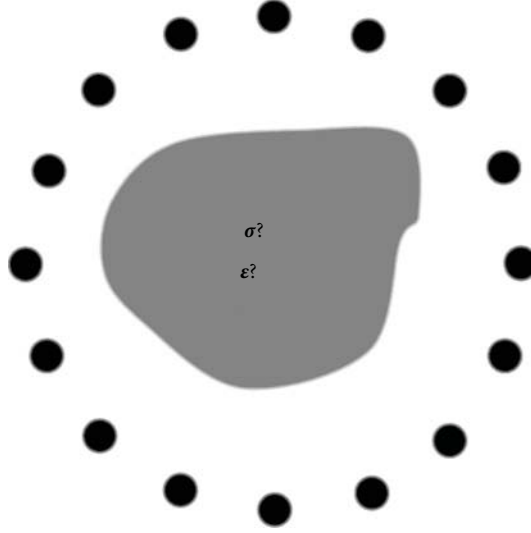


FIGURE 1: The microwave inverse scattering problem. The object with unknown dielectric properties is surrounded by an array of antenna. The objective is to determine the unknown dielectric properties based on the measured return signals from the antennas [18].

computed tomography (CT), projection of the environment can be obtained by sending electromagnetic waves from one antenna element and receiving the scattered signals from all other antenna elements. By changing the roles of antennas from transmitter to receivers, or rotating the antenna array, multiple views of the unknown object from different angles can be obtained. The objective of microwave inverse scattering problem is to determine for the unknown dielectric profile of the object based on these measured projections.

In this work, we would like to mimic the microwave breast imaging setup as described in [16–18]. The breast volume is placed inside a circular array with 17 monopole antenna elements. The breast volume is illuminated with 1 antenna acting as transmitter and the other antennas acting as receivers such that a projection of the breast volume is obtained. Each antenna element of the array takes turn and the projections of the breast volume from different angles are obtained. In [16–18], the measurement is performed using vector network analyzer (VNA) in frequency domain up to 8 GHz. Depending on the size of the object [16], only a portion of the bandwidth is chosen in frequency domain and the frequency samples are then transformed to the time domain using an inverse Fourier transform followed by a windowing to synthesis a Gaussian amplitude-modulated pulse with sinusoidal carrier. A cost function of the measured electric field $E_{m,n}^{\text{measured}}(t)$ and the simulated scattering electric field $E_{m,n}^{\text{simulated}}(t, \epsilon_r(i, j, k), \sigma(i, j, k))$ is defined and given by

$$\begin{aligned}
 & F(\epsilon_r(i, j, k), \sigma(i, j, k)) \\
 &= \int_0^T \sum_{m=1}^M \sum_{n=1}^N \left(\left| E_{m,n}^{\text{measured}}(t) \right. \right. \\
 &\quad \left. \left. - E_{m,n}^{\text{simulated}}(t, \epsilon_r(i, j, k), \sigma(i, j, k)) \right|^2 \right) dt.
 \end{aligned} \tag{1}$$

Here, $\epsilon_r(i, j, k)$ are $\sigma(i, j, k)$ the dielectric properties of the assumed breast volume in the simulation environment using FDTD and (i, j, k) is the index of the Yee cell in the FDTD simulation. M and N are the number of transmitting and receiving antennas, respectively, and the small letters m and n label the antenna elements. The cost function (1) is minimized using a gradient-based optimization algorithm.

3. Forward Scattering of the Breast Volume under Different Polarization States

In this study, the breast volume shown in Figure 2(a) is considered. It is a hemisphere with radius of 6 cm. The entire breast volume is illuminated from 23 MHz to 3 GHz with 128 samples in frequency domain. The relative permittivity and conductivity of the tissue is given by the widely used Debye model [3, 4] shown in Figure 3. For the case with a tumor inside the breast model, a dielectric sphere centres at the position of $(x = 15 \text{ mm}, y = 15 \text{ mm}, z = 30 \text{ mm})$, equivalently $r = 36.7 \text{ mm}$, $\theta = 54.7^\circ$, $\varphi = 45^\circ$) is added. Different sizes of tumor (spheres) with radius of 5 mm, 10 mm, and 15 mm are considered and the dielectric profiles of the tumor can be found in Figure 3. To simulate the breast, imaging scenario without using actual antenna elements, the elevation angle of $\theta_t = \theta_r = 105^\circ$ is considered ($\theta = 0^\circ$ corresponds to the positive z axis). The subscript t and r correspond to transmitting and receiving, respectively. The coordinate system and the cross-section view of the breast volume, tumor location, and excitation angle are shown graphically in Figures 2(b) to 2(d). The incident plane wave together with the corresponding scattered far-field at 18 different azimuth directions φ are equally spaced within the circle (i.e., $\Delta\varphi = 20^\circ$ separation). Both the forward and back scattering directions are considered. For instance, for the plane wave excitation coming from $\theta_t = 105^\circ$, $\varphi_t = 40^\circ$ ($\varphi = 0^\circ$ corresponds to the positive x axis), the scattered far field at

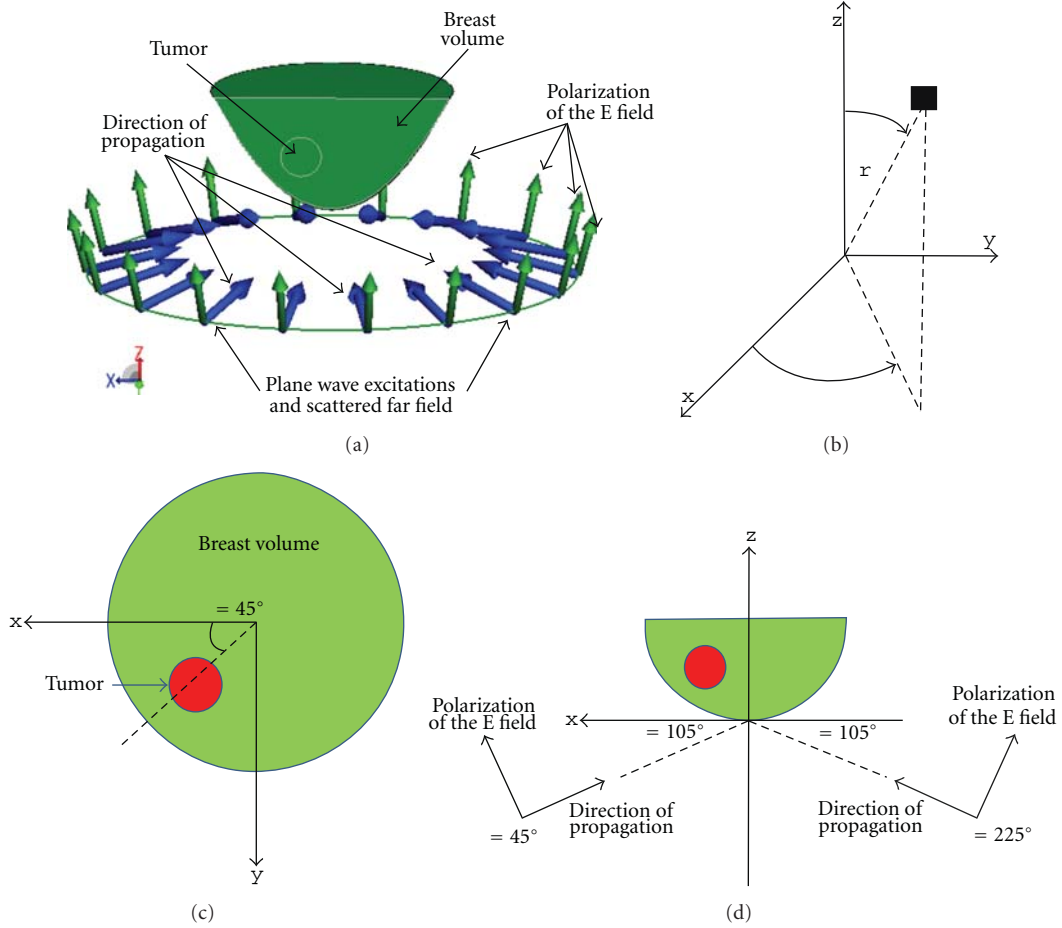


FIGURE 2: (a) The breast volume under plane wave illumination in FEKO environment. (b) The Spherical coordinate system (r, θ, φ) and the corresponding Cartesian coordinate system (x, y, z) that are used in the FEKO environment. (c) Cross-sectional views $(x-y)$ plane of the breast volume under plane wave illumination. (d) Cross-sectional view $(\varphi = 45^\circ, \theta = 90^\circ)$ of the breast volume under plane wave illuminations from $\theta_i = 105^\circ, \varphi_i = 45^\circ$, and $\varphi_i = 225^\circ$, respectively.

all directions (i.e., $\theta_r = 105^\circ, \varphi_r = 0^\circ, 20^\circ, 40^\circ, 60^\circ, \dots, 320^\circ$, and 340°) is determined. The computation is done using the commercial hybrid finite element and moment method solver FEKO in the frequency domain [30]. The incident plane wave and scattered far fields under the rectangular and circular polarization basis are considered. For each pair of incidence and scattered directions, the Sinclair polarization matrix of the breast volume is a function of frequency and aspects. This can be given by [31]

$$[S(f, \varphi_t, \varphi_r)] = \begin{bmatrix} S_{AA}(f, \varphi_t, \varphi_r) & S_{AB}(f, \varphi_t, \varphi_r) \\ S_{BA}(f, \varphi_t, \varphi_r) & S_{BB}(f, \varphi_t, \varphi_r) \end{bmatrix}_{\theta_t = \theta_r = 105^\circ}, \quad (2)$$

where

$$S_{AB}(f, \varphi_t, \varphi_r) = \frac{E_{r,B}(f, \varphi_t, \varphi_r)}{E_{t,A}(f, \varphi_t, \varphi_r)}. \quad (3)$$

The first subscript (A or B) in each term in the matrix corresponds to the transmitting polarization state and the second subscript corresponds to the receiving polarization

state. Each element $S_{AB}(f, \varphi_t, \varphi_r)$ is essentially the ratio of the scattered (received) electric field and the incident (transmitted) electric field. Vertical (V) and horizontal (H) are utilized for linear while left-handed (L) and right-handed (R) are used for circular polarization basis.

4. Numerical Results

4.1. Monostatic Responses for the Cases with Three Different Tumor Sizes. As an example, the monostatic amplitude responses of the breast volume at $\varphi_t = \varphi_r = 240^\circ$ in frequency domain under different polarization states are shown in Figure 4. Both linear and circular polarization states are considered. Three cases with different radius of the tumors, 5 mm, 10 mm, and 15 mm, are considered and the corresponding amplitude responses are plotted in red, cyan, and black, respectively, in Figure 4. Under monostatic configurations (i.e., $\varphi_t = \varphi_r$), $S_{VH} = S_{HV}$ and $S_{LR} = S_{RL}$.

At frequencies below 1 GHz, it is observed in Figure 4 that the amplitude responses for the four breast volumes are similar for the two linear copolarized and the four circular

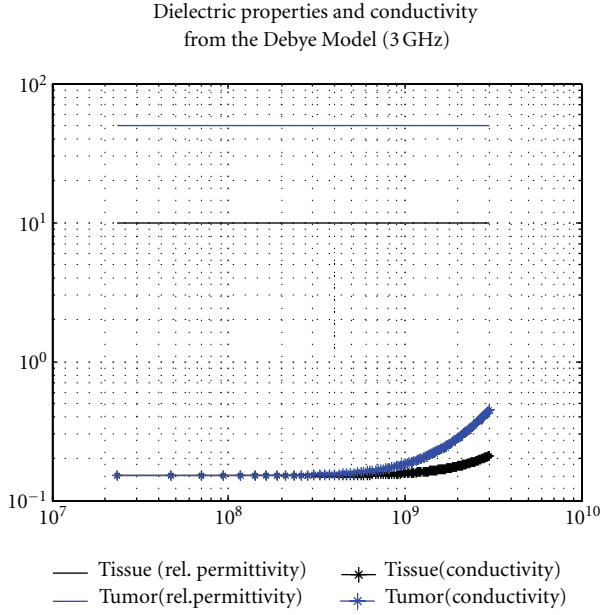


FIGURE 3: Dielectric Profiles of the breast volume with healthy tissue and tumor using the Debye model. The Debye model is given by $\epsilon(f) = \epsilon_\infty - j\sigma/(2\pi f\epsilon_0) + (\epsilon_s - \epsilon_\infty)/(1 + jf/f_p)$, where $\epsilon_0 = 8.854 \times 10^{-12}$ F/m, $f_p = 25$ GHz, and $\sigma = 0.15$ S/m. For healthy tissue, $\epsilon_s = 10$ and $\epsilon_\infty = 7$. For the tumor, $\epsilon_s = 50$ and $\epsilon_\infty = 35$ [3].

polarized states. It is apparent that, for the case with 15 mm tumor (black) and 10 mm tumor (cyan), the amplitude response is different to the other two cases when the frequencies are above 1.5 GHz. The results for the case with a 5 mm tumor (red) are almost the same to the reference data (blue) for almost all polarization basis which are difficult to distinguish by visual inspection (except the case VH = HV). It could potentially give a more distinguishable forward dataset for small tumor if VH or HV data is considered. The results indicate that the amplitude responses could be more distinguishable in some polarimetric states than the other, especially in the higher end of the frequency response. Next, the corresponding phase responses as a function of frequency under different polarization states are shown in Figure 5. Similar to the amplitude responses, the phase response for all cases are very similar comparing the reference data (blue) and the 5 mm tumor (red) (except the case VH = HV). The phase responses for the cases with 10 mm (cyan) and 15 mm (black) tumor have more significant differences at above 1 GHz in all cases.

4.2. Quantitative Measures as a Function of Transmitting and Receiving Directions. Consider the entire setup that involves a large amount of data ($N_{tx} = N_{rx} = 18$ and 8 polarization states, $18 \times 18 \times 8 = 2592$ sets), visual inspection is not feasible in practice. In view of this, we quantify the differences of the amplitude response between the two cases, that is, breast volume without tumor (reference) and breast volume with

a tumor. The relative difference between each frequency sample can be given by

$$S_{AB,diff,amplitude}(f, \varphi_t, \varphi_r) = \frac{||S_{AB,ref}(f, \varphi_t, \varphi_r)| - |S_{AB,tumor}(f, \varphi_t, \varphi_r)||}{|S_{AB,ref}(f, \varphi_t, \varphi_r)|} \quad (4)$$

$$\times 100\%.$$

A relative measure is chosen here as the scattered electric field varies as the intensity of the incident electric field changes. To quantify the difference of the data at different transmitter/receiver configurations, the “mean differences” of the data at each transmitter and receiver directions, MD_{AB} , which takes the average from all frequency samples can be given by

$$MD_{AB,amplitude}(\varphi_t, \varphi_r) = \frac{[\sum_{f=\Delta f}^{N\Delta f} S_{AB,diff,amplitude}(f, \varphi_t, \varphi_r)]}{N}. \quad (5)$$

As an example, comparisons between the cases with a 5 mm tumor and the reference data are chosen. This is the case with the smallest differences of the monostatic responses based on the visual inspection when comparing with the reference data. If we could get some insights from this case, it would be more apparent for the other two cases with larger tumors. The results are shown in Figures 6(a) to 6(h). It is observed that $MD_{AB,amplitude}$ varies as the transmitter/receiver configurations change. The $MD_{AB,amplitude}$ s for VV, HH, and the circular polarization basis are less than 4%. More than 1000% of $MD_{AB,amplitude}$ s are observed for the VH, and HV. Such high values for VH and HV are due to the fact that the cross-polarized component for the case without tumor is almost zero due to the geometrical symmetry. In reality, due to the inhomogeneous nature of human tissue, such high values cannot be achieved. The results under the circular polarization basis are also included. It is shown that the largest $MD_{AB,amplitude}$ values for LL and RR ($\sim 10\%$) are higher than those of VV and HH ($\sim 5\%$). According to the heterogeneities shown in Figures 6(e) and 6(f), it seems to show that on average the differences of the forward data under LL and RR polarization are higher than those of the VV and HH. In particular, it is interesting to observe that high values of $MD_{AB,amplitude}$ occur at the diagonal axis, which corresponds to the back-scattered direction. For the cross-polarized components (VH, HV, LR, and RL), it is worth noting that the two second diagonals that correspond to the two-dimensional direct path (180° differences in φ) also have relative high data contrast. Similarly, comparing Figures 6(g) and 6(h) with Figures 6(a) and 6(b), it seems to show that on average the LR and RL have less differences. To evaluate this properly, another measure will shortly be introduced and we will come back to this later in the next subsection.

Without the loss of generality, similar measures are also made for the phase, given by

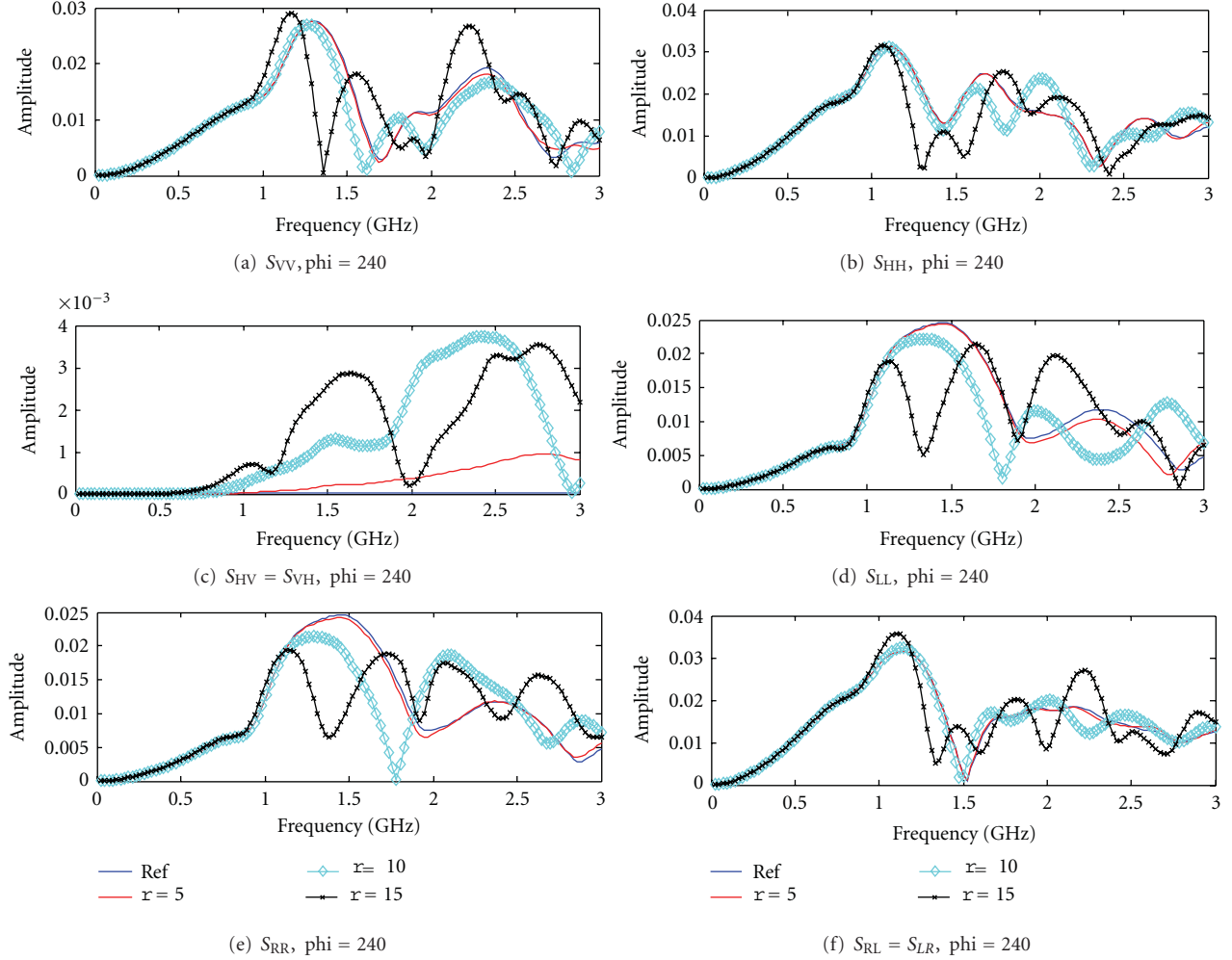


FIGURE 4: Amplitude response from breast volumes in frequency domain at $\theta = 105^\circ$, $\varphi_t = \varphi_r = 240^\circ$. (a) S_{VV} , (b) S_{HH} , (c) $S_{HV} = S_{VH}$, (d) S_{LL} , (e) S_{RR} , and (f) $S_{RL} = S_{LR}$.

$$\begin{aligned}
 S_{AB,\text{diff,phase}}(f, \varphi_t, \varphi_r) &= |\angle S_{AB,\text{ref}}(f, \varphi_t, \varphi_r) - \angle S_{AB,\text{tumor}}(f, \varphi_t, \varphi_r)|, \\
 MD_{AB,\text{phase}}(\varphi_t, \varphi_r) &= \frac{\left[\sum_{f=\Delta f}^{N\Delta f} S_{AB,\text{diff,phase}}(f, \varphi_t, \varphi_r) \right]}{N}.
 \end{aligned} \tag{6}$$

Here, the absolute phase difference is given in terms of degree. For instance, if the two phase angles are 3° and 357° , respectively, $S_{AB,\text{diff,phase}}(f, \varphi_t, \varphi_r)$ would be equal to 6° instead of 354° . As a result, the maximum and minimum value would be 180° and 0° , respectively. The objective here is to quantify the changes of the phase angle when the tumor is included. The direction of clockwise or anticlockwise is not of interest. The results are shown in Figures 7(a) to 7(h). Similar conclusions can be drawn from the visual inspections of the figures: (i) larger maximum values of $MD_{AB,\text{phase}}(\varphi_t, \varphi_r)$ for LL and RR than VV and HH, (ii)

visually the figures look more heterogeneous for LL and RR than VV and HH which probably shows that on average the data contrast of LL and RR is higher (we will come back to it later), (iii) most differences occur along the diagonals which shows that it is important for the back-scattered data, (iv) relatively large contrast also occur at the two second diagonals that correspond to the two-dimensional direct transmission path, (v) significant contrast under VH and HV data. In addition, it is also worth noting that such high values shown in Figures 6 and 7 occur at $\varphi_t = \varphi_r \approx 220^\circ - 260^\circ$ but not $\varphi_t = \varphi_r = 40^\circ - 60^\circ$, which is where the tumor is located ($\varphi_t = \varphi_r = 45^\circ$). To understand this, the breast volume under the two excitations with vertically polarized electric field and the corresponding current distributions at 2 GHz are shown in Figures 8(a) to 8(c). The problem is first shown in Figure 2(d). For the case without a tumor, the breast volume is symmetric and thus the current distribution under the excitation of $\varphi = 45^\circ$ is a mirror image of that under the excitation of $\varphi = 225^\circ$. The current distributions for the cases of (i) without the tumor under the excitation of $\theta = 105^\circ$, $\varphi = 45^\circ$, with the 5 mm tumor under the excitation

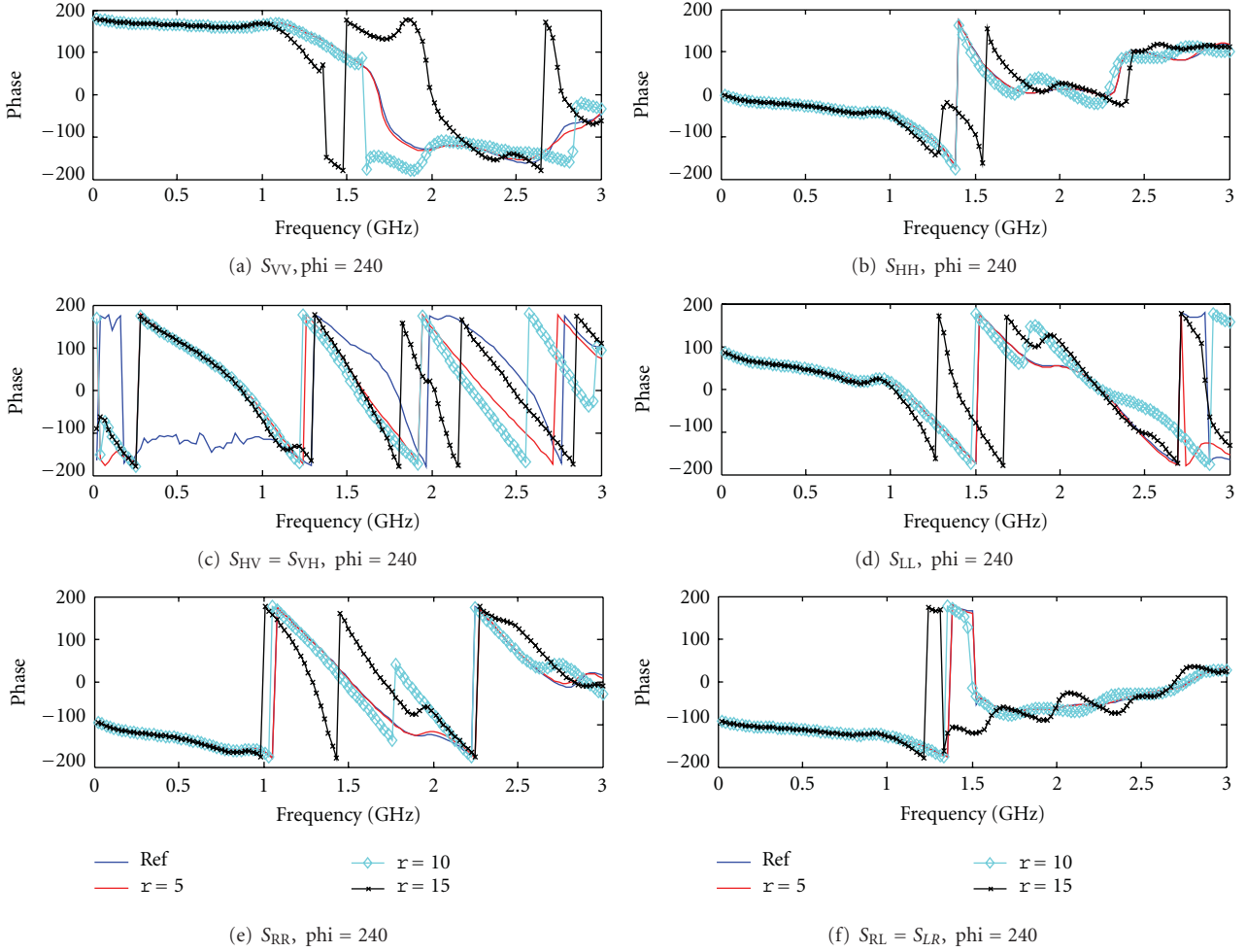


FIGURE 5: Phase amplitude response from breast volumes in frequency domain at $\theta = 105^\circ$, $\varphi_t = \varphi_r = 240^\circ$. (a) S_{VV} , (b) S_{HH} , (c) $S_{HV} = S_{VH}$ (d) S_{LL} , (e) S_{RR} , and (f) $S_{RL} = S_{LR}$.

of (ii) $\theta = 105^\circ$, $\varphi = 45^\circ$, and of (iii) $\theta = 105^\circ$, $\varphi = 225^\circ$ are shown in Figures 8(a) to 8(c), respectively. For a fair visual comparison, the figures are set to the same intensity scale from 0 mA/m to 13.50 mA/m. When the breast volume is illuminated from $\theta = 105^\circ$, $\varphi = 45^\circ$, it is observed that the maximum amplitude of the induced current is increased when the tumor is introduced. In particular, the maximum current amplitude is located at the tumor with ~ 7.5 mA/m. When the excitation changes to $\theta = 105^\circ$, $\varphi = 225^\circ$, the maximum current is again located at the tumor and is now increased to ~ 13.50 mA/m. Comparing the current distribution of the tumor under the two different excitation, on average the current distribution is higher in the latter case which shows that the tumor is better illuminated. The above observation can be explained by the fact that the complexity of the scattering phenomena inside the breast volume. First, the breast surface is curvative and the reflection coefficient (air-breast volume) varies as a function of incident angles, frequency and polarization. Due to the curvative nature of the breast surface, the breast volume is not evenly illuminated even under plane wave illumination. Second, the higher-order electromagnetic interactions between the tumor and

the breast volume (tumor-breast interface) and the air-breast interface could help focusing the energy toward the tumor. In general, such higher-order interactions are complicated and cannot be easily analyzed. To sum up, using full-wave electromagnetic simulation, it is found that the larger amplitude of the induced current on the tumor and the better data contrast of the copolarized response are resulted under the illumination of $\theta = 105^\circ$, $\varphi = 225^\circ$.

4.3. Cases with Tumors with Lower Contrast. A large-scale study about experimental measurements of dielectric properties of tumors has been conducted and reported in [26, 27]. The results have shown that the dielectric properties are far much lower than the earlier findings with 300% or even 500% of contrast. With this in mind, we would like to investigate how the contrast could affect the forward data. Here, tumors with relative permittivity of $\epsilon_r = 40$ down to $\epsilon_r = 15$, with the conductivity of $\sigma = 0.1$ S/m, together with the previous cases, will be considered.

In order to get an overall picture about the differences of the amplitude and phase response for each polarization

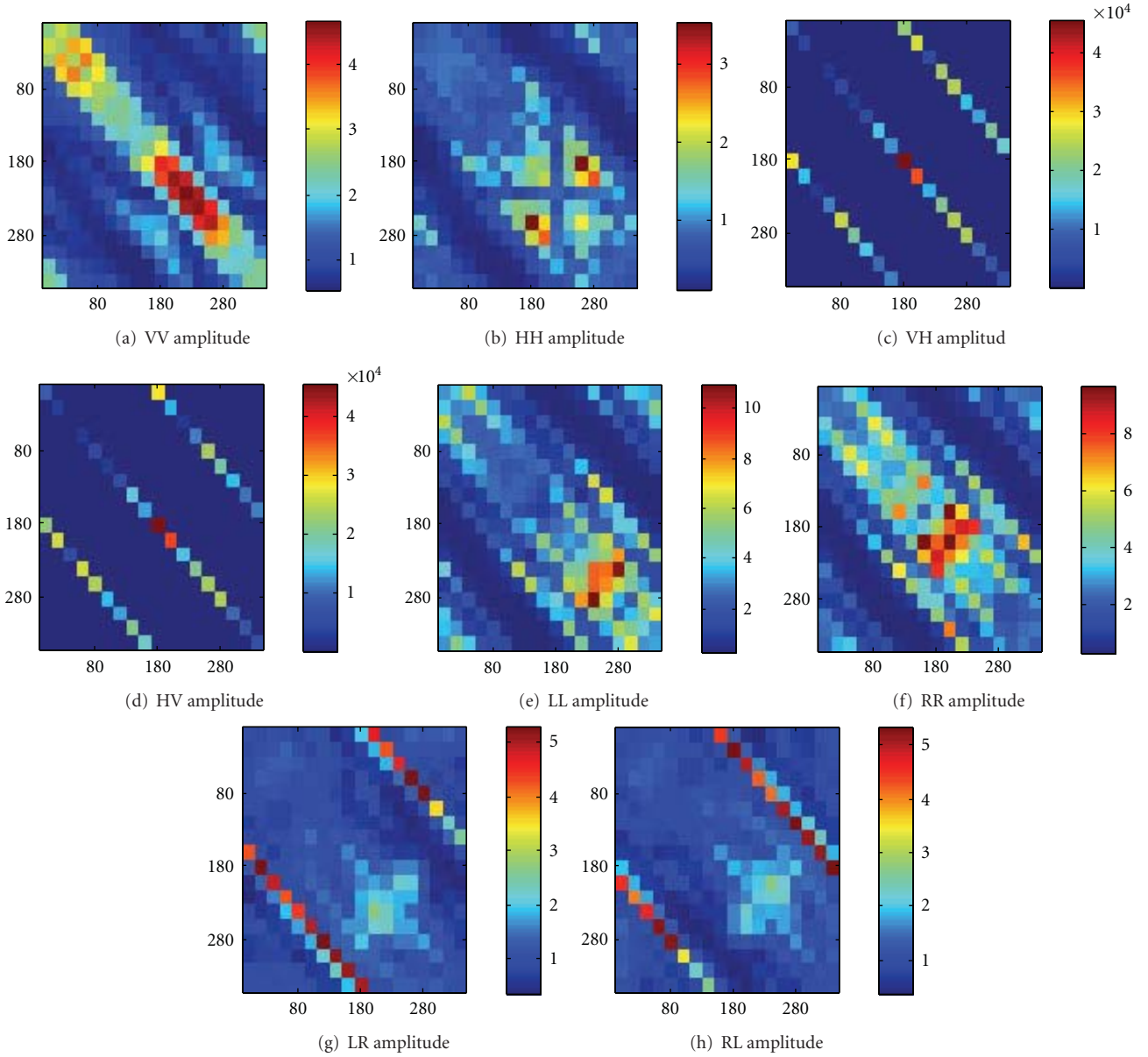


FIGURE 6: $MD_{AB,amplitude}$ for different transmitter/receiver combinations. The comparison is made between the reference data (no tumor) with the case with 5 mm tumor with the dielectric properties given in Figure 3. (a) VV, (b) HH, (c) HV, (d) VH, (e) LL, (f) RR, (g) RL, and (h) LR. The vertical axis corresponds to the aspects of the incidence ($\varphi_t = 0^\circ$ to 340°) and the horizontal axis corresponds to the aspects of the scattered far field ($\varphi_r = 0^\circ$ to 340°).

states, the mean values of MD_{xy} , denoted as MMD_{xy} , can be given by

$$MMD_{AB,amplitude} = \frac{\left[\sum_{\varphi_r=0^\circ}^{340^\circ} \sum_{\varphi_t=0^\circ}^{340^\circ} MD_{AB,amplitude}(\varphi_t, \varphi_r) \right]}{[N_{tx} \times N_{rx}]},$$

$$MMD_{AB,phase} = \frac{\left[\sum_{\varphi_r=0^\circ}^{340^\circ} \sum_{\varphi_t=0^\circ}^{340^\circ} MD_{AB,phase}(\varphi_t, \varphi_r) \right]}{[N_{tx} \times N_{rx}]}. \quad (7)$$

The corresponding results are shown in Figures 9(a) and 9(f). Figure 9(a) shows the $MMD_{AB,amplitude}$ for the cases

with 5 mm tumor ($r = 5$) but with different dielectric properties of (i) Debye, (ii) $\varepsilon_r = 40$, $\sigma = 0.1$ S/m, (iii) $\varepsilon_r = 30$, $\sigma = 0.1$ S/m, (iv) $\varepsilon_r = 20$, $\sigma = 0.1$ S/m, and (v) $\varepsilon_r = 15$, $\sigma = 0.1$ S/m. As the contrast increases, higher values of $MMD_{AB,amplitude}$ s result which indicates that contrast does play a role here. It is interesting to see that the increase of the dielectric contrast gives a proportional change of the data contrast for the same tumor size. For instance, as the relative permittivity changes from 30 to 40, the $MMD_{xy,amplitude}$ values for the 5 mm tumor (Figure 9(a)) and 10 mm tumor (Figure 9(b)) increase from 1.5% to 2% and 10% to 15% (about one third) for LL and RR

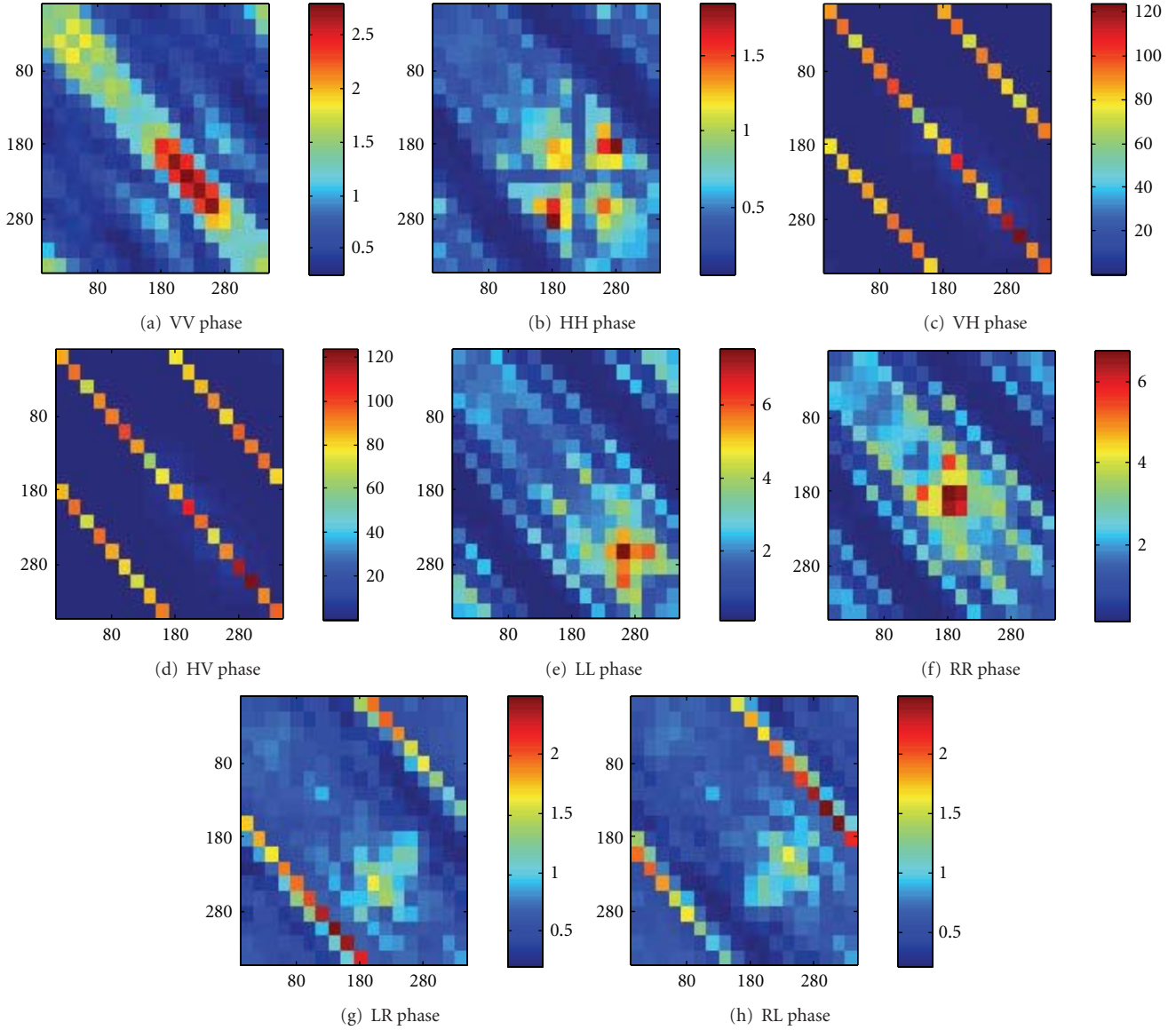


FIGURE 7: $MD_{AB,phase}$ for different transmitter/receiver combinations. The comparison is made between the reference data (no tumor) with the case with 5 mm tumor with the dielectric properties given in Figure 3(b). (a) VV, (b) HH, (c) HV, (d) VH, (e) LL, (f) RR, (g) RL and (h) LR. The vertical axis corresponds to the aspects of the incidence ($\varphi_t = 0^\circ$ to 340°) and the horizontal axis corresponds to the aspects of the scattered far-field ($\varphi_r = 0^\circ$ to 340°).

polarization states. However, the maximum data contrast that can be obtained for the 5 mm tumor is less than 2.5% with the maximum dielectric contrast of approximately 5. Next, we consider the results for the 10 mm tumor ($r = 10$) and the 15 mm tumor ($r = 15$) shown in Figures 9(b) and 9(c), respectively. As the tumor size increases, $MMD_{xy,amplitude}$ values increase from $<2.5\%$ to $\sim 15\%$ and $\sim 30\%$, respectively. This again shows that the contrast is more significant with larger tumor. The results here indicate that the tumor size plays a relatively more important role in terms of the “contrast of the forward data” than the dielectric contrast of the tumor with the background. If we consider the case of a 5 mm tumor (Figure 9(a)), increasing the contrast from 1.5 times ($\epsilon_{r,tumor}/\epsilon_{r,tissue} \approx 15/10 = 1.5$)

to 5 ($\epsilon_{r,tumor}/\epsilon_{r,tissue} \approx 50/10 = 5$) times could perhaps raise increasing the data contrast from 0.5% to 2%, but increasing the tumor size (from 5 mm to 15 mm radius) can significantly increase the contrast to up to 10%. Similar conclusions can also be drawn for the phase responses shown in Figures 9(d) to 9(f).

Compare to our previous visual observations, for the same tumor size, the results from the LL and RR polarization states have larger $MMD_{AB,amplitude}$ and $MMD_{AB,phase}$ values than the other polarization states which indicates higher level of contrast in the forward data. For the 5 mm tumor, VV has got a larger $MMD_{AB,amplitude}$ and $MMD_{AB,phase}$ than those of HH, VH, HV, RL, and LR. Such findings further confirm the observations we had made earlier.

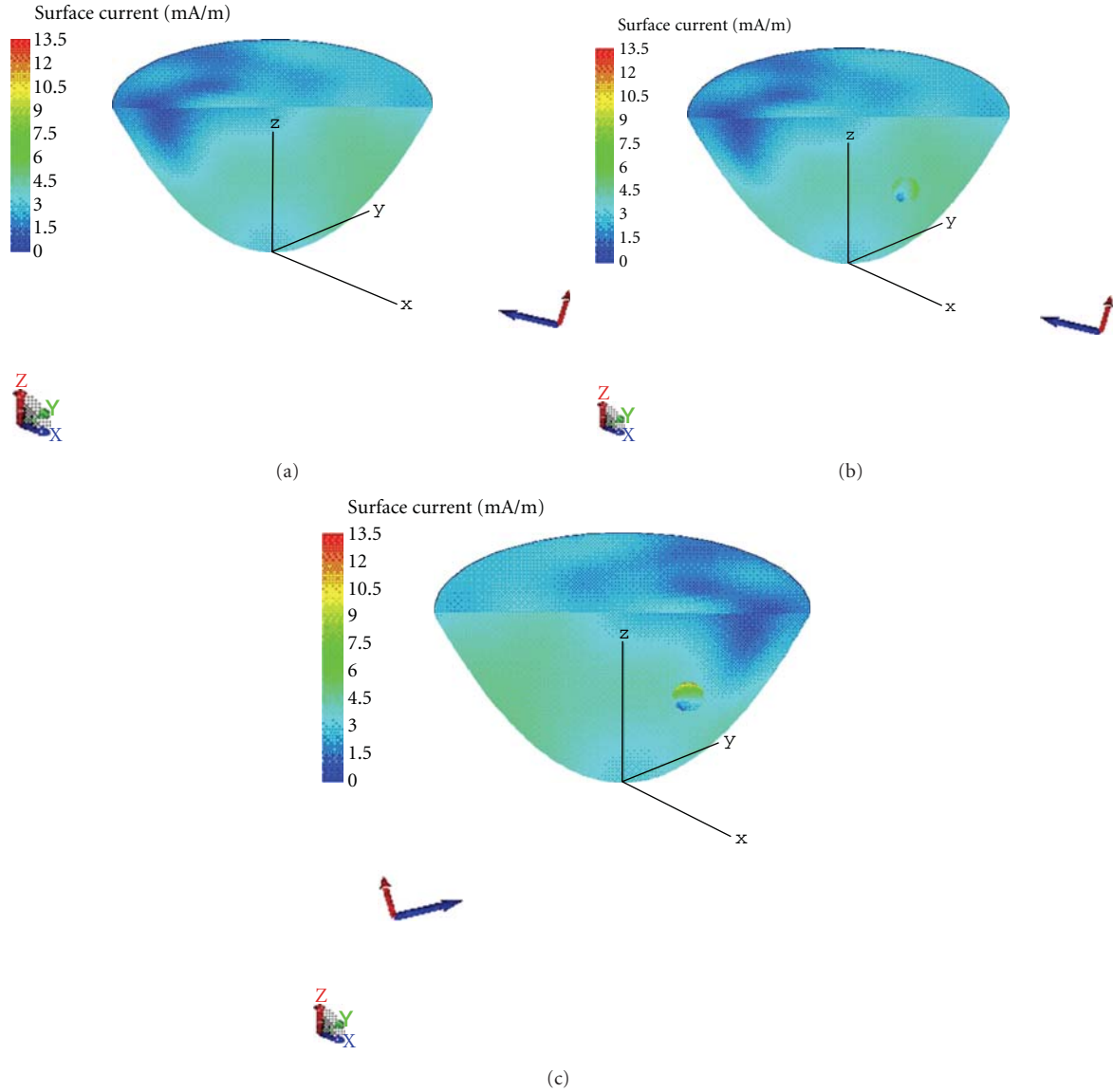


FIGURE 8: (a) Current distribution of the breast volume under the plane wave excitation with vertical polarized electric field from the aspect of $\theta_t = 105^\circ$, $\varphi_t = 45^\circ$. (b) Current distribution of the breast volume with the 5 mm tumor under the plane wave excitation with vertical polarized electric field from the aspect of $\theta_t = 105^\circ$, $\varphi_t = 45^\circ$. (c) Current distribution of the breast volume with the 5 mm tumor under the plane wave excitation with vertical polarized electric field from the aspect of $\theta_t = 105^\circ$, $\varphi_t = 225^\circ$.

The results for VH and HV are plotted separately in Figure 10 as the values of $MMD_{AB,amplitude}$ are much higher than the other polarization states, ranging from 100% up to 2000%. Such high values of $MMD_{AB,amplitude}$ are due to the fact that VH and HV responses are theoretically zero due to the geometrical symmetric feature of the breast volume when there is no tumor. Figure 10(a) shows the $MMD_{AB,amplitude}$ values under HV polarization state. The horizontal axis corresponds to the tumor size and the three lines correspond to tumor with different dielectric properties. Similar to the previous findings, the $MMD_{AB,amplitude}$ values increase with the tumor size. Increasing the dielectric contrast could increase the contrast of the forward data, but for small tumor (5 mm), increasing the dielectric contrast does not

give much changes to the dataset with relatively small variations of $MMD_{AB,amplitude}$ and $MMD_{AB,phase}$ shown in Figures 10(a) and 10(b). The same conclusions are drawn for HV polarization states, as shown in Figures 10(c) and 10(d).

4.4. Feasibility Measures in Terms of Signal Level. The above findings show that the higher contrast of the forward data can be obtained under the copolarized case for circular polarization basis and cross-polarized cases for linear polarization basis. The next question we have to answer is if it is possible to measure the signal, especially for the VH and HV cases as the signal level could be very low (the high $MMD_{AB,amplitude}$ values are due to the null response when there is no tumor). In view of this, the mean and minimum

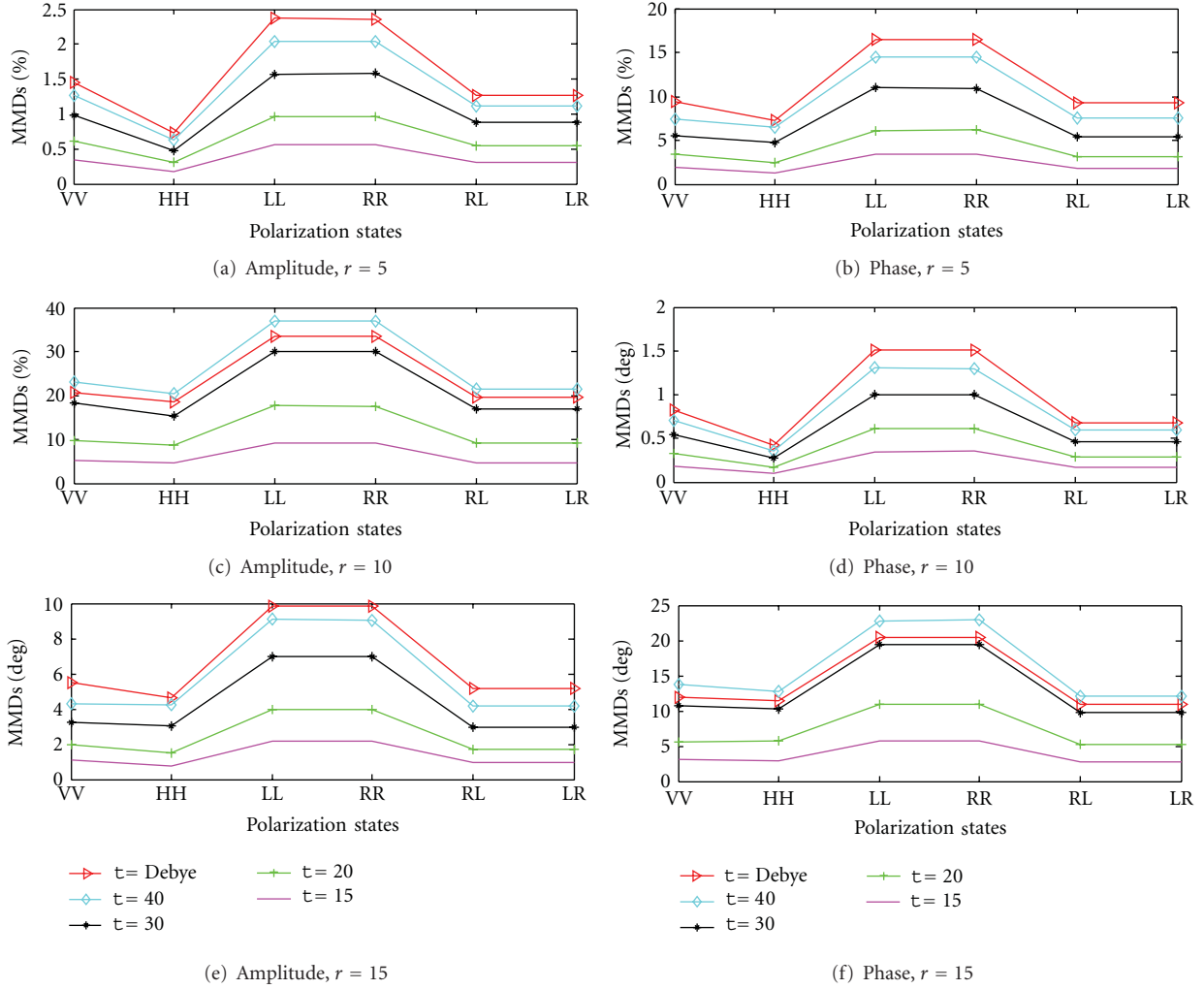


FIGURE 9: MMD_{AB} for different polarization states with tumor of different sizes. In each figure, three different dielectric properties of the tumor are considered (i) Debye (Figure 3), (ii) $\epsilon_r = 40$, $\sigma = 0.1$ S/m, (iii) $\epsilon_r = 30$, $\sigma = 0.1$ S/m, (iv) $\epsilon_r = 20$, $\sigma = 0.1$ S/m, and (v) $\epsilon_r = 15$, $\sigma = 0.1$ S/m. $MMD_{AB, \text{amplitude}}$ for tumor with radius of (a) 5 mm, (b) 10 mm, and (c) 15 mm. $MMD_{AB, \text{phase}}$ for tumor with radius of (d) 5 mm, (e) 10 mm, and (f) 15 mm.

values of the scattering parameters as a function of frequency are introduced and given by

$$\begin{aligned}
 S_{AB, \text{mean}}(f) &= \frac{\left[\sum_{\phi_r=0^\circ}^{340^\circ} \sum_{\phi_t=0^\circ}^{340^\circ} 20 \log_{10} |S_{AB}(f, \phi_t, \phi_r)| \right]}{[N_{tx} \times N_{rx}]} \\
 &= \frac{\left[\sum_{\phi_r=0^\circ}^{340^\circ} \sum_{\phi_t=0^\circ}^{340^\circ} 20 \log_{10} \left| \frac{E_{r,B}(f, \phi_t, \phi_r)}{E_{t,A}(f, \phi_t, \phi_r)} \right| \right]}{[N_{tx} \times N_{rx}]}, \\
 S_{AB, \text{min}}(f) &= \min \left\{ 20 \log_{10} |S_{AB}(f, \phi_t, \phi_r)| \right\} \\
 &= \min \left\{ 20 \log_{10} \left| \frac{E_{r,B}(f, \phi_t, \phi_r)}{E_{t,A}(f, \phi_t, \phi_r)} \right| \right\}.
 \end{aligned} \tag{8}$$

The results shown in Figures 11(a) to 11(d) are the case of the breast volume with the 5 mm tumor with the properties of $\epsilon_r = 15$, $\sigma = 0.1$ S/m, that is, the case with the small-

est tumor and lowest dielectric contrast. For both linear and circular polarization states, the mean values of the scattering parameters are within 60 dB dynamic range when the frequency is above 500 MHz. The minimum values of the scattering parameters are shown in Figures 11(c) and 11(d). The results show that the minimum values of the scattering parameters are within -80 dB below the transmitting signal for circular polarization states, as well as VV and HH (above 500 MHz). For VH and HV, however, it goes far below -100 dB which could be difficult to measure. With the current state-of-the-art of VNA, we are able to measure signals down to -130 dB accurately. In practice, however, together with practical considerations such as antenna mismatch and cable loss, the signals level would be at least another 10 dB to 15 dB lower. As a result, accurate measurement of VH and HV signals for breast volumes with small tumors is not easy to achieve using VNA. Proper design of the receiving modules with matching antenna and front-end electronics becomes significantly crucial. On the other

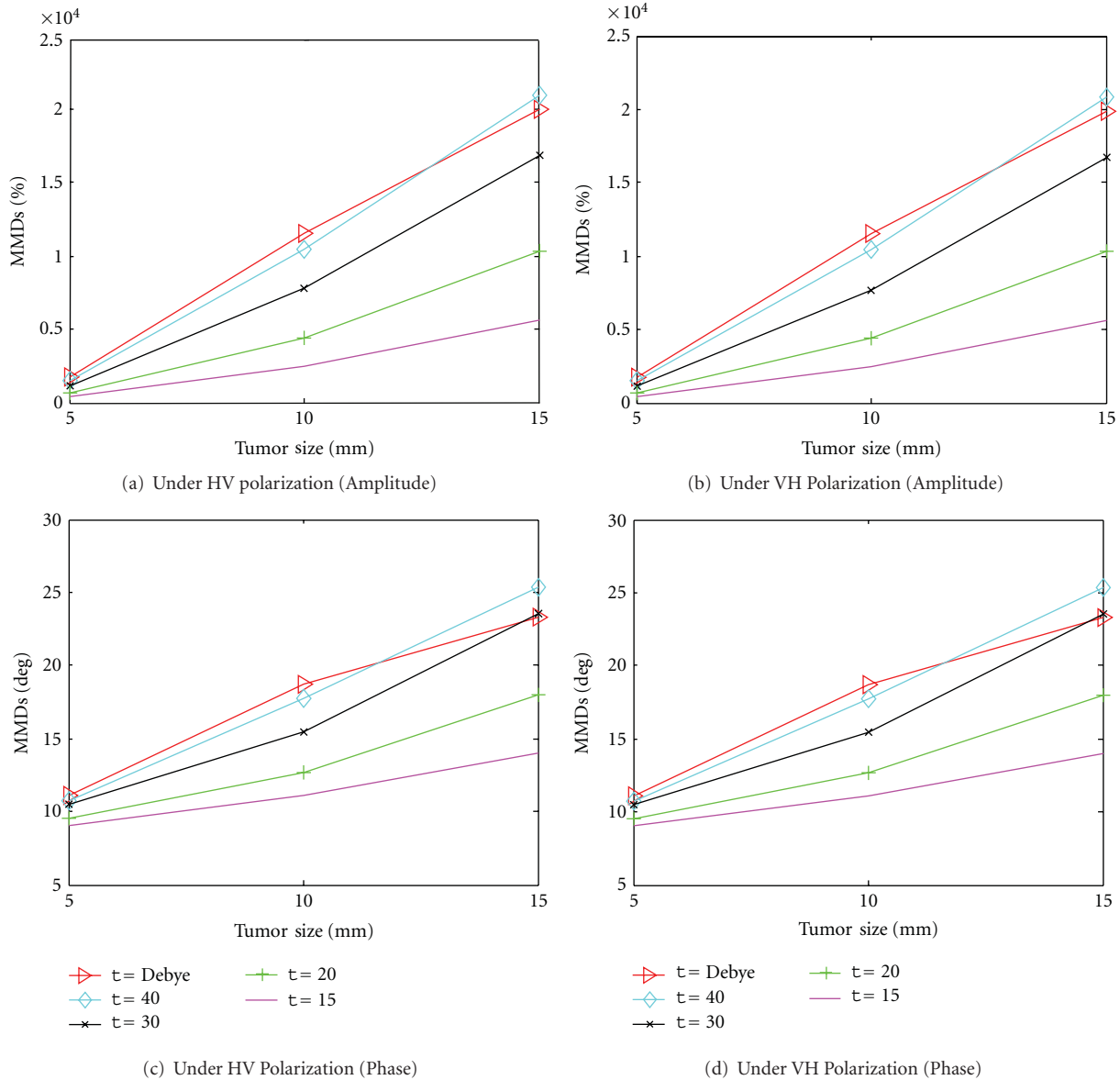


FIGURE 10: $MMD_{AB,amplitude}$ and $MMD_{AB,phase}$ for the scattering problems with tumor of different sizes. In each figure, three different dielectric properties of the tumor are considered (i) Debye (Figure 3), (ii) $\epsilon_r = 40$, $\sigma = 0.1$ S/m, (iii) $\epsilon_r = 30$, $\sigma = 0.1$ S/m, (iv) $\epsilon_r = 20$, $\sigma = 0.1$ S/m, and (v) $\epsilon_r = 15$, $\sigma = 0.1$ S/m. (a) $MMD_{AB,amplitude}$ for HV polarization state, (b) $MMD_{AB,amplitude}$ for VH polarization state, (c) $MMD_{AB,phase}$ for HV polarization state, (d) $MMD_{AB,phase}$ for VH polarization state.

hand, it would be feasible to measure the circular polarized signals using VNA (>500 MHz, minimum values between -60 dB to -80 dB + another 20 dB losses for mismatches).

5. Discussions and Conclusions

UWB forward scattering data from breast volumes with different tumor sizes and different dielectric properties are studied. Based on the configurations of the forward scattering study in this paper, several points can be summarized. To achieve good contrast of the amplitude and phase responses of the forward data between the cases with and without tumor, the excitation frequency should be at least 1 GHz as

the lower-frequency components correspond mainly to the scattering from the entire breast volume. At the same time, the return signal level is relative low when the frequency is below 500 MHz. This shows that the breast volume is not well excited. Secondly, it is also found that there are higher contrast of the scattering data in the back-scattered direction for all cases and the direct path for cross polarized cases. This implies the importance of having the back scattered field and the direct path response in the microwave imaging setup. Thirdly, comparing the forward scattering data under different polarization states and basis, VH and HV components have the highest contrast due to the geometrical symmetry when there is no tumor inside the breast volume. Regarding

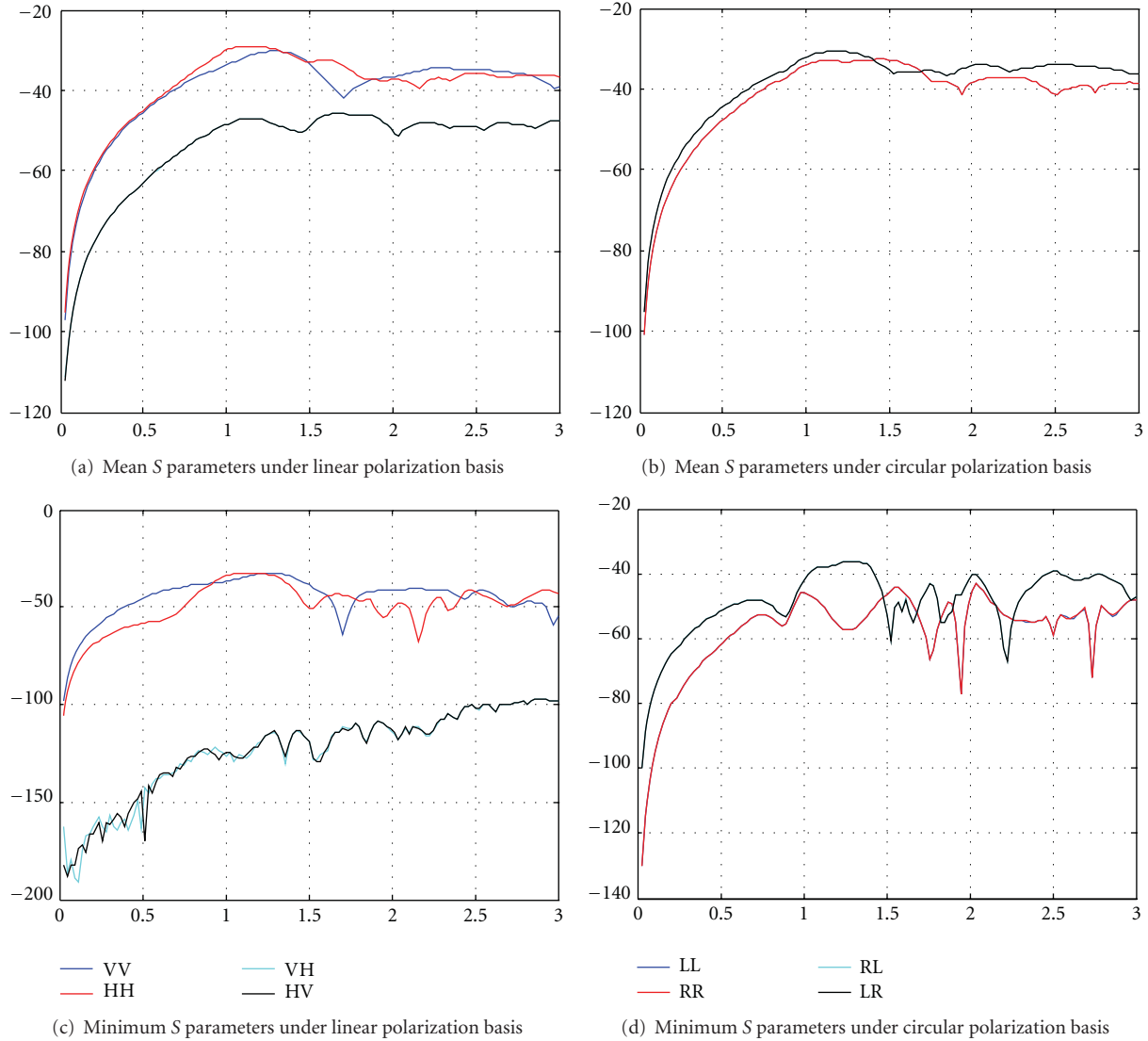


FIGURE 11: $S_{AB,\text{mean}}(f)$ and $S_{AB,\text{min}}(f)$ for the scattering problem of the breast volume with a 5 mm tumor with the dielectric properties of $\epsilon_r = 15$, $\sigma = 0.1$ S/m. (a) $S_{AB,\text{mean}}(f)$ for linear polarization states, (b) $S_{AB,\text{mean}}(f)$ for circular polarization states, (c) $S_{AB,\text{min}}(f)$ for linear polarization states and (d) $S_{AB,\text{min}}(f)$ for circular polarization states.

other polarization states, the LL and RR polarization states give better data contrast than the others. Potentially, LL and RR can be used for microwave imaging using existing VNA that can give reasonable accuracies with more than 100 dB of dynamic range. If one would like to use VH and HV, proper design of front-end microwave circuits and antenna are needed such that the mismatch can be minimized.

This work opens the door for further investigations of better datasets for the microwave breast imaging by considering different polarization states and basis. Although the setup is relatively simple with homogenous breast volume, surprisingly it is found that the existence of small tumor ($r = 5$ mm) is not highly revealed in the forward data even if the dielectric contrast is about 5 times. Potentially, better data contrast could be obtained for small tumor with

higher excitation frequency, but at the same time attenuation increases. Our previous study on a similar problem has found that the conductivity of human tissue can significantly attenuate the higher-order interactions of metallic objects inside human tissue when the excitation frequency goes beyond 4 GHz [32–35]. As a result, higher excitation frequencies were not considered in this work. Future work needs to focus on practical issues such as the choice of polarization states, antenna elements, array configurations, matching liquid, and more realistic tissue model in the simulation [26, 27]. At the same time, the results here for VH and HV only apply for homogenous breast models. To investigate the feasibilities of using linear cross-polarized signals, we also need to use anatomically and electromagnetically realistic breast model in future simulations.

Acknowledgments

This work was supported by the Swedish Research Council under Grant no. 2010-7262-78830-59. The authors would particularly like to acknowledge the comprehensive and useful comments of the reviewers and editor of this paper.

References

- [1] E. C. Fear and M. A. Stuchly, "Microwave detection of breast cancer," *IEEE Transactions on Microwave Theory and Techniques*, vol. 48, no. 1, pp. 1854–1863, 2000.
- [2] E. C. Fear, S. C. Hagness, P. M. Meaney, M. Okoniewski, and M. A. Stuchly, "Enhancing breast tumor detection with near-field imaging," *IEEE Microwave Magazine*, vol. 3, no. 1, pp. 48–56, 2002.
- [3] S. C. Hagness, A. Taflove, and J. E. Bridges, "Two-dimensional FDTD analysis of a pulsed microwave confocal system for breast cancer detection: fixed-focus and antenna-array sensors," *IEEE Transactions on Biomedical Engineering*, vol. 45, no. 12, pp. 1470–1479, 1998.
- [4] X. Li and S. C. Hagness, "A confocal microwave imaging algorithm for breast cancer detection," *IEEE Microwave and Wireless Components Letters*, vol. 11, no. 3, pp. 130–132, 2001.
- [5] E. C. Fear, X. Li, S. C. Hagness, and M. A. Stuchly, "Confocal microwave imaging for breast cancer detection: localization of tumors in three dimensions," *IEEE Transactions on Biomedical Engineering*, vol. 49, no. 8, pp. 812–822, 2002.
- [6] X. Li, S. K. Davis, S. C. Hagness, D. W. Van Der Weide, and B. D. Van Veen, "Microwave imaging via space-time beamforming: experimental investigation of tumor detection in multilayer breast phantoms," *IEEE Transactions on Microwave Theory and Techniques*, vol. 52, no. 8, pp. 1856–1865, 2004.
- [7] X. Li, E. J. Bond, B. D. Van Veen, and S. C. Hagness, "An overview of ultra-wideband microwave imaging via space-time beamforming for early-stage breast-cancer detection," *IEEE Antennas and Propagation Magazine*, vol. 47, no. 1, pp. 19–34, 2005.
- [8] J. M. Sill and E. C. Fear, "Tissue sensing adaptive radar for breast cancer detection: study of immersion liquids," *Electronics Letters*, vol. 41, no. 3, pp. 113–115, 2005.
- [9] J. M. Sill and E. C. Fear, "Tissue sensing adaptive radar for breast cancer detection—experimental investigation of simple tumor models," *IEEE Transactions on Microwave Theory and Techniques*, vol. 53, no. 11, pp. 3312–3319, 2005.
- [10] W. C. Khor, M. E. Bialkowski, A. Abbosh, N. Seman, and S. Crozier, "An ultra wideband microwave imaging system for breast cancer detection," *IEICE Transactions on Communications*, vol. E90-B, no. 9, pp. 2376–2381, 2007.
- [11] R. Nilavalan, A. Gbedemah, I. J. Craddock, X. Li, and S. C. Hagness, "Numerical investigation of breast tumour detection using multi-static radar," *Electronics Letters*, vol. 39, no. 25, pp. 1787–1789, 2003.
- [12] M. Klemm, I. J. Craddock, J. A. Leendertz, A. Preece, and R. Benjamin, "Radar-based breast cancer detection using a hemispherical antenna array—experimental results," *IEEE Transactions on Antennas and Propagation*, vol. 57, no. 6, pp. 1692–1704, 2009.
- [13] Q. Fang, P. M. Meaney, S. D. Geimer, A. V. Streltsov, and K. D. Paulsen, "Microwave image reconstruction from 3-D fields coupled to 2-D parameter estimation," *IEEE Transactions on Medical Imaging*, vol. 23, no. 4, pp. 475–484, 2004.
- [14] T. Rubæk, P. M. Meaney, P. Meincke, and K. D. Paulsen, "Non-linear microwave imaging for breast-cancer screening using Gauss-Newton's method and the CGLS inversion algorithm," *IEEE Transactions on Antennas and Propagation*, vol. 55, no. 8, pp. 2320–2331, 2007.
- [15] T. Rubæk, O. S. Kim, and P. Meincke, "Computational validation of a 3-D microwave imaging system for breast-cancer screening," *IEEE Transactions on Antennas and Propagation*, vol. 57, no. 7, pp. 2105–2115, 2009.
- [16] A. Fhager, P. Hashemzadeh, and M. Persson, "Reconstruction quality and spectral content of an electromagnetic time-domain inversion algorithm," *IEEE Transactions on Biomedical Engineering*, vol. 53, no. 8, Article ID 1658154, pp. 1594–1604, 2006.
- [17] A. Fhager and M. Persson, "Using a priori data to improve the reconstruction of small objects in microwave tomography," *IEEE Transactions on Microwave Theory and Techniques*, vol. 55, no. 11, pp. 2454–2462, 2007.
- [18] A. Fhager, *Microwave tomography*, Ph.D. thesis, Department of Signals and Systems, Chalmers University of Technology, Göteborg, Sweden, 2006.
- [19] J. D. Shea, P. Kosmas, S. C. Hagness, and B. D. Van Veen, "Contrast-enhanced microwave imaging of breast tumors: a computational study using 3D realistic numerical phantoms," *Inverse Problems*, vol. 26, article 074009, 2010.
- [20] J. D. Shea, P. Kosmas, S. C. Hagness, and B. D. Van Veen, "Three-dimensional microwave imaging of realistic numerical breast phantoms via a multiple-frequency inverse scattering technique," *Medical Physics*, vol. 37, no. 8, pp. 4210–4226, 2010.
- [21] J. Zhang and E. C. Fear, "Preliminary investigation of breast tumor detection using cross-Vivaldi antenna," in *Proceedings of the 29th Annual International Conference of the Engineering in Medicine and Biology Society (EMBS '05)*, September 2005.
- [22] S. Noghianian and I. Craddock, "Microwave imaging's practical issues," in *Special sessions in IEEE International Symposium on Antennas and Propagation*, Toronto, Ontario, Canada, July 2010.
- [23] X. Zeng, A. Fhager, M. Persson, P. Linner, and H. Zirath, "Accuracy evaluation of ultra-wideband time domain measurement systems for microwave imaging," *IEEE Transactions on Antennas and Propagation*, vol. 59, no. 11, pp. 4279–4285, 2011.
- [24] X. Zeng, A. Fhager, P. Linner, M. Persson, and H. Zirath, "Experimental investigation of the accuracy of an ultra-wideband time domain microwave tomography system," *IEEE Transactions on Instrumentation and Measurement*, vol. 60, no. 12, pp. 3939–3949, 2011.
- [25] Z. Q. Zhang, Q. H. Liu, C. Xiao, E. Ward, G. Ybarra, and W. T. Joines, "Microwave breast imaging: 3-D forward scattering simulation," *IEEE Transactions on Biomedical Engineering*, vol. 50, no. 10, pp. 1180–1189, 2003.
- [26] M. Lazebnik, L. McCartney, D. Popovic et al., "A large-scale study of the ultrawideband microwave dielectric properties of normal breast tissue obtained from reduction surgeries," *Physics in Medicine and Biology*, vol. 52, no. 10, article 001, pp. 2637–2656, 2007.
- [27] M. Lazebnik, D. Popovic, L. McCartney et al., "A large-scale study of the ultrawideband microwave dielectric properties of normal, benign and malignant breast tissues obtained from cancer surgeries," *Physics in Medicine and Biology*, vol. 52, no. 20, pp. 6093–6115, 2007.
- [28] M. Pastorino, *Microwave Imaging*, John Wiley & Sons, 2010.

- [29] W. M. Boerner, M. B. El-Arini, C. Y. Chan, and P. M. Mastoris, "Polarization dependence in electromagnetic inverse problems," *IEEE Transactions on Antennas and Propagation*, vol. AP-29, no. 2, pp. 262–271, 1981.
- [30] FEKO EM Software & Systems S.A., (Pty) Ltd, 32 Techno Lane, Technopark, Stellenbosch, 7600, South Africa.
- [31] H. Mott, *Remote Sensing with Polarmetric Radar*, Wiley-IEEE Press, New York, NY, USA, 2007.
- [32] H. S. Lui and N. V. Z. Shuley, "Detection of depth changes of a metallic target buried in a frequency-dependent lossy half-space using the E-pulse technique," *IEEE Transactions on Electromagnetic Compatibility*, vol. 49, no. 4, pp. 868–875, 2007.
- [33] H. S. Lui, N. V. Z. Shuley, and A. D. Rakic, "A novel, fast, approximate target detection technique for metallic target below a frequency dependant lossy halfspace," *IEEE Transactions on Antennas and Propagation*, vol. 58, no. 5, Article ID 5422612, pp. 1669–1710, 2010.
- [34] H. S. Lui, N. Shuley, and M. Persson, "Joint time-frequency analysis of transient electromagnetic scattering from a sub-surface target," *IEEE Antennas and Propagation Magazine*. In press.
- [35] H. S. Lui, F. Aldhubaib, N. V. Z. Shuley, and H. T. Hui, "Sub-surface target recognition based on transient electromagnetic scattering," *IEEE Antennas and Propagation Magazine*, vol. 57, no. 10, Article ID 5196768, pp. 3398–3401, 2009.

Research Article

A Prototype System for Measuring Microwave Frequency Reflections from the Breast

J. Bourqui, J. M. Sill, and E. C. Fear

Department of Electrical Engineering, Schulich School of Engineering, University of Calgary, Calgary, AB, Canada T2N 1N4

Correspondence should be addressed to J. Bourqui, bourquij@ucalgary.ca

Received 30 September 2011; Accepted 16 January 2012

Academic Editor: Ian Craddock

Copyright © 2012 J. Bourqui et al. This is an open access article distributed under the Creative Commons Attribution License, which permits unrestricted use, distribution, and reproduction in any medium, provided the original work is properly cited.

Microwave imaging of the breast is of interest for monitoring breast health, and approaches to active microwave imaging include tomography and radar-based methods. While the literature contains a growing body of work related to microwave breast imaging, there are only a few prototype systems that have been used to collect data from humans. In this paper, a prototype system for monostatic radar-based imaging that has been used in an initial study measuring reflections from volunteers is discussed. The performance of the system is explored by examining the mechanical positioning of sensor, as well as microwave measurement sensitivity. To gain insight into the measurement of reflected signals, simulations and measurements of a simple phantom are compared and discussed in relation to system sensitivity. Finally, a successful scan of a volunteer is described.

1. Introduction

Microwave imaging has been proposed as an alternative breast imaging modality [1]. The basic premise is that different tissues in the breast have different electromagnetic properties, and these differences may be exploited to create images. General approaches to active microwave imaging include microwave tomography [2] and radar-based methods [3–5]. Microwave tomography involves measuring signals transmitted through the breast and reconstructing images by matching measured data with signals obtained from simulated models containing iteratively updated property estimates. Microwave tomography has been tested with simulations and experimental measurements of phantoms (e.g., [6]) and simulations of realistic breast models [7]. Moreover, a research group at Dartmouth College has performed extensive patient studies with prototype systems. The resulting images have demonstrated average microwave frequency properties that increase with breast density [8], as well as agreement between features detected on microwave images and known clinical histories [9]. Radar-based microwave techniques create images by processing reflections of wideband or ultrawideband (UWB) signals from the breast. These images indicate the presence and

location of significantly scattering objects. Testing of radar-based approaches has involved simulations with realistic breast models [3, 10], testing with phantoms [5, 11, 12] and early-stage clinical investigations [13]. To date, a group at Bristol University has reported imaging of patients using a multistatic radar system. Therefore, in spite of the growing body of literature related to microwave breast imaging, there are very few reports of work with patients or volunteers. This likely reflects the significant technical challenges involved in sensor design and implementation, measurement hardware, and development of patient interfaces.

In this paper, we describe a prototype system that is based on a monostatic radar approach and has been termed the TSAR (tissue sensing adaptive radar) method. The TSAR prototype system differs from previously reported prototype systems for microwave imaging in that a single antenna is scanned around the breast in order to collect data. A multistatic system inherently collects more information than its monostatic counterpart. On the other hand, a single-sensor method can be designed to produce a focused beam increasing the reflected power from small features. Given the potential high attenuation in breast tissues, this is likely beneficial for sensing smaller malignant regions. In addition, a monostatic system allows more relaxed requirements for

the UWB sensor. A larger sensor permits using lower frequencies without limitations due to mutual coupling. The ability to place the sensor at an infinite number of locations around the breast is also very attractive in terms of adaptability to patients, as well as for image reconstruction performance. However these advantages are at the cost of a more complex positioning system and longer repositioning time compared to electronically switched antennas as in [13]. In order to assess the performance of our prototype system, a study is performed of the mechanical sensor positioning, as well as of the microwave measurement sensitivity and perturbation. This provides insight into the capabilities and limitations of the system. Next, we compare simulations and measurements of a simple phantom. While both simulations and experimental work have previously been carried out for tomography and radar-based imaging, only a few papers directly compare simulations and measurements of phantoms (e.g., [6, 14]). Our phantom represents the shape of the breast in a simplified way and consists of one material with an inclusion of a different material. Although the properties of the model differ from those of breast tissues, the phantom has stability in properties and shape that permit evaluation of the repeatability of results. In addition, the reflections from the phantom are interpreted relative to the system sensitivity. After validation, the prototype system is used to collect reflections from volunteers. To gain insight into these measurements, comparison with simulations of volunteer-specific breast models is attempted.

2. Prototype System and Procedure

2.1. System Description. The TSAR prototype system is shown in Figure 1. The prototype consists of a padded bed placed over a cylindrical tank filled with canola oil. The woman to be scanned lies prone on the bed, and a hole in the top of the bed permits one breast to extend into the tank.

The cylindrical tank is filled with canola oil to improve the matching between the breast skin and the sensor attached to a positioning arm. The canola oil exhibits a relative permittivity of 2.5 with a conductivity below 0.04 S/m up to 12 GHz. A laser is also mounted to the positioning arm to record the breast outline. To scan the sensor around the breast, the arm moves vertically and the entire tank rotates. Dimensions of the tank and hole as well as antenna location are provided in Figure 2. The scanning region in the vertical (z) direction spans from 24 mm to 141 mm below the top of the lid. The circular opening in the lid has a diameter of 130 mm while the tip of the sensor is located 70 mm away from the center of the opening to avoid contact with the breast skin. To monitor the scan procedure, a camera is mounted on the side of the tank and transmits images to the operator.

Microwave measurements are collected with a custom antenna. The antenna utilized in this work is a balanced antipodal Vivaldi antenna with a director (BAVA-D) [15]. This antenna has a bandwidth (S_{11} better than -10 dB) from 2.4 to 18 GHz. The director narrows the beam of the antenna compared to a standard BAVA design, thus focusing



FIGURE 1: TSAR system used to scan volunteers.

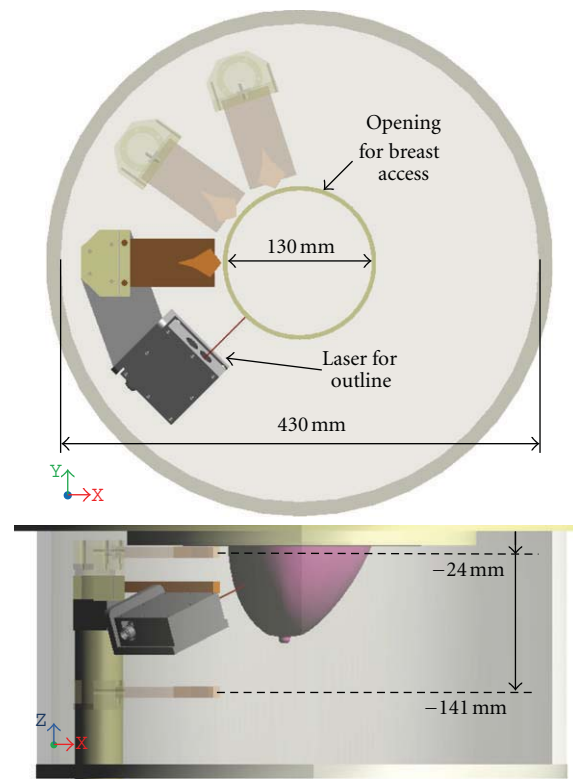


FIGURE 2: Top and side views of the TSAR prototype system tank with dimensions. Additional antenna locations are shown (shaded antenna body) to illustrate the tank rotation and arm movement. For better clarity, the laser is not shown for the additional antenna positions.

more energy into the breast. Measurements are acquired with a vector network analyzer (VNA) (8722ES, Agilent Technologies, Palo Alto, CA, USA). The antenna is connected to the VNA via a 3 m long cable, and a guiding system helps to move the cable in a reproducible way. The cable guiding system is indicated in Figure 1. The system is calibrated at the end of the cable where the antenna is connected. Measurements are taken at 1601 points over the frequency range from 50 MHz to 15 GHz with a port power of -5 dBm. As discussed in Section 3, an intermediate frequency (IF) bandwidth of 1 kHz and averaging over 3 frequency sweeps

are used to reduce the system noise floor. The resulting data are transformed into the time domain after weighting with the spectrum of the differentiated Gaussian pulse given by:

$$V(t) = V_0^*(t - t_0)^* e^{-(t-t_0)/\tau^2}, \quad (1)$$

where V_0 is used to adjust the amplitude of the pulse, $\tau = 62.5$ ps, and $t_0 = 4\tau$.

2.2. Volunteer Scan Procedures. We have scanned several volunteers with the prototype system (Study No. 21859, as approved by the University of Calgary Conjoint Health Research Ethics Board). Our study involves a TSAR scan of one breast, as well as a scan of both breasts with magnetic resonance (MR) imaging. During a TSAR scan, the antenna is physically moved to a number of locations encircling the breast at various elevations (Figure 3). Data collected at the same elevation are termed a row. For a complete scan, data are collected at a number of rows. For the volunteer scan, the number of rows, separation between rows, and number of antenna locations in a row are initially estimated with the MR images, then updated after observing digital images of the breast in the TSAR scanner. Our experience indicates that adjustments to TSAR scan patterns designed with MR images are necessary to compensate for the changes in breast shape and extent due to the flotation of the breast in oil. We note that the rotation of the tank and the vertical movement of the arm used to scan the antenna around the breast are both automated and actuated by step motors, which are controlled by a custom software code. The process of moving the sensors and collecting measurements takes less than 30 minutes for 1 breast scanned at up to 200 antenna locations.

The reflections are calibrated by performing two sets of measurements and then using responses from known objects to orient reflections in time. First, a scan is collected with the volunteer positioned in the scanner and another scan is acquired with an empty tank. To initially calibrate the data, the signals recorded with the empty tank are subtracted from signals recorded with the volunteer present. Identical antenna locations are used with both scans. Next, reflections from metal plates placed at two known distances from the antenna are collected. The differences in time of arrival of the two reflections are used to confirm the dielectric constant of the immersion medium. The known locations of the plates are also used to identify the reflection from the antenna aperture in the signals. The aperture reflection is then located in time in order to identify distances of objects relative to the end of the antenna.

Finally, the reflected signals are used to create images. First, the dominant reflections between the immersion liquid and object (e.g., oil/skin interface) are removed by approximating the reflections at a target antenna. For simple models such as the hemisphere used later in this paper, it is sufficient to use straightforward methods for this approximation. In this case, the reflections recorded at antennas located in the same row are time-shifted and scaled to match the target signal [16]. More sophisticated algorithms are typically required to deal with more complex scenarios. Next, 3D images are formed by scanning the focal point through the

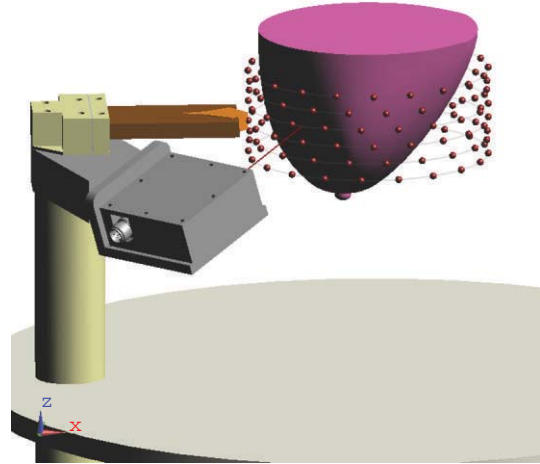


FIGURE 3: View of the scan pattern used for measurement. Each sphere corresponds to an antenna location. Antennas located on a common row are connected by lines.

imaging region and using a time-shift-and-sum beamformer to identify components of the reflections at appropriate antennas that originate from the same physical location [16]. An estimate of the surface of the phantom is incorporated into this focusing procedure [17].

3. System Performance and Validation

As evident from the description in Section 2, the TSAR measurement system is rather complex. Many aspects of the system can alter the measurement quality, which in turn will influence the quality of the reconstructed images. We consider 3 different types of effects: (1) the positioning performance, (2) the microwave measurement sensitivity, and (3) perturbation. In this section, these different aspects are assessed or validated in order to define the overall system performance.

3.1. Positioning Performance. Correct positioning of the sensor is critical in two aspects. First, good mechanical precision is required for repeatability of measurements. As described in Section 2, each scan is calibrated with reference measurements collected during a scan with the exact same pattern but without the volunteer or patient present (empty tank). This operation removes the unwanted effects of the environment (e.g., reflections from the tank) from the measured signals. Therefore, good positioning repeatability is needed to guarantee that the unwanted effects are reproduced between the two scans. Second, good mechanical accuracy is necessary for proper image reconstruction as the signals are spatially focused based on the antenna positions. Good agreement between the desired and actual antenna positions in the scan is therefore required. The positioning precision and accuracy are related to the mechanical play and

TABLE 1: Measured mechanical play for the elevation axis. All values are in mm.

| Test Iteration | Without software compensation | | With software compensation | |
|----------------|-------------------------------|--------|----------------------------|--------|
| | Downward | Upward | Downward | Upward |
| 1 | 0.11 | 0.07 | 0.02 | 0.01 |
| 2 | 0.10 | 0.10 | -0.01 | -0.01 |
| 3 | 0.10 | 0.08 | -0.03 | -0.01 |
| 4 | 0.06 | 0.07 | -0.02 | -0.01 |

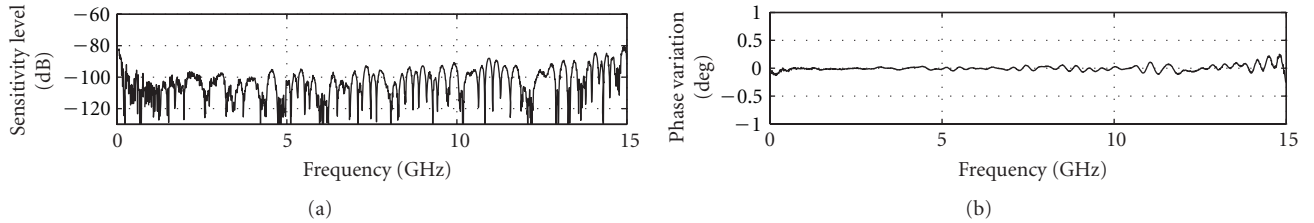


FIGURE 4: Sensitivity calculated using two successive static measurements.

the ability to achieve the correct displacement; both of these parameters will be evaluated.

Two independent axes are used to bring the sensor into position, namely, the azimuth ($^{\circ}$) (tank rotation) and the elevation (mm) (arm movement). Specifications of $\pm 0.1^{\circ}$ and ± 0.1 mm for the displacement tolerance with a mechanical play of maximum 0.1° and 0.1 mm have been defined for each axis. These correspond to no more than 0.6 mm of error when identifying focal points in the worst-case scenario.

In order to validate these requirements, specific movement sequences are realized and expected positions are compared with a measurement of the actual position. For the elevation axis, the position is measured with a digital caliper attached to the moving arm. The assessment of the azimuth position is achieved by measuring the displacement on the outer edge of the rotating tank. Given the very large external diameter of the tank (520 mm), small angular displacements translate into large displacements at its outer edge. Note that the external diameter also includes a lip placed around the tank to collect excess oil, which contributes to the large difference when compared to the inside diameter given in Figure 2. This technique allows us to determine whether the azimuth movement passed or failed the specification, however no numerical values are extracted.

For the elevation axis, the validation shows that the displacement error is within tolerance with a maximum of ± 0.07 mm and an average of ± 0.04 mm. On the other hand, the mechanical play of the elevation axis is, in general, very close to the maximum allowed value and exceeded the limit in one of the test iterations. Therefore, an automated compensation of the mechanical play is implemented in the software used to control the TSAR prototype, showing significant improvement. The measured mechanical play results with and without software compensation are shown in Table 1.

All the azimuth tests passed the specification requirements successfully. However, movement with resolution of

0.25° creates a consistent displacement error that accumulates and creates larger positioning error. This behavior naturally occurs due to the intrinsic angular resolution of the step motor. This behavior is avoided by allowing displacements with a minimum resolution of 0.5° .

3.2. Microwave Measurement Sensitivity. Since the reflections from internal breast tissues are expected to be very weak, good measurement sensitivity is a key aspect of the system. As described in Section 2, the calibrated data result from a subtraction of two successive scans: one with the volunteer present and one with an empty tank. Therefore, the sensitivity can be defined as the smallest signal that can be recovered after the subtraction operation. To assess the sensitivity of the microwave measurement system, a broadband load standard (Agilent 85052D) is connected instead of the antenna and two measured reflected signals are subtracted. Smaller differences correspond to better sensitivity.

The sensitivity is directly influenced by the measurement noise floor of the VNA receiver. Reduction of the IF bandwidth and averaging a number of measurements can significantly improve the noise level. The smallest IF bandwidth with a large amount of averaging would be ideal for sensitivity. However, these actions considerably increase the measurement time to impractical values. The maximum scan time for TSAR is set to 30 minutes for 200 measurements. Accounting for mechanical displacement time, the microwave measurement for each location has to be achieved in 8 seconds for a total of 26.6 minutes dedicated to the RF measurement. An IF bandwidth of 1000 Hz with averaging of 3 signals shows the best sensitivity among the combinations that fit the time criteria. Figure 4 shows the sensitivity that is achieved with these settings and the broadband load attached. A sensitivity below -90 dB is achieved over almost the entire frequency band. The phase variation is below 0.2° with exception of the upper limit

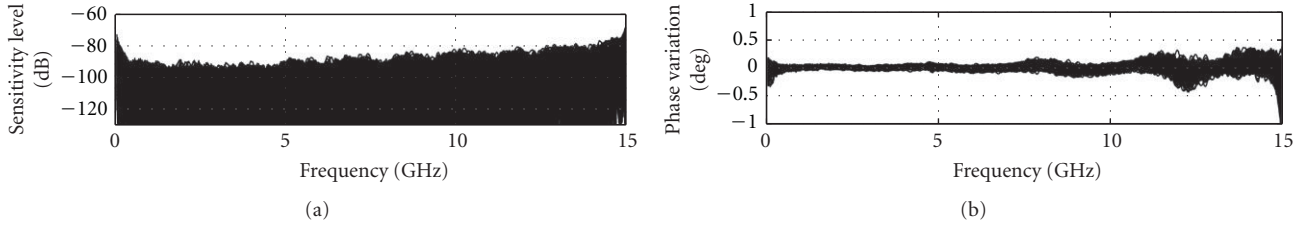


FIGURE 5: Sensitivity calculated based on a pair of 200 static measurements (no change of position) with a broadband load instead of the antenna. Measurement pairs are separated in time by 30 minutes to reproduce the time frame of two consecutive full TSAR scans.

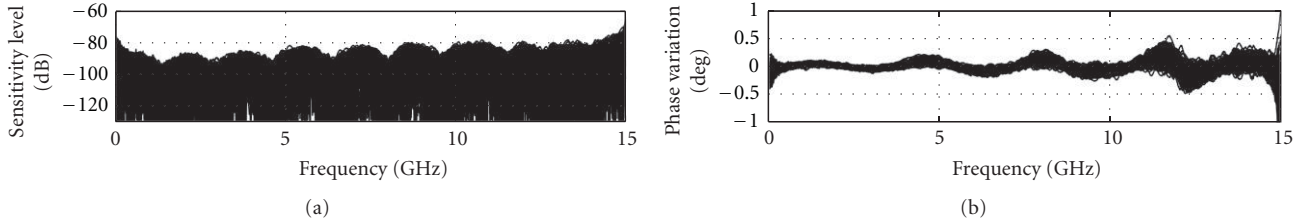


FIGURE 6: Sensitivity calculated based on a pair of full TSAR scans (200 positions) with a broadband load instead of the antenna. The load is physically moved with the prototype system to 200 locations.

of the frequency band. This result can be considered as the best sensitivity that the system can achieve as the two measurements considered are collected in an ideal scenario in which no time elapsed and nothing moved between measurements.

The stability of the reflection measurement with respect to time will also influence the sensitivity. A 30-minute span occurs between the signals measured during the volunteer scan and the calibration scan. To evaluate the effect of this time delay on the sensitivity, 200 successive measurements of the broadband load are collected for two consecutive iterations, replicating the same time frame as a volunteer scan. As in the previous case, the system does not move. Figure 5 shows the 200 corresponding sensitivity curves, which sit mostly below -80 dB except for the extremes of the frequency band. The corresponding phase variation is below 0.5° with an increase towards the end of the spectrum. The correlation between the phase variation and the sensitivity is obvious from Figure 5. Overall we observe that, due to the drift inherent in the VNA, a 30-minute time span between measurements decreases the microwave measurement sensitivity by roughly 10 dB.

3.3. Microwave Measurement Perturbation Immunity. A perturbation is defined as any phenomena (internal or external) that will induce unpredictable interference in the measured signals and thus affect the measurement sensitivity. A number of perturbation sources are identified and the solutions to mitigate their effect are described.

The first perturbation arises from the change of the cable response. As the antenna is moved to various locations, the cable shape is changed which predominantly affects its phase response. To reduce the negative effect on the sensitivity, a guiding system shown in Figure 1 has been implemented.

This system helps to ensure that the cable position is repeatable when the antenna is positioned and repositioned at a certain location. Identical cable positions translate to similar electrical responses that can be removed during the calibration process. The performance of this technique is illustrated in Figure 6, which shows the sensitivity calculated when the system is moved through two full TSAR scans (200 positions) with the broadband load attached instead of the antenna. When comparing with the corresponding static sensitivity (Figure 5), we observe only a slight increase of the phase variation, which translates to a fairly limited degradation of the sensitivity. An additional set of results is generated without any cable compensation by taking the difference between the 200 measurements and one selected measurement from the second scan. In this way, the cable position is different for each of the measurements in a given pair. For this scenario, the sensitivity sits at around -70 dB, so we estimate that the cable guiding system improves the sensitivity by about 10 dB.

The other perturbations are related to the signals detected by the antenna. The reflections from the breast are of interest, while reflections from other objects or sources can be subtracted during the calibration process as long as they are stable between measurements. However, any unpredictable signals that cannot be removed with the calibration process are considered as perturbations and need to be minimized. The unwanted signal sources have been classified into three groups: (a) lab environment reflections (room, equipment, people, etc.), (b) immersion liquid movement, and (c) general electromagnetic smog. Different mechanisms are implemented to alleviate these perturbations. First, the lab environment reflection (a) is easily removed using the time gating implemented in the VNA. The measured data are gated between 0 and 3.6 ns in order to remove reflections that originate from outside of the measurement tank. The

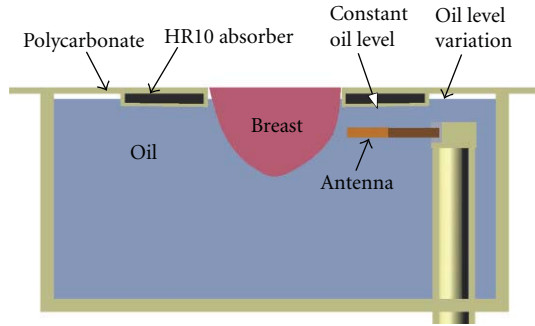


FIGURE 7: Profile view of the specially designed lid.

immersion liquid movement (b) is induced by the movement of the tank itself but most predominantly by the fluctuation of the tank volume due to the moving arm displacement. As the volume changes, the liquid level changes and creates reflections that cannot be replicated since these reflections are also affected by the volume of the breast itself. To minimize this effect, the tank lid is designed with additional material added around the hole through which the breast extends (Figure 7). This keeps the liquid level constant in the vicinity of the antenna aperture, while allowing fluctuation in liquid level behind the antenna where radiation is an order of magnitude less. This additional region consists of a polycarbonate shell filled with HR10 absorber (Emerson and Cuming Microwave Products, Randolph, MA, USA).

Finally, the electromagnetic smog (c) is generated by electrical apparatus around the lab and the outside world. To increase the electromagnetic immunity, absorbers are placed at strategic locations around the measurement tank in conjunction with shielding material.

Figure 8 shows the typical sensitivity of the TSAR prototype, when the previously mentioned techniques are in place, the antenna is attached and the immersion liquid is present. When compared to Figure 6, a significant decrease in magnitude sensitivity is noted, resulting in sensitivity between -50 and -60 dB, while phase variation increases slightly. The very large peaks in the phase variation happen at resonances where the phase changes drastically while being difficult to resolve by the VNA due to the weakness of the reflected signal. Overall, a sensitivity reduction of 30 dB is observed. As the reflection coefficients of the broadband matched load and antenna are around -30 and -10 dB, respectively, the phase variation intrinsically has greater impact on the sensitivity with the antenna attached. However, since the BAVA-D ringing is extremely small, the increase in reflection is mostly located in the antenna structure, as shown by the time domain representation in Figure 9. The antenna structure ends at approximately 1.5 ns in time and only the components of the signal beyond this point are significant for imaging purposes. We use a Tukey window, shown in Figure 9, to evaluate the sensitivity of the signal occurring after the antenna structure. As shown in Figure 9, the sensitivity sits overall between -70 to -80 dB. The lower frequencies are ignored since the antenna does not

radiate well below 2 GHz. Based on these values, we assess that 10 dB are lost in sensitivity when the antenna is attached instead of the load (i.e., compared to Figure 6).

Overall, the TSAR prototype may be expected to have reflection sensitivity between -70 to -80 dB. The VNA itself demonstrates a sensitivity level of -90 dB and is therefore more than capable of measuring signals greater than the reflection sensitivity. Moreover, numerous technical challenges arise when consistent performance needs to be maintained while scanning around a cylindrical volume. The TSAR system has demonstrated excellent mechanical accuracy and repeatability, and the modifications to the prototype system aimed at ensuring measurement sensitivity appear to enhance performance. This has resulted in a prototype system that demonstrates acceptable performance for our application.

4. Hemispherical Breast Model

The basic performance of the prototype system has been examined, however it is also of interest to validate reflections from test objects by comparing simulated and measured results. First, the hemispherical breast model used for this investigation is described. Reflection data are analyzed in relation to the previously presented performance metrics. Images created with simulated and measured data are also discussed.

The model used for this work has a relatively simple shape and composition and is described in detail in [18]. The model consists of a cylindrical section (diameter of 10 cm) attached to a hemispherical section with radius of 5 cm. A series of rings is located on the hemisphere in attempt to mimic the shape of the nipple. The model is made of a low-loss dielectric material with relative permittivity of 15. This phantom contains a cylindrical inclusion consisting of a Teflon rod of 7.9 mm diameter and 19.4 mm length. The inclusion is located in the hemispherical region at a radial distance of 25 mm from the centre of the model. The model is placed in the scanner, and the BAVA-D antenna is used to obtain measurements. For a full scan of the model, the antenna is scanned to 7 rows (vertical locations) separated by 1 cm and to 20 locations per row. A second scan of the empty tank is performed for calibration purposes. The antenna locations are the same as those used in the scan of the phantom. The reflections recorded with an empty tank are subtracted from those recorded with the model present. Reflections collected at the row of antennas located at the center of the inclusion are shown in Figure 10. Dominant reflections are expected from the oil/phantom interface and are shown to be very similar for one row of measurements. The response from the inclusion is also evident after 2 ns for antennas located closer to this object.

Next, simulations are performed in order to gain further insight into the measured data. The detailed simulation model includes aspects of the system that are expected to influence the reflected signals. Specifically, the model includes a replica of the breast phantom, a BAVA-D antenna, the top of the tank, and the immersion liquid (Figure 11).

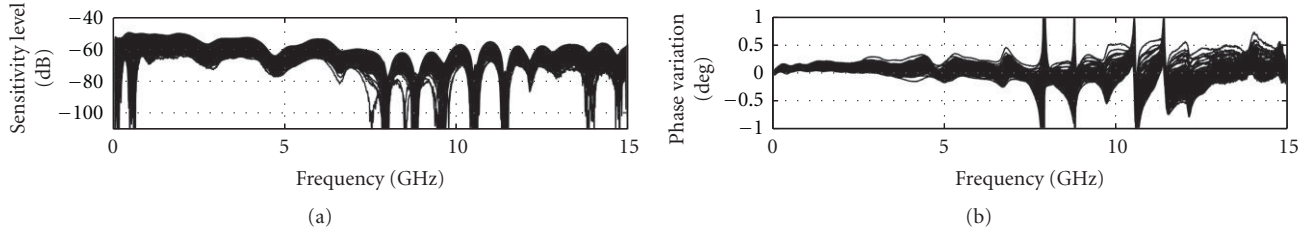


FIGURE 8: Sensitivity calculated based on a pair full TSAR scan (200 positions) with the antenna attached and immersion medium present (as per a volunteer scan).

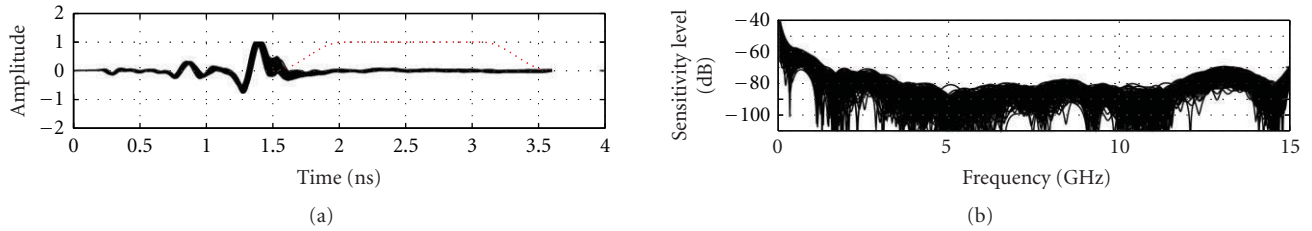


FIGURE 9: Time domain representation and noise level of the later-time antenna response (under dashed window).

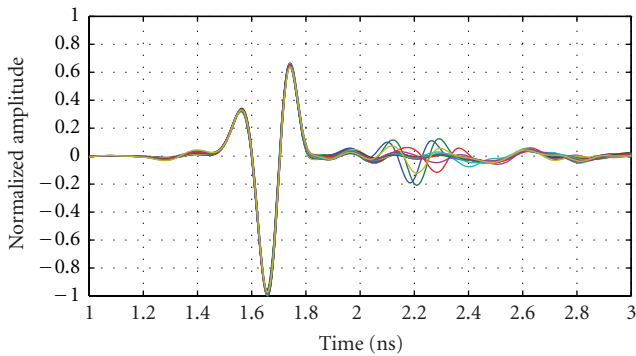


FIGURE 10: Measured reflections from the breast phantom at 20 antenna locations encircling the model. Measurements are collected with the antennas positioned at the same z -location as the inclusion.

Simulations are performed using SEMCAD (SPEAG, Zurich, Switzerland), which uses a finite difference time domain (FDTD) solver, and the antenna is excited with the UWB pulse described in (1). Results obtained with the breast phantom are shown in Figure 12 for one row of antennas (also located at the level of the inclusion in the phantom). Similar to Figure 10, dominant reflections are expected from the oil/phantom interface and are shown to be very similar for one row of simulations.

To investigate the similarity between the dominant reflections with measured and simulated data, we apply Tukey windows to isolate the first reflection (mean extent of 0.83 ns and positioned relative to the maximum absolute response in each signal). Correlations between these windowed reflections for the data shown in Figures 10 and 12 are on average 0.99. For the 140 antenna locations used to scan the phantom, simulations and measurements show mean correlation of 0.98 with standard deviation of 0.014.

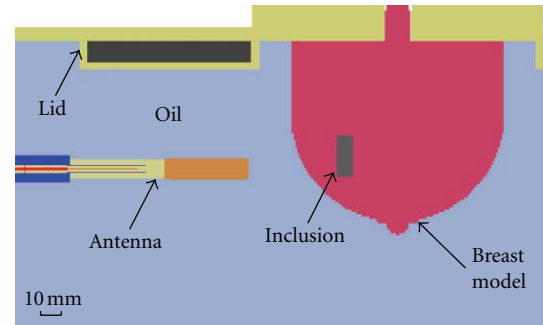


FIGURE 11: Cross-section through the voxelized simulation model of phantom showing components of the prototype included to more accurately model reflections.

Next, we examine and compare the later-time responses from simulation and measurement models by again using a Tukey window to isolate reflections occurring after the dominant reflection. Figure 13 shows results for an antenna located the closest to the inclusion, while Figure 14 shows results for an antenna at the same location but without any inclusion present in the breast model. We note that the simulated and measured data are in good agreement for the case containing the inclusion, as both time and frequency domain results are similar. When the inclusion is present, a reflection of about -40 dB is reached, which is easily detected given the sensitivity of our measurement system. Without an inclusion present (Figure 14), a lower reflection is noted in the later-time response. On average, the reflected signal without an inclusion present is 7 dB lower for the measured data and 11 dB lower for the simulated data. The signals magnitudes in Figure 14(b) are very similar between simulations and measurements while still within the sensitivity of the system. This suggests that part of these

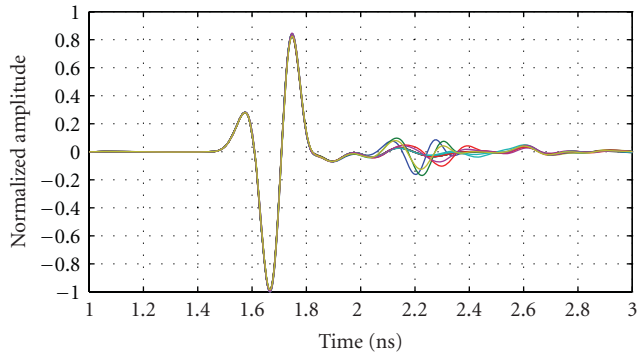


FIGURE 12: Simulated calibrated reflections from the breast phantom at 20 antenna locations encircling the phantom. Reflections are simulated with the antennas positioned at the same z -location as the inclusion.

smaller responses are indeed components of the reflected signals, likely originating from subtle sources such as the late-time response from the interface between oil and the model. Therefore, the TSAR prototype system demonstrates the ability to accurately record these fine details caused by larger reflected signals.

Finally, the simulated and measured data are used to create images. Phantoms with and without the inclusion are imaged and results obtained for measured data are shown in Figure 15. Similar results are obtained for simulated data, however images are not shown as the results appear very similar to those in Figure 15. The inclusion is easily detected and localized, and maximum response of the inclusion is located 23 mm from the center of the model. The location error likely results from challenges in orienting reflections precisely in time, as well as the discrete nature of the imaging procedure. The maximum response of the inclusion is compared to the response at the same location in the inclusion-free image. For measured data, the response with the inclusion is 14.1 dB greater than the inclusion-free case, demonstrating the enhancement of the inclusion response achieved through both reduction of common reflections and coherent summation via the focusing algorithm. For simulated data, the ratio is 47.4 dB, demonstrating the higher similarity between the simulated reflections, as well as the inherent differences between measurements and simulations.

Overall, the investigation of the breast model indicates good agreement between simulations and measurements, which validates the accuracy of our measurements. The response from the inclusion is easily measured given the sensitivity of our system, and images clearly detect and localize the inclusion.

5. Initial Measurements with a Volunteer

The work with the hemispherical model provides an assessment of the similarities between simulated and measured data for the TSAR prototype. These results suggest that simulations of a realistic breast model may provide a means to interpret measured reflections from human volunteers,

TABLE 2: TSAR scan parameters.

| Parameter | Value |
|---|------------|
| Vertical scan extent (mm) | -20 to -70 |
| Number of rows | 6 |
| Separation between rows (mm) | 10 |
| Number of antennas per row | 20 |
| Separation of neighboring antennas ($^{\circ}$) | 18 |
| Rotational offset between rows ($^{\circ}$) | 6 |

as the dominant reflections are expected to be similar for measurements and simulations.

A detailed analysis of a volunteer study is performed, using TSAR and MR scans. A volunteer is scanned with the TSAR prototype using the scan pattern presented in Table 2 (note that the origin of the vertical axis is coincident with the bottom of the lid) and measurement parameters discussed in Section 2. MR images are collected with a 1.5 Tesla Siemens Sonata MR Scanner and breast coil. The scanning sequence is T1-weighted (Gradient Echo VIBE with variant SP/OSP). With this sequence, fat is suppressed and glandular tissue has higher pixel intensity in images. The pixel size is $0.4297 \text{ mm} \times 0.4297 \text{ mm} \times 1.2 \text{ mm}$, and 112 images are collected for this volunteer.

To permit us to compare simulated and measured data, the MR images are translated into a model suitable for use with SEMAD. Mapping pixel intensity in MR images to electromagnetic property values involves several approximations, and the procedure used to create the breast model follows that described in [10] with the breast interior represented with 16 tissues. A cross-section of the realistic model used in simulations is shown in Figure 16. The MR and TSAR scans are both collected with the volunteer in the prone position, however the extent and shape of the breast differ when comparing the two systems. The key difference is that breast also floats in the oil used as the immersion liquid in the TSAR scanner. To compensate for this effect, the voxel size in the z -direction (Figure 16) is reduced from 0.4297 to 0.36 mm. To approximate the locations at which the measurements are collected, the nipple is used as a landmark and we assume that, at the antenna row closest to the top of the tank, the breast is centered in the scanner. Specifically, the location of the row of antennas closest to the nipple is determined from digital images collected during the TSAR scan. This information is used to position the antennas in simulation, and the scan pattern described in Table 2 is replicated. Reflections from the breast model are simulated using the pulse in (1).

The measured data from the volunteer are compared with simulations of the volunteer-specific model. Figure 17 shows normalized reflections from a simulation of the compressed breast and the corresponding experimental measurement. Figure 17 shows that the signals are in reasonable agreement with differences likely resulting from the fact that the simulated skin is modeled as a 2.14 mm layer, while the thickness of the skin approximated from the MR images ranges between 1.5 mm and 3.0 mm. Similar results are

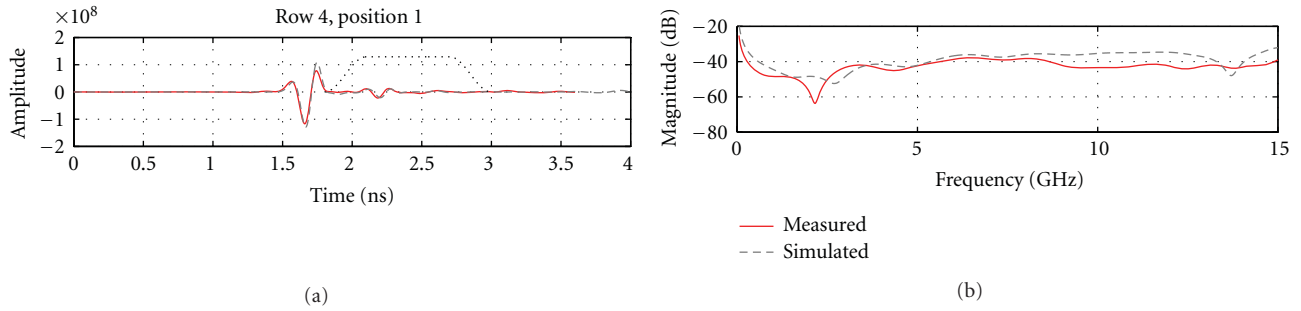


FIGURE 13: (a) Calibrated reflection from the breast model recorded by the antenna situated the closest to the inclusion. Dotted line shows the extent of the Tukey window that is used to isolate the later-time response. (b) The frequency response of the later-time component of the signals.

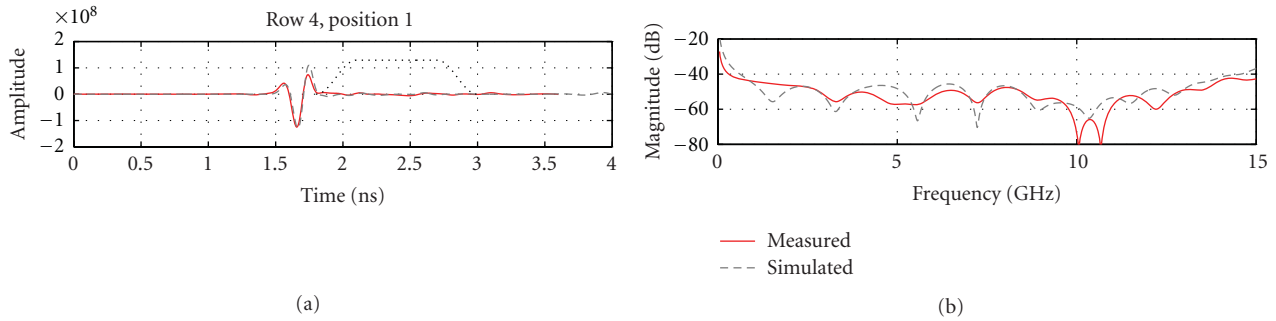


FIGURE 14: (a) Calibrated reflection from the breast model recorded at the same position as in Figure 13 but without any inclusion present. Dotted line shows the extent of the Tukey window that is used to isolate the later-time response. (b) The frequency response of the later-time component of the signals.

observed for the majority of antenna locations, as confirmed by calculating the correlation between the measured and simulated signals. For 116 out of 120 signals, the correlation is 0.9 or better, demonstrating the similarity between measured and simulated skin reflections recorded as the antenna is scanned around the breast. The outliers likely originate from areas of the model where skin thicknesses are significantly different when compared to the actual skin thickness of the volunteer. Therefore, the TSAR prototype is capable of measuring reflections from volunteers and comparison of measurements and simulations suggests that the measured reflections are reasonable. However, detailed analysis of later-time reflections is not considered, as numerous differences between the model and volunteer are present (e.g., breast shape differs from MR to TSAR and antenna locations are approximated). This makes this comparison of small later-time reflections extremely challenging.

6. Conclusions

In this paper, a prototype system for monostatic radar-based imaging of the breast is described. This system scans a single UWB antenna around the breast in order to collect data, therefore differing from prototype systems for multistatic radar-based imaging and tomography. The paper first focuses on evaluating the performance of the system, as this is key for gaining insight into the capabilities and limitations of the prototype. For example, the motion

of the sensor impacts the system performance, so the accuracy and repeatability of sensor positioning are assessed, showing minimal errors. Microwave measurement sensitivity is defined as the differences between two reflection measurements and is used to examine the effects of time-delay between measurements, system motion and cable flex. Differences in measurements with a broadband load attached show that time delay and motion do degrade the sensitivity. By controlling cable positioning, improving measurement environment repeatability and applying techniques such as time-gating the reflections, the microwave measurement sensitivity during the TSAR scan is assessed to be between -70 and -80 dB. In addition, the metrics examined appear to be informative and may be used to evaluate performance of monostatic radar-based imaging systems.

Once the system performance is evaluated, simulations and measurements of a simple phantom are compared. Although much work with both simulations and measurements has been reported for microwave imaging systems, there are only a few reports directly comparing these results. Both early and late-time reflections recorded from a simple phantom show very good agreement. Moreover, reflections from homogeneous phantoms are compared with reflections from phantoms containing inclusions, demonstrating that the response of the inclusion is easily detected given the sensitivity of the system. In addition, the measurement of the weaker later-time reflections from the phantom

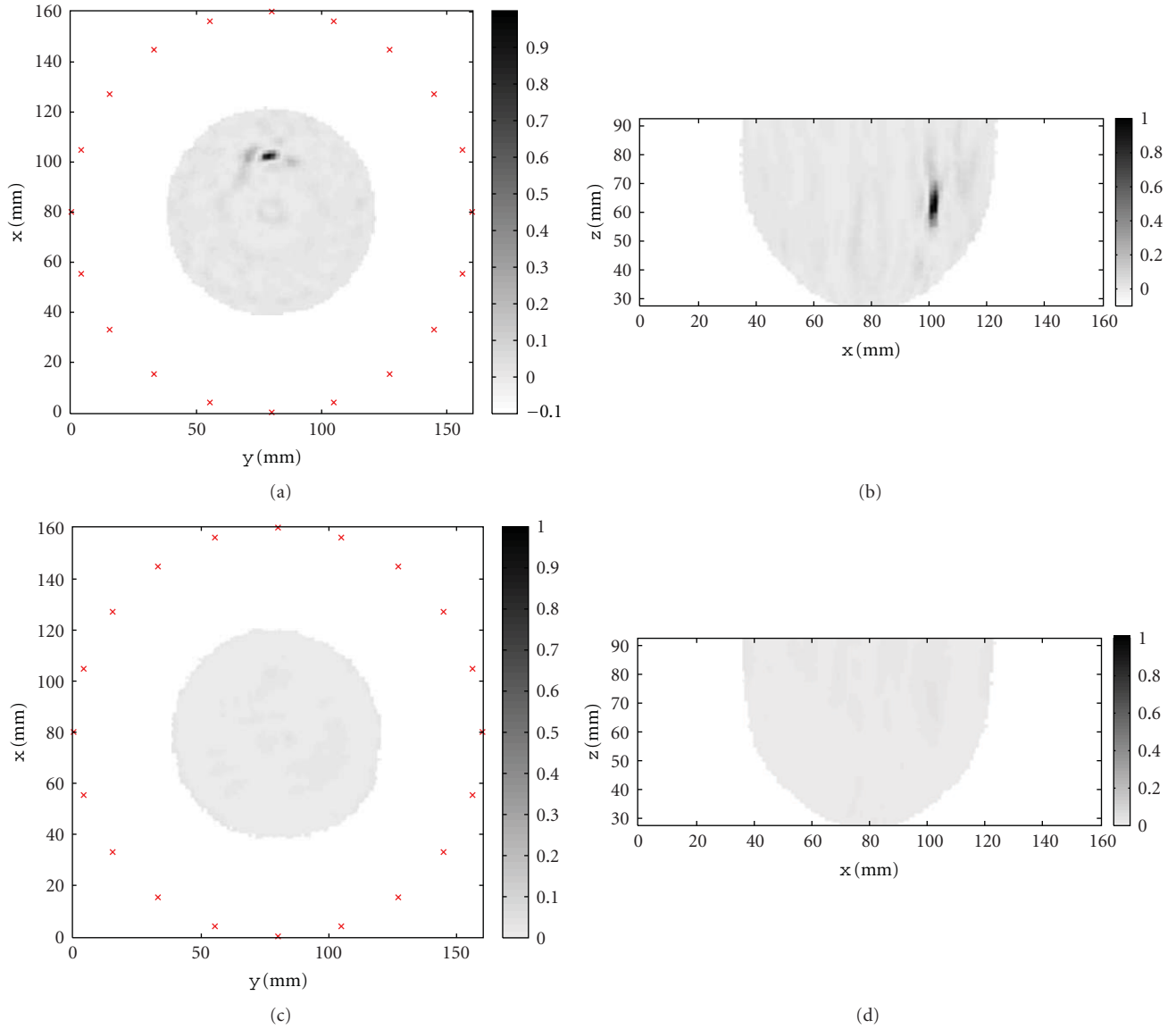


FIGURE 15: Images of the hemispherical model created from measured data: (a) slice through the inclusion location perpendicular to the axis of the cylinder and (b) slice through the inclusion location parallel to the axis of the cylinder. The images for the phantom without the inclusion are shown in (c) and (d).

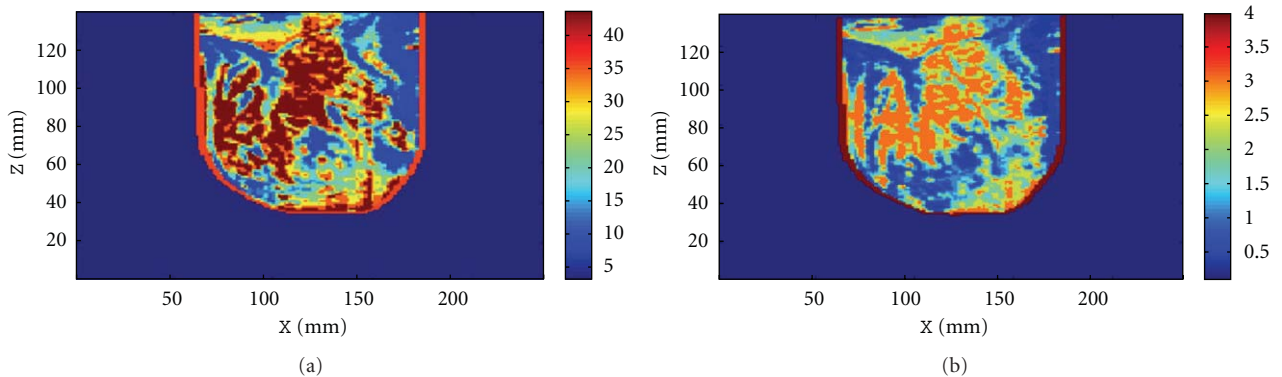


FIGURE 16: Permittivity (a) and conductivity (b) distribution in cross-section of a simulated breast model after adjustment for floatation in oil.

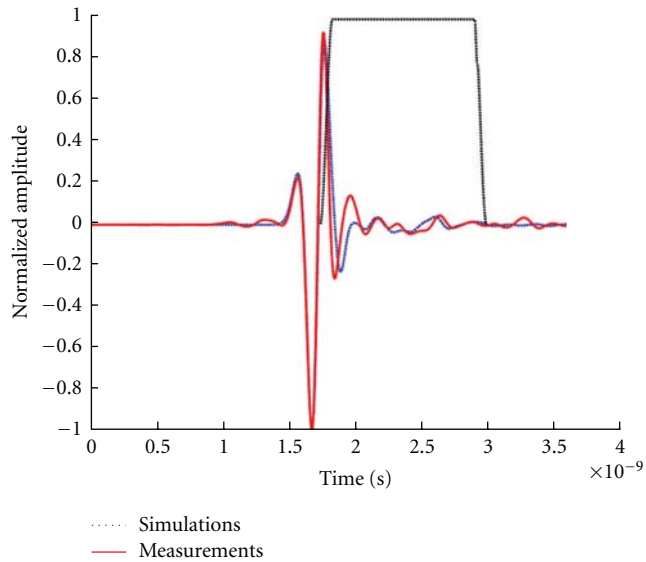


FIGURE 17: Reflections recorded in experiments and simulations. A Tukey window applied to isolate late-time reflections is shown. The reflections are normalized to the maximum value and shifted in order to align the skin responses.

correlate with simulated results, bringing confidence to the measurement accuracy. The resulting images indicate the inclusion is easily detected and localized.

Finally, a scan of a volunteer is described and analysed. In order to interpret the reflections, a volunteer-specific breast model is created. The early-time reflections in simulations and measurements are in excellent agreement, given the known differences between the volunteer and model. This provides confidence that the measured signals correspond to reflections from the breast tissues.

Measurement perturbation due to breast movement induced by volunteer movement or by potential turbulence during sensor displacement were not considered in this paper. Given the length of the scan time (30 minutes), patient movement is expected. However, considering the resolution of a biomedical microwave imaging system (subcentimeter scale), small movements are not expected to significantly affect image quality. For comparison, breast MRI can take up to 40 minutes while achieving image resolution in the millimeter scale. It is also important to observe that for both modalities the patients lie in a prone position with the chest wall resting on the breast coil or the measurement tank lid. In this configuration, movement occurring during patient breathing has only a limited impact on the breast position as the breasts do not significantly move relative to the chest wall. Based on the volunteers scanned so far (12), no significant breast movements have been observed between the digital images recorded at each antenna position. Breast movement during antenna displacement or while the VNA is sweeping could not be assessed visually. However, the good correlation between the measured signals and simulated counterpart using the patient specific model suggests that movement during the VNA sweep is minimal.

Future work includes improving the agreement between the simulated and measured reflections from volunteers and patients, especially the later-time responses. For example, the laser surface measurement of the breast may be used to more accurately deform the MR-based breast model. Combined with knowledge of microwave measurement sensitivity, simulations of the realistic breast models may be used to gain insight into the ability to detect a range of tumors located at different locations in breasts containing a variety of tissue distributions.

Acknowledgments

The authors would like to thank Dr. Richard Frayne for his support of this study. This work was supported by the Natural Sciences and Engineering Research Council of Canada and the Alberta Heritage Foundation for Medical Research.

References

- [1] R. J. Brenner and Y. Parisky, "Alternative breast-imaging approaches," *Radiologic Clinics of North America*, vol. 45, no. 5, pp. 907–923, 2007.
- [2] D. Li, P. M. Meaney, T. Raynolds, S. A. Pendergrass, M. W. Fanning, and K. D. Paulsen, "Parallel-detection microwave spectroscopy system for breast imaging," *Review of Scientific Instruments*, vol. 75, no. 7, pp. 2305–2313, 2004.
- [3] X. Li, E. J. Bond, B. D. van Veen, and S. C. Hagness, "An overview of ultra-wideband microwave imaging via space-time beamforming for early-stage breast-cancer detection," *IEEE Antennas and Propagation Magazine*, vol. 47, no. 1, pp. 19–34, 2005.
- [4] M. Klemm, I. J. Craddock, J. A. Leendertz, A. Preece, and R. Benjamin, "Radar-based breast cancer detection using a hemispherical antenna array—experimental results," *IEEE Transactions on Antennas and Propagation*, vol. 57, no. 6, pp. 1692–1704, 2009.
- [5] J. M. Sill and E. C. Fear, "Tissue sensing adaptive radar for breast cancer detection—experimental investigation of simple tumor models," *IEEE Transactions on Microwave Theory and Techniques*, vol. 53, no. 11, pp. 3312–3319, 2005.
- [6] P. M. Meaney, K. D. Paulsen, S. D. Geimer, S. A. Haider, and M. W. Fanning, "Quantification of 3-D field effects during 2-D microwave imaging," *IEEE Transactions on Biomedical Engineering*, vol. 49, no. 7, pp. 708–720, 2002.
- [7] D. W. Winters, J. D. Shea, P. Kosmas, B. D. van Veen, and S. C. Hagness, "Three-dimensional microwave breast imaging: dispersive dielectric properties estimation using patient-specific basis functions," *IEEE Transactions on Medical Imaging*, vol. 28, no. 7, Article ID 4781569, pp. 969–981, 2009.
- [8] S. P. Poplack, K. D. Paulsen, A. Hartov et al., "Electromagnetic breast imaging: average tissue property values in women with negative clinical findings," *Radiology*, vol. 231, no. 2, pp. 571–580, 2004.
- [9] R. J. Halter, T. Zhou, P. M. Meaney et al., "The correlation of *in vivo* and *ex vivo* tissue dielectric properties to validate electromagnetic breast imaging: initial clinical experience," *Physiological Measurement*, vol. 30, no. 6, pp. S121–S136, 2009.
- [10] D. J. Kurrant and E. C. Fear, "An improved technique to predict the time-of-arrival of a tumor response in radar-based breast

- imaging,” *IEEE Transactions on Biomedical Engineering*, vol. 56, no. 4, Article ID 4760233, pp. 1200–1208, 2009.
- [11] M. Klemm, J. A. Leendertz, D. Gibbins, I. J. Craddock, A. Preece, and R. Benjamin, “Microwave radar-based breast cancer detection: imaging in inhomogeneous breast phantoms,” *IEEE Antennas and Wireless Propagation Letters*, vol. 8, Article ID 5337879, pp. 1349–1352, 2009.
- [12] S. M. Salvador and G. Vecchi, “Experimental tests of microwave breast cancer detection on phantoms,” *IEEE Transactions on Antennas and Propagation*, vol. 57, no. 6, pp. 1705–1712, 2009.
- [13] M. Klemm, I. Craddock, J. Leendertz, A. Preece, and R. Benjamin, “Experimental and clinical results of breast cancer detection using UWB microwave radar,” in *Proceedings of the IEEE International Symposium on Antennas and Propagation and USNC/URSI National Radio Science Meeting (APSURSI ’08)*, p. 4, July 2008.
- [14] M. Guardiola, S. Capdevila, and L. Jofre, “UWB BiFocusing tomography for breast tumor detection,” in *Proceedings of the 3rd European Conference on Antennas and Propagation (EuCAP ’09)*, pp. 1855–1859, March 2009.
- [15] J. Bourqui, M. Okoniewski, and E. C. Fear, “Balanced antipodal vivaldi antenna with dielectric director for near-field microwave imaging,” *IEEE Transactions on Antennas and Propagation*, vol. 58, no. 7, Article ID 5452983, pp. 2318–2326, 2010.
- [16] E. C. Fear, X. Li, S. C. Hagness, and M. A. Stuchly, “Confocal microwave imaging for breast cancer detection: localization of tumors in three dimensions,” *IEEE Transactions on Biomedical Engineering*, vol. 49, no. 8, pp. 812–822, 2002.
- [17] T. C. Williams, J. Bourqui, T. R. Cameron, M. Okoniewski, and E. C. Fear, “Laser surface estimation for microwave breast imaging systems,” *IEEE Transactions on Biomedical Engineering*, vol. 58, no. 5, pp. 1193–1199, 2011.
- [18] E. C. Fear, J. Bourqui, M. A. Campbell, and T. Williams, “Antenna evaluation for ultra-wideband microwave imaging,” *International Journal of Antennas and Propagation*, vol. 2010, Article ID 850149, 8 pages, 2010.

Research Article

Bone Dielectric Property Variation as a Function of Mineralization at Microwave Frequencies

Paul M. Meaney,¹ Tian Zhou,² Douglas Goodwin,³ Amir Golnabi,¹
Elia A. Attardo,¹ and Keith D. Paulsen¹

¹Thayer School of Engineering, Dartmouth College, Hanover, NH 03755, USA

²Kuang-Chi Institute of Advanced Technology, Shenzhen, Guangdong 518000, China

³Dartmouth-Hitchcock Medical Center, Lebanon NH, 03756, USA

Correspondence should be addressed to Paul M. Meaney, paul.meaney@dartmouth.edu

Received 23 September 2011; Accepted 16 January 2012

Academic Editor: Ian Craddock

Copyright © 2012 Paul M. Meaney et al. This is an open access article distributed under the Creative Commons Attribution License, which permits unrestricted use, distribution, and reproduction in any medium, provided the original work is properly cited.

A critical need exists for new imaging tools to more accurately characterize bone quality beyond the conventional modalities of dual energy X-ray absorptiometry (DXA), ultrasound speed of sound, and broadband attenuation measurements. In this paper we investigate the microwave dielectric properties of *ex vivo* trabecular bone with respect to bulk density measures. We exploit a variation in our tomographic imaging system in conjunction with a new soft prior regularization scheme that allows us to accurately recover the dielectric properties of small, regularly shaped and previously spatially defined volumes. We studied six excised porcine bone samples from which we extracted cylindrically shaped trabecular specimens from the femoral heads and carefully demarrowed each preparation. The samples were subsequently treated in an acid bath to incrementally remove volumes of hydroxyapatite, and we tested them with both the microwave measurement system and a micro-CT scanner. The measurements were performed at five density levels for each sample. The results show a strong correlation between both the permittivity and conductivity and bone volume fraction and suggest that microwave imaging may be a good candidate for evaluating overall bone health.

1. Introduction

Osteoporosis is a major health problem for roughly 55% of the US population of 50 years of age or older. It is characterized by low bone mass and structural deterioration which leads to increased fragility and risk of fracture. Fifty percent (50%) of women and 25% of men over age 50 will have an osteoporosis-related bone fracture. The most typical fractures occur in the hip, spine, wrist, and ribs, of which the hip and vertebral fractures can require long-term care and even cause death in as many as 24% of hip fracture cases [1]. This dynamic aspect of bone physiology may facilitate the use of dielectric interrogation as a means of imaging bone health.

Assessing bone health may be a particularly good opportunity to exploit dielectric properties for screening, diagnosis, and in the overall management of bone treatment. In parallel with previous broadband tissue dielectric

property studies [2–11], bone has received special attention. For instance, clinicians have used electrical currents to stimulate bone growth for several decades [12–15]. With such treatment it is essential to both understand the reaction of the bone to electrical stimulation as well as understand the tissue dielectric properties for guiding the therapy. In addition, the dielectric properties, themselves, may provide clinically useful information with respect to assessing overall bone health as in the case of osteoporosis and monitoring osteogenic response to treatment. These properties have been studied extensively up to 5 MHz [16–19]; however, tests beyond this frequency have not proved useful to date [20]. At lower frequencies, electrical impedance spectroscopy (EIS) techniques, including parallel plate capacitance cells, have been used to retrieve accurate dielectric properties [21, 22]. In fact, measurements have been made using conventional open-ended coaxial dielectric probes at frequencies as high

as 3 GHz, but remain unpublished. The primary reason is that the dielectric probe technique is inherently ill-suited to this type of measurement. While researchers have performed experiments to determine the proximal limits of heterogeneities when testing homogeneous materials and liquids using these probes [23], first-hand experience suggests that measurements with these probes on inhomogeneous targets are dominated by the tissue in direct contact with the probe. Given the heterogeneous nature of trabecular bone samples and the potential for property and texture variations between the less disturbed internal zones and the bone surfaces because of the extensive manipulation involved in preparing the samples, it is not surprising that these probe measurements have been inconclusive. More recent *in vivo* animal studies by Gabriel et al. [8] indicate that dramatic dielectric property changes occur with age in bone (not seen in other tissue types). This dynamic aspect of bone physiology may facilitate exploitation of dielectric interrogation as a means of bone health imaging.

The baseline studies by Gabriel et al. [5–7] and others have proved useful in establishing nominal, frequency-dependent property ranges for different tissue types and have set the stage for further investigation of whether variations in individual tissue dielectric properties can be predictive of various maladies. Studies by Joines et al. [24] and Lazebnik et al. [25, 26] have explored whether tumors exhibit dielectric properties distinct from their normal organ. Additionally, at frequencies below 2 GHz where the ionic flow dominates the overall conductivity effect [27, 28], tissue conductivity has been shown to vary linearly with temperature, and this mechanism has been utilized in investigations of noninvasive temperature monitoring in conjunction with thermal therapy [29, 30]. Similar work has been performed in other fields to look at tissue property variations based on physiological phenomena other than cancer. For instance, in comparable studies of ultrasound computed tomography, Sehgal et al. [31, 32] showed that the speed of sound and broadband attenuation varied considerably for liver samples depending on overall fat and tumor content. Given that the only substantive variations in the tissues tested in that study were the fat and water content levels, dielectric mixture laws such as the Maxwell-Fricke relationships would also naturally predict similar variations [3].

In the area of ultrasound, researchers have performed numerous studies of the effect of bone density on the speed of sound and broadband attenuation, and several devices have been developed and approved by the FDA for testing bone health. For instance, the Lunar Achilles system produced by GE Healthcare (Waukesha, WI, USA) and the Sahara Clinical Bone Sonometer manufactured by Hologic (Bedford, MA, USA) are both FDA approved and used routinely in clinical situations. In the ultrasound experiments performed by Wu et al. [33], trabecular bone samples were tested with both dual X-ray absorptiometry (DXA) and ultrasound transmission techniques to assess whether correlations exist between bone mineral density (BMD) and the ultrasound metrics—speed of sound and broadband attenuation. The samples were tested at a baseline with both techniques and at several subsequent times after demineralization through

submersion in acidic solvents. The ultrasound measurements were performed with the bone specimens placed in water to assess overall bulk property changes as the hydroxyapatite was progressively removed and artificially replaced by the water. (Note that hydroxyapatite is the main constituent of the mineralized portion of the bone and is generally referred to as bone mineral.)

We have followed a similar path for this dielectric property study except the DXA X-ray tests have been replaced with more exact X-ray micro-CT measurements to determine the bone sample constituent proportions. Furthermore, we have replaced the ultrasound transmission measurements with microwave tomographic images. These tissue samples do not readily lend themselves to standard dielectric probe measurements because the trabecular bone samples are fragile and their surfaces are uneven given their intricate architecture. Instead, we have applied a newly developed microwave tomographic approach utilizing a soft prior regularization that is well suited for testing the bulk properties of small samples of known geometries [34, 35]. The samples were placed in a test tube filled with saline of known size in a predetermined location within the illumination zone of our microwave tomographic system. Prior knowledge of the sample shape, size, and location was applied in the regularization scheme as part of the standard image reconstruction process [34] to recover estimates of the specimen dielectric properties. This measurement approach is not unlike the ultrasound CT technique described by Schreiman et al. [36] for isolated tissue samples where the configuration geometry was also well known. While replacement of the bone marrow with saline does not perfectly mimic the process that normal bone undergoes during aging and/or unnatural bone loss, it does validate the overall notion that tissue bulk dielectric properties are functions of the individual properties and volume fractions of its constituents. *In situ* dielectric changes will likely occur in more complicated patterns, but these measurements may still provide important information on tissue pathology and health.

In this paper we describe the process used in these experiments including the tissue preparation, X-ray CT, and microwave imaging approaches. We illustrate the technique of applying the microwave tomographic method with soft prior regularization to recover accurate values of the dielectric properties of the bone tissue samples and the associated tools used to assess the radiographic bone properties from the micro-CT data. Finally, we present results demonstrating the correlation between the bone dielectric properties and the X-ray data metrics.

2. Methods

2.1. Bone Sample Preparation. We acquired several intact, porcine femurs from the surgical labs at Dartmouth Hitchcock Medical Center from animals that had been euthanized according to IACUC (Institutional Animal Care and Use Committee) approved protocols. The bones were mechanically stripped of all flesh using surgical blades and then

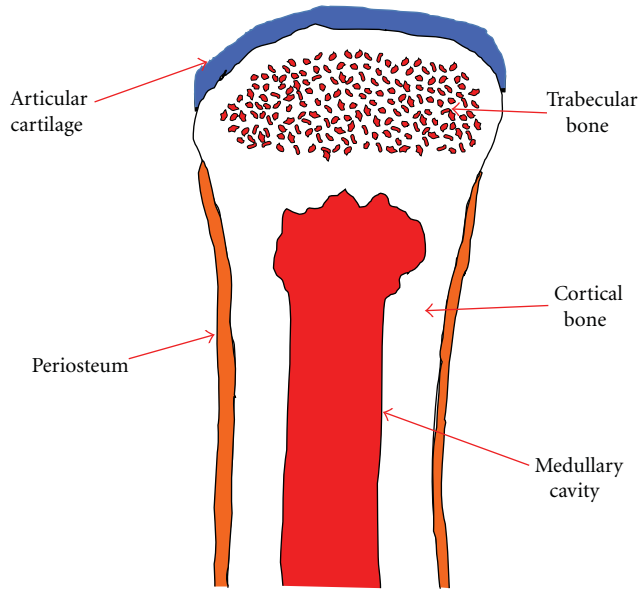


FIGURE 1: Schematic diagram of a portion of a long bone showing the articular cartilage, trabecular bone, cortical bone, medullary cavity, and periosteum.

mounted in a bench vise under a ventilation hood. Two 2 cm diameter by roughly 3 cm long cylindrical specimens were recovered from both femur ends using a hole saw to extract only trabecular bone samples. The remaining cortical shells at either end were cut off with a simple coping saw. The bone samples were then soaked in formalin for 4 weeks. Figure 1 shows a schematic diagram of one end of a long bone illustrating the trabecular bone in relation to the other components.

We applied a standard protocol used in the Anatomy Department at Dartmouth Medical School for removing the embedded marrow. This involved soaking each sample in commercially available ammonia (3% solution) baths for two weeks, followed by full-week immersions in 75%, 50%, 25% and 0% ammonia solutions (percentages with respect to the original 3% solution). During each week, the solutions were repeatedly refreshed to maximize the solvent effect. The progressive decrease in ammonia concentrations was designed to dissolve all of the marrow (high concentration of fatty material) even within the deepest portions of the trabecular bone specimens while also minimizing potential damage to the intricate trabecular structure. The first set of micro-CT images at the start of the experiments verified that the marrow had been completely removed.

2.2. Bone Testing Procedure. The flow graph in Figure 2 illustrates the procedures used for testing and processing the demarrowed bone samples. These steps are described in more detail below.

(1) Removal of All Water from the Samples. This involved placing the samples in a custom desiccator attached to an in-house vacuum source for a minimum of 4 days. We also

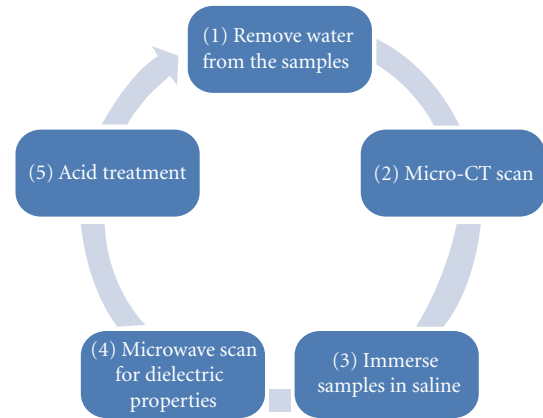


FIGURE 2: Experimental procedure flow for investigating the *in vitro* relationship between bone mineral and dielectric properties of porcine trabecular bone specimens.

documented the weight, length, and diameter of each sample at this step.

(2) Micro-CT of Each Bone Sample. We used a GE eXplore Locus SP micro-CT system with GE MicroView 2.1.2 software for reconstructing and analyzing the images. The protocol included using an 80 KeV/80 mAmp X-ray source, and data was acquired with a 0.5° increment between views. Photographs were taken of all samples in the X-ray chamber to note the various physical landmarks (growth plate and uneven height features) for registration with the microwave imaging tests. The baseline resolution for this configuration was 28 microns; however, because we applied a 2×2 binning strategy during the reconstruction process to reduce noise, the effective resolution was reduced to 56 microns. In this case, we chose cylindrical regions of interest because of the sample shape (Figure 3). The GE analysis algorithms have the capability of calculating values for: BMD-bone mineral density, BMC-bone mineral content, TMD-tissue mineral density, TMC-tissue mineral content, and bone volume fraction (BVF), where $BVF = ((\text{Bone Volume}) / (\text{Total Sample Volume})) * 100\%$. According to the manufacturer, both BMD and BMC use parameters set by the user-selected region of interest (ROI), and the resulting bone values are affected by factors other than bone (e.g., soft tissue, air). Having air included in the ROI has particularly deleterious effects; therefore, the TMC and BVF parameters are more biologically meaningful. These values were computed utilizing calibrations against known phantoms supplied by the manufacturer. The data acquisition time was roughly 2.5 hours for full scans while the associated micro-CT image reconstruction process required 10 minutes for each sample.

(3) Immersion of Bone Samples in Saline. For microwave imaging purposes, the samples were submerged in a 0.9% saline solution in an 18 mm diameter plastic test tube with 0.5 mm wall thickness for 24 hours. The dielectric properties of the plastic over the range of 900–1300 MHz were $\epsilon_r = 2.8$ and $\sigma = 0.01$ S/m. After this, the test tubes were placed in

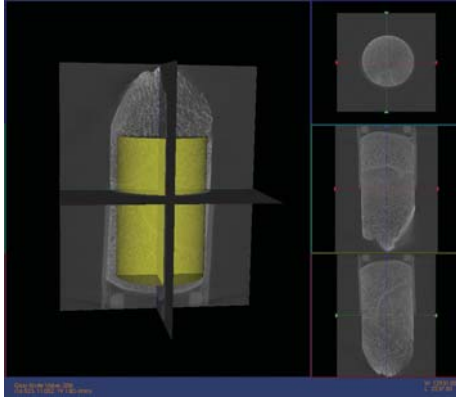


FIGURE 3: Micro-CT scan of a sample bone specimen. The yellow cylinder is the region of interest for extracting bone mineral parameters. The size of the ROI is kept constant in the longitudinal study for each specimen. The ROI is located at approximately the same position to minimize variation.

a pressure chamber with a vacuum applied for 10 minutes. This was followed by 10 minutes in the same chamber with 45 lbs/inch² of applied pressure. This two-step procedure was repeated three times as a way of minimizing any trapped air bubbles within the samples.

(4) *Microwave Measurements.* For the dielectric property study, the test tubes were placed at a position 3 cm offset from the center within the illumination chamber (Figure 4). The tank consisted of 16 monopole antennas suspended in an 80:20 mixture of glycerin and water which surrounded the bone samples. The dielectric properties of the liquid mixture were $\epsilon_r = 28.0, 24.9, 22.5$, and $\sigma = 1.01, 1.19, 1.35$ S/m for 900, 1100, and 1300 MHz, respectively. Each antenna individually broadcasts a single-frequency, continuous wave signal with the remaining 15 antennas acting as receivers. This process was repeated for all 16 antennas acting as the transmitter and at 11 frequencies (500–2500 MHz at a step size of 200 MHz) to produce 2640 measurements (16 transmitters \times 15 receivers \times 11 frequencies). This data was then used in our Gauss-Newton 2D imaging algorithm while applying our soft prior regularization to extract accurate reconstructions of the properties within the test tube zone. The soft prior reconstruction mesh (Figure 5) illustrates the isolation of the test tube region from the remaining homogeneous coupling bath. (The test tube region was on the left, instead of on the right in Figure 4 because the reconstruction software is oriented for viewing from the bottom of the tank to the top.) It is essentially a mirror image of that observed from the top. This mesh information is then included with the reconstruction algorithm to provide nearly homogeneous values for the target zone (note, the properties of the surrounding zone are known from direct measurements). Single-frequency images were recovered in under 2 minutes while allowing the algorithm to converge for 20 iterations. The bone samples were then rinsed for 10 minutes in tap water before the next process.

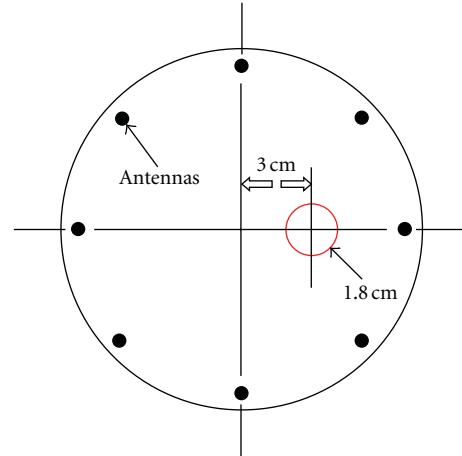


FIGURE 4: Position of the test tube with respect to the microwave antennas within the imaging tank (top view). (There are 16 antennas in total, only 8 are shown for simplicity. The antennas are positioned equiangularly on a 15.2 cm diameter circle.)

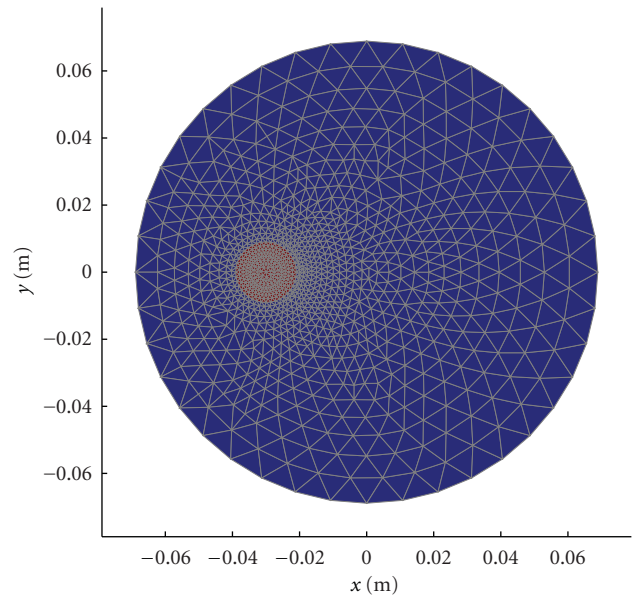


FIGURE 5: Soft prior mesh for the microwave image reconstruction comprised of 1107 nodes and 2092 triangular elements.

We investigated whether orientation of the test tube had any deleterious effect on our measurements. For several test cases, the test tube containing the bone specimen was rotated 0°, 90°, 180°, and 270° and scanned with the microwave tomographic imaging (MTI) system. The standard deviations for relative permittivity and conductivity were 0.35 and 0.026 S/m, respectively. Even with this low level of variation, orientation was taken into consideration during the process. Each bone specimen was marked with ink and maintained in the same direction for all scans.

(5) *Acid Treatment.* The bone samples were suspended in a 5% nitric acid (bone decalcifier) solution for approximately

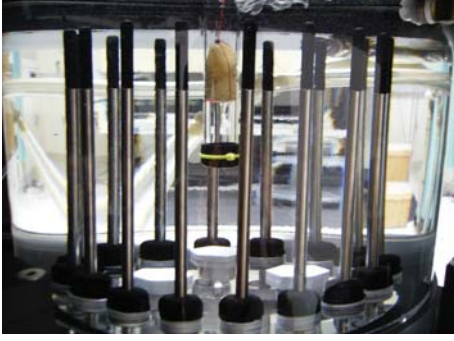


FIGURE 6: Microwave data acquisition of a saline-saturated bone sample in a test tube submerged in an 80% glycerin bath (side view).

2 hours to remove a controlled percentage of the mineralization. We determined that most bone samples typically began with roughly 40% mineral density and that each 2.1-hour acid treatment decreased the density in increments of approximately 10%. The protocol of acid treatment allowed us to recover 5 measurements for each sample at different mineral densities. All samples were rinsed in tap water for 10 minutes after each session to terminate the oxidation process.

2.3. Microwave Imaging with Soft Prior Regularization. Figure 6 shows the microwave imaging configuration for interrogating the trabecular bone samples. As described

above, each sample was immersed in a 0.9% saline solution within an 18 mm diameter test tube. The reconstruction mesh (Figure 5) only encompasses the sample domain since the properties of the surrounding liquid are known and are not reconstructed. The minimization statement for the Gauss-Newton reconstruction utilizing the soft prior regularization approach is given as

$$\min \|\Gamma^m - \Gamma^c(k^2)\|^2 + \|\Phi^m - \Phi^c(k^2)\|^2 + \lambda L\{k^2 - k_{\text{bk}}^2\}, \quad (1)$$

where Γ^m and Γ^c are the measured and computed log magnitude values, Φ^m and Φ^c are the measured and computed phase values, k^2 is the complex wave number squared distribution at the current iteration, k_{bk}^2 is the wave number squared for the surrounding background coupling medium, λ is the soft prior regularization parameter and L is the soft prior matrix. k^2 comprises the permittivity and conductivity images through the relationship $k^2 = \omega^2\mu\epsilon + j\omega\mu\sigma$, where ω is the frequency in radians, μ is the magnetic permeability, and ϵ and σ are the electrical permittivity and conductivity, respectively. Note that the first two terms are essentially the implementation of our log transformation in the Gauss-Newton algorithm which is described in detail in Meaney et al. [37]. (All of the details of this approach are described in more detail in Golnabi et al. [35].) The critical aspect of the soft prior regularization is the composition of the matrix L

$$L = \begin{bmatrix} R_1 \\ R_2 \end{bmatrix} \begin{bmatrix} 1 & -\frac{1}{N_1} & \dots & -\frac{1}{N_1} & 0 & \dots & \dots & \dots & 0 \\ -1 & 1 & \dots & -\frac{1}{N_1} & \dots & \dots & \dots & \dots & \dots \\ \dots & \dots \\ -\frac{1}{N_1} & -\frac{1}{N_1} & \dots & 1 & 0 & \dots & \dots & \dots & 0 \\ 0 & \dots & \dots & 0 & 1 & -\frac{1}{N_2} & \dots & \dots & -\frac{1}{N_2} \\ \dots & \dots & \dots & \dots & -\frac{1}{N_2} & 1 & \dots & \dots & \dots \\ \dots & \dots & \dots & \dots & \dots & -\frac{1}{N_2} & \dots & \dots & \dots \\ \dots & 1 & -\frac{1}{N_2} \\ 0 & \dots & \dots & 0 & -\frac{1}{N_2} & \dots & \dots & -\frac{1}{N_2} & 1 \end{bmatrix} \quad (2)$$

Equation (2) shows the L matrix constructed with regions R_1 and R_2 grouped accordingly. As shown in Figure 5, R_1 is the background region (blue), and R_2 is the region that has the bone specimen (red). There are N_1 and N_2 nodes in regions R_1 and R_2 , respectively. Based on the formation of the regularization matrix L , $L^T L$ can be viewed as an approximation of a second-order Laplacian smoothing operator inside each region that limits the smoothing across the boundary of distinct regions [38].

3. Results

We used six bone specimens in this experiment, and each was scanned by both the micro-CT and microwave tomography systems between intervening demineralization treatments. For all samples, the dry mass and diameters decreased 50.90% and 12.17% on average, respectively, with associated standard deviations of 5.88% and 2.72%, respectively. Figure 7 shows representative 1100 MHz soft

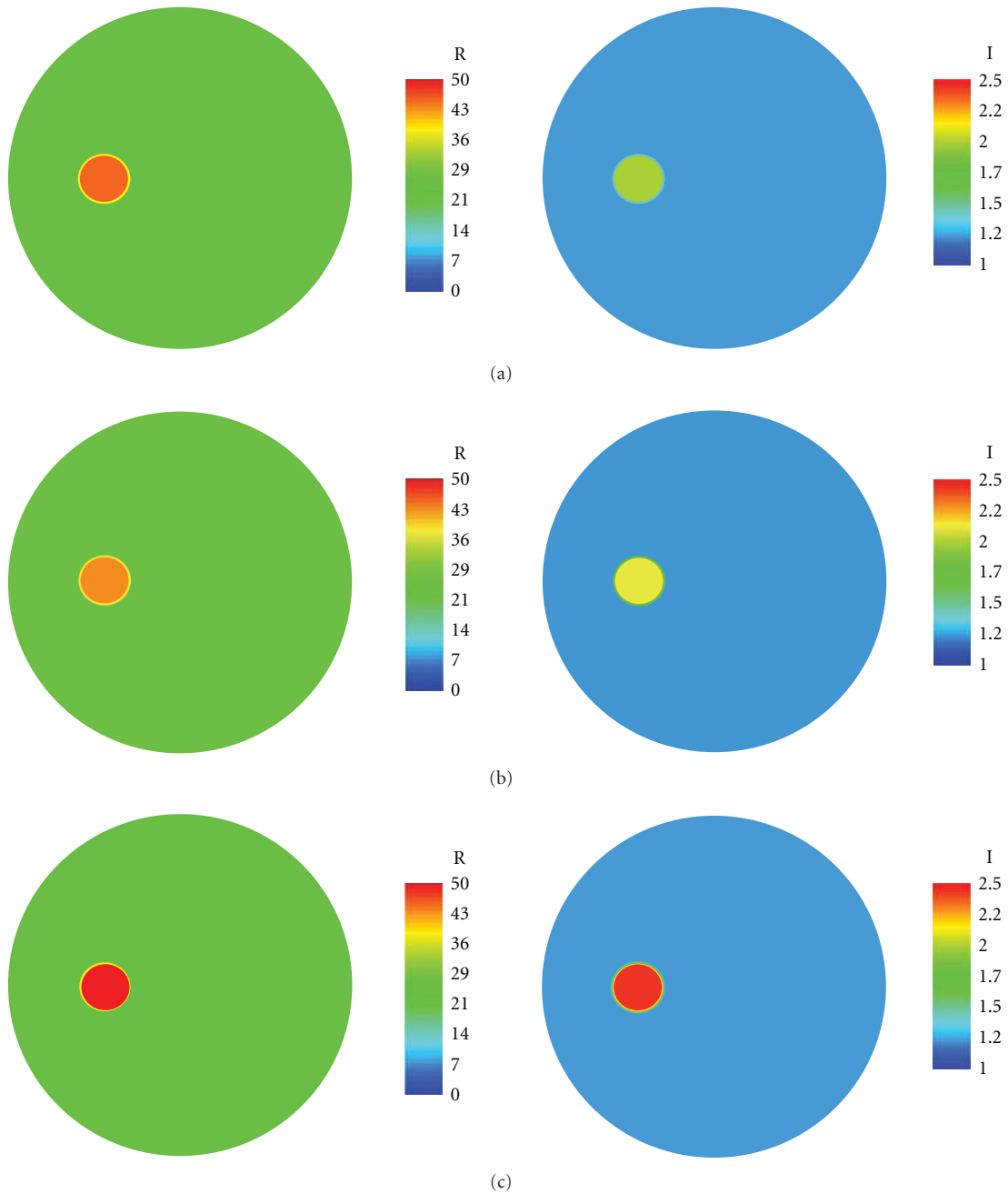


FIGURE 7: Reconstructed permittivity images (left) of the (a) 1st, (b) 2nd, and (c) 5th microwave scan of a saline-saturated bone specimen in a test tube at 1100 MHz, respectively. The green background shows the permittivity of the coupling liquid (80% glycerin) inside the imaging tank. The images on the right are the corresponding conductivity images.

prior permittivity and conductivity images at the (a) first, (b) second, and (c) final imaging scans. The bath was the same for all sessions as illustrated by the backgrounds of each image being identical to the others. It is interesting to note that while the dry diameters shrunk slightly from the acid treatments, when the samples were immersed in the saline, they expanded to fit snugly against the test tube walls. The properties of the recovered targets demonstrated a clear increasing trend from the first to the last imaging session.

The data for the six samples were pooled and analyzed. Figure 8 shows the scatter plots for the dielectric properties versus BVF at three frequencies (0.9, 1.1, and 1.3 GHz). Overall, both properties show a distinct downward trend with respect to bone volume fraction for all frequencies. The P values for both relative permittivity and conductivity at all three frequencies are less than the 0.05 threshold for significance. These relationships are further confirmed with the Pearson product-moment correlation coefficients

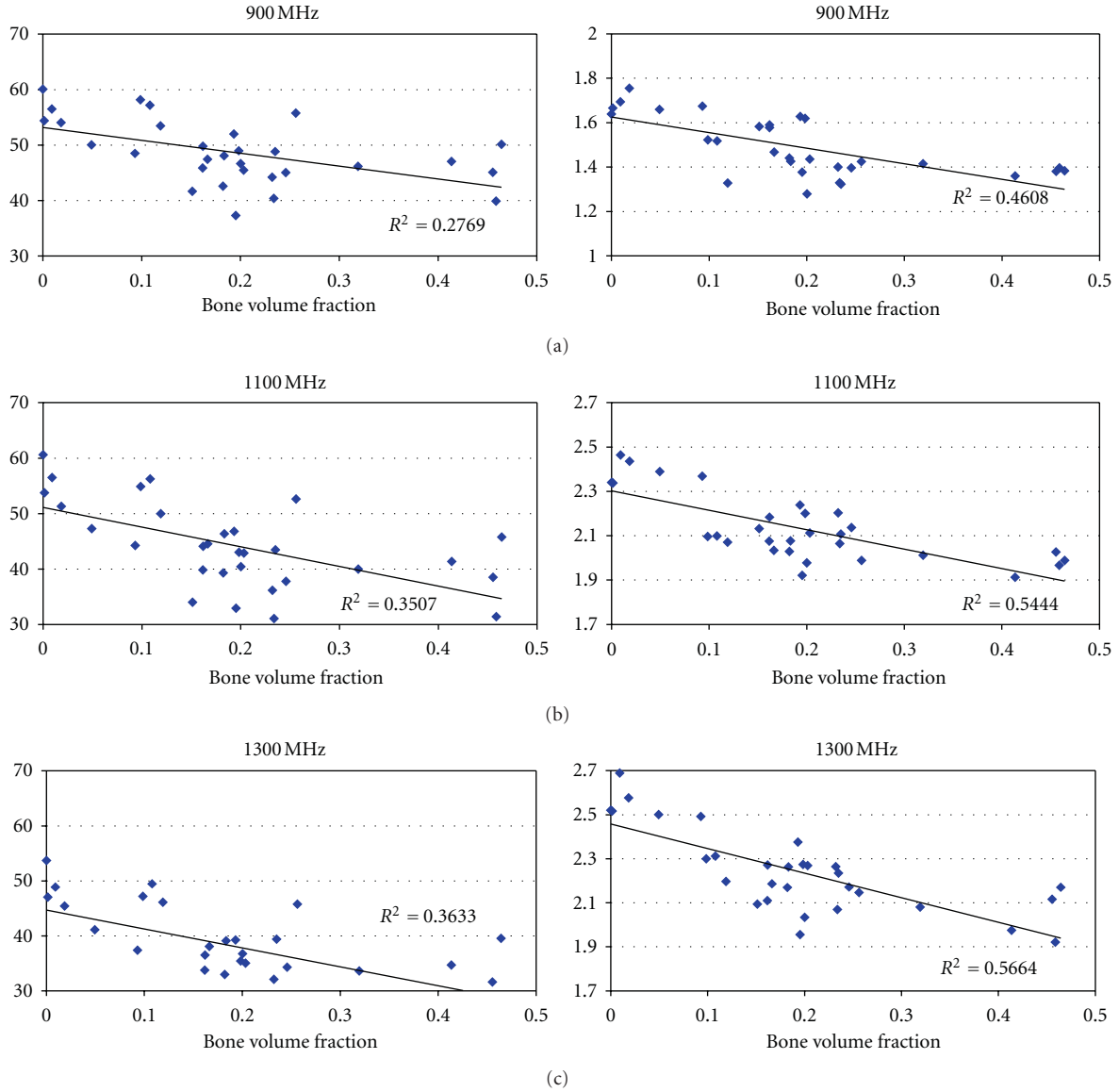


FIGURE 8: Scatter plot of dielectric properties versus bone volume fraction for saline-saturated bone specimens for different frequencies ($n = 30$).

(PMCC) summarized in Table 1. (The Pearson coefficients are a measure of the strength of linear dependence between two variables and are defined as the covariance of the two variables divided by the product of their standard deviations.) The correlation coefficients for the relative permittivity and conductivity with respect to BVF are above the threshold (in terms of their absolute values) for statistical significance with $n = 30$. The conductivity Pearson coefficients are consistently higher than those for the permittivity suggesting a higher level of correlation.

4. Discussion and Conclusions

We have successfully applied our microwave imaging system to assess the dynamic dielectric properties of bone tissue

TABLE 1: Values for Pearson product-moment correlation coefficient of the dielectric properties and BVF.

| Frequency (GHz) | Pearson r_{ϵ_r} versus BVF | Pearson r_{σ} versus BVF | Threshold for statistical significance ($n = 30$) |
|-----------------|-------------------------------------|---------------------------------|---|
| 0.9 | -0.53 | -0.68 | -0.37 |
| 1.1 | -0.59 | -0.74 | -0.37 |
| 1.3 | -0.60 | -0.75 | -0.37 |

samples. This is particularly important in the setting of measuring bone samples where other techniques such as open-ended dielectric probes have failed. The results are consistent with what would be predicted by Maxwell-Fricke mixture laws [4]; that is, with the decreased mineralization

(low dielectric property values) and increased saline (higher properties), the bulk dielectric properties of the saline-saturated bone sample increased. They are consistent with the findings from Chakkalakal et al. in that the variations in dielectric properties are determined by the content in the pore holes [21], although the operating frequencies and variation mechanisms of dielectric property dispersions differ. The results further confirm the flexibility and strength of the soft prior regularization strategy in the context of microwave imaging.

In addition, these results suggest a mechanism to explain the correlation between bone dielectric properties and age observed by Peyman et al. [11]. While these relationships were hypothesized because of the dynamic nature of bone tissue and the heavy dependence of tissue dielectric properties on water content [3], it was essential that these results be confirmed in direct investigations.

The measurement conditions for these experiments were suboptimal with respect to assessing the natural property variations as functions of bone density. In the body, the pore holes are filled with blood vessels and marrow. A future study should extend these measurements to *in vivo* or freshly excised bones to determine the contribution of these materials in the pore holes to the dielectric properties. The bone density variations could be induced directly by varying the animal diets, especially the mineral content, to provide more realistic controls. Notwithstanding, these results are a promising first step towards understanding the relationship between dielectric properties and bone density metrics and set the stage for exploiting this mechanism for microwave bone imaging as a clinical diagnostic tool.

Acknowledgments

This work was funded by NIH/NCI Grant no. PO1-CA080139. The authors would like to thank Drs. Douglas W. Van Citters and Eugene Santos from Thayer School of Engineering for their valuable discussions.

References

- [1] U.S. Department of Health and Human Services, "The 2004 Surgeon General's Report on Bone Health and osteoporosis: what it means to you." U.S. Department of Health and Human Services, Office of the Surgeon General, 2004.
- [2] K. R. Foster, J. L. Schepps, R. D. Stoy, and H. P. Schwan, "Dielectric properties of brain tissue between 0.01 and 10 GHz," *Physics in Medicine and Biology*, vol. 24, no. 6, article no. 008, pp. 1177–1187, 1979.
- [3] K. R. Foster and J. L. Schepps, "Dielectric properties of tumor and normal tissues at radio through microwave frequencies," *Journal of Microwave Power*, vol. 16, no. 2, pp. 107–119, 1981.
- [4] K. R. Foster and H. P. Schwan, "Dielectric properties of tissues," in *Handbook of Biological Effects of Electromagnetic Fields*, C. Polk and E. Postow, Eds., pp. 25–100, CRC Press, Boca Raton, Fla, USA, 1996.
- [5] C. Gabriel, S. Gabriel, and E. Corthout, "The dielectric properties of biological tissues: I. Literature survey," *Physics in Medicine and Biology*, vol. 41, no. 11, pp. 2231–2249, 1996.
- [6] S. Gabriel, R. W. Lau, and C. Gabriel, "The dielectric properties of biological tissues: II. Measurements in the frequency range 10 Hz to 20 GHz," *Physics in Medicine and Biology*, vol. 41, no. 11, pp. 2251–2269, 1996.
- [7] S. Gabriel, R. W. Lau, and C. Gabriel, "The dielectric properties of biological tissues: III. Parametric models for the dielectric spectrum of tissues," *Physics in Medicine and Biology*, vol. 41, no. 11, pp. 2271–2293, 1996.
- [8] C. Gabriel, A. Peyman, and E. H. Grant, "Electrical conductivity of tissue at frequencies below 1 MHz," *Physics in Medicine and Biology*, vol. 54, no. 16, pp. 4863–4878, 2009.
- [9] A. Peyman, A. A. Rezazadeh, and C. Gabriel, "Changes in the dielectric properties of rat tissue as a function of age at microwave frequencies," *Physics in Medicine and Biology*, vol. 46, no. 6, pp. 1617–1629, 2001.
- [10] A. Peyman, S. J. Holden, S. Watts, R. Perrott, and C. Gabriel, "Dielectric properties of porcine cerebrospinal tissues at microwave frequencies: in vivo, in vitro and systematic variation with age," *Physics in Medicine and Biology*, vol. 52, no. 8, article no. 013, pp. 2229–2245, 2007.
- [11] A. Peyman, C. Gabriel, E. H. Grant, G. Vermeeren, and L. Martens, "Variation of the dielectric properties of tissues with age: the effect on the values of SAR in children when exposed to walkie-talkie devices," *Physics in Medicine and Biology*, vol. 54, no. 2, pp. 227–241, 2009.
- [12] R. K. Aaron, D. M. Ciombor, and B. J. Simon, "Treatment of nonunions with electric and electromagnetic fields," *Clinical Orthopaedics and Related Research*, vol. 419, pp. 21–29, 2004.
- [13] E. Fukada and I. Yasuda, "On the piezoelectric effect of bone," *Journal of the Physical Society of Japan*, vol. 12, no. 10, pp. 1158–1162, 1957.
- [14] J. C. Gan and P. A. Glazer, "Electrical stimulation therapies for spinal fusions: current concepts," *European Spine Journal*, vol. 15, no. 9, pp. 1301–1311, 2006.
- [15] K. Kawamoto, W. C. Kim, Y. Tsuchida et al., "Effects of alternating current electrical stimulation on lengthening callus," *Journal of Pediatric Orthopaedics Part B*, vol. 14, no. 4, pp. 299–302, 2005.
- [16] A. A. Marino, R. O. Becker, and C. H. Bachman, "Dielectric determination of bound water of bone," *Physics in Medicine and Biology*, vol. 12, no. 3, article no. 309, pp. 367–378, 1967.
- [17] S. Saha and P. A. Williams, "Comparison of the electrical and dielectric behavior of wet human cortical and cancellous bone tissue from the distal tibia," *Journal of Orthopaedic Research*, vol. 13, no. 4, pp. 524–532, 1995.
- [18] S. R. Smith and K. R. Foster, "Dielectric properties of low-water-content tissues," *Physics in Medicine and Biology*, vol. 30, no. 9, pp. 965–973, 1985.
- [19] G. T. Swanson and J. F. Lafferty, "Electrical properties of bone as a function of age, immobilization and vibration," *Journal of Biomechanics*, vol. 5, no. 3, pp. 261–266, 1972.
- [20] J. Sierpowska, *Electrical and dielectric characterization of trabecular bone quality*, Doctoral Dissertation, Kuopio University, Kuopio, Finland, 2007.
- [21] D. A. Chakkalakal, M. W. Johnson, M. A. Harper, and J. L. Katz, "Dielectric properties of fluid-saturated bone," *IEEE Transactions on Biomedical Engineering*, vol. 27, no. 2, pp. 95–100, 1980.
- [22] S. Saha, G. N. Reddy, and J. A. Albright, "Factors affecting the measurement of bone impedance," *Medical and Biological Engineering and Computing*, vol. 22, no. 2, pp. 123–129, 1984.
- [23] D. M. Hagl, D. Popovic, S. C. Hagness, J. H. Booske, and M. Okoniewski, "Sensing volume of open-ended coaxial probes for dielectric characterization of breast tissue at microwave

- frequencies,” *IEEE Transactions on Microwave Theory and Techniques*, vol. 51, no. 4 I, pp. 1194–1206, 2003.
- [24] W. T. Joines, Y. Zhang, C. Li, and R. L. Jirtle, “The measured electrical properties of normal and malignant human tissues from 50 to 900 MHz,” *Medical Physics*, vol. 21, no. 4, pp. 547–550, 1994.
- [25] M. Lazebnik, D. Popovic, L. McCartney et al., “A large-scale study of the ultrawideband microwave dielectric properties of normal, benign and malignant breast tissues obtained from cancer surgeries,” *Physics in Medicine and Biology*, vol. 52, no. 20, pp. 6093–6115, 2007.
- [26] M. Lazebnik, L. McCartney, D. Popovic et al., “A large-scale study of the ultrawideband microwave dielectric properties of normal breast tissue obtained from reduction surgeries,” *Physics in Medicine and Biology*, vol. 52, no. 10, article no. 001, 2007.
- [27] K. R. Foster, J. L. Schepps, and H. P. Schwan, “Microwave dielectric relaxation in muscle. A second look,” *Biophysical Journal*, vol. 29, no. 2, pp. 271–281, 1980.
- [28] M. Lazebnik, M. C. Converse, J. H. Booske, and S. C. Hagness, “Ultrawideband temperature-dependent dielectric properties of animal liver tissue in the microwave frequency range,” *Physics in Medicine and Biology*, vol. 51, no. 7, pp. 1941–1955, 2006.
- [29] P. M. Meaney, M. W. Fanning, K. D. Paulsen et al., “Microwave thermal imaging: initial in vivo experience with a single heating zone,” *International Journal of Hyperthermia*, vol. 19, no. 6, pp. 617–641, 2003.
- [30] P. M. Meaney, K. D. Paulsen, M. W. Fanning, D. Li, and Q. Fang, “Image accuracy improvements in microwave tomographic thermometry: phantom experience,” *International Journal of Hyperthermia*, vol. 19, no. 5, pp. 534–550, 2003.
- [31] C. M. Sehgal, G. M. Brown, R. C. Bahn, and J. F. Greenleaf, “Measurement and use of acoustic nonlinearity and sound speed to estimate composition of excised livers,” *Ultrasound in Medicine and Biology*, vol. 12, no. 11, pp. 865–874, 1986.
- [32] C. M. Sehgal, B. R. Porter, and J. F. Greenleaf, “Ultrasonic nonlinear parameters and sound speed of alcohol-water mixtures,” *Journal of the Acoustical Society of America*, vol. 79, no. 2, pp. 566–570, 1986.
- [33] C. Wu, C. Glüer, Y. Lu, T. Fuerst, D. Hans, and H. K. Genant, “Ultrasound characterization of bone demineralization,” *Calcified Tissue International*, vol. 62, no. 2, pp. 133–139, 1998.
- [34] A. Golnabi, P. M. Meaney, M. W. Fanning, and K. D. Paulsen, “Bulk tissue dielectric measurements using microwave imaging with a soft prior regularization,” in *Proceedings of the URSI International Symposium on Antenna Technology and Applied Electromagnetics (ANTEM '09)*, Banff, Canada, 2009.
- [35] A. H. Golnabi, P. M. Meaney, S. D. Geimer, M. W. Fanning, and K. D. Paulsen, “Comparison of no-prior and soft-prior regularization in biomedical microwave imaging,” *International Journal of Medical Physics*, vol. 36, no. 2, pp. 125–136, 2011.
- [36] J. S. Schreiman, J. J. Gisvold, J. F. Greenleaf, and R. C. Bahn, “Ultrasound transmission computed tomography of the breast,” *Radiology*, vol. 150, no. 2, pp. 523–530, 1984.
- [37] P. M. Meaney, K. D. Paulsen, B. W. Pogue, and M. I. Miga, “Microwave image reconstruction utilizing log-magnitude and unwrapped phase to improve high-contrast object recovery,” *IEEE Trans. Medical Imaging*, vol. 20, pp. 104–116, 2001.
- [38] D. R. Lynch, *Numerical Partial Differential Equations for Environmental Scientists and Engineers: a First Practical Course*, Springer, Berlin, Germany, 2005.

Research Article

Surface Wave Multipath Signals in Near-Field Microwave Imaging

**Paul M. Meaney,¹ Fridon Shubitidze,¹ Margaret W. Fanning,¹ Maciej Kmiec,²
Neil R. Epstein,¹ and Keith D. Paulsen^{1,3}**

¹Thayer School of Engineering, Dartmouth College, Hanover, NH 03755, USA

²Department of Radiology, Dartmouth Medical School, Hanover, NH 03755, USA

³Norris Cotton Cancer Center, Dartmouth-Hitchcock Medical Center, Lebanon, NH 03756, USA

Correspondence should be addressed to Paul M. Meaney, paul.meaney@dartmouth.edu

Received 14 September 2011; Revised 10 January 2012; Accepted 18 January 2012

Academic Editor: Elise Fear

Copyright © 2012 Paul M. Meaney et al. This is an open access article distributed under the Creative Commons Attribution License, which permits unrestricted use, distribution, and reproduction in any medium, provided the original work is properly cited.

Microwave imaging techniques are prone to signal corruption from unwanted multipath signals. Near-field systems are especially vulnerable because signals can scatter and reflect from structural objects within or on the boundary of the imaging zone. These issues are further exacerbated when surface waves are generated with the potential of propagating along the transmitting and receiving antenna feed lines and other low-loss paths. In this paper, we analyze the contributions of multi-path signals arising from surface wave effects. Specifically, experiments were conducted with a near-field microwave imaging array positioned at variable heights from the floor of a coupling fluid tank. Antenna arrays with different feed line lengths in the fluid were also evaluated. The results show that surface waves corrupt the received signals over the longest transmission distances across the measurement array. However, the surface wave effects can be eliminated provided the feed line lengths are sufficiently long independently of the distance of the transmitting/receiving antenna tips from the imaging tank floor. Theoretical predictions confirm the experimental observations.

1. Introduction

Multipath signals occur in numerous microwave and RF applications when an unwanted portion of the original transmission propagates along any alternate path and ultimately couples to the receiver distorting the amplitude and phase of the desired signal [1–4]. If the amplitude of the multipath signal is sufficiently large, its impact can be considerable. In multistatic radar and communication systems, these types of interference are most often caused by reflections of either the main beam or side lobes with objects near or actually in the beam path. Classic examples include main beam propagation close to the earth's surface with associated reflections off of the ground or water (Figure 1(a)) [5]. Various approaches can be used to filter or compensate for these reflections through time-gating [6] and signal time synchronization [7].

The potential for interference from multipath signals increases substantially in near-field applications (Figure 1(b)), especially in situations where the receiving and transmitting hardware are integrated. A common form occurs when

multiple receive channels are employed with inadequate channel isolation. Commercially available multichannel network analyzers (e.g., ZVT8 by Rohde & Schwarz; Munich, Germany) utilize robust strategies to minimize these signal coupling problems. We are developing multichannel transmitting arrays for medical microwave imaging which exploit near-field concepts to produce electrical property maps (permittivity and conductivity) of tissues of interest [8, 9] and have addressed the issue by incorporating (a) dedicated mixers for each channel, (b) additional solid state switches for isolation, (c) double- and triple-braided coaxial cables, and (d) compartmentalized RF circuitry. The implementation has proven effective for our application achieving channel/signal isolation greater than 130 dB [8]. An alternative data acquisition strategy integrates a commercial, 2-port network analyzer with an electronic switching network to feed an array of antennas [10–12] which is effective but also has limitations because (i) dynamic range is constrained by the provisions of the network analyzer, (ii) two-way signal loss is

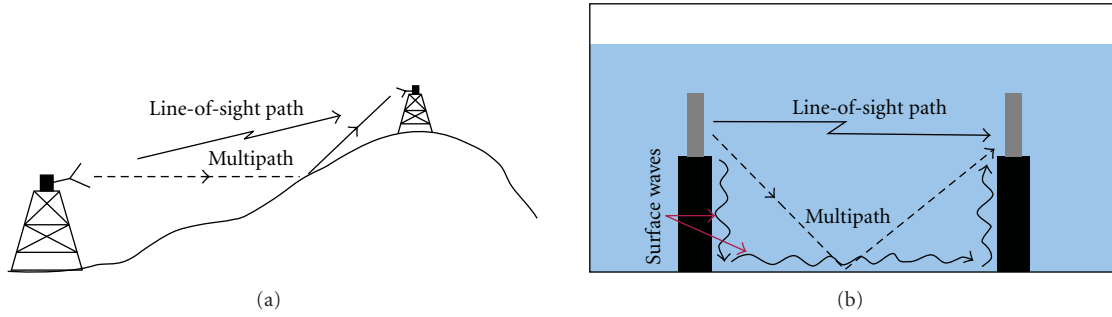


FIGURE 1: (a) Illustration of a bistatic communication between antenna towers and line-of-site versus possible multipath signals and (b) near-field imaging tank in a liquid medium with possible reflection and surface wave propagation paths.

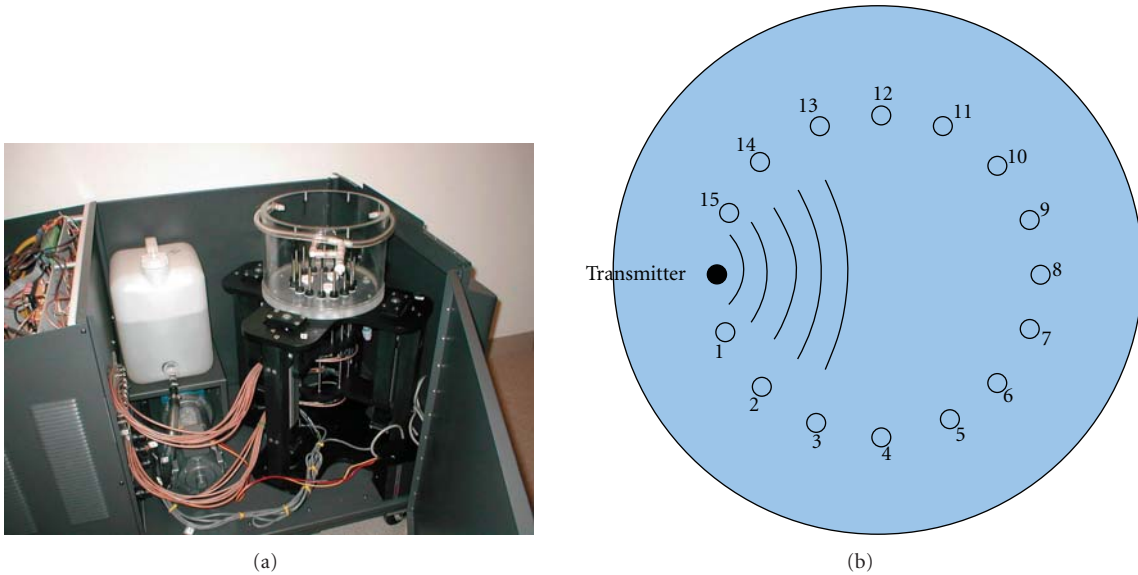


FIGURE 2: (a) Photograph of the inside of the clinical imaging system showing the imaging tank, liquid reservoir, and antenna motion system. The microwave electronics are housed behind the firewall to the left; (b) schematic diagram of the antenna array configuration.

incurred through the network, and (iii) the switching matrix has relatively poor cross-channel isolation [10].

Equally important in near-field imaging is the multiple paths a signal can take within the imaging zone. Figures 2(a) and 2(b) show a photograph of our clinical breast imaging tank and a schematic diagram of the antenna configuration, respectively. In this situation, the array of 16 monopole antennas surrounds the breast and can be moved to multiple vertical positions. The antennas and target are submerged in a solution of glycerin and water which is lossy over the operating frequency range (700 MHz–3 GHz). Early empirical tests have indicated that reflections off the tank side walls do not impact the desired signals for an array with the antennas mounted on a 15.2 cm diameter circle [13]. Likewise, analysis of the monopole beam patterns as a function of frequency has shown that artifacts are minimal when the array approaches the liquid interface at the top of the tank [14].

With respect to reflections off the bottom surface, the base of the tank was at least 1.8 wavelengths (at the lowest

frequency) below the active sections of the antennas in our initial clinical installation when the array was located at its lowest position during an exam. Since minimal multipath signals resulted from reflections off the top liquid surface, symmetry would suggest that the same should be true for the base of the tank (Figure 1(b)). However, surface waves can cause multipath signals that can be especially difficult to eliminate in near-field systems. Their excitation can be complex, but their propagation characteristics along two material interfaces, whether planar or along cylindrically shaped structures, have previously been studied in depth [15–20]. Surface waves can readily propagate at the interface of two dielectric materials or one conductor juxtaposed directly with a dielectric. Their propagation and attenuation characteristics are nominally determined by the electrical properties of the two materials. In addition, their amplitude decays exponentially away from the interface in the perpendicular direction as a function of the lossiness of the complementary materials [15].

It should be noted that these investigations have stemmed partially from our efforts to perform microwave tomographic images on patients in an actual MR scanner for the purpose of exploiting the refined spatial resolution of the MR along with the more specific nature of the tissue dielectric properties. The MR bore is quite small and places a significant constraint of space for the microwave system. Initial attempts included shortening the antenna feed lines associated with the shorter illumination tank. This was where we first encountered multipath signal corruption which subsequently led to this study.

In the following sections, we discuss the theoretical underpinnings of these modes for the geometries present in our system. We demonstrate cases from our current imaging system, where the measurements indicate corruption of the desired signals from multipath signals associated with the base of the tank. We then show experiments that allow us to partially isolate the effects to surface waves propagating along other pathways. We realize that there are a number of propagation modes around the antennas, their feedlines and the tank surfaces, of which the surface waves are only one possible contributor, but understanding these contributions is important. We present an initial strategy for minimizing the effects of these signals which may be instructive for designing other near-field imaging systems, including simulations confirming the earlier theoretical discussion and validating our feedline design strategy.

2. Methods

2.1. MultiPath Corruption. A challenging situation occurs when a portion of the transmitted signal propagates along an unwanted path and recombines with the original signal at the receiver. Because both occur at the same frequency, filtering is generally ineffective. Time-gating strategies can sometimes be effective when the nature of the multipath signal is well understood [1, 2]. Attenuation is another means of dealing with these unwanted signals. The potential influence of a multipath signal when the original transmission is a continuous wave can be written as

$$\text{Resultant Signal} = A_{\text{comb}} \cos(\omega t + \phi_{\text{comb}}), \quad (1)$$

where

$$\begin{aligned} \phi_{\text{comb}} &= A_{\text{comb}} \tan^{-1} \left(\frac{B_1}{A_1} \right), \\ A_{\text{comb}} &= \sqrt{A_1^2 + B_1^2}, \\ A_1 &= [A_{\text{de}} \cos \phi_{\text{de}} + A_{\text{mp}} \cos \phi_{\text{mp}}], \\ B_1 &= [A_{\text{de}} \sin \phi_{\text{de}} + A_{\text{mp}} \sin \phi_{\text{mp}}]. \end{aligned} \quad (2)$$

Here, A_{de} , A_{mp} , ϕ_{de} , and ϕ_{mp} are the desired and multipath signal amplitudes and phases, respectively, ω is the operating frequency, and t is time. For example, if the magnitude of the multipath signal is 25 dB below that of the desired signal, the maximum possible amplitude and phase errors in the resultant signal would be 0.48 dB and 3.22° , respectively. For

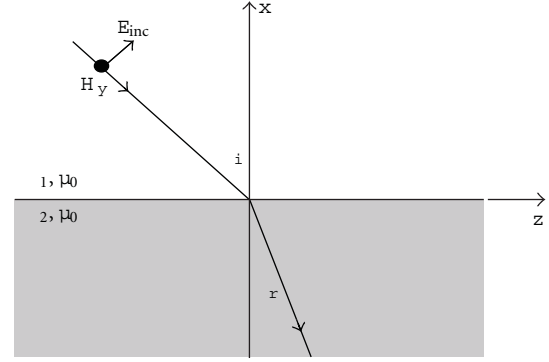


FIGURE 3: Diagram of a plane wave incident on a planar interface between two dielectric materials.

a -15 dB multipath signal, these values increase to 1.42 dB and 10.24° . Clearly, the resultant phase and amplitude errors can become very significant for multipath signals that are on the same order of magnitude as the desired signals. It should be noted that there can be many multipath contributions with a range of amplitude and phase contributions. This single contributor analysis serves to give a flavor that the unwanted effects can be significant and is generalizable to multiple sources.

2.2. Surface Wave Analysis

2.2.1. Planar Interface between Plexiglas Base and Coupling Liquid. The first surface mode to be considered involves propagation along the interface between the tank base and coupling liquid. Following the analysis by Stratton [15], Figure 3 shows a plane wave in Region 1 impinging on an interface ($x = 0$) with Region 2. In this case, the magnetic field (H_y) is only oriented in the y -direction (out of the page). The complex relative dielectric properties in the two regions are $\epsilon_1 = \epsilon'_1 - j\epsilon''_1$ and $\epsilon_2 = \epsilon'_2 - j\epsilon''_2$, respectively. The classic surface wave solution occurs when the reflection coefficient is zero (at the Brewster angle), which is complex-valued in this instance. If A is the amplitude of the incident plane wave, then the magnetic component of the incident and transmitted waves can be represented as

$$\begin{aligned} H_y &= A e^{[jh_1 x - j\beta z]}, \quad x > 0, \\ H_y &= A e^{[jh_1 x - j\beta z]}, \quad x < 0, \end{aligned} \quad (3)$$

where $h_1^2 + \beta^2 = k_1^2$ and $h_2^2 + \beta^2 = k_2^2$ are needed to satisfy the wave equation, k_1 and k_2 are the wave numbers for the two regions, and β is the propagation constant.

The wave impedances for the two regions are given by

$$\begin{aligned} \bar{Z}_1 &= \frac{h_1}{k_1} Z_1 = \frac{h_1}{k_1} Z_0 \frac{1}{\sqrt{\epsilon'_1 - j\epsilon''_1}}, \\ \bar{Z}_2 &= \frac{h_2}{k_2} Z_2 = \frac{h_2}{k_2} Z_0 \frac{1}{\sqrt{\epsilon'_2 - j\epsilon''_2}}, \end{aligned} \quad (4)$$

where \bar{Z}_1 and \bar{Z}_2 are the free space impedances in the corresponding regions, and \bar{Z}_1 and \bar{Z}_2 are the associated wave impedances [21, 22]. This yields

$$h_1 \kappa = h_2, \quad (5)$$

where

$$\kappa = \frac{\varepsilon_2}{\varepsilon_1} = \frac{\varepsilon_2' - j\varepsilon_2''}{\varepsilon_1' - j\varepsilon_1''}. \quad (6)$$

From these relationships, we can solve for

$$\begin{aligned} h_1 &= k_0 \sqrt{\frac{\varepsilon_1(1-\kappa)}{1-\kappa^2}}, \\ h_2 &= k_0 \sqrt{\frac{\varepsilon_1 \kappa^2(1-\kappa)}{1-\kappa^2}}, \\ \beta &= k_0 \sqrt{\frac{\varepsilon_1 \kappa(1-\kappa)}{1-\kappa^2}}. \end{aligned} \quad (7)$$

2.2.2. Metallic Coaxial Conductor Surrounded by the Coupling Liquid. In this situation, we are primarily interested in surface waves propagating along the outside of a coaxial cable, and their associated attenuation as a function of distance after the mode has been sufficiently established. For this analysis, we will consider the case of a coaxial line which is abruptly terminated by an open end (Figure 4).

A coaxial cable supports a TEM-mode electromagnetic field which is incident on the cable opening. Part of the signal is partially reflected into the cable, while a second portion is transmitted as a surface wave propagating along the outside of the surrounding cable. The fields transmitted into the surrounding space can be determined from the distribution at the coaxial opening which can be found by solving the integral equation for the radial component of the electric field over the opening:

$$\begin{aligned} \frac{1}{4\pi\rho} + j\omega\varepsilon_c \int_a^b E_\rho(\rho', 0) K_c(\rho, \rho') \rho' d\rho' \\ = \frac{j\omega\varepsilon_1}{\pi} \int_a^b E_\rho(\rho', 0) K_c(\rho, \rho') \rho' d\rho' \int_0^\pi \cos\phi' \frac{e^{-jkr}}{r} d\phi', \end{aligned} \quad (8)$$

where ε_c and ε_1 are the complex-valued permittivity of the coaxial cable insulator and the surrounding dielectric materials, respectively, a and b are inner and outer coaxial radii, respectively, ω is the operating frequency in radians, and k is the wavenumber in the coupling liquid, where μ_0 is the free space magnetic permeability. ρ' and ρ are the radial cylindrical coordinates within and outside of the coaxial cable, respectively, ϕ' is the angular coordinate within the coaxial cable, and r is defined as $r = \sqrt{\rho^2 + \rho'^2 - 2\rho\rho' \cos\phi'}$. The variable $K_c(\rho, \rho')$ is represented as

$$K_c(\rho, \rho') = j \sum_{n=0}^{\infty} \frac{\varphi_n(\rho) \varphi_n(\rho')}{A_n^2 \beta_n}, \quad (9)$$

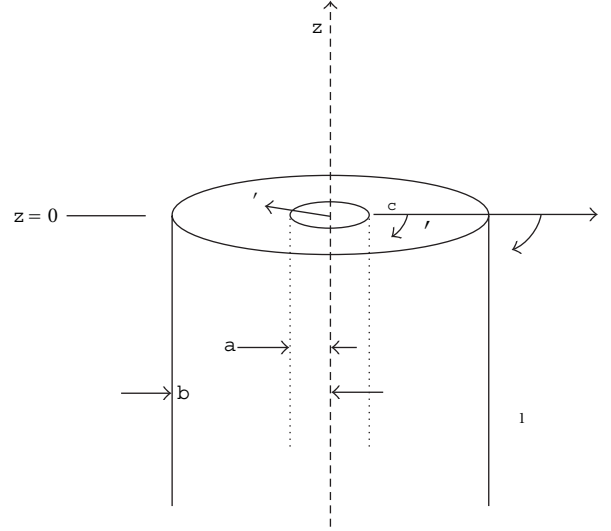


FIGURE 4: Illustration of the excitation of coaxial surface waves and associated coordinates.

where

$$\begin{aligned} \varphi_n(\rho) &= Y_0(\gamma_n a) J_1(\gamma_n \rho) - J_0(\gamma_n a) Y_1(\gamma_n \rho), \\ \beta_n &= \begin{cases} \sqrt{k_c^2 - \gamma_n^2}, & k_c > \gamma_n \\ \pm j\sqrt{\gamma_n^2 - k_c^2}, & k_c < \gamma_n, \end{cases} \\ A_n^2 &= \frac{2}{\pi^2 \gamma_n^2} \left[\frac{J_0^2(\gamma_n a)}{J_0^2(\gamma_n b)} - 1 \right], \quad n > 0, \\ A_0^2 &= \ln \frac{b}{a}. \end{aligned} \quad (10)$$

The eigenvalue γ_n are solutions of the characteristic equation:

$$Y_0(\gamma_n a) J_1(\gamma_n b) = J_0(\gamma_n a) Y_1(\gamma_n b), \quad (11)$$

where J_n and Y_n are Bessel functions of the first and second kind of order n , respectively, and k_c is the wavenumber inside the coaxial line. Once $E_\rho(\rho', z=0)$ is determined, then electric and magnetic fields can be found at any point (ρ, z) in the surrounding medium from

$$E_\rho(\rho, z) = \frac{1}{\pi} \int_a^b E_\rho(\rho', 0) \rho' \int_0^\pi \left(jk + \frac{1}{R'} \right) z \cos\phi' \frac{e^{-jkR'}}{R'} d\phi' d\rho', \quad (12)$$

or

$$\begin{aligned} E_\rho(\rho, z) &= \frac{1}{\pi} \int_a^b E_\rho(\rho', 0) \rho' \\ &\quad \times \int_0^\pi \left[\frac{1}{\rho} - \left(jk + \frac{1}{R'} \right) \right] \frac{\rho - \rho' \cos\phi'}{R'} \frac{e^{-jkR'}}{R'} d\phi' d\rho' \\ H_\phi(\rho, z) &= \frac{j\omega\varepsilon_1}{\pi} \int_a^b E_\rho(\rho', 0) \rho' \\ &\quad \times \int_0^\pi \cos\phi' \frac{e^{-jkR'}}{R'} d\phi' d\rho', \end{aligned} \quad (13)$$

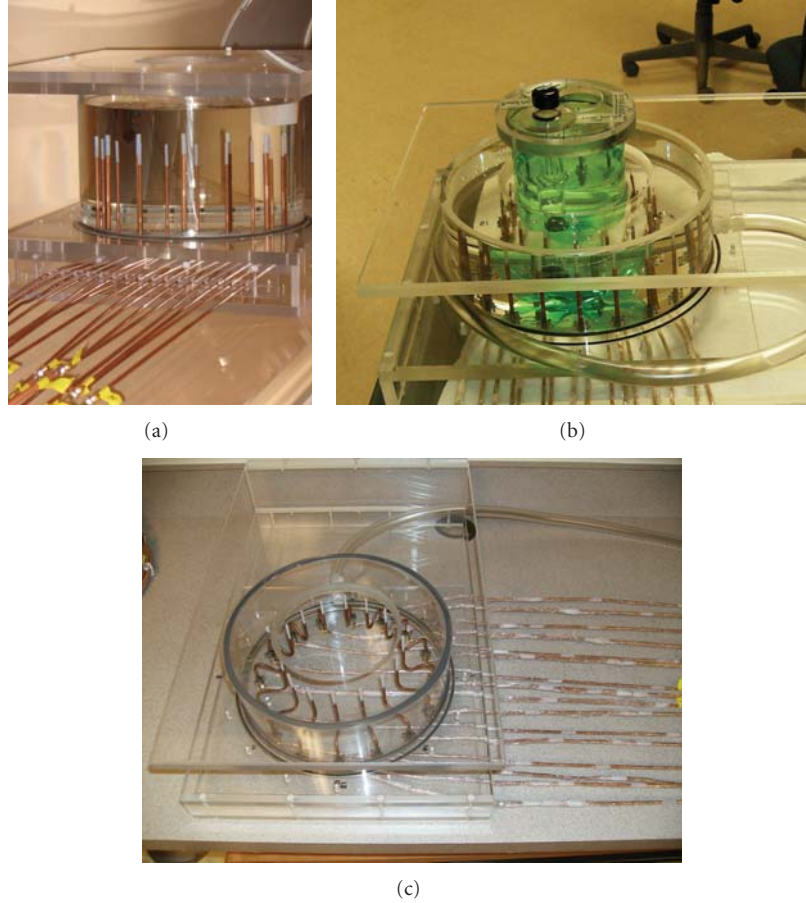


FIGURE 5: Photographs of the three imaging tanks and antennas used in experiments: (a) taller tank with straight 10 cm feed line lengths, (b) shorter tank with the straight 5 cm feed line lengths, and (c) the short tank with the 10 cm feed line lengths in a serpentine shape.

where

$$R' = \sqrt{z^2 + \rho^2 + \rho'^2 - 2\rho\rho' \cos \phi'}. \quad (14)$$

From these equations it follows that the electromagnetic fields inside the surrounding medium decay approximately as $e^{-jkR'}$.

2.3. Breast Imaging System. Figure 2(a) shows the illumination tank used in our current clinical breast imaging system. Each monopole antenna consists of an exposed length (3.8 cm) of 2.2 mm diameter semirigid coaxial cable with only the center conductor and insulating Teflon layer intact. For mechanical robustness, the coaxial feed line is enclosed in a 6.4 mm diameter rigid stainless steel tube, and the active section of the antenna is covered with an accompanying length of a Delrin cylinder acting as a protective radome. The space between the copper coaxial outer conductor and the stainless steel sleeve is sealed at either end with silver epoxy to eliminate wave propagation along the gap. The antennas have a nominal return loss of -10 dB over the bandwidth of 700–3000 MHz. The black Delrin fittings at the antenna/tank base contain hydraulic seals through which the antenna feeds pass to allow vertical motion of the array while eliminating

any coupling fluid leakage. The 16 antennas are positioned on a 15.2 cm diameter circle, and both sets of 8 interleaved antennas are supported by individual mounting plates under the tank which provide independent motion of the array in groups of 8. The tank is fabricated out of Plexiglas with an inner wall diameter of 27.3 cm and thickness of 1.3 cm, and the base has a thickness of 2.5 cm. All connecting cables are double-braided to minimize stray radiation. In these experiments, the antennas were positioned at heights close to the tank base (that were not used in any clinical exams) to study the multipath phenomenon in detail.

2.4. Experimental Imaging Tanks. Figures 5(a), 5(b), and 5(c) show three illumination tanks with different heights, arrays of monopole antennas, and coaxial feed lines that were fabricated from the same Plexiglas and had identical diameters and wall/base thicknesses as Figure 2(a) tank. The feed lines passed through holes in the base of each tank and were fastened to SMA flange connectors which were bolted to the tank floor. The tanks were filled with an 80 : 20 glycerin/water mixture with the liquid level 1.5 cm above the antenna tips. In Figures 5(a) and 5(c), the feed lines were both 10 cm long; however, the latter was bent in a serpentine shape such that the top height of the feed line was only 5 cm above the tank

floor. The feed line in Figure 5(b) was straight and was only 5 cm long.

2.5. Material Dielectric Properties. In these experiments, we used Plexiglas for the tank materials with a dielectric constant of $\epsilon_r = 2.7$ that was effectively lossless in this frequency range [23]. The dielectric properties of the 80:20 glycerin/water bath are plotted in Figure 6 as a function of frequency.

3. Results and Discussion

3.1. Clinical System Experiment. Utilizing the clinical system described in Section 2.2, a +5 dBm signal was transmitted at multiple frequencies over the 700–2500 MHz range from a single antenna and received at the remaining 15 antennas. This sequence was repeated for the array positioned at multiple heights above the tank base. Receive antenna amplitudes are plotted for representative frequencies in Figure 7. At 900 MHz, the measured levels are high for the receivers closest to the transmitter (relative receiver numbers 1, 2, 14, and 15) compared to the rest of the array and do not change dramatically with changes in antenna height. However, the amplitudes are considerably lower for the more distant receive antennas. For antenna heights 7 cm or greater (above the tank floor), the attenuation follows a smooth curve hitting a maximum at antenna 8 (which is furthest away from the transmitter being located on the opposite side of the array). At antenna heights 5 cm and lower, the signal levels begin to deviate from this smooth pattern. The behavior is consistent with the three frequencies shown in Figure 7. Given that the distance from the antennas to the tank side walls did not change during the experiments, and that the antennas were sufficiently far from the liquid/air interface at all times for any array heights (10 cm in the worst case), the corruption of these most distantly received signals appears to be caused by multipath propagation associated with antenna tip proximity to the base of the tank most probably due to reflections off of the tank base or surface wave propagation along the dielectric interfaces.

3.2. Experimental Tanks. In this set of experiments, we utilized the illumination tanks and antennas described in Section 2.3. Figures 8(a) and 8(b) show the received signals for a single transmitter over a range of frequencies for straight feed line lengths of 10 cm and 5 cm (tanks in Figures 5(a) and 5(b)), respectively. For the longer (10 cm) lines in Figure 8(a), the field patterns appear well-behaved like those in the previous section, when the array was positioned at the largest heights above the tank floor. However, the patterns for the shorter (5 cm) line lengths in Figure 8(b) exhibit corruption of the signals resulting from the longer propagation distances similarly to when the array heights were closest to the base of the tank for the clinical system (in Figure 7). These corrupted signals are nominally between -50 to -70 dBm and occur in uneven patterns relative to the same signals from the longer feed lines which reach -80 to -90 dBm at the furthest antenna. For the shorter propagation distances (i.e., the signals received at antennas 1–4 and 12–15), the

attenuation patterns from the shorter and longer feed lines are similar (Figure 8(b) versus 8(a)). These results suggest that the unwanted multipath signal effect is the same in both the experimental tanks and the clinical system tests in the previous section and depends on the antenna height from the base of the tank. However, in Figure 8(c), the antenna feed length is exactly the same as in Figure 8(a), but is curved such that the antenna tip is the same height above the tank floor as the antennas in Figure 8(b) (which led to signal corruption); yet, the measurement results emulate those in Figure 8(a) (which are not corrupted). Here, the active part of the antennas is still positioned on the same 15.2 cm diameter circle as in the other two tanks. These findings show that the principle signal corruption observed in Figure 8(b) is not due to reflections off the tank floor; otherwise it would have appeared in Figure 8(c) since the antennas are at the same position above the base for both Figures 8(b) and 8(c). It should be noted that the signal disruptions for this situation appear more substantial than that for the antennas used in the clinical system as discussed in Section 3.1. This is very likely due to differences in the designs of the hydraulic seals, feedline shielding, and antenna radome for the other system.

More likely, the multipath signals in Figure 8(b) (with short feed lines) result from surface waves traveling along the outside of the coaxial lines, across the Plexiglas/liquid and/or Plexiglas/air interface and back up the outside of the receiver coaxial feed. The theoretical considerations in Section 2.2 indicate that the attenuation along the coaxial lines is far more substantial than from the planar tank-base surface wave modes. Figure 9(a) shows a plot of attenuation as a function of frequency for 15.2 cm of Plexiglas/liquid surface waves and indicates that very little attenuation of a surface wave propagating along this interface occurs at the frequencies we used. Thus, in our experiments, the real source of surface wave attenuation comes from propagation along the outside of the coaxial lines. Figure 9(b) shows plots of the attenuation that results from single 5 and 10 cm lengths of feed line in the coupling fluid. The theoretical predictions of attenuation along the two 5 cm antenna feed lengths (transmit and receive) and the path along the Plexiglas base/liquid interface are approximately 70 dB ($\{2 \times 34 \text{ dB}\} + 2 \text{ dB}$) for the 1 GHz case (values interpolated from Figures 9(a) and 9(b)). Given a transmit power level of +5 dBm, the resultant -65 dBm multipath signal for the shorter line would easily corrupt the desired -81 dBm signal (Figure 8(a)). The 140 dB attenuation for the longer lines easily solves this problem. Only when the feed lines are nearly doubled in length, and the associated surface wave attenuation increased accordingly is the corruption of the desired signals reduced to an acceptable level.

3.3. Simulated Field Distributions. Along with the analytical discussion in Sections 2.1 and 2.2, we have also performed simulations of the configurations described in Section 2.4. Figures 10(a), 10(b), and 10(c) show the 900 MHz electric field magnitude distributions for the long and short, straight antenna feed and the longer, serpentine structure, respectively. These simulations were computed using ANSYS

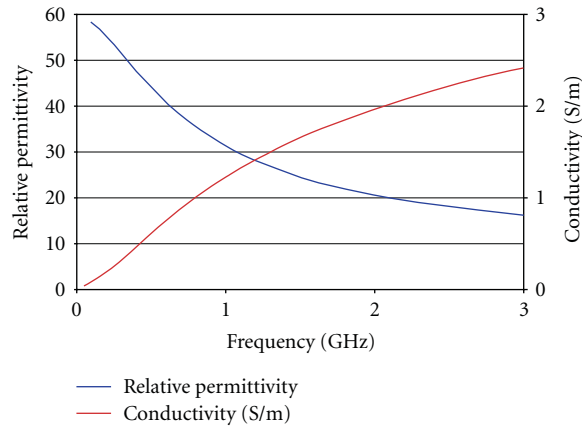


FIGURE 6: Dielectric properties of the 80 : 20 glycerin : water bath.

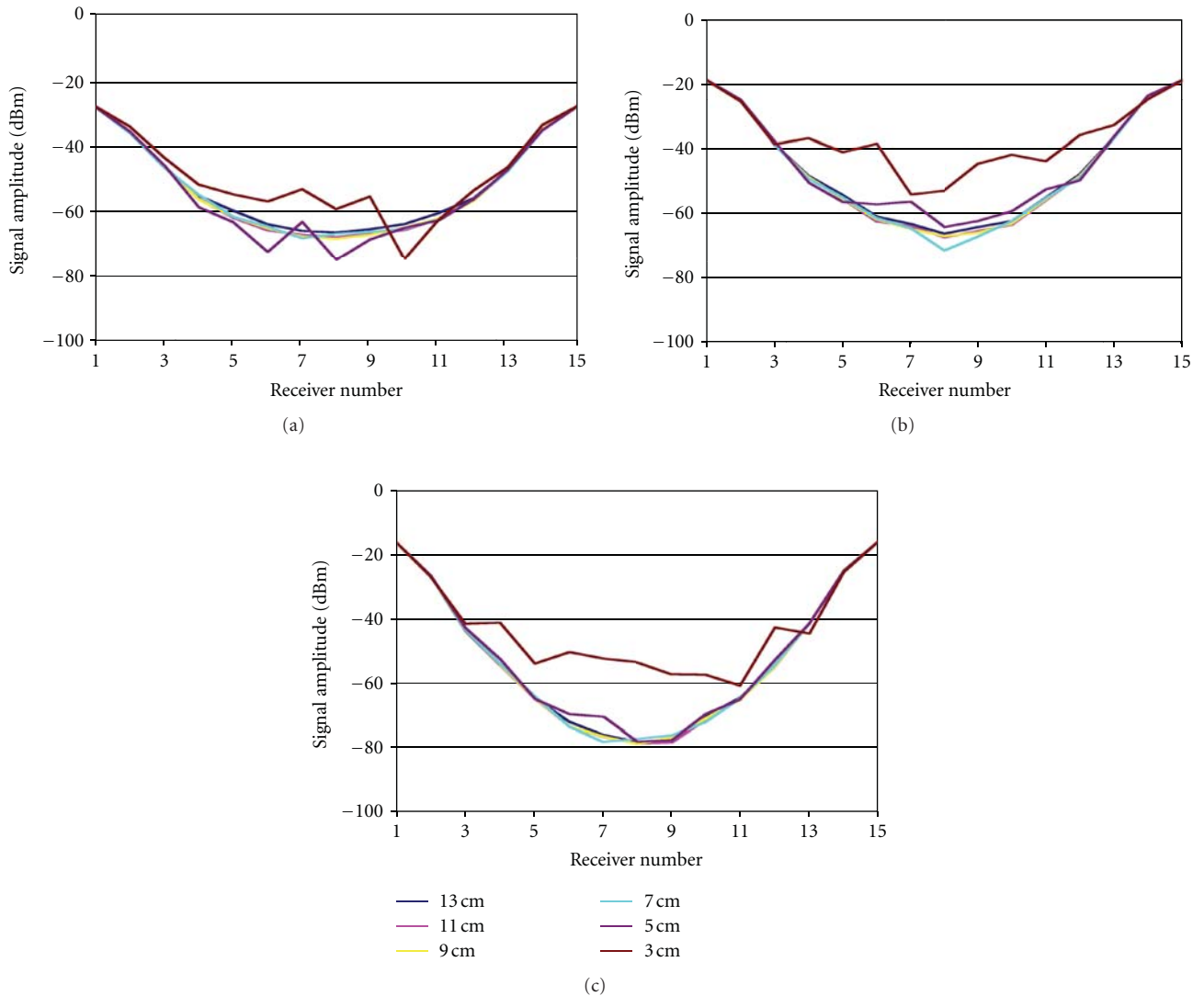


FIGURE 7: Signal amplitudes measured at the receivers with the clinical system in Figure 2 for a single transmitter over a range of antenna heights above the tank base (3, 5, 7, 9, 11, and 13 cm) for (a) 900, (b) 1300, and (c) 1700 MHz, respectively.

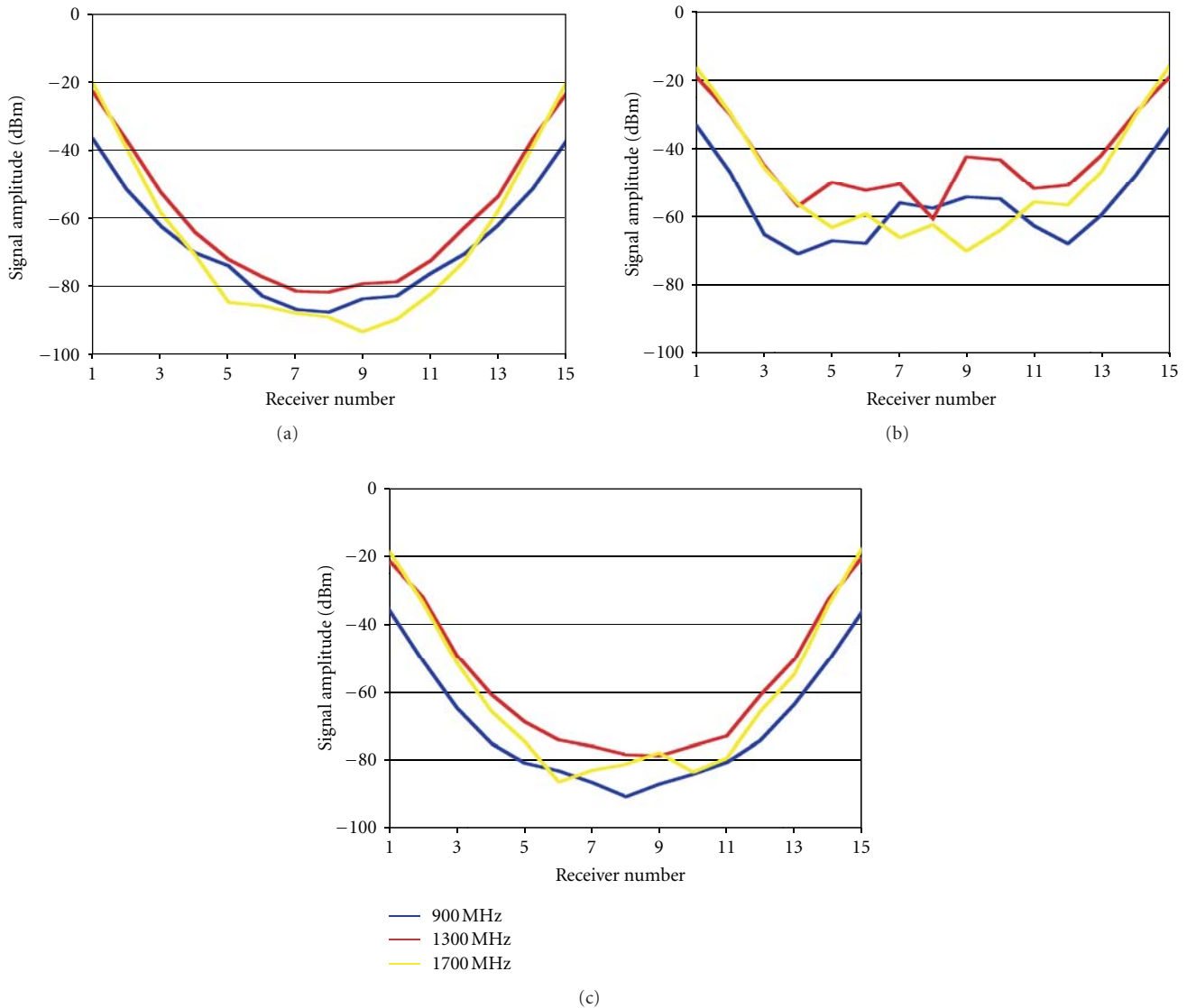


FIGURE 8: Signal amplitudes measured at the receivers for a single transmitter in the experimental imaging tanks in Figure 5 at 900, 1300, and 1700 MHz with the (a) 10 cm straight, (b) 5 cm straight, and (c) 10 cm curved coaxial feedlines, respectively.

(Burlington, MA, USA) HFSS version 13.0. For all cases, there is a reasonably broad antenna pattern emanating outwards from the active part of the antennas, and this feature is reasonably similar for all feed line types. For the straight feeds—especially the longer one, it is clear that there are considerable surface currents generated along the coaxial lines. For the shorter straight one, there is a high degree of field strength along the coaxial line within the Plexiglas volume below the horizontal interface. The fields along the interface generally agree with our previous notion that the surface waves preferentially propagate within the lower-loss medium (in this case the Plexiglas) as can be seen by the substantially greater amplitudes directly under the line.

The results for the serpentine feedlines are consistent with previous results in that the field strength in the Plexiglas is lower than that for the short, straight line case. Figure 11

shows a plot of the field strength just below the liquid interface from a point directly underneath the antenna extending 140 cm to the right for all three corresponding plots. The field values are considerably less for the longer straight line but are also less for the serpentine cases compared to the short, straight cases. For the serpentine case, there seems to be some signal coupling between the lower feedline bend and the Plexiglas. As discussed in Section 1, surface waves do decay exponentially from the surfaces, and given the proximity of the feedlines and the liquid/Plexiglas interface, some coupling is expected.

4. Conclusion

The potentially debilitating effects of unwanted multipath signals is a critical consideration in translating near-field

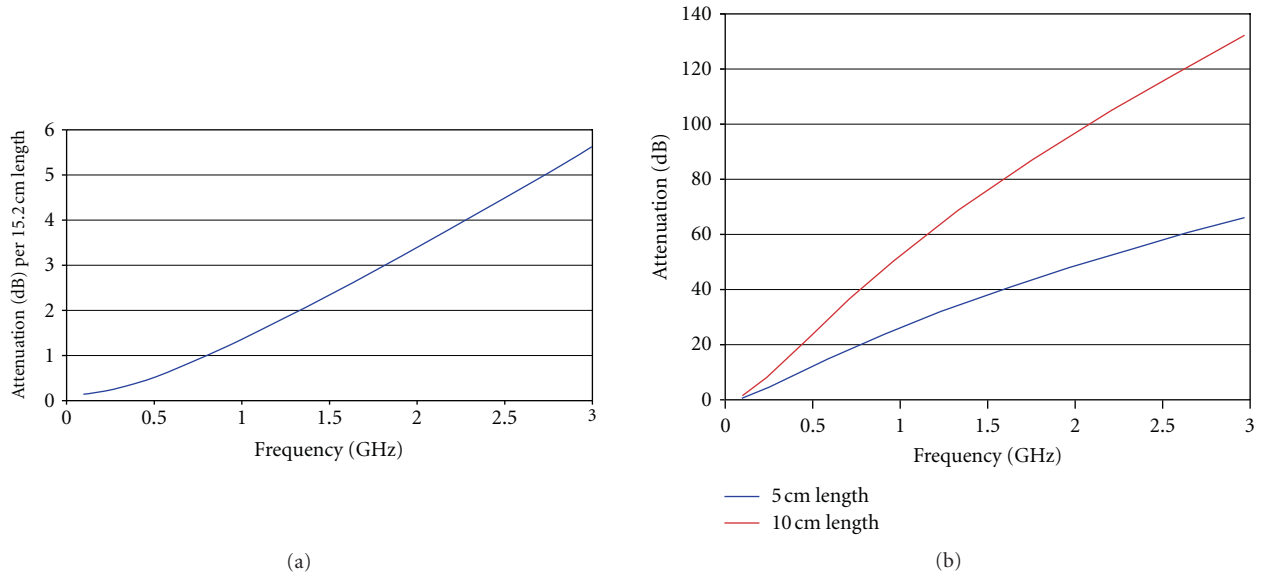


FIGURE 9: Surface wave attenuation as a function of frequency for (a) the planar mode at the interface between Plexiglas and the bath for a 15.2 cm length and (b) the coaxial mode with a lossy dielectric (80 : 20 glycerin : water bath) surrounding a metal conductor for 5 and 10 cm lengths.

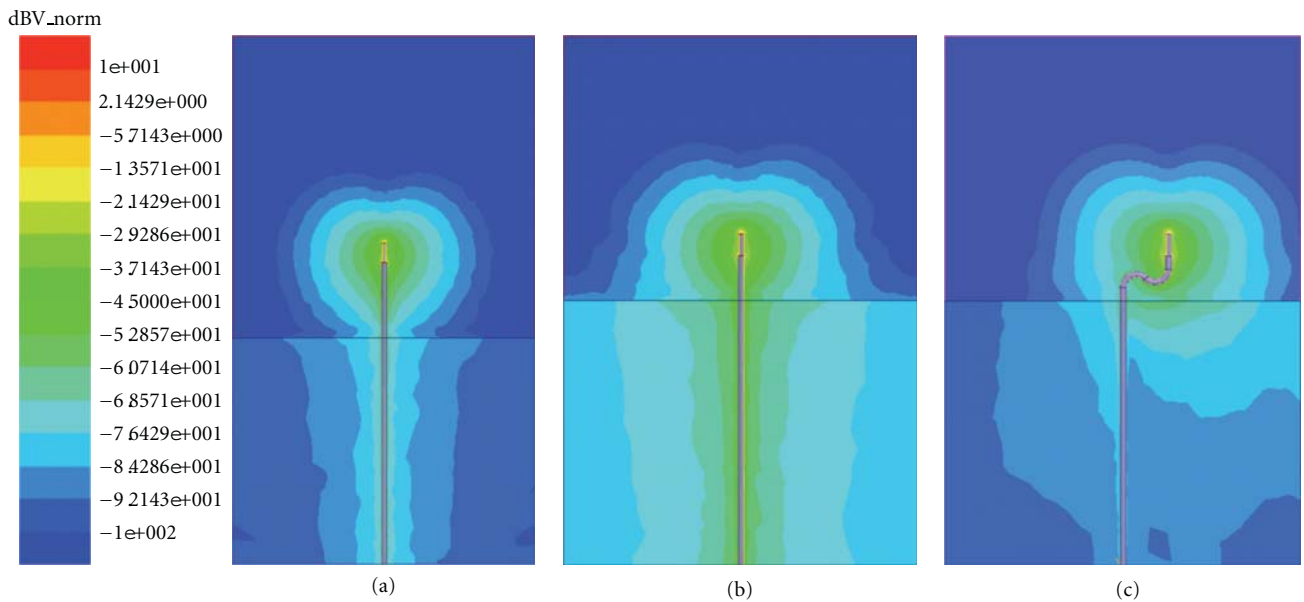


FIGURE 10: Simulated 900 MHz electric field magnitude distributions (in dB and normalized with respect to the field at the antenna tip) for the (a) long, straight coaxial feed, (b) short, straight coaxial feed, and (c) the longer, serpentine structure.

microwave imaging approaches into clinical and commercial systems. For our noncontacting antenna approach, surface waves (relative to signal reflections from the imaging tank walls) appear to cause the biggest effects as they propagate along the outside of the transmitting coaxial line across the illumination tank floor and back up the coaxial feed lines of the receivers. When the imaging tank is deep and the transmitting/receiving antenna tips are sufficiently far above the

tank base, the surface wave signals are adequately suppressed relative to the transmissions through tissue. The results presented here indicate that 9-10 cm of distance along the feed line is adequate. However, reducing the tank depth is of interest for practical reasons and is essential in some settings and appears possible because reflections from the floor of the tank are still too small to degrade the measured signals propagating through tissue. Indeed, we found that antenna tip

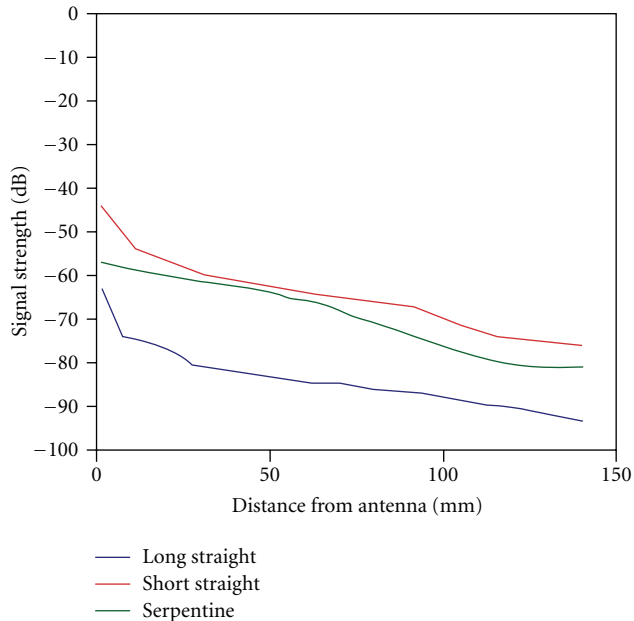


FIGURE 11: Graph of the 900 MHz electric field magnitudes (dB) along the lower side of the Plexiglas: liquid interface from the point directly under the antenna and extending horizontally for all three distributions shown in Figure 10.

distances as little as 5 cm from the tank floor maintain receiver signal fidelity across the array provided the surface wave contributions are attenuated through an equivalent feedline length approaching 10 cm. These findings are significant because they indicate that the antenna array and imaging tank geometry can be altered substantially by manipulating the shape of the antenna feed line, which can be exploited to ensure sufficient surface wave attenuation. There are certainly other mechanisms for multipath propagation including coupling of fields from the feedlines directly to portions of the breast tissue outside the immediate plane of propagation and are certainly good topics for further investigation.

Acknowledgment

This paper was supported in part by NIH Grant UC no. R33-CA102938.

References

- [1] J. Gao, F. Su, and G. Xu, "Multipath effects cancellation in ISAR image reconstruction," in *Proceedings of the International Conference on Microwave and Millimeter Wave Technology (ICMMT '07)*, pp. 1–4, April 2007.
- [2] V. F. Mecca, D. Ramakrishnan, and J. L. Krolik, "MIMO radar space-time adaptive processing for multipath clutter mitigation," in *Proceedings of the 4th IEEE Sensor Array and Multichannel Signal Processing Workshop Proceedings (SAM '06)*, pp. 249–253, July 2006.
- [3] D. B. Trizna, "Model for Brewster angle damping and multipath effects on the microwave radar sea echo at low grazing angles," *IEEE Transactions on Geoscience and Remote Sensing*, vol. 35, no. 5, pp. 1232–1244, 1997.
- [4] T. A. Seliga and F. J. Coyne, "Potential enhancements to the performance of ASDE radars derived from multistatic radar principles," in *Proceedings of the 20th Conference on Digital Avionics Systems*, pp. 7C4/1–7C4/16, October 2001.
- [5] H. R. Anderson, *Fixed Broadband Wireless System Design*, John Wiley & Sons, Chichester, UK, 2003.
- [6] R. C. Qiu, "A study of the ultra-wideband wireless propagation channel and optimum UWB receiver design," *IEEE Journal on Selected Areas in Communications*, vol. 20, no. 9, pp. 1628–1637, 2002.
- [7] G. R. Lennen, "Signal timing synchronizer," U.S. Patent no 5 402 450, 1995.
- [8] D. Li, p. M. Meaney, T. Raynolds, S. A. Pendergrass, M. W. Fanning, and K. D. Paulsen, "Parallel-detection microwave spectroscopy system for breast imaging," *Review of Scientific Instruments*, vol. 75, no. 7, pp. 2305–2313, 2004.
- [9] p. M. Meaney, M. W. Fanning, T. Raynolds et al., "Initial Clinical Experience with Microwave Breast Imaging in Women with Normal Mammography," *Academic Radiology*, vol. 14, no. 2, pp. 207–218, 2007.
- [10] H. Jiang, C. Li, D. Pearlstone, and L. L. Fajardo, "Ultrasound-guided microwave imaging of breast cancer: tissue phantom and pilot clinical experiments," *Medical Physics*, vol. 32, no. 8, pp. 2528–2535, 2005.
- [11] M. Klemm, I. J. Craddock, J. A. Leendertz, A. Preece, and R. Benjamin, "Radar-based breast cancer detection using a hemispherical antenna array—experimental results," *IEEE Transactions on Antennas and Propagation*, vol. 57, no. 6, pp. 1692–1704, 2009.
- [12] C. Yu, M. Yuan, J. Stang et al., "Active microwave imaging II: 3-D system prototype and image reconstruction from experimental data," *IEEE Transactions on Microwave Theory and Techniques*, vol. 56, no. 4, Article ID 4472845, pp. 991–1000, 2008.
- [13] p. M. Meaney, K. D. Paulsen, A. Hartov, and R. K. Crane, "An active microwave imaging system for reconstruction of 2-D electrical property distributions," *IEEE Transactions on Biomedical Engineering*, vol. 42, no. 10, pp. 1017–1026, 1995.
- [14] C. J. Fox, p. M. Meaney, F. Shubitidze, L. Potwin, and K. D. Paulsen, "Characterization of an implicitly resistively-loaded monopole antenna in lossy liquid media," *International Journal of Antennas and Propagation*, vol. 2008, Article ID 580782, 9 pages, 2008.
- [15] J. S. Stratton, *Electromagnetic Theory*, John Wiley & Sons, Hoboken, NJ, USA, 2007.
- [16] G. Goubau, "Single conductor surface-wave transmission lines," in *Proceedings of the Institute of Radio Engineers (IRE '51)*, vol. 39, pp. 619–624, 1951.
- [17] G. Kreifeldt, "An analysis of surface-detected EMG as an amplitude-modulated noise," in *Proceedings of the International Conference of Medicine and Biological Engineering*, Chicago, Ill, USA, 1989.
- [18] S. S. Attwood, "Surface-wave propagation over a coated plane conductor," *Journal of Applied Physics*, vol. 22, no. 4, pp. 504–509, 1951.
- [19] J. R. Wait, "A Note on surface waves and ground waves," *IEEE Transactions on Antennas and Propagation*, vol. 13, no. 6, pp. 996–997, 1965.
- [20] J. R. Wait, "The Ancient and Modern History of EM Ground-Wave Propagation," *IEEE Antennas and Propagation Magazine*, vol. 40, no. 5, pp. 7–24, 1998.

- [21] C. W. Harrison and D. C. Chang, "Theory of the annular slot antenna based on duality," *IEEE Transactions on Electromagnetic Compatibility*, vol. 13, no. 1, pp. 8–14, 1971.
- [22] D. V. Blackham and R. D. Pollard, "An improved technique for permittivity measurements using a coaxial probe," *IEEE Transactions on Instrumentation and Measurement*, vol. 46, no. 5, pp. 1093–1099, 1997.
- [23] R. L. Cravey, R. I. Tiemsin, K. Bussell, and K. L. Dudley, "Dielectric property measurements in the electromagnetic properties measurement laboratory," NASA TM-110147, 1995 and TM-110321, 1997.

Research Article

Three-Dimensional Near-Field Microwave Holography for Tissue Imaging

Reza K. Amineh, Ali Khalatpour, Haohan Xu, Yona Baskharoun, and Natalia K. Nikolova

Department of Electrical and Computer Engineering, McMaster University, Hamilton, ON, Canada L8S4K1

Correspondence should be addressed to Reza K. Amineh, khalajr@mcmaster.ca and Natalia K. Nikolova, talia@mail.ece.mcmaster.ca

Received 1 October 2011; Accepted 21 December 2011

Academic Editor: Elise Fear

Copyright © 2012 Reza K. Amineh et al. This is an open access article distributed under the Creative Commons Attribution License, which permits unrestricted use, distribution, and reproduction in any medium, provided the original work is properly cited.

This paper reports the progress toward a fast and reliable microwave imaging setup for tissue imaging exploiting near-field holographic reconstruction. The setup consists of two wideband TEM horn antennas aligned along each other's boresight and performing a rectangular aperture raster scan. The tissue sensing is performed without coupling liquids. At each scanning position, wideband data is acquired. Then, novel holographic imaging algorithms are implemented to provide three-dimensional images of the inspected domain. In these new algorithms, the required incident field and Green's function are obtained from numerical simulations. They replace the plane (or spherical) wave assumption in the previous holographic methods and enable accurate near-field imaging results. Here, we prove that both the incident field and Green's function can be obtained from a single numerical simulation. This eliminates the need for optimization-based deblurring which was previously employed to remove the effect of realistic non-point-wise antennas.

1. Introduction

Microwaves have been used for imaging and detection ever since the technology to generate and receive them became available. Microwaves penetrate many objects and materials which are optically opaque such as living tissues, wood, ceramics, plastics, clothing, concrete, and soil. Various imaging methods have been developed in applications such as remote sensing, underground surveillance, concealed weapon detection, through-the-wall imaging, and nondestructive testing and evaluation. For a more complete coverage, the reader is referred to [1]. Many of the data-processing algorithms currently developed for near-field tissue sensing are rooted in these prior methods.

Microwave imaging of tissues dates back to the 1970s, when Larsen and Jacobi carried out extensive experiments with imaging canine kidneys [2]. They were successful in producing two-dimensional (2D) images where various tissues were clearly discernible. They measured the transmitted signal between two antennas facing each other along boresight (similar to the illustration in Figure 1). The imaged

organ was scanned in a plane perpendicular to the line connecting the two antennas. Thus, the recorded signal was obtained as a function of two position coordinates, x and y , relative to a reference point on the imaged organ. Such data acquisition approach is often referred to as raster scanning. Raster scanning is also suitable for holographic reconstruction and is adopted in our work.

The major challenges in microwave tissue imaging include difficulties in coupling the microwave power into the tissue, significant tissue loss, relatively coarse resolution, significant tissue heterogeneity, and relatively low contrast between malignant and healthy tissues.

The active microwave systems currently considered for tissue imaging can be classified in four large groups [5]: optimization-based microwave imaging, confocal radar-based imaging, microwave tomography, and microwave holography.

The work here employs the latter approach. In modern microwave holography (e.g., see [6–9]), coherent (magnitude and phase) back-scattered signals are acquired on a surface, similarly to the conventional optical holography.

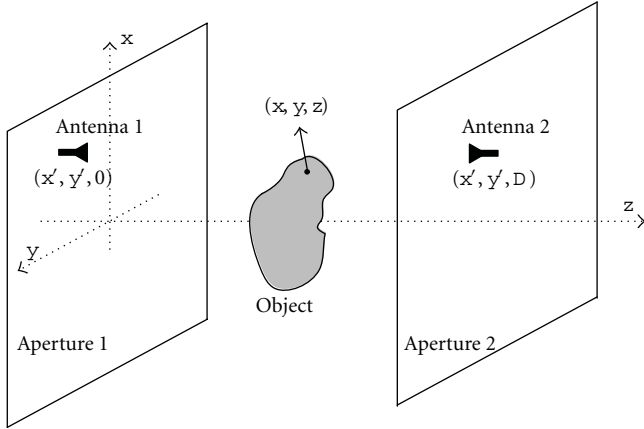


FIGURE 1: Microwave holography setup.

However, the reconstruction of the object is based on a sequence of direct and inverse Fourier transforms (FTs). The data acquired on the surface is used simultaneously in a single reconstruction process to obtain the 3D reflectivity distribution of the object. It can be shown [10] that this reconstruction is based on the linear Born approximation. Microwave holography provides a framework where, with wideband frequency information, a 3D image of the object is obtained in quasi-real time. In the case of a single-frequency measurement, it provides a 2D image of the object's cross-section in a plane parallel to the acquisition plane (e.g., see [7]). Microwave holographic imaging based on rectangular and cylindrical aperture scanning has proven reliable and is employed in concealed weapon detection, for example, [6–9].

In [11], we extended the single-frequency 2D holographic image reconstruction to near-field microwave imaging. This method employs not only the back-scattered (as in [7]) but also the forward-scattered signals. The additional information from the forward-scattered signals improves the image quality and enables localization of the object in the range direction. In contrast to previous work, this method does not make any assumptions about the incident field such as plane, spherical, or cylindrical wave representations. The incident field is derived in a numeric form either through simulation or measurement. This is important in near-field imaging where the object is close to the antenna and the planar or spherical approximations of the illuminating wave are not valid. Green's function was still assumed to be a spherical wave.

In [10], we extend the 2D near-field holographic imaging technique in [11] to 3D imaging when wideband information is available. The proposed method has a number of distinct features and advantages compared to the previously proposed 3D holographic techniques. First, the method allows for incorporating forward-scattered signals in addition to the back-scattered signals. This additional information leads to more accurate reconstruction results and also allows for the significant suppression of image artifacts in the range direction. Second, the method allows for an incident-field distribution represented in numeric form. This distribution

can be obtained either through simulation or through measurement with the particular antenna setup and medium. Third, it also allows for numeric input of Green's function, that is, the set of signals due to point scatterers in the given medium and received by the given antennas. These can be efficiently obtained through simulation as proposed here. The accurate representations of the incident field and Green's function for the particular problem are crucial in near-field imaging where analytical approximations such as plane or spherical waves are not adequate. Fourth, the numerical form of the incident field and Green's function necessitates a new inversion procedure. Previous 3D holography methods [7] relied on the analytical (exponential) form of the incident field and Green's function in order to cast the inversion expression in the form of a 3D inverse FT. This limits the technique to homogeneous background problems with far-zone measurements. Re-sampling of the data in k_z space is also necessary, which may lead to errors. This procedure is inapplicable with numeric representations of the incident field and Green's function. Instead, in [10] we solve a system of equations in each spatial frequency pair (k_x, k_y) and apply 2D inverse FT to the least-square solution at planes (slices) at all desired range locations. Note that the systems of equations have much smaller dimensions compared to the systems of equations in regular optimization-based microwave imaging techniques. This reduces the ill-posedness of the problem significantly. Thus, the 3D object is reconstructed as a set of 2D slice images in parallel planes along the range. The algorithm proves to be robust to high levels of noise.

In [10, 11], we employed copolarized dipole antennas to acquire the data. These antennas are small. Thus, the acquired data was assumed to be obtained from point sources/receivers. This allowed us to apply the holographic algorithms without any additional processing. However, this is not the case when in real practice we deal with non-point-wise antennas. In [12], we discussed that when we employ a real antenna structure to collect the data, additional processing is required prior to applying holographic image reconstruction. We employed blind de-convolution (deblurring) to eliminate the integration (blurring) effect of the non-point-wise antenna aperture. The major drawback of the deblurring processing is that it is based on nonlinear optimization procedures, which may fail to converge to the true solution.

Here, first we present a general vectorial formulation of 3D near-field microwave holography. Then, we show how the previously proposed scalar holographic algorithms can be derived from this more general formulation. Further, by using the reciprocity principle, we show that both the incident field and Green's function can be obtained in a single numerical simulation. This relatively simple theoretical development results in major progress in microwave near-field holography since not only we eliminate the required simulations to obtain Green's function, but also we do not need to apply "deblurring" signal processing. This is due to the fact that in this approach of obtaining Green's function, the antenna structure is part of the medium.

We examine the performance of the 2D and 3D image reconstruction techniques when employing TEM horn

antennas [13] by a number of simulation and experimental examples.

2. Vectorial Holographic Microwave Imaging

The microwave holography setup considered here employs planar raster scanning. It consists of two antennas and an object in between as shown in Figure 1. When using the linear Born approximation [14], the scattered field is given by

$$\mathbf{E}^{\text{sc}}(\mathbf{r}_P) \approx \iiint_{V_Q} \underline{\underline{\mathbf{G}}}(\mathbf{r}_P, \mathbf{r}_Q) \cdot \mathbf{E}^{\text{inc}}(\mathbf{r}_Q) [k_s^2(\mathbf{r}_Q) - k_b^2] d\mathbf{r}_Q, \quad (1)$$

where \mathbf{E}^{sc} is the scattered field, $\underline{\underline{\mathbf{G}}}(\mathbf{r}_P, \mathbf{r}_Q)$ is Green's dyadic function, \mathbf{E}^{inc} is the incident field, k_s and k_b are the wavenumbers of the scatterer and the background media, respectively, and V_Q is the inspected volume. We assume that k_b is constant in V_Q . The position vectors \mathbf{r}_P and \mathbf{r}_Q give the locations of the observation and scattering points, respectively.

2.1. The Forward Model. As shown in Figure 1, the antennas perform a 2D scan while moving together on two separate parallel planes positioned at $z = 0$ and $z = D$. Assume that at any measurement frequency f_l ($l = 1, 2, \dots, N_f$) we know the incident field $\mathbf{E}^{\text{inc}}(0, 0, 0; x, y, z; f_l)$ at any point $\mathbf{r}_P = (x, y, z)$ in the inspected volume when the transmitting antenna is at $(0, 0, 0)$. In addition, assume that all components of Green's tensor $G_i^j(x, y, z; 0, 0, D; f_l)$, $i, j = x, y, z$, are known for an i -polarized point source, at (x, y, z) and the j -polarized response at $(0, 0, D)$. For brevity, we introduce the notations:

$$\begin{aligned} \mathbf{E}^{\text{inc}}(x, y, z, f_l) &\equiv \mathbf{E}^{\text{inc}}(0, 0, 0; x, y, z; f_l), \\ \underline{\underline{\mathbf{G}}}(x, y, z, f_l) &\equiv \underline{\underline{\mathbf{G}}}(x, y, z; 0, 0, D; f_l). \end{aligned} \quad (2)$$

Let $E_j^{\text{sc}}(x', y', D, f_l)$, $j = x, y, z$, be the j th component of the forward scattered E -field received at $\mathbf{r}_Q = (x', y', D)$. This implies that the transmitting antenna is at $(x', y', 0)$ since it moves together with the receiving antenna. The back-scattered field is analyzed similarly with $\mathbf{r}_Q = (x', y', D = 0)$.

In a homogeneous or layered medium (where the layers are in x - y planes), the incident field and Green's tensor for the case where the antenna pair is at (x', y') can be obtained from those in (2) by a simple translation:

$$\begin{aligned} \mathbf{E}^{\text{inc}}(x', y', 0; x, y, z; f_l) &= \mathbf{E}^{\text{inc}}(x - x', y - y', z, f_l), \\ \underline{\underline{\mathbf{G}}}(x', y', 0; x, y, z; f_l) &= \underline{\underline{\mathbf{G}}}(x - x', y - y', z, f_l). \end{aligned} \quad (3)$$

Then, as per (1), each j -component ($j = x, y, z$) of the scattered field is written as

$$\begin{aligned} E_j^{\text{sc}}(x', y', D, f_l) &\approx \\ \int_z \int_y \int_x f(x, y, z, f_l) \cdot \sum_{m=x,y,z} g_m^j(x' - x, y' - y, z, f_l) dx dy dz, \end{aligned} \quad (4)$$

where

$$\begin{aligned} f(x, y, z, f_l) &= k_s^2(x, y, z, f_l) - k_b^2(f_l), \\ g_m^j(x, y, z, f_l) &= E_m^{\text{inc}}(-x, -y, z, f_l) \\ &\times G_m^j(-x, -y, z, f_l) \quad m = x, y, z. \end{aligned} \quad (5)$$

We refer to $f(x, y, z, f_l)$ as the contrast function. For simplicity, we assume that the contrast function is frequency-independent, that is, $f(x, y, z) \equiv f(x, y, z, f_l)$. The modification of the algorithm when dealing with dispersive media has been presented in [10]. Notice that (4) also implies that the scatterer is isotropic, that is, contrast function is independent of the polarization of the incident field.

In (4), the integral over x and y can be interpreted as a 2D convolution integral. Thus, the 2D FT of $E_j^{\text{sc}}(x', y', D, f_l)$ ($j = x, y, z$) is written as

$$E_j^{\text{sc}}(k_x, k_y, D, f_l) \approx \int_z F(k_x, k_y, z) \cdot \sum_{m=x,y,z} G_m^j(k_x, k_y, z, f_l) dz, \quad (6)$$

where $F(k_x, k_y, z)$ and $G_m^j(k_x, k_y, z, f_l)$ are the 2D FTs of $f(x, y, z)$ and $g_m^j(x, y, z, f_l)$, $m = x, y, z$, respectively; k_x and k_y are the Fourier variables with respect to x and y , respectively.

To reconstruct the contrast function, we first approximate the integral in (6) by a discrete sum in z for the N_z reconstruction planes:

$$\begin{aligned} E_j^{\text{sc}}(k_x, k_y, D, f_l) &\approx \sum_{n=1}^{N_z} F(k_x, k_y, z_n) \\ &\cdot \sum_{m=x,y,z} G_m^j(k_x, k_y, z_n, f_l) \Delta z \quad j = x, y, z, \end{aligned} \quad (7)$$

where Δz is the distance between two neighboring reconstruction planes.

2.2. Inversion Procedure. For the setup shown in Figure 1, there could be four antenna configurations when performing the raster scan: (1) antenna 1 and antenna 2 are both x -polarized (X-X case); (2) antenna 1 is x -polarized while antenna 2 is y -polarized (X-Y case); (3) antenna 1 is y -polarized while antenna 2 is x -polarized (Y-X case); (4) antenna 1 and antenna 2 are both y -polarized (Y-Y case).

Four complex S-parameters are acquired at the two antenna terminals at each frequency for each of the four polarization cases listed above. These four S-parameters constitute four separate scattered signals expressed in (1) (two reflection and two transmission coefficients). Thus, by performing wide-band measurements at N_f frequencies,

from (7) N_f equations at each spatial-frequency pair (k_x, k_y) is obtained as

$$\begin{aligned}
 E_j^{\text{sc}}(k_x, k_y, D, f_1) \\
 &\approx \sum_{m=x,y,z} G_m^j(k_x, k_y, z_1, f_1) F(k_x, k_y, z_1) \Delta z + \dots \\
 &+ \sum_{m=x,y,z} G_m^j(k_x, k_y, z_{N_z}, f_1) F(k_x, k_y, z_{N_z}) \Delta z \\
 &\vdots
 \end{aligned} \tag{8}$$

$$\begin{aligned}
 E_j^{\text{sc}}(k_x, k_y, D, f_{N_f}) \\
 &\approx \sum_{m=x,y,z} G_m^j(k_x, k_y, z_1, f_{N_f}) F(k_x, k_y, z_1) \Delta z + \dots \\
 &+ \sum_{m=x,y,z} G_m^j(k_x, k_y, z_{N_z}, f_{N_f}) F(k_x, k_y, z_{N_z}) \Delta z.
 \end{aligned}$$

Note that in (8), the subscript j denotes the polarization of the receiving antenna. For each configuration mentioned above, $4 \times N_f$ equations are obtained. Then, the systems of equations for all four antenna configurations are combined to form a larger system of equations. In general, this results in a system of $12 \times N_f$ decoupled equations, which must be solved for $F(k_x, k_y, z_n)$, $n = 1, 2, \dots, N_z$. Note that typically $N_z < N_f$.

At each spatial frequency pair (k_x, k_y) , a system of equations as in (8) is solved in least-square sense to find $F(k_x, k_y, z_n)$, $n = 1, 2, \dots, N_z$. We emphasize that the system of equations obtained at each (k_x, k_y) is much smaller than the system of equations normally produced in optimization-based microwave imaging techniques. This significantly reduces the ill-posedness of our approach. Inverse 2D FT is applied to $F(k_x, k_y, z_n)$, to reconstruct a 2D slice of the function $f(x, y, z_n)$ at each $z = z_n$ plane. Then, the normalized modulus of $f(x, y, z_n)$, $|f(x, y, z_n)|/M$, where M is the maximum of $|f(x, y, z_n)|$ for all z_n , is plotted versus x and y to obtain a 2D slice image of the object at each $z = z_n$ plane, $n = 1, 2, \dots, N_z$. By putting together all N_z slice images, a 3D image of the object is obtained.

3. Obtaining Green's Dyadic Function

Here, we assume that the antennas are fed by a coaxial cable. We also assume that the coaxial port is at an x - y plane, as illustrated in Figure 2, and the scattered field due to a point-scatterer at point S is sampled on the x -axis of the coaxial port at point P . Since the coaxial cable only supports TEM wave propagation along the cable (only the radial component of the E -field exists inside the cable), the sampled field at

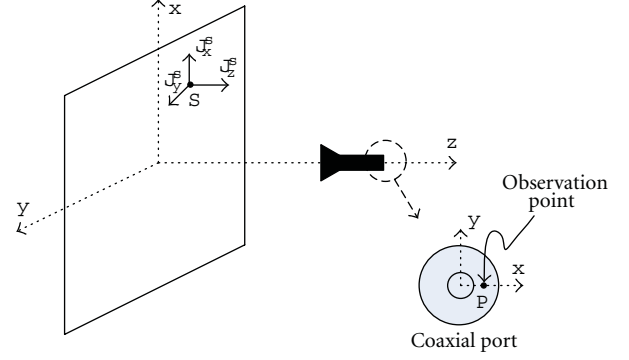


FIGURE 2: Illustration of the coaxial port for the receiving antenna with a point P on the port, on the x -axis and a point-scatterer at S .

point P has an x -component only. Thus, the dyadic Green's function with the general expression of

$$\underline{\underline{\mathbf{G}}}(\mathbf{r}_P, \mathbf{r}_S) = \begin{bmatrix} G_x^x(\mathbf{r}_P, \mathbf{r}_S) & G_y^x(\mathbf{r}_P, \mathbf{r}_S) & G_z^x(\mathbf{r}_P, \mathbf{r}_S) \\ G_x^y(\mathbf{r}_P, \mathbf{r}_S) & G_y^y(\mathbf{r}_P, \mathbf{r}_S) & G_z^y(\mathbf{r}_P, \mathbf{r}_S) \\ G_x^z(\mathbf{r}_P, \mathbf{r}_S) & G_y^z(\mathbf{r}_P, \mathbf{r}_S) & G_z^z(\mathbf{r}_P, \mathbf{r}_S) \end{bmatrix} \tag{9}$$

is simplified as

$$\underline{\underline{\mathbf{G}}}(\mathbf{r}_P, \mathbf{r}_S) = \begin{bmatrix} G_x^x(\mathbf{r}_P, \mathbf{r}_S) & G_y^x(\mathbf{r}_P, \mathbf{r}_S) & G_z^x(\mathbf{r}_P, \mathbf{r}_S) \\ 0 & 0 & 0 \\ 0 & 0 & 0 \end{bmatrix}. \tag{10}$$

By convention, in the paired argument of Green's tensor, the 1st position vector denotes the observation point while the 2nd position vector denotes the excitation point.

To obtain this dyadic Green's function, one approach is to excite sequentially all x -, y -, and z -polarized sources at the positions $S(x, y, z)$ of all the points (pixels) at all reconstruction planes and to obtain the E -field response resulting at point P . This approach is prohibitively inefficient. Instead, we employ the reciprocity principle. If a medium is reciprocal [14], the dyadic Green's function fulfills

$$\underline{\underline{\mathbf{G}}}(\mathbf{r}_P, \mathbf{r}_S) = \underline{\underline{\mathbf{G}}}^T(\mathbf{r}_S, \mathbf{r}_P), \tag{11}$$

where $\underline{\underline{\mathbf{G}}}(\mathbf{r}_S, \mathbf{r}_P)$ implies that the source is at point P while the observation point is at point S . The superscript T in (11) denotes transposition. According to (11), we have

$$\begin{aligned}
 &\begin{bmatrix} G_x^x(\mathbf{r}_P, \mathbf{r}_S) & G_y^x(\mathbf{r}_P, \mathbf{r}_S) & G_z^x(\mathbf{r}_P, \mathbf{r}_S) \\ 0 & 0 & 0 \\ 0 & 0 & 0 \end{bmatrix} \\
 &= \begin{bmatrix} G_x^x(\mathbf{r}_S, \mathbf{r}_P) & G_x^y(\mathbf{r}_S, \mathbf{r}_P) & G_x^z(\mathbf{r}_S, \mathbf{r}_P) \\ G_y^x(\mathbf{r}_S, \mathbf{r}_P) & G_y^y(\mathbf{r}_S, \mathbf{r}_P) & G_y^z(\mathbf{r}_S, \mathbf{r}_P) \\ G_z^x(\mathbf{r}_S, \mathbf{r}_P) & G_z^y(\mathbf{r}_S, \mathbf{r}_P) & G_z^z(\mathbf{r}_S, \mathbf{r}_P) \end{bmatrix}.
 \end{aligned} \tag{12}$$

From (12), it follows that

$$\begin{aligned}
G_x^x(\mathbf{r}_P, \mathbf{r}_S) &= G_x^x(\mathbf{r}_S, \mathbf{r}_P), \\
G_y^x(\mathbf{r}_P, \mathbf{r}_S) &= G_x^y(\mathbf{r}_S, \mathbf{r}_P), \\
G_z^x(\mathbf{r}_P, \mathbf{r}_S) &= G_x^z(\mathbf{r}_S, \mathbf{r}_P), \\
G_y^y(\mathbf{r}_S, \mathbf{r}_P) &= G_y^y(\mathbf{r}_S, \mathbf{r}_P) = G_y^z(\mathbf{r}_S, \mathbf{r}_P) = 0, \\
G_z^z(\mathbf{r}_S, \mathbf{r}_P) &= G_z^z(\mathbf{r}_S, \mathbf{r}_P) = G_z^x(\mathbf{r}_S, \mathbf{r}_P) = 0.
\end{aligned} \tag{13}$$

This indicates that we can excite the x -component at point P (coaxial port excitation) and observe the x -, y -, and z -components of the field at each point (pixel) at each reconstruction plane.

Notice that the incident field $\mathbf{E}^{\text{inc}}(x, y, z)$ is obtained in exactly the same way. Thus, only one simulation per polarization configuration is required to obtain both the incident field and the elements of Green's dyadic function. The final expression for the scattered field in terms of \mathbf{E}^{inc} only is

$$\begin{aligned}
\mathbf{E}^{\text{sc}}(x', y', D, f_i) \\
\approx \int_z \int_y \int_x f(x, y, z, f_i) \mathbf{E}^{\text{inc}}(x' - x, y' - y, z, f_i) \\
\cdot \mathbf{E}^{\text{inc}}(x' - x, y' - y, D - z, f_i) dx dy dz,
\end{aligned} \tag{14}$$

where \mathbf{E}^{sc} is the forward scattered field due to the transmitting antenna at the plane $z = 0$ and captured by the receiving antenna at the plane $z = D$. Since we only consider the TEM mode inside the coaxial feed of the antenna, \mathbf{E}^{sc} is a scalar describing the radial component of that mode. In measurements, \mathbf{E}^{sc} is represented by the transmission scattering parameter of the two-port system formed by the two antennas and the imaged object. Note that (14) applies also to the case of a backscattered field if we set $D = 0$.

We emphasize that, in general, for each of the four possible mutual configurations of the two antennas (X-X, X-Y, Y-X, or Y-Y) described in Section 2.2, (14) provides a set of four equations for the four scattering parameters acquired with this two-port system.

4. Scalar Holographic Imaging [10, 11]

In the scalar holographic imaging, it is assumed that the antennas are linearly polarized, for example, x -polarized [10, 11]. In this case, the radiation field of the x -polarized antennas can be reasonably approximated by TM_x polarization. Thus, we consider the x -components of the incident and scattered E -fields only. This leads to a scalar Green's function which is the G_x^x element of the full dyadic in (9). Thus, the expression in (4) (for nondispersive media as discussed in Section 2) is simplified as

$$\begin{aligned}
E_x^{\text{sc}}(x', y', f_i) \\
\approx \int_z \int_y \int_x f(x, y, z) \cdot g_0(x' - x, y' - y, z, f_i) dx dy dz,
\end{aligned} \tag{15}$$

where

$$g_0(x, y, z, f_i) = E_x^{\text{inc}}(-x, -y, z, f_i) G_x^x(-x, -y, z, f_i). \tag{16}$$

Subsequently, the discretization, the construction of the systems of equations at each (k_x, k_y) pair employing all frequencies, and the reconstruction of the 2D images at all range locations are implemented in the same manner as explained above.

In order to perform 2D holographic imaging, it suffices to collect data at a single frequency [11]. The object is positioned at $z = \bar{z}$ and its thickness along the z -axis is assumed to be negligible. When using data at a single frequency, we can reconstruct a 2D image at the plane of the object. At a single frequency, (16) is simplified as

$$E_x^{\text{sc}}(x', y', D) \approx \int_y \int_x f(x, y, \bar{z}) \cdot g_0(x' - x, y' - y, \bar{z}) dx dy. \tag{17}$$

Next, $E_x^{\text{sc}}(x', y', D)$ is interpreted as a 2D convolution integral. This allows for the expression of the 2D FT $E_x^{\text{sc}}(k_x, k_y, D)$ of $E_x^{\text{sc}}(x', y', D)$ as

$$E_x^{\text{sc}}(k_x, k_y, D) \approx F(k_x, k_y, \bar{z}) G_0(k_x, k_y, \bar{z}), \tag{18}$$

where $F(k_x, k_y, \bar{z})$ and $G_0(k_x, k_y, \bar{z})$ are the 2D FT of $f(x, y, \bar{z})$ and $g_0(x, y, \bar{z})$, respectively. Finally, the reconstructed reflectivity function of the object is obtained as

$$f(x, y, \bar{z}) \approx F_{2D}^{-1} \left\{ \frac{E_x^{\text{sc}}(k_x, k_y, D)}{G_0(k_x, k_y, \bar{z})} \right\}, \tag{19}$$

where F_{2D}^{-1} denotes the inverse 2D FT. The reconstructed image can then be obtained as the magnitude of the reflectivity function $|f(x, y, \bar{z})|$.

Note that (19) is a formal reconstruction formula and it can be seen as the "maximum likelihood solution" if the collected data suffer from incompleteness and/or noise. The latter factors are often the cause for ill-posedness. However, the technique is very robust to noise and is not ill-posed. This is due to two factors. First, we provide sufficient sampling (in the Nyquist sense) in the scanned apertures. Second, we note that the incident field due to our antennas has a sharp peak in the middle of the reconstruction plane $z = \bar{z}$ while it quickly decreases toward the edges of this plane. This is mostly due to the dissipation of the power in the lossy background medium which causes significant attenuation for signals traveling along longer paths. Therefore, $G_0(k_x, k_y, \bar{z})$ varies smoothly as a function of k_x and k_y and the value of G_0 is always significantly greater than zero for the considered wavenumbers. Hence, the division in (19) does not lead to ill-posedness of the inversion problem.

We should note that because of the finite size of the apertures, not all the wavenumbers (k_x, k_y) can be measured. This imposes lower and upper limits on k_x and k_y , which in turn limits the cross-range resolution of the images as discussed in [11].

The collected data from each S-parameter can be processed using (19) to create an image of the object. In this case,

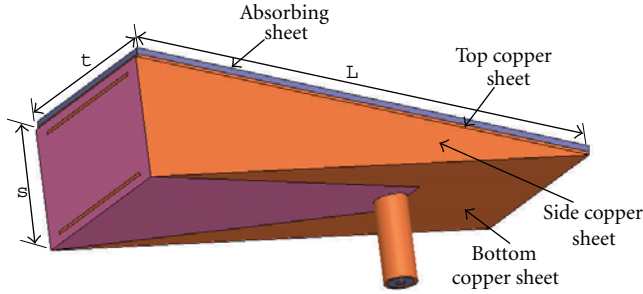


FIGURE 3: The TEM horn placed in a dielectric medium with relative permittivity of 10 with copper sheets on all outer surfaces except the front aperture and a microwave absorbing sheet on the top surface. $L = 74$ mm, $s = 19$ mm, and $t = 30$ mm.

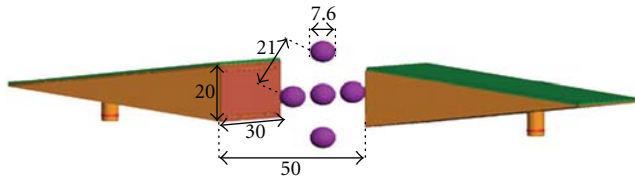


FIGURE 4: The simulation setup in FEKO. The dimensions are in mm.

we obtain four separate images with various resolutions. To reconstruct a single image, the datasets of all S -parameters can be used simultaneously where a least-square solution is sought as discussed in [11] and similarly to the inversion procedure given in Section 2.2.

5. Results

In this section, we present the results of 2D and 3D vector holographic imaging when employing real antennas. We obtain both the incident field and Green's function in a single numerical simulation as discussed in Section 3. Also, both tangential components of the field (x - and y -components) are considered on the reconstruction planes. Obviously, this leads to improved reconstruction results compared to the scalar holography in which only the co-polarized component of the field is considered on the reconstruction planes.

We employ simulation data to validate both 2D and 3D holography algorithms. However, due to the availability of only transmission S -parameters in our current measurement setup, we present experimental results only for 2D holography. We do not incorporate reflection S -parameters in the simulated 2D results for congruence with the measurements. According to our experience, the availability of the reflection S -parameters is crucial for 3D holography reconstruction. We note that the use of a multisensor array on the receiving side would enable 3D holography with transmission signals only; however, this system is currently under development.

5.1. TEM Horn Antenna Tailored for an Aperture Raster Scanning Setup. The design, fabrication, and characterization of an ultra-wideband antenna for near-field microwave imaging of dielectric objects has been presented in [13] together with an imaging setup based on raster scanning. The focus here

is on an application in microwave breast tumor detection. This TEM-horn antenna (shown in Figure 3) operates as a sensor with the following properties: (1) direct contact with the imaged body, (2) more than 90% of the microwave power is coupled directly into the tissue, (3) ultra-wideband impedance match, (4) excellent decoupling from the outside environment, (5) small size, and (6) simple fabrication.

The near-field imaging setup employs planar aperture raster scanning. It consists of two antennas aligned along each other's boresight and moving together to scan two parallel apertures. The imaged object lies between the two apertures.

5.2. 2D Holographic Imaging Results. To verify the proposed processing algorithms, we present simulation and experimental results first employing 2D holographic imaging. The properties of the background medium and the objects are chosen to be close to those of biological healthy and cancerous tissues, respectively.

In the first example, we use FEKO [15] simulation data from the 2D raster scanning of five spheres with $\epsilon_r = 15$ and $\sigma = 2$ S/m embedded inside a medium with $\epsilon_r = 10$ and $\sigma = 1$ S/m as shown in Figure 4. The diameter of the spheres is 7.6 mm and the center-to-center distance between the spheres on the periphery is 21 mm and the center-to-center distance between each sphere on the periphery and the central sphere is 15 mm. The distance between the antenna apertures is 50 mm.

The antennas perform 2D scan on a region of size 90 mm \times 90 mm with spatial sampling rate of 5 mm. At each sampling position, the complex S_{21} is measured at 5 GHz, 7 GHz, and 9 GHz.

Figure 5(a) shows the raw images created from calibrated $|S_{21}|$ obtained with the simulation setup in Figure 4. Calibration scheme has been discussed in [10, 11]. The spheres cannot be distinguished from each other at 5 GHz. At 7 GHz and 9 GHz, the resolution improves but still the image quality is poor. Then, we apply the holographic imaging algorithm to the complex-valued S_{21} . Figure 5(b) shows the reconstructed images. It is observed that the objects are vividly distinguished and the quality of the images is much improved.

We also combined the data obtained from 5 GHz, 7 GHz, and 9 GHz in a single least-square-based image reconstruction algorithm as explained in Section 4. Figure 6 shows the reconstructed image in which the objects are clearly discernible.

In the second example, we use the measured data from the 2D raster scanning setup shown in Figure 7. Two objects are embedded in a brick-shaped phantom. The objects are two spheres with $\epsilon_r \approx 50$ and $\sigma \approx 4$ S/m resembling tumors. They are made of alginate powder and are embedded inside the glycerin-based phantom emulating tissue with $\epsilon_r \approx 7$ and $\sigma \approx 1$ S/m, at 7 GHz. The diameter of the spheres is about 10 mm and the center-to-center distance between the spheres is about 16 mm. The phantom is compressed between two thin plexi-glass sheets. The distance between the antenna apertures after this compression is 50 mm including

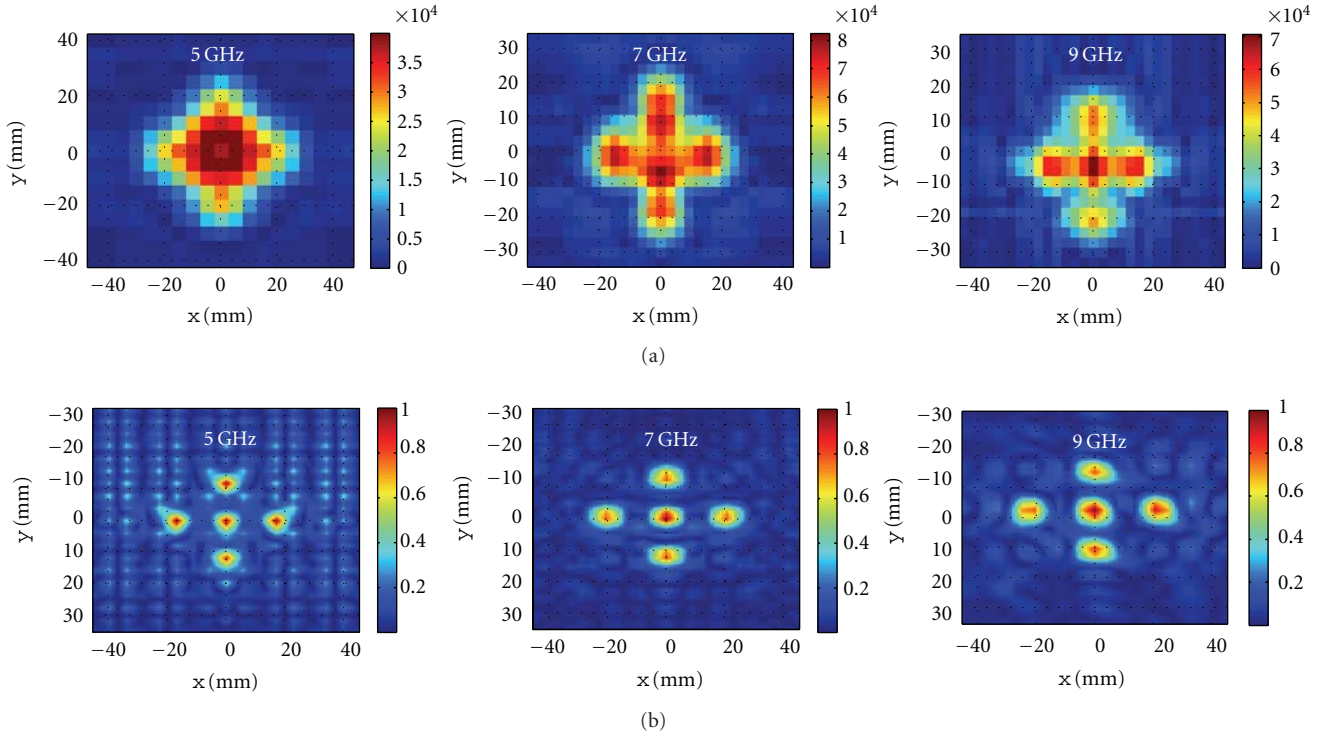


FIGURE 5: (a) Raw images obtained from calibrated $|S_{21}|$ at 5 GHz, 7 GHz, and 9 GHz, (b) normalized images after applying 2D holographic imaging at 5 GHz, 7 GHz, and 9 GHz.

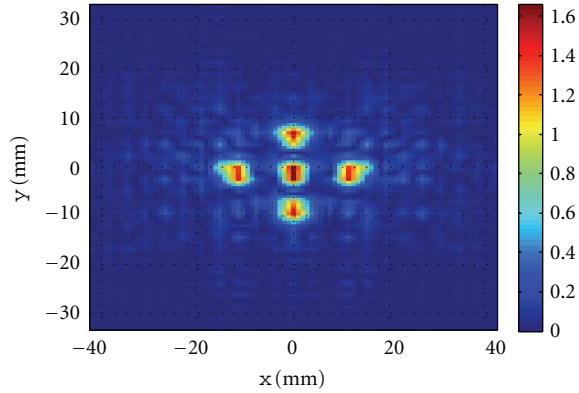


FIGURE 6: Image obtained when combining the data simulated at 5, 7, and 9 GHz in a single reconstruction process based on the least-square solution.

the sheets. The antennas perform 2D scan on a region of size 70 mm \times 70 mm with a spatial sampling rate of 5 mm. This scanning is performed by an automatic positioning system. At each sampling position, the complex transmission S-parameter between the two antennas (S_{21}) is measured at 7 GHz and 9 GHz using a vector network analyzer (VNA). The VNA averaging and resolution bandwidth are set to 16 and 1 KHz, respectively. To improve the accuracy of the measurements (obtain signal well above the noise floor of VNA), an amplifier is employed in the transmitter side and a three-stage low-noise amplifier was employed in the receiver side.

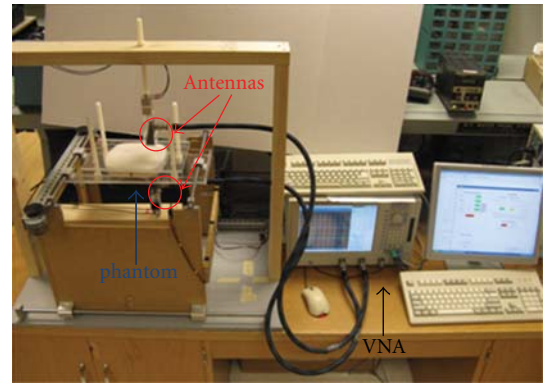


FIGURE 7: Experimental setup for aperture raster scanning.

Figure 8(a) shows the raw images created from the calibrated $|S_{21}|$ obtained from the measurement setup shown in Figure 7. The two tumor stimulants cannot be distinguished clearly. Then, we apply the 2D holographic imaging algorithm to the complex-valued S_{21} . Figure 8(b) shows the reconstructed images. As seen in this figure, the objects are clearly discernible.

Also, similar to the simulation results, we employed the data obtained at 7 and 9 GHz in a single image reconstruction technique based on least-square solution. Figure 9 shows the reconstructed image. The two objects can be distinguished well in this image.

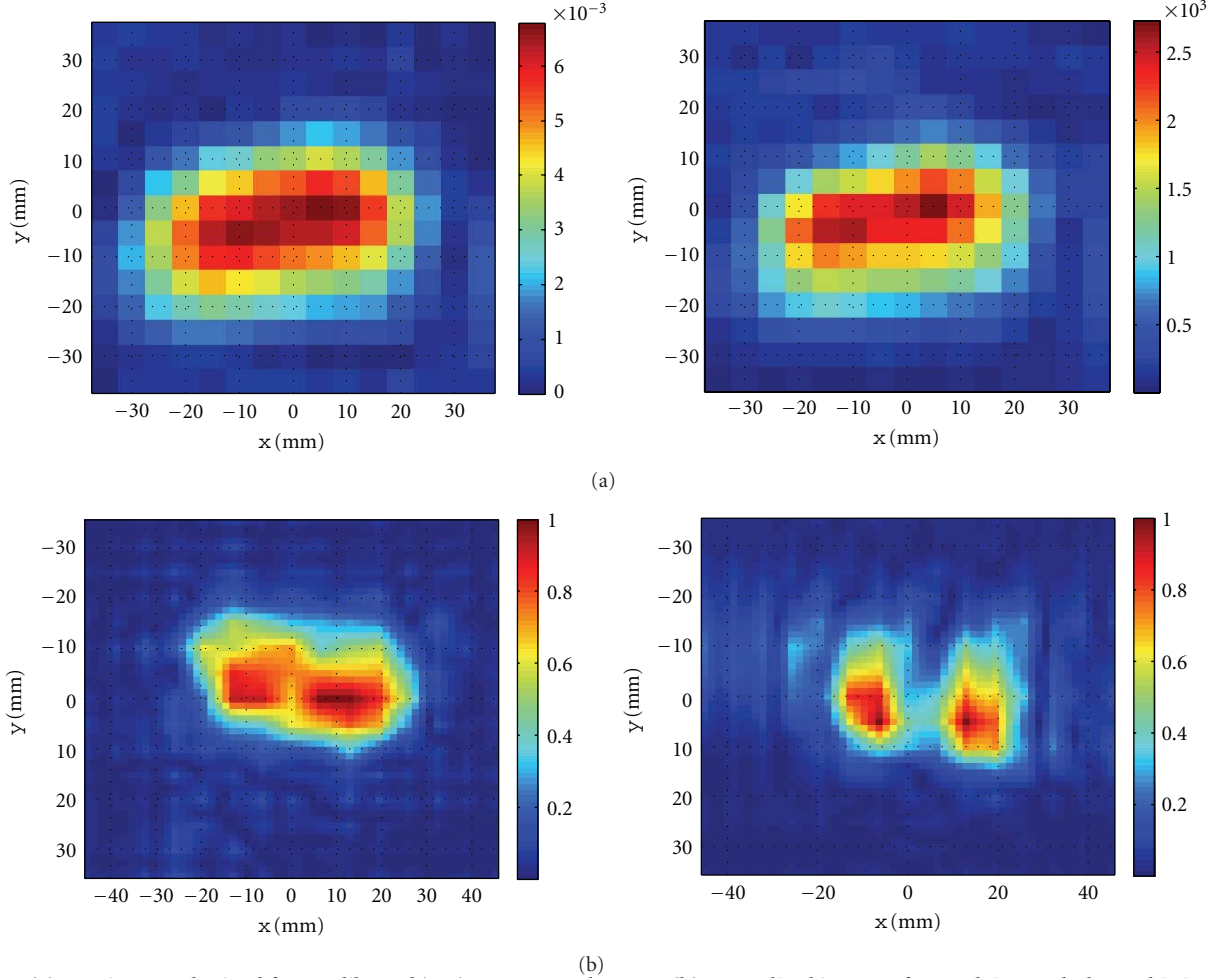


FIGURE 8: (a) Raw images obtained from calibrated $|S_{21}|$ at 7 GHz and 9 GHz, (b) normalized images after applying 2D holographic imaging at 7 GHz and 9 GHz.

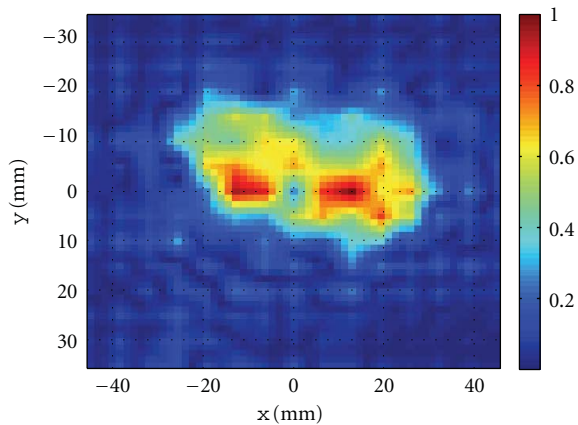


FIGURE 9: Normalized image obtained when combining the measured data obtained at 7 and 9 GHz in a single reconstruction process based on the least-square solution.

5.3. 3D Holographic Imaging Results. In this section, we present the simulation results for implementing 3D holographic image reconstruction for the two examples shown in Figure 10.

In the first example, as illustrated in Figure 10(a), two small objects with properties $\epsilon_r = 15$ and $\sigma = 1$ S/m are placed at a range position of 15 mm inside a homogeneous background medium with $\epsilon_r = 10$ and $\sigma = 0.5$ S/m. The diameter of the spheres is 5.6 mm and the center-to-center distance between them is 16 mm. Two antennas perform 2D raster scan on the rectangular apertures placed at $z = 0$ and $z = 50$ mm with size 72 mm \times 102 mm. The spatial sampling rate in both x and y directions is 3 mm. The simulated reflection and transmission S-parameters are obtained from in the frequency range 3 GHz to 10 GHz with a step of 0.5 GHz. The incident field and Green's function for the antennas are obtained from a single simulation of one antenna in the absence of the objects as described in Section 3.

The 3D holographic image reconstruction algorithm is applied to the collected data. The contrast function is reconstructed on the planes the size of which is 140 mm \times 140 mm. The planes are at $z = 5, 15, 25, 35,$ and 45 mm. The distance between the planes (10 mm) is larger than the minimum range resolution of 7 mm computed here from the 7 GHz bandwidth. As explained in [7, 10], the range resolution is inversely proportional to the bandwidth of the system. Although far-field propagation has been assumed

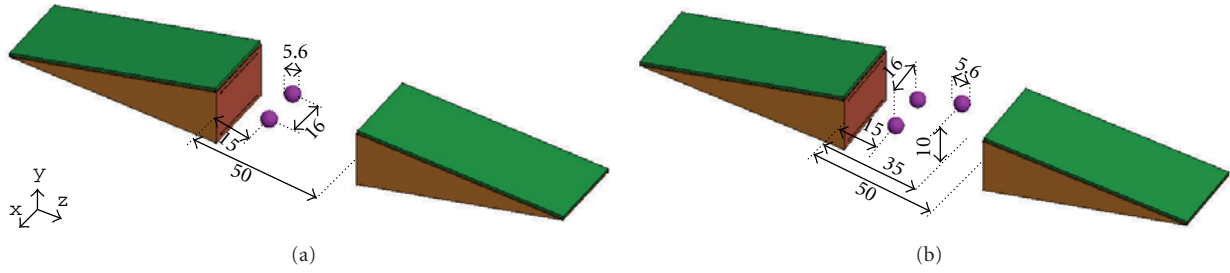


FIGURE 10: Simulation setup for two examples where spherical objects with diameter of 5.6 mm and properties $\epsilon_r = 15$ and $\sigma = 11$ S/m are embedded inside a homogeneous background medium with properties $\epsilon_r = 10$ and $\sigma = 0.5$ S/m; (a) two objects placed at the range position $z = 15$ mm with center-to-center distance of 16 mm and (b) two objects placed at the range position $z = 15$ mm with center-to-center distance of 16 mm and a third object centered at $(0, 10, 35)$. The dimensions are in mm.

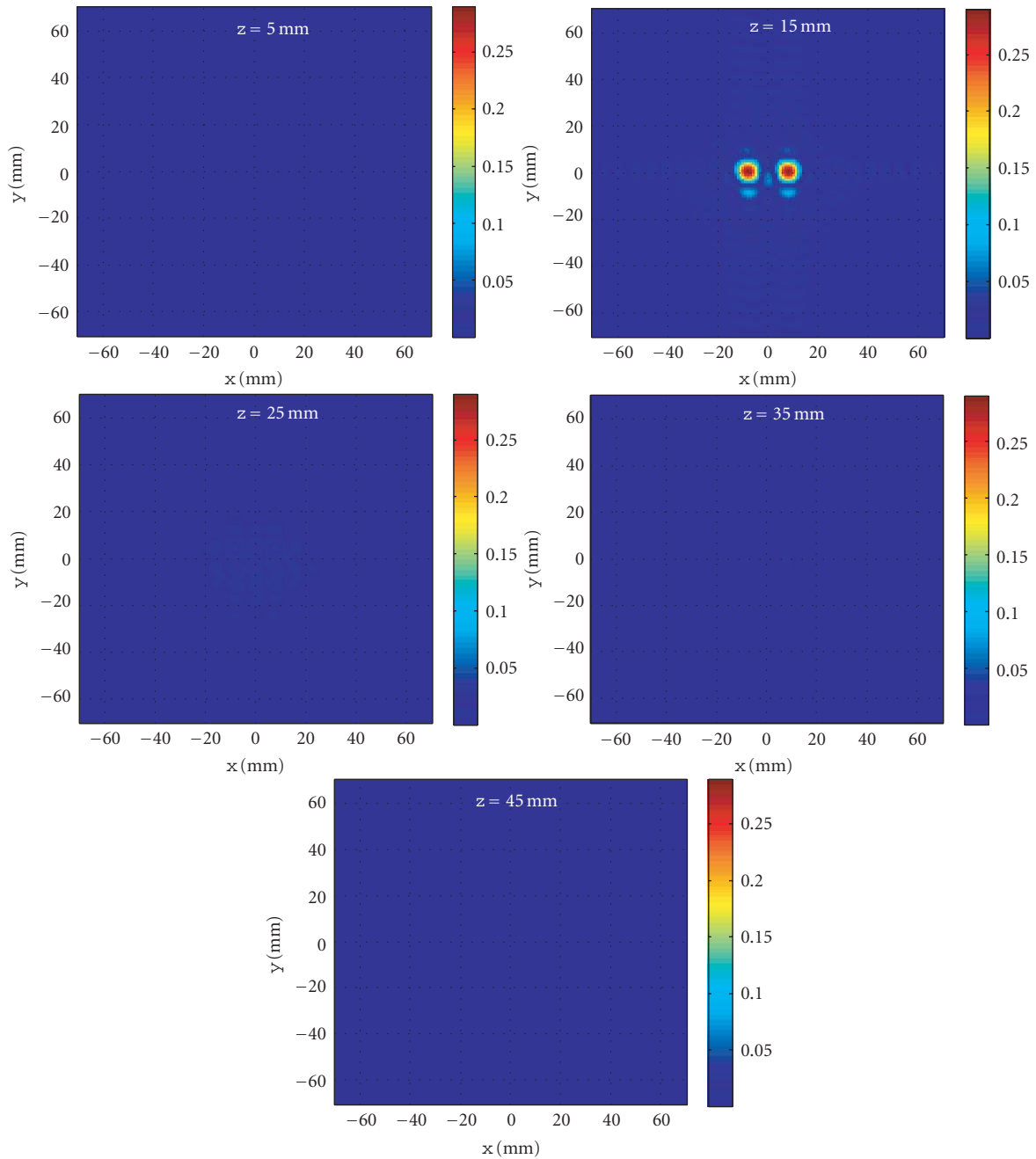


FIGURE 11: Reconstructed images for the example shown in Figure 10(a) after applying 3D holographic image reconstruction algorithm.

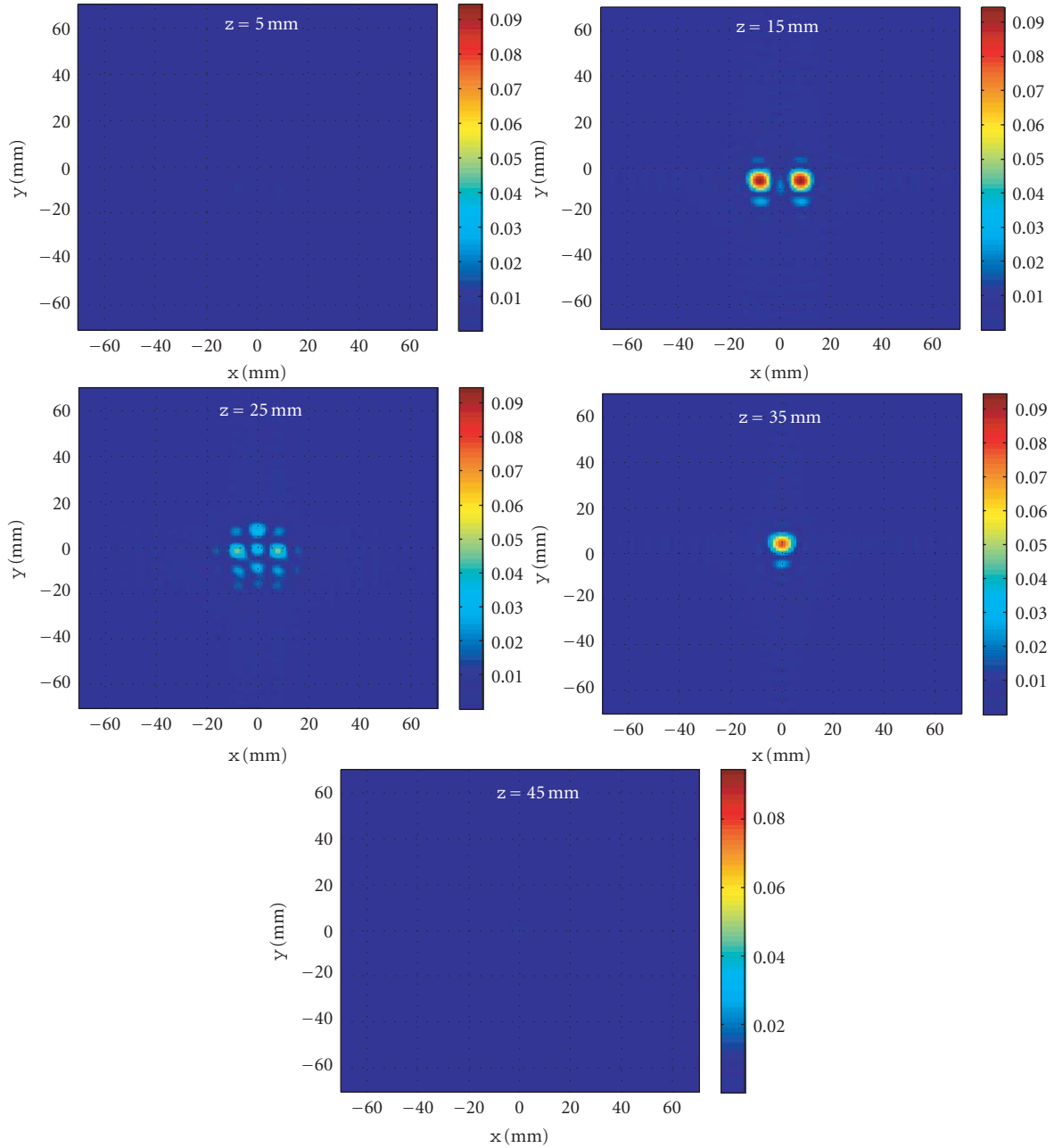


FIGURE 12: Reconstructed images for the example shown in Figure 10(b) after applying 3D holographic image reconstruction algorithm.

in deriving the formula for range resolution, the expression gives a good approximation in the case of near-field measurements [10].

Figure 11 shows the reconstructed images. The two objects are reconstructed correctly in the plane at $z = 15$ mm. The image reconstructed at $z = 25$ mm shows weak artifacts and the images at other range positions correctly do not show the presence of any objects.

In the second example, as illustrated in Figure 10(b), three small spherical objects with properties $\epsilon_r = 15$ and $\sigma = 1$ S/m are embedded between the two antennas inside a homogeneous background medium with $\epsilon_r = 10$

and $\sigma = 0.5$ S/m. The diameter of the spheres is 5.6 mm. Two of the objects are placed at a range position of 15 mm and the center-to-center distance between them is 16 mm. The third object is centered at the position (0, 10, 35) mm. Two antennas perform 2D raster scan on the rectangular apertures placed at $z = 0$ and $z = 50$ mm. The size of the scanned apertures is 48 mm \times 60 mm. The spatial sampling rate in both x and y directions is 3 mm. The simulated reflection and transmission S -parameters are obtained in the frequency range from 3 to 10 GHz with steps of 0.5 GHz. The incident field and Green's function for the antennas are obtained from a single

simulation of one antenna in free space as described in Section 3.

The 3D holographic image of the contrast function is obtained on planes of size $140\text{ mm} \times 140\text{ mm}$ at $z = 5, 15, 25, 35,$ and 45 mm .

Figure 12 shows the reconstructed images. The three objects are reconstructed well at the correct positions $z = 15\text{ mm}$ and $z = 35\text{ mm}$. The reconstructed image at $z = 25\text{ mm}$ shows some artifacts. However, the maximum of the reconstructed contrast $|f(x, y, z_3)|$ (image at $z = 25\text{ mm}$) is more than two times smaller than the maximum of $|f(x, y, z_2)|$ reconstructed at $z = 15\text{ mm}$. The images at the other range positions correctly do not show the presence of any objects.

It is worth noting that the difference between the scales in the images of Figures 11 and 12 is due to the application of the artifact removal technique, first proposed in [10].

6. Conclusion

In this paper, for the first time, we presented the formulations for a full vectorial 3D microwave holography. We also discussed how this full vector formulation reduces to the scalar microwave holography when considering two linearly polarized antennas oriented in a copolarized manner. Furthermore, we described a new approach based on the reciprocity principle to obtain Green's function from the same simulation used to obtain the incident field. This significantly mitigates the computational burden to obtain Green's function as well as eliminates the need for implementing "deblurring" algorithms prior to microwave holography when employing non-point-wise antennas.

We employed our recently proposed TEM-horn antennas in a rectangular aperture raster scanning setup to acquire wideband S-parameters. The capabilities of the proposed processing techniques in reconstructing the shape of the objects in 2D and 3D spatial domains were demonstrated through a number of simulations and experiments. The algorithms can reconstruct the object's shapes in quasi-real time. The images obtained from both simulations and measurements suffer from some artifacts. The artifacts in the experimental results are larger. In general, they are due to the measurement noise caused by the environment and the equipment, by the slight mis-match between the simulated and experimental performance of the antennas, as well as finite apertures. The artifacts in the simulated data are weaker. They are due to the numerical noise in obtaining the S-parameters, incident field, and Green's function as well as the finite aperture sizes. Proper signal processing techniques can be employed to reduce the artifacts.

The presented techniques are promising in the microwave imaging of tissues where they can provide an initial guess for the interior of the tissue while further processing would be employed to take into account the heterogeneity of the tissues.

References

[1] M. Pastorino, *Microwave Imaging*, Wiley, Hoboken, NJ, USA, 2010.

[2] L. E. Larsen and J. H. Jacobi, Eds., *Medical Applications of Microwave Imaging*, IEEE Press, 1986.

[3] L. E. Larsen and J. H. Jacobi, "Microwave interrogation of dielectric targets—part I: by scattering parameters," *Medical Physics*, vol. 5, no. 6, pp. 500–508, 1978.

[4] L. E. Larsen and J. H. Jacobi, "Microwave interrogation of dielectric targets—part II: by microwave time delay spectroscopy," *Medical Physics*, vol. 5, no. 6, pp. 509–513, 1978.

[5] N. K. Nikolova, "Microwave imaging for breast cancer," *IEEE Microwave Magazine*, vol. 12, no. 7, pp. 78–94, 2011.

[6] D. M. Sheen, D. L. McMakin, and T. E. Hall, "Near field imaging at microwave and millimeter wave frequencies," in *Proceedings of the IEEE MTT-S International Microwave Symposium (IMS '07)*, pp. 1693–1696, June 2007.

[7] D. M. Sheen, D. L. McMakin, and T. E. Hall, "Three-dimensional millimeter-wave imaging for concealed weapon detection," *IEEE Transactions on Microwave Theory and Techniques*, vol. 49, no. 9, pp. 1581–1592, 2001.

[8] D. Sheen, D. McMakin, and T. Hall, "Near-field three-dimensional radar imaging techniques and applications," *Applied Optics*, vol. 49, no. 19, pp. E83–E93, 2010.

[9] J. Detlefsen, A. Dallinger, and S. Schelkshorn, "Effective reconstruction approaches to millimeter-wave imaging of humans," in *Proceedings of the 28th General Assembly of International Union of Radio Science*, pp. 23–29, 2005.

[10] R. K. Amineh, M. Ravan, A. Khalatpour, and N. K. Nikolova, "Three-dimensional near-field microwave holography using reflected and transmitted signals," *IEEE Transactions on Antennas and Propagation*, vol. 59, no. 12, pp. 4777–4789, 2011.

[11] M. Ravan, R. K. Amineh, and N. K. Nikolova, "Two-dimensional near-field microwave holography," *Inverse Problems*, vol. 26, no. 5, Article ID 055011, 2010.

[12] A. Khalatpour, R. K. Amineh, H. Xu, Y. Baskharoun, and N. K. Nikolova, "Image quality enhancement in the microwave raster scanning method," in *Proceedings of the IEEE/MTT-S International Microwave Symposium (IMS '11)*, USA, 2011.

[13] R. K. Amineh, M. Ravan, A. Trehan, and N. K. Nikolova, "Near-field microwave imaging based on aperture raster scanning with TEM horn antennas," *IEEE Transactions on Antennas and Propagation*, vol. 59, no. 3, pp. 928–940, 2011.

[14] W. Chew, *Waves and Fields in Inhomogeneous Media*, IEEE Press, Piscataway, NJ, USA, 1995.

[15] EM softwares & systems-S.A. (Pty) Ltd. <http://www.feko.info>.

Research Article

Using X-Ray Mammograms to Assist in Microwave Breast Image Interpretation

Charlotte Curtis,¹ Richard Frayne,² and Elise Fear¹

¹Department of Electrical and Computer, Schulich School of Engineering, University of Calgary, Calgary, AB, Canada T2N 1N4

²Department of Radiology, University of Calgary, Calgary, AB, Canada T2N 2T9

Correspondence should be addressed to Charlotte Curtis, cfcurtis@ucalgary.ca

Received 29 September 2011; Accepted 28 December 2011

Academic Editor: Paul Meaney

Copyright © 2012 Charlotte Curtis et al. This is an open access article distributed under the Creative Commons Attribution License, which permits unrestricted use, distribution, and reproduction in any medium, provided the original work is properly cited.

Current clinical breast imaging modalities include ultrasound, magnetic resonance (MR) imaging, and the ubiquitous X-ray mammography. Microwave imaging, which takes advantage of differing electromagnetic properties to obtain image contrast, shows potential as a complementary imaging technique. As an emerging modality, interpretation of 3D microwave images poses a significant challenge. MR images are often used to assist in this task, and X-ray mammograms are readily available. However, X-ray mammograms provide 2D images of a breast under compression, resulting in significant geometric distortion. This paper presents a method to estimate the 3D shape of the breast and locations of regions of interest from standard clinical mammograms. The technique was developed using MR images as the reference 3D shape with the future intention of using microwave images. Twelve breast shapes were estimated and compared to ground truth MR images, resulting in a skin surface estimation accurate to within an average Euclidean distance of 10 mm. The 3D locations of regions of interest were estimated to be within the same clinical area of the breast as corresponding regions seen on MR imaging. These results encourage investigation into the use of mammography as a source of information to assist with microwave image interpretation as well as validation of microwave imaging techniques.

1. Introduction

X-ray mammography is the current gold standard breast imaging technique [1]. Mammography provides high-resolution 2D images of the breast in each of the cranial-caudal (CC) and medial-lateral oblique (MLO) directions and is capable of resolving fine structures such as microcalcifications. However, mammography has been shown to have low sensitivity and specificity among premenopausal women and women with dense breasts [2]. In cases where mammography is ambiguous, complementary imaging techniques such as magnetic resonance (MR) or ultrasound may be used.

Different modalities rely on different tissue properties in order to generate an image; for example, X-ray image contrast results from tissue density, whereas ultrasound imaging relies on acoustic impedance. Examining multiple modalities can provide diagnostic information that might be missed if only a single imaging technique was used [2].

Because of the advantages of combining information from different sources, there is benefit in continuing to develop new imaging methods.

Various studies have measured differences in the electromagnetic (EM) properties of fatty, fibroglandular, and cancerous breast tissues, suggesting a possible source of image contrast [3]. These differences are the basis for development of patient-friendly, safe, and inexpensive imaging techniques. Specifically, EM tomography and radar-based approaches have been proposed [4, 5]. Both techniques require the woman to lie prone on the examination table with the breast extending through a hole in the table top into a tank of immersion liquid; this is similar to patient positioning in MR image acquisition, with the additional presence of the immersion liquid [6]. An antenna emitting low-powered nonionizing EM radiation is then used to illuminate the breast. The waves travelling through the breast are reflected from internal structures and recorded on one or more receiving antennas.

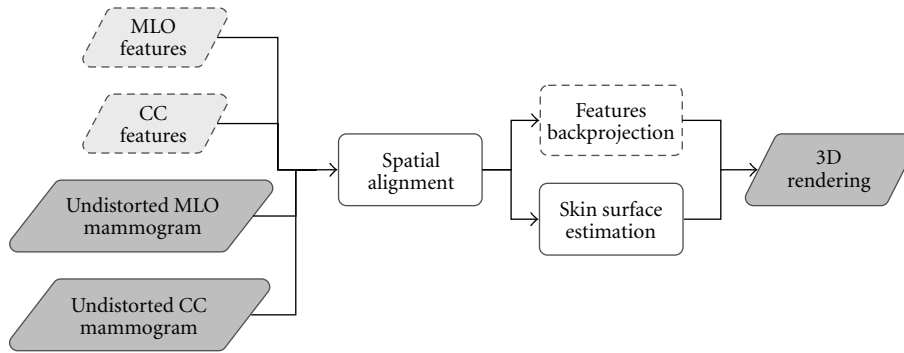


FIGURE 1: Overview of the estimation algorithm. Dotted outlines indicate steps performed only on images with identifiable features.

Tissue sensing adaptive radar (TSAR) is a 3D radar-based microwave imaging technique that is currently in the preliminary stages of clinical testing [7]. Compared to MR (the current 3D breast imaging modality), TSAR is less costly, less invasive as no contrast agent is required, and does not exclude patients with metallic implants or claustrophobia [6]. While initial results are promising, it is challenging to interpret the TSAR images without 3D images collected with another modality. To this end, the preliminary TSAR study included collection of MR images. However, MR scans are not typically part of patient care and add considerable time and expense to research studies.

Mammograms are a routine procedure in breast cancer cases [1]. Using these data to assist in interpreting TSAR would remove the dependence on MR in future studies, allowing for a greater patient cohort. However, mammograms cannot be directly compared to 3D imaging techniques. The specific aim of this work is to develop a method of interpreting mammograms in 3D. While the ultimate goal is to visualize mammograms in conjunction with TSAR images, MR images provide an effective tool to assist in the development and validation of this approach.

To use mammograms to interpret TSAR data, the 2D information must be translated into 3D space. However, mammograms are only obtained at two orientations, approximately 45° apart. Furthermore, the breast is compressed up to 50% of its original diameter, causing significant distortion of the 2D images [8]. These two issues are the main challenges in estimating 3D information from mammograms.

This paper presents a method to estimate the 3D skin surface and 3D location of regions of interest from standard two-view mammograms. The accuracy of the estimation is quantified by directly comparing to MR images and computing the difference between estimated and true skin surface in four anatomical directions.

Previous work in reconstructing the surface of the skin from mammograms has been presented in only three related publications [9–11]. The technique employed by Yam et al. and Kita et al. involved eroding the breast contour to compensate for compression, followed by fitting curves under the assumption that the MLO view approximates the ML view [9, 10]. Behrenbruch et al. refined this work by registering mammograms to MR images for more accurate compression

compensation [11]. However, none quantified the accuracy of their results to known 3D geometry; this work will address that issue. Similarly, the same works present methods for estimating the 3D location of suspicious regions seen on mammograms, but due to differences in acquisition geometry only Behrenbruch et al. were able to directly compare to MR images, while Kita used relative metrics.

2. Methods

Figure 1 shows an overview of the methods used to estimate ROIs and the skin surface in 3D.

First, the distortion due to compression is compensated through registration with a 3D reference shape. Next, the two mammographic views and their corresponding skin contours are aligned spatially to represent physical imaging planes. The contours are then used to estimate the skin surface by fitting ellipses to coronal slices of the breast at equally spaced intervals. In cases where features such as lesions could be identified on all data sets, the 3D locations of the features are estimated through 3D backprojection. Finally, the skin surface and features are rendered in 3D and compared to MR images.

2.1. Mammogram Preprocessing. In acquiring mammograms, the breast is compressed up to 50% of its original diameter, causing significant anatomical distortion of the tissues and leading to CC and MLO projection images consisting of different tissue configurations [12]. An estimation of the projections through the undistorted breast shape is therefore desirable in order to estimate the 3D structures. In this work, distortion of the mammograms was reduced through registration with projection images formed from MR images [13]; in the future, it is anticipated that TSAR images will be used to create these projection images.

The registration technique used a combination of landmark- and intensity-based registration to reduce distortion of both the external shape and the internal tissues of the mammograms [13]. This technique is similar to that described by Behrenbruch et al. [11]. In addition to registration of the two images, a contour defining the breast boundary and the locations of three anatomical landmarks

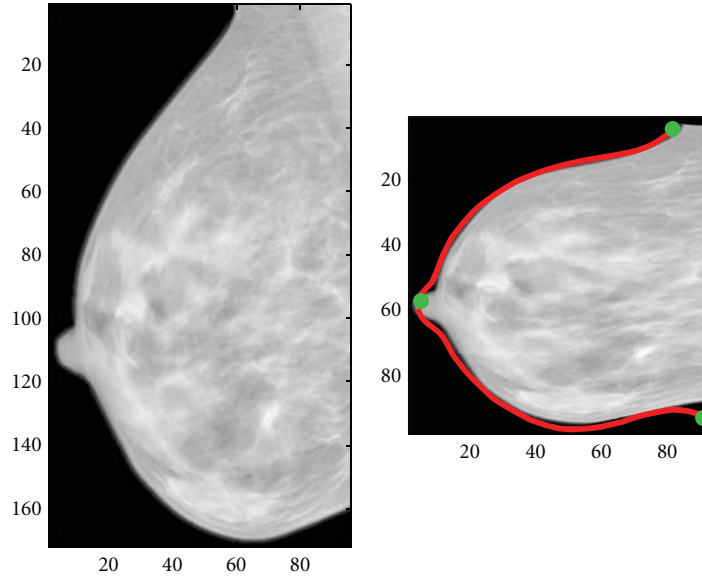


FIGURE 2: Original mammogram (left) was registered to an MR projection image to remove the distortion resulting from mammographic compression. The resulting image (right) is reduced to approximately 70% of the original surface area.

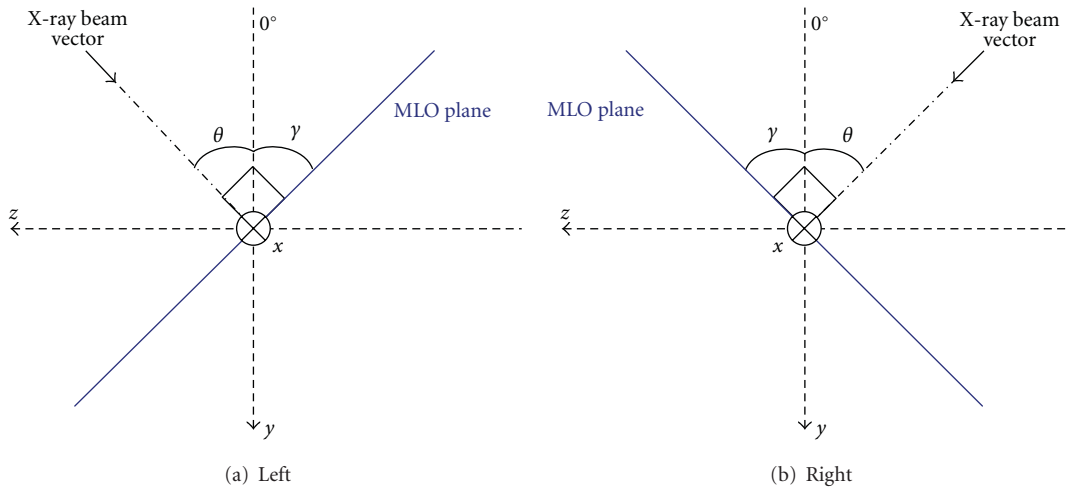


FIGURE 3: Illustration of MLO mammographic acquisition angles.

were automatically obtained through segmentation of the background followed by curvature computation. Figure 2 shows an example of the difference in shape between the original mammogram and the undistorted version. Due to the expansion of tissues during mammographic compression, the surface area of the undistorted mammogram is approximately 30% smaller than the original.

The three circular markers of Figure 2 are anatomical landmarks located at the nipple and the two regions of maximum curvature where the breast meets the chest wall. The contour defining the boundary of the breast as seen on the MR projection is shown to illustrate the accuracy of the shape following registration. After this preprocessing step, only mammographic data are used to obtain the 3D estimates.

2.2. Spatial Alignment. The preprocessing procedure of the previous section served to map the 2D mammographic projections into an undistorted 2D projection space. However, the relative alignment of the CC and MLO mammograms is unknown, as a given feature visible in the projected image can be located at any point along the X-ray beam vector (illustrated in Figure 3). Certain assumptions about the spatial alignment of the CC and MLO breast contours must be made in order to begin estimating the skin surface.

Unlike previous work, which assumed a 90° difference of projection angles between the CC and MLO views, this work uses the MLO acquisition angle provided in the metadata of digital mammograms. The MLO data (image, landmarks, and contour) were rotated according to the reciprocal of this angle in order to spatially align the two views. Figure 3 shows

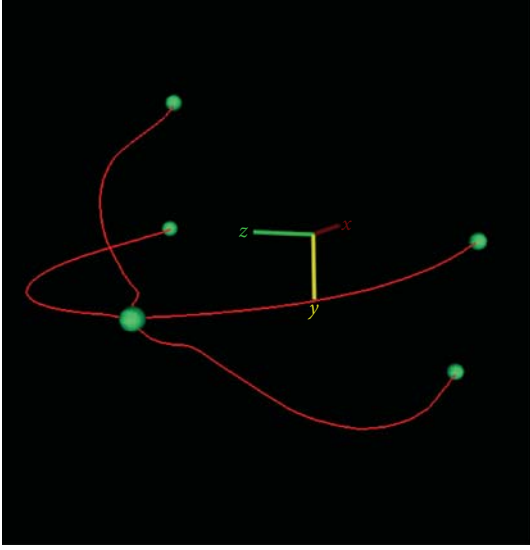


FIGURE 4: Sparse wireframe formed by spatially aligning CC and MLO breast contours.

an example of a typical MLO acquisition angle θ , with γ indicating the angle of rotation applied to the MLO image and contour data. Using the coordinate system shown in Figure 3, the CC view was rotated by 90° so as to lie on the zx plane.

Following rotation, translation of the two images was required to further align the views in an approximation of acquisition geometry. The nipple landmarks were chosen as the $[0, 0, 0]$ spatial coordinate, as by definition the landmarks in the two images are at the same location.

Further spatial alignment required further assumptions.

- (i) The contour of the mammogram, describing the largest edge or shadow of the breast, is located at the centre of the volume along the X-ray beam vector.
- (ii) The MLO data provide nipple location in the y -axis.
- (iii) The CC data provide nipple location in the z -axis.
- (iv) The centroid of a coronal slice taken at the chest wall corresponds to the intersection of the midpoints between the chest wall landmarks of both views.

Using these assumptions, the two image contours were aligned by rotating the CC view about the z -axis and the MLO view about the y -axis. The resulting geometry is an estimate of the orientation of the two imaging planes during acquisition of the mammograms. An example of the two contours, which form a sparse wireframe model, is shown in Figure 4. These data alone are used as the prior information for the skin surface estimation.

2.3. Skin Surface Estimation. Examination of a given zy or coronal plane of the breast as seen in MR reveals that the breast is roughly elliptical in cross-section [14]; this fact has been used in producing breast models for numerical

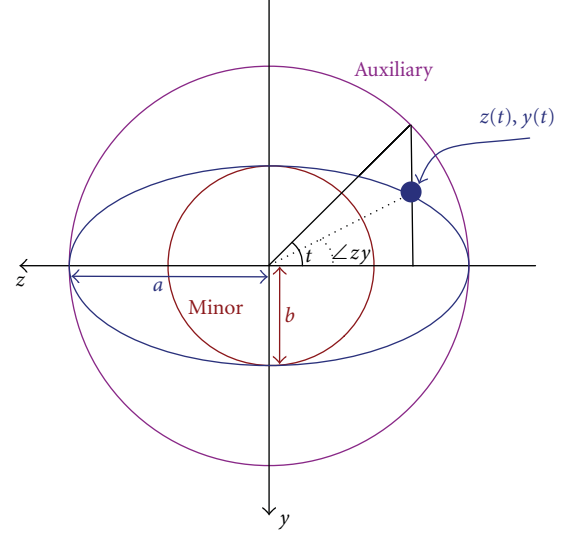


FIGURE 5: Ellipse in canonical position ($\phi = 0$, $[z_c, y_c] = [0, 0]$).

simulations and will be used to build the skin surface model in this work. The ellipse equation in parametric form is

$$\begin{aligned} z(t) &= z_c + a \cos t \cos \phi - b \sin t \sin \phi, \\ y(t) &= y_c + a \cos t \sin \phi + b \sin t \cos \phi, \end{aligned} \quad (1)$$

where $[z_c, y_c]$ is the centre of the ellipse, a and b are the scaling factors for the major and minor axes, respectively, ϕ is the angle of the major axis, and the parameter t ranges from 0 to 2π . These variables are depicted in Figure 5.

Any coronal plane intersects the wireframe model of Figure 4 at four points. However, four points are insufficient data for ellipse fitting. Furthermore, the four intersected points are not orthogonal to each other, resulting in an uneven distribution around the ellipse.

To obtain the best fitting ellipse for the four known data points of a coronal slice, the centre point $[z_c, y_c]$ was assumed to be the centroid of the four points. The rotation angle ϕ was set to zero, reducing (1) to two equations with three unknowns a , b , and t . The t parameter was estimated using the angle of the vector from the centre point to the absolute value of each data point ($\angle z\gamma$ in Figure 5), providing four solutions to (1) and allowing for a least squares fit to be determined. The data were then rotated iteratively to various angles ϕ , and the least squares fitting was repeated until the best ϕ was determined.

With all the parameters of (1) determined, an ellipse was created and displayed at the specified x location. This process was repeated for the desired number of ellipses along the x axis; Figure 6 shows a sample skin surface estimation. In this example, only five coronal slices are shown for clarity; in evaluating results, twenty slices will be rendered for a more complete skin surface estimation.

2.4. Internal Feature Estimation. The skin surface estimate described in the previous section describes the general shape of the breast and provides a frame of reference to compare

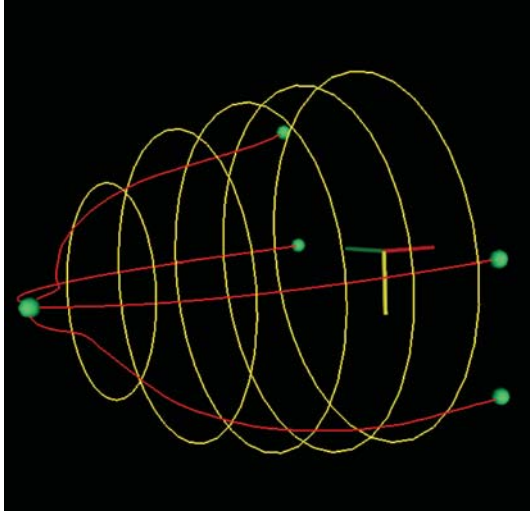


FIGURE 6: Sample skin surface estimation.

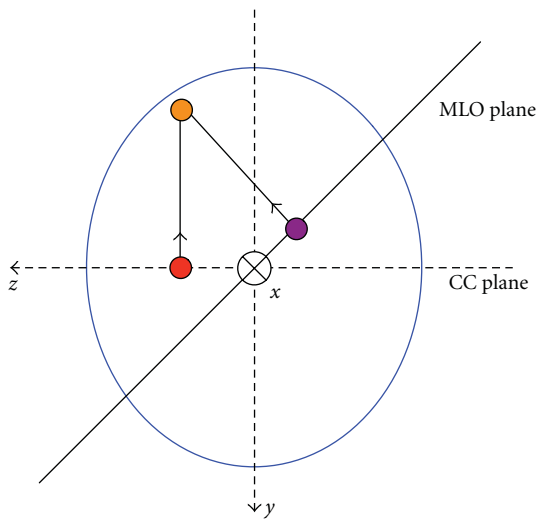


FIGURE 7: Reconstruction of internal feature points.

the two modalities. However, identification of a particular region of interest (ROI) is of even greater utility, providing the 3D location of particular features of the breast. As mammograms provide 2D views of ROIs, these regions can be identified and their 3D location computed and displayed relative to the skin surface estimation.

For the purpose of identifying the general ROI in 3D space, ROIs as seen on the undistorted mammograms were modelled as simple spheres. Corresponding features on the CC and MLO views were identified in consultation with a radiologist and marked as 2D circles through an interactive display. These points were then located in 3D space using only the mammographic data by calculating the intersection of the two lines orthogonal to the imaging planes as illustrated by Figure 7.

This is computed as follows:

$$\begin{aligned} x &= \frac{x_{cc} + x_{mlo}}{2}, \\ y &= y_{mlo} + \frac{z_{mlo} - z_{cc}}{\tan^{-1} \gamma}, \\ z &= z_{cc}, \end{aligned} \quad (2)$$

with γ as indicated in Figure 3. The radius of the 3D sphere was taken as the average of the two 2D circles.

3. Results and Discussion

The skin surface estimation technique was applied to six sets of patient data, resulting in a total of twelve breast models. Mammograms were collected digitally according to the Canadian standards, yielding CC and MLO images at varying resolutions. Both contrast-enhanced and fat-suppressed T1-weighted MR images were collected, also in compliance with the Canadian breast imaging protocols. For the purposes of image registration and comparison with mammography, the fat-suppressed structural MR images were used.

With the assistance of a radiologist, regions of interest on the data sets were identified. Only one was a candidate for internal feature location estimation due to a need for discrete lesion visibility on all three images (CC, MLO, and MR).

For each data set, an MR image was loaded and displayed to provide ground truth geometry. This image was aligned as accurately as possible relative to the feature estimation model, but it should be noted that alignment is subject to errors due to the assumptions made in aligning the wireframe model.

3.1. Skin Surface Estimation. Figures 8 and 9 show sagittal and axial views of a central MR slice with the estimated skin surface overlaid. Figure 8 is the data set used to describe methods, while Figure 9 is the data set containing the lesion.

Examination of the skin estimations of both Figures 8 and 9 shows that, despite independent reconstruction at each coronal slice, a smooth contour is achieved. Furthermore, the algorithm succeeds in capturing the breast shape even when large interpatient variations are present.

The sagittal view of the estimation shown in Figure 9(a) shows that the ellipse technique has failed to completely capture the cranial-caudal asymmetry of the breast shape. This is likely due to the large breast making contact with the side of the MR coil, resulting in a downturned nipple and distorted MR geometry. However, the axial view (undistorted at this location) shows excellent medial-lateral correspondence.

A coronal cross-section of the sample data set at two different locations is shown in Figure 10. Due to deformation of the breast near the chest wall caused by contact with the MR coil, the estimated ellipse fails to accurately capture the shape at this location (Figure 10(a)). However, near the centre of the breast, the ellipse approximation is more reasonable (Figure 10(b)). To quantify errors in estimated skin outline, the difference between the true skin surface as

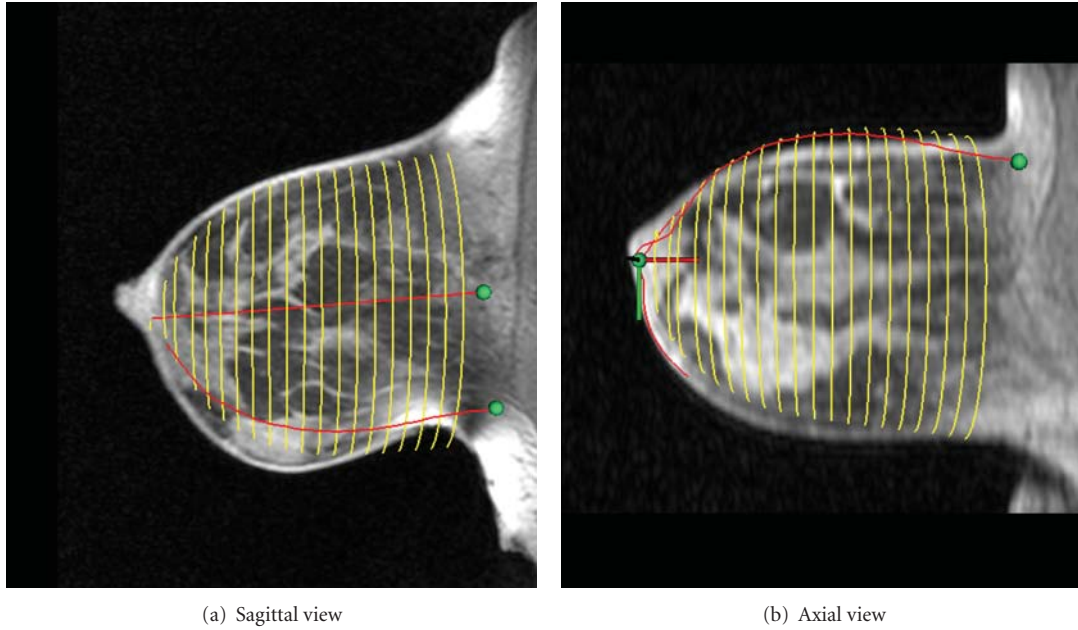


FIGURE 8: Comparison of estimated skin surface with MR (sample data set).

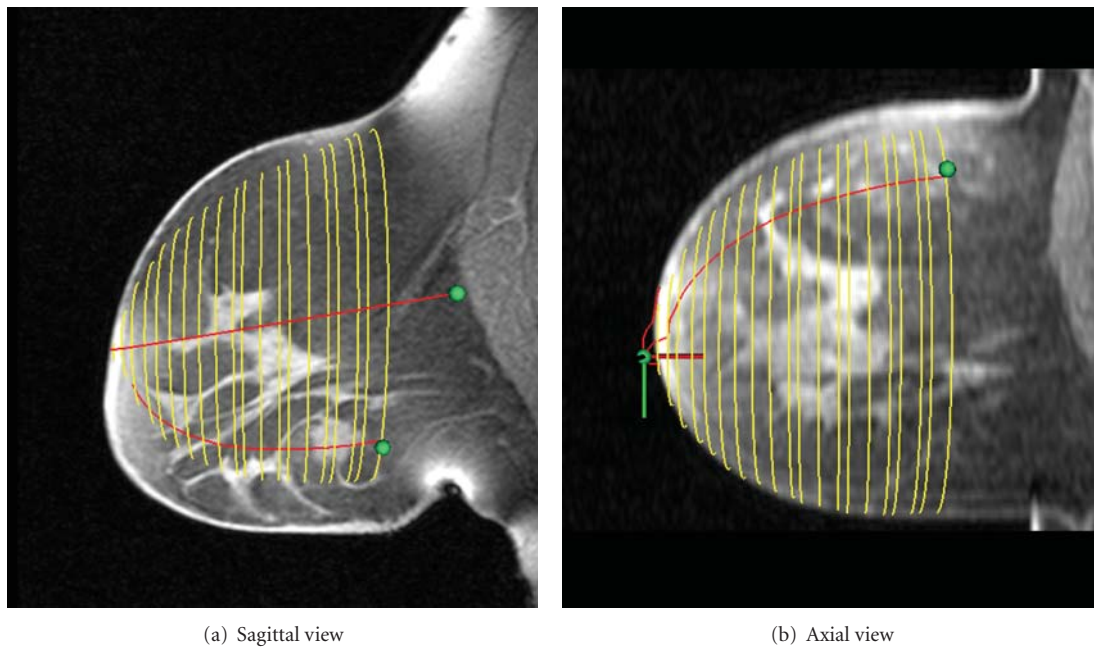


FIGURE 9: Comparison of estimated skin surface with MR (data set with lesion).

seen in a coronal slice of the MR image and the estimated surface was calculated at the medial, lateral, cranial, and caudal directions. These errors are indicated by the arrows in Figure 10.

The skin estimation errors were computed such that negative errors represent underestimation of the breast surface. To observe the relationship between coronal slice location and estimation error, the errors were plotted against coronal slice location (x -axis). The resulting error plots are shown in

Figure 11 for the two sample data sets. In both cases, it is clear that the cranial and caudal errors tend to exceed the medial and lateral errors. Furthermore, all of the errors tend to be negative, suggesting a consistent underestimation of the true skin surface.

To examine trends across all data sets, the absolute values of the skin estimation errors were plotted against x -axis location for all data sets (Figures 12(a) and 12(b)). These plots also show the best-fit linear regression for each

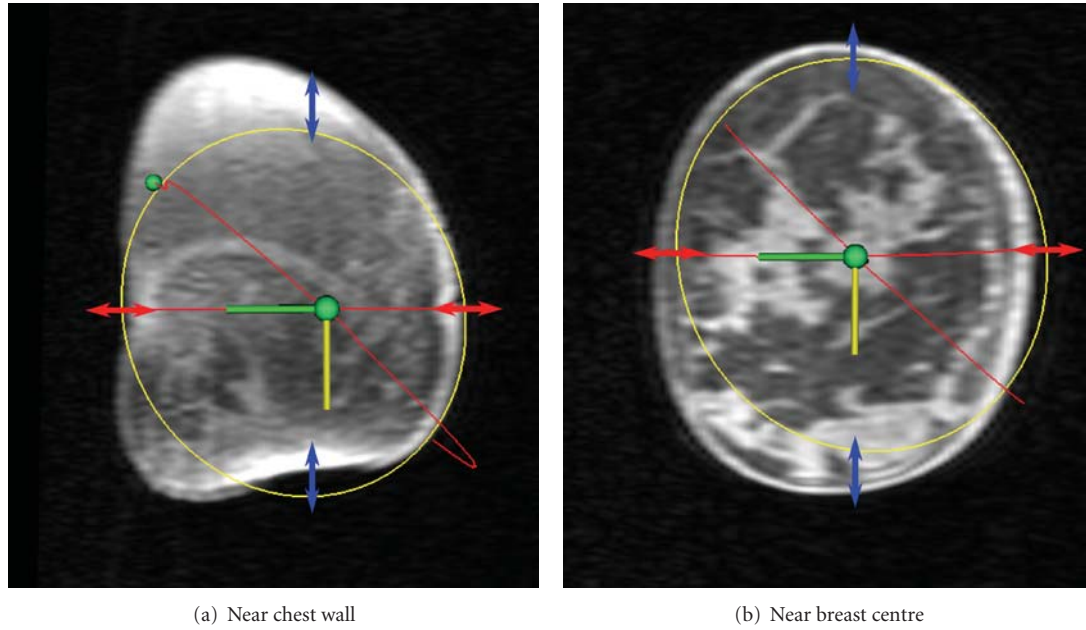


FIGURE 10: Comparison of estimated skin surface with MR. Arrows indicate error between estimated and true skin surface at four anatomical directions (arrow size exaggerated for visibility).

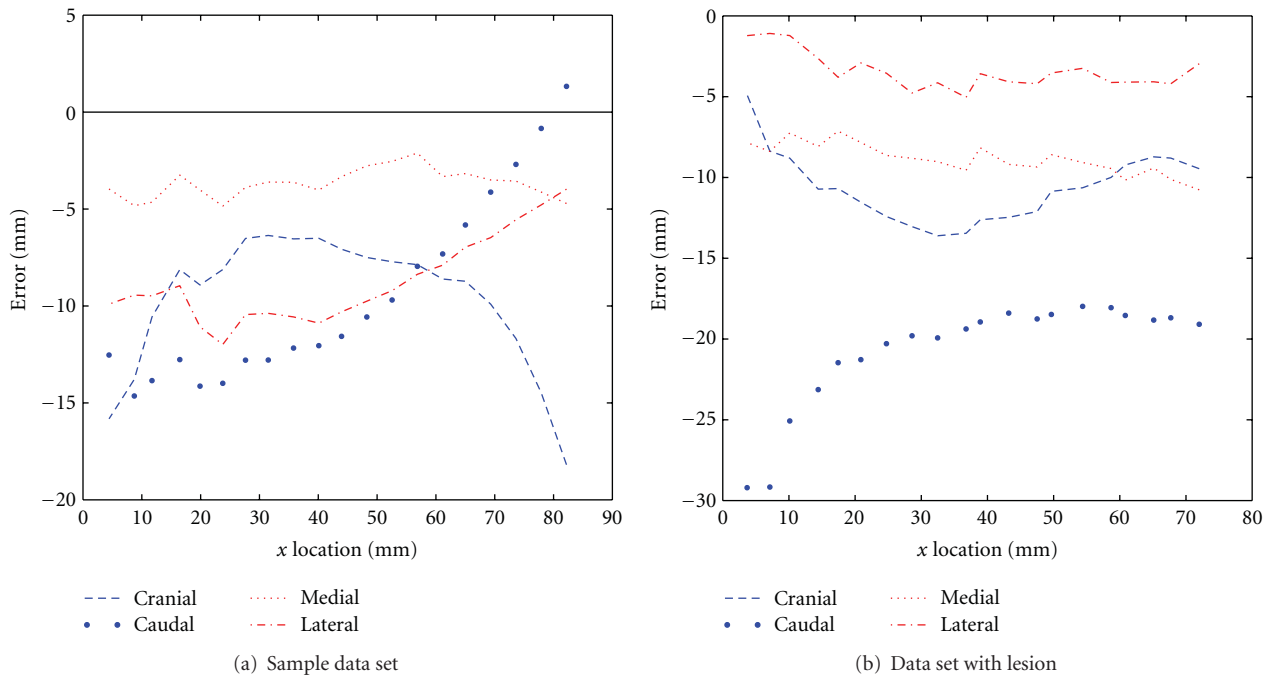


FIGURE 11: Skin estimation error versus coronal slice (x) location for two data sets.

individual direction, as well as both directions taken together. It should be noted that these best-fit lines are used only to illustrate trends and are not intended as a model of the data, as no linear relationship is expected to exist.

In both cranial-caudal and medial-lateral directions, the best-fit line for the combined data suggests a slight trend of

increasing accuracy towards the chest wall. However, this may be partially a result of the nonelliptical shape of the breast at the chest wall as seen in Figure 10(a), leading to underestimation of the true error at these x locations. Similarly, the error at the nipple may be exaggerated due to the small coronal cross-section, where a slight misalignment

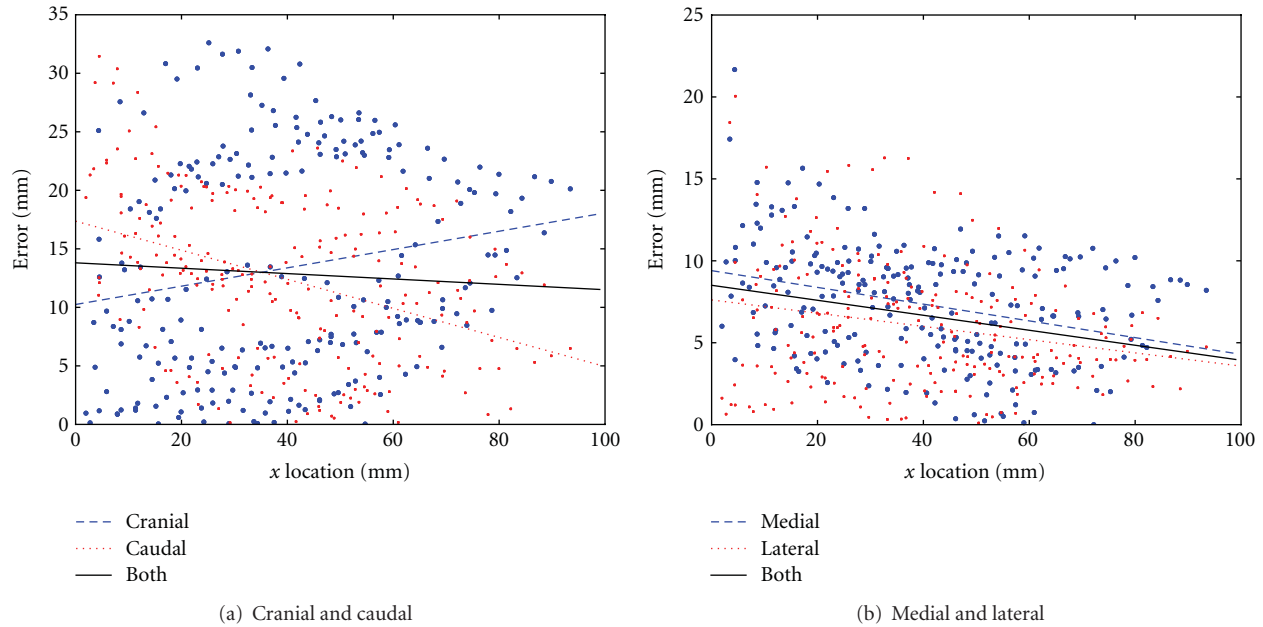
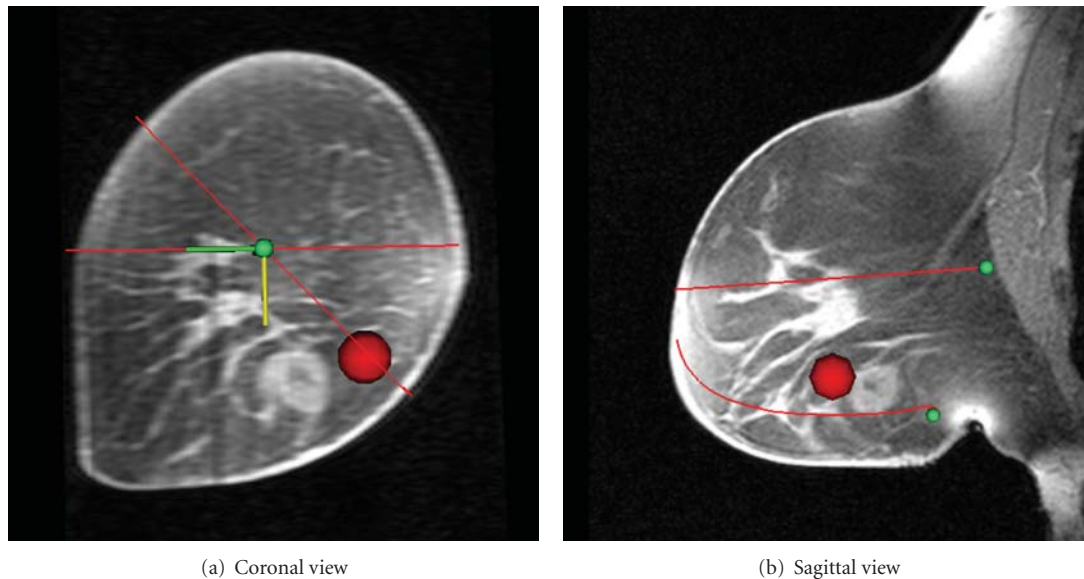
FIGURE 12: Skin estimation error versus x location.

FIGURE 13: Comparison between feature reconstructed from mammograms and corresponding feature seen on MR.

can result in significant error. A more reasonable conclusion is that the error is approximately consistent along the x -axis of the breast.

Comparing Figures 12(a) and 12(b) confirms that the skin estimation technique is more accurate and consistent in the medial and lateral directions. This can be explained by the relative lack of data in the cranial-caudal direction due to the 45° angle between image planes. Since previous work assumed that the images were separated by 90° , it is likely that the current work is more accurate [10]. However, it is not possible to directly compare the two methods, as previous work did not assess errors relative to a ground truth.

Overall, the skin surface estimation was accurate to an average contour deviation of 13 mm in the cranial-caudal direction and 6 mm in the medial-lateral direction. This is considered acceptable given the number of assumptions required and the limited information available for estimating the 3D skin surface. As this is the first work to quantify the accuracy of a 3D skin surface estimation created from mammograms, it is difficult to determine whether this result is comparable to that of previous publications.

3.2. Internal Feature Estimation. Figure 13 shows a comparison between a reconstructed feature and the MR volume of

the only data set containing a discrete feature visible in both modalities. The sphere marks the estimated region of the lesion resulting from backprojection, and the corresponding lesion on the MR is clearly visible as an opaque mass. The 3D Euclidean distance between the centroids of the true and estimated lesion location is approximately 12 mm. While it might seem reasonable to compare this value to the differences in Euclidean distance from lesion to nipple reported by Kita et al. in 2002, the two metrics are not in fact identical [10]. In the current work, Euclidean distance between lesion centroids accounts for absolute differences, whereas in Kita's work the two vectors may have different directions with a small difference in Euclidean distance. Similarly, this result cannot be compared to the error metric computed in the 2D mammographic space used by Behrenbruch et al. [11].

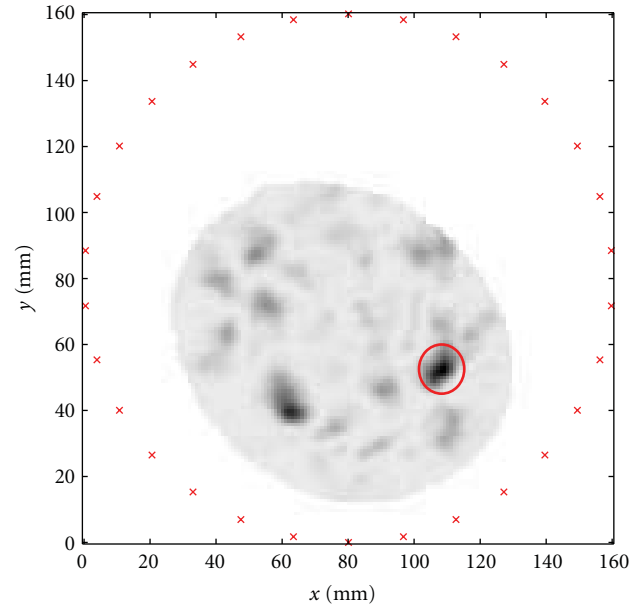
The radiology report for this patient states "mass lesion 4 o'clock right breast." From visual inspection of Figure 13(a), the estimated 3D feature is indeed located at 4 o'clock. More precisely, the angle formed between the vectors from the ellipse centre to the two points (true and estimated lesion centroids) is 20° . This places the estimated lesion location within the same hour (30°) of the breast as the ground truth, providing a reasonably accurate 3D location of the lesion as seen on mammography. This metric is comparable to the "direction at front view" metric reported by Kita et al. and within a similar range of values [10].

The major difference between the methods described in this work and the methods of Kita et al. is the mapping of features into the prone acquisition geometry of MR imaging. As this similar to the geometry used for TSAR imaging, 3D ROI prediction from mammography will enable interpretation of TSAR images without reliance on MR data.

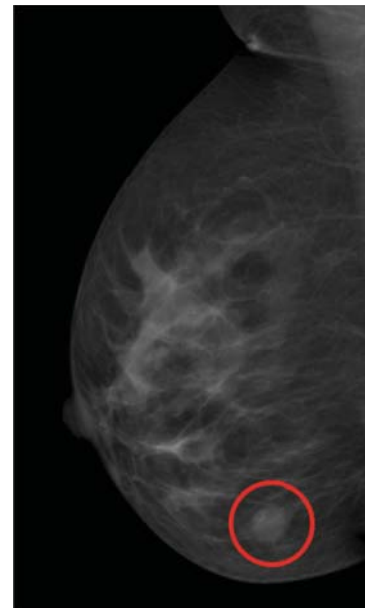
As a preliminary example, Figure 14 shows the experimentally acquired TSAR image and original MLO mammogram of this patient. Current TSAR protocol consists of immersing the breast in canola oil, then illuminating in a cylindrical pattern with a BAVA-D antenna described in [15]. At 200 antenna locations, measurement data are collected from 50 MHz to 15 GHz using a vector network analyzer. Concurrent to microwave data collection, a laser is used to obtain an accurate estimate of the skin location [16]. These data provide knowledge of the skin surface and are used to assist with processing the microwave data, which is then formed into an image using the delay-and-sum algorithm [17].

The 3D model of Figure 13(a) places the tumour at 4 o'clock, which is in agreement with the MR data and the radiologist's report. Even though Figure 13 was created in MR space instead of TSAR space, the identified ROI is likely to compare to the circled region of enhancement detected by TSAR, also located at 4 o'clock. However, it is difficult for a nonradiologist to identify the corresponding lesions circled in Figure 14.

Due to the immersion medium used in TSAR acquisition, the breast floats and changes shape relative to MR imaging, where the breast is hanging freely. This can be observed in Figures 13 and 14, which have very different shapes despite being images from the same patient. This illustrates the difficulties in comparing results from different modalities. In this



(a) TSAR image (coronal)



(b) MLO mammogram

FIGURE 14: Comparison between experimental TSAR image and MLO mammogram with corresponding lesion encircled.

example, it appears that the mammographic reconstruction is a closer match to the TSAR image than the MR data, but this is a coincidence resulting from a slight rotation of the breast between the MR and the TSAR images.

The data for the TSAR image shown in Figure 14(a) was acquired in a narrow range of slices around the anticipated tumour location. This resulted in an image that does not include the nipple or the chest wall landmarks. In the future, TSAR images will be used to remove the distortion from mammograms, but this was not possible in the current work as the landmarks are essential for matching breast area.

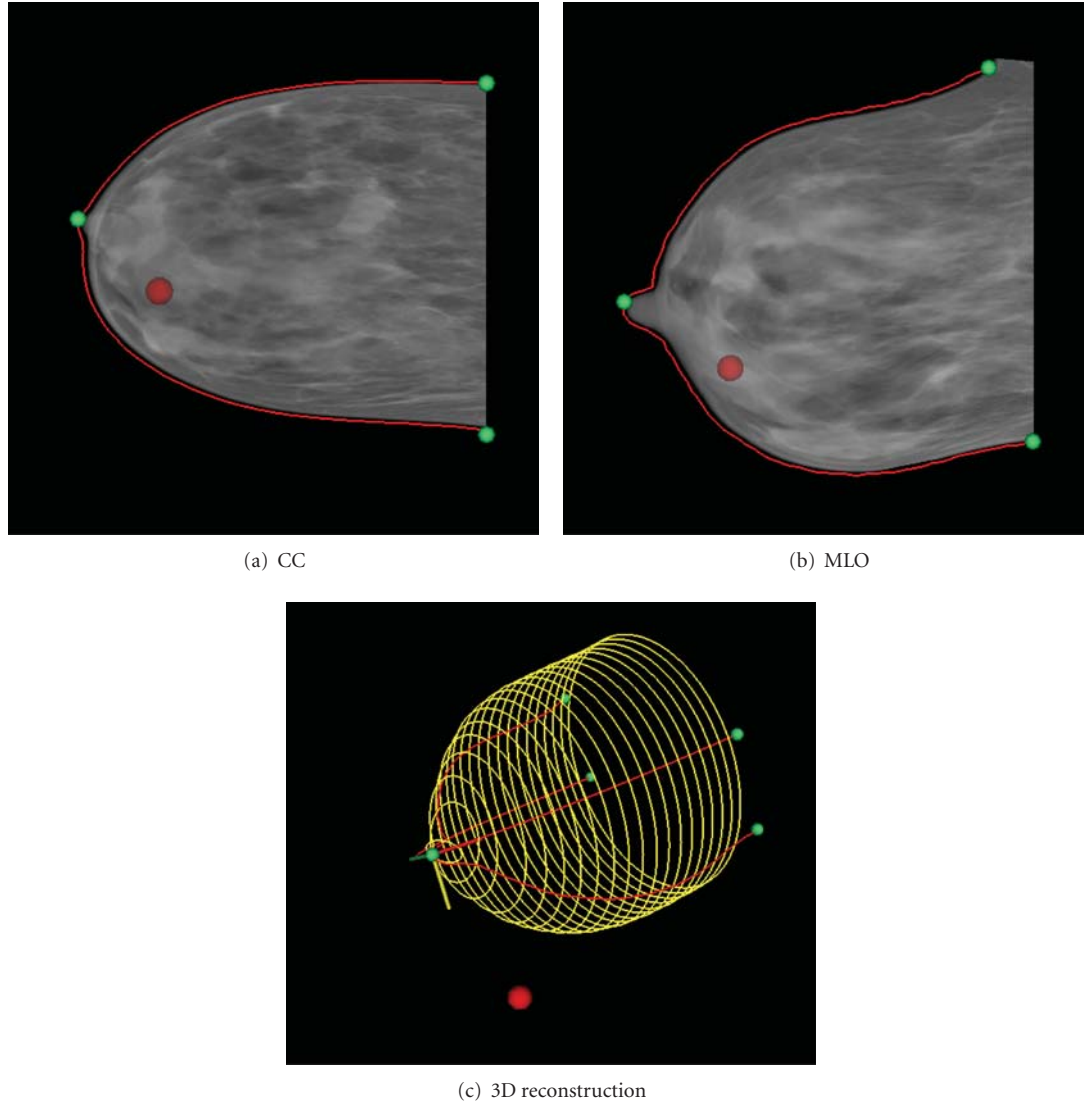


FIGURE 15: Identification of non-corresponding lesions results in mapping outside the breast volume.

Therefore, the method was developed and tested using MR images in place of TSAR, demonstrating the effectiveness of the technique.

3.3. Verification of Corresponding Features. A final application for the 3D estimation methods described in this paper is as a verification of features seen on mammography. Radiologists undergo extensive training in order to interpret medical images; without such experience, identification of the same feature on both mammographic views is difficult. However, once the ROI is reconstructed in 3D, it becomes obvious whether the two visible features correspond. Figure 15 shows a data set where a suspected lesion is identified on the CC and MLO views. To the untrained eye, these locations could reasonably correspond, but the reconstruction (Figure 15(c)) clearly shows that the identified locations cannot exist within the breast. This verification has the potential to

assist researchers and engineers in identifying true regions of interest.

4. Limitations

The comparison between MR ground truth and mammographic estimation is subject to errors related to the assumptions in aligning the two mammographic planes (see Section 2.2). This can be observed visually in Figure 10(b), where the MLO plane appears to be shifted relative to the true coronal cross-section. Such errors are not likely to impact the overall breast shape significantly, though improvements to the alignment would result in better error metrics.

In addition, each step of the method described in this work requires significant estimation and a large number of assumptions. As such, the technique has inherent inaccuracies and details that cannot be recovered with only two

mammographic views, and the estimation should not be taken as an exact model of the 3D breast. However, for the intended purposes of assisting with microwave image interpretation, the accuracies obtained should suffice.

5. Conclusion

The skin surface and internal feature estimation techniques described in this paper have been found to be sufficiently accurate to assist with microwave image interpretation and provide a means of comparing TSAR results to the gold standard of mammography. While similar estimation techniques have been presented in the past, quantification of accuracy as compared to MR imaging is novel in the literature.

Future work will be to modify the mammogram undistortion technique to account for the geometric differences introduced by the TSAR immersion liquid. Following this, the 3D mammographic information will be incorporated into current TSAR image processing protocols.

Acknowledgment

The authors would like to thank Dr. Bobbie Docktor for her assistance in identifying radiographic features.

References

- [1] Steering Committee on Clinical Practice Guidelines for the Care and Treatment of Breast Cancer, "The palpable breast lump: information and recommendations to assist decision-making when a breast lump is detected," *Canadian Medical Association Journal*, vol. 158, supplement 3, pp. S3–S8, 1998.
- [2] C. Brekelmans, M. Kriege, I. Obdeijn et al., "Factors affecting sensitivity and specificity of screening mammography and MRI in women with an inherited risk for breast cancer," *Breast Cancer Research and Treatment*, vol. 100, no. 1, pp. 109–119, 2006.
- [3] A. J. Surowiec, S. S. Stuchly, J. R. Barr, and A. Swarup, "Dielectric properties of breast carcinoma and the surrounding tissues," *IEEE Transactions on Biomedical Engineering*, vol. 35, no. 4, pp. 257–263, 1988.
- [4] E. Bond, B. D. Van Veen, X. Li, and S. C. Hagness, "An overview of ultra-wideband microwave imaging via space-time beamforming for early-stage breast-cancer detection," *IEEE Antennas and Propagation Magazine*, vol. 47, no. 1, pp. 19–34, 2005.
- [5] J. Shea, P. Kosmas, B. V. Veen, and S. Hagness, "Three-dimensional microwave tomography for breast imaging and cancer detection," in *Proceedings of the International Conference on Biomedical Applications of Electrical Impedance Tomography*, pp. 5–6, 2009.
- [6] E. C. Fear, P. M. Meaney, and M. A. Stuchly, "Microwaves for breast cancer detection?" *IEEE Potentials*, vol. 22, no. 1, pp. 12–18, 2003.
- [7] J. Bourqui, J. Garrett, and E. Fear, "Measurement and analysis of microwave frequency signals transmitted through the breast," *International Journal of Biomedical Imaging*, vol. 2012, Article ID 562563, 11 pages, 2012.
- [8] D. J. Dowsett, P. A. Kenny, and R. E. Johnston, *The Physics of Diagnostic Imaging*, Oxford University Press, 2006.
- [9] M. Yam, M. Brady, R. Highnam, C. Behrenbruch, R. English, and Y. Kita, "Three-dimensional reconstruction of micro-calcification clusters from two mammographic views," *IEEE Transactions on Medical Imaging*, vol. 20, no. 6, pp. 479–489, 2001.
- [10] Y. Kita, E. Tohno, R. Highnam, and M. Brady, "A CAD system for the 3D location of lesions in mammograms," *Medical Image Analysis*, vol. 6, no. 3, pp. 267–273, 2002.
- [11] C. Behrenbruch, K. Marias, P. Armitage et al., "Fusion of contrast-enhanced breast MR and mammographic imaging data," *The British Journal of Radiology*, vol. 77, pp. 311–340, 2003.
- [12] N. Ruiter, R. Stotzka, T. Müller, H. Gemmeke, J. Reichenbach, and W. Kaiser, "Model-based registration of X-ray mammograms and MR images of the female breast," *IEEE Transactions on Nuclear Science*, vol. 53, no. 1, pp. 204–211, 2006.
- [13] C. Curtis, R. Frayne, and E. Fear, "Semiautomated multimodal breast image registration," *International Journal of Biomedical Imaging*, vol. 2012, Article ID 890830, 14 pages, 2012.
- [14] E. Zastrow, S. K. Davis, M. Lazebnik, F. Kelcz, B. D. Van Veen, and S. C. Hagness, "Development of anatomically realistic numerical breast phantoms with accurate dielectric properties for modeling microwave interactions with the human breast," *IEEE Transactions on Biomedical Engineering*, vol. 55, no. 12, pp. 2792–2800, 2008.
- [15] J. Bourqui, M. Okoniewski, and E. C. Fear, "Balanced antipodal vivaldi antenna with dielectric director for near-field microwave imaging," *IEEE Transactions on Antennas and Propagation*, vol. 58, no. 7, pp. 2318–2326, 2010.
- [16] T. Williams, E. Fear, J. Bourqui, T. Cameron, and M. Okoniewski, "Laser surface estimation for microwave breast imaging systems," *IEEE Transactions on Biomedical Engineering*, vol. 58, no. 5, pp. 1193–1199, 2011.
- [17] E. C. Fear, S. C. Hagness, P. M. Meaney, M. Okoniewski, and M. A. Stuchly, "Enhancing breast tumor detection with near-field imaging," *IEEE Microwave Magazine*, vol. 3, no. 1, pp. 48–56, 2002.

Research Article

Microwave Breast Imaging System Prototype with Integrated Numerical Characterization

Mark Haynes, John Stang, and Mahta Moghaddam

*Applied Physics Program, Basic Radiological Sciences Ultrasound Group, and Radiation Laboratory,
Department of Electrical Engineering and Computer Science, University of Michigan, Ann Arbor, MI 48109-2122, USA*

Correspondence should be addressed to Mark Haynes, mshaynes@umich.edu

Received 2 October 2011; Accepted 7 December 2011

Academic Editor: Paul Meaney

Copyright © 2012 Mark Haynes et al. This is an open access article distributed under the Creative Commons Attribution License, which permits unrestricted use, distribution, and reproduction in any medium, provided the original work is properly cited.

The increasing number of experimental microwave breast imaging systems and the need to properly model them have motivated our development of an integrated numerical characterization technique. We use Ansoft HFSS and a formalism we developed previously to numerically characterize an S -parameter-based breast imaging system and link it to an inverse scattering algorithm. We show successful reconstructions of simple test objects using synthetic and experimental data. We demonstrate the sensitivity of image reconstructions to knowledge of the background dielectric properties and show the limits of the current model.

1. Introduction

A number of experimental systems for microwave breast imaging have been developed in recent years. These systems test full-wave inverse scattering algorithms [1–4] as well as synthetic aperture beam focusing techniques [5]. While imaging algorithms abound in the literature, techniques to properly model, characterize, and calibrate these systems have lagged behind algorithm development. Investigators have started to identify characterization as a major task, which must be addressed in order to fully evaluate the efficacy of microwave imaging for breast cancer detection. Part of this evaluation involves separating modeling errors from intrinsic algorithm artifacts in the final images. Thus, there is a need for accurate models of experimental systems, as well as methods that efficiently incorporate these models into the imaging algorithms.

The task of characterizing a microwave breast imaging system for inverse scattering, as compared to a free-space system, is complicated by several factors. Specifically, the antennas are not isolated in the background media but exist as part of the surrounding structure. Also, compact arrangements of many antennas create a cavity-like imaging geometry, and the transmitter incident fields include all background multiple scattering. Finally, the antennas and

object are in each others near-fields, so object-cavity scattering should be modeled.

In trying to characterize breast imaging systems, investigators have turned to full numerical simulation. The antenna cavity in [6] was modeled using Ansoft HFSS and only used for antenna design and sensitivity analysis. In [7], dipole sources of an inverse scattering experiment were modeled with HFSS and calibration constants used to scale the antenna incident fields. HFSS has also been used to obtain antenna incident fields in a near-field and open, antenna setup [8]; however, ad hoc methods have been used to calibrate the scattered field S -parameter data for the inverse scattering algorithm. In more recent work [9], CST Microwave Studio was used to study and tune antenna performance in a breast imaging cavity. Also, finite-volume time-domain solvers of [10] modeled wide-band antennas for time-domain beam focusing. The most complete work to date is [11], where an FEM forward solver is used to simulate the entire breast in the presence of the antennas, but computational complexity remains a challenge. Despite the growing use of numerical solvers to model breast imaging systems, there has been no clear or formal way of incorporating the results from full-wave numerical models into the imaging algorithms.

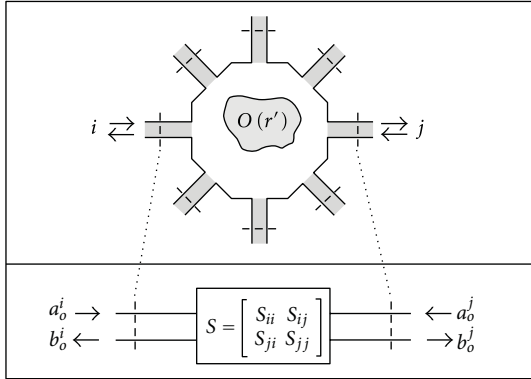


FIGURE 1: Microwave network model of cavity and scattering object. S-parameters are measured between the reference planes on the transmission lines.

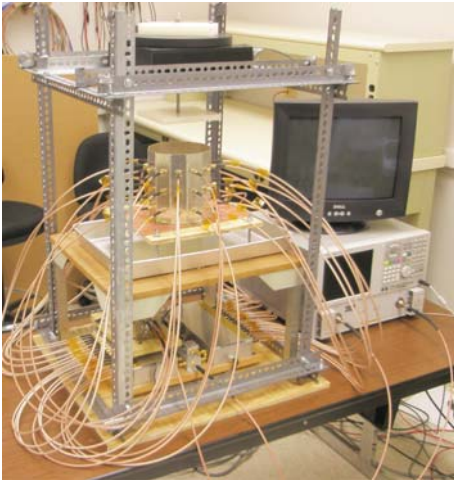


FIGURE 2: Breast imaging system prototype. The imaging cavity is connected to the VNA through a solid-state switching matrix. A rotator is mounted above and turns suspended objects for multiple transmitter views.

The task of characterizing any inverse scattering system can be divided into three parts: (1) determining the incident fields produced by the antennas in the absence of the object, (2) determining the background dyadic Green's function, that is, modeling the interactions between the object and its surroundings if necessary, and (3) linking the volume integrals in the imaging algorithms to measurable transmit and receive voltages. The purpose of this paper is to show how we use HFSS and a formalism we developed in previous work [12] to solve parts (1) and (3) of this characterization problem, in order to make a numerical characterization and inverse scattering algorithm consistent with an S-parameter based prototype breast imaging system.

The inverse scattering algorithm we use is the Born iterative method (BIM) with multivariate-covariance cost function [13–15]. This cost function allows us to experimentally choose the regularization parameters based on our prior knowledge of system noise and expected range of permittivities. The forward solver used in the BIM requires

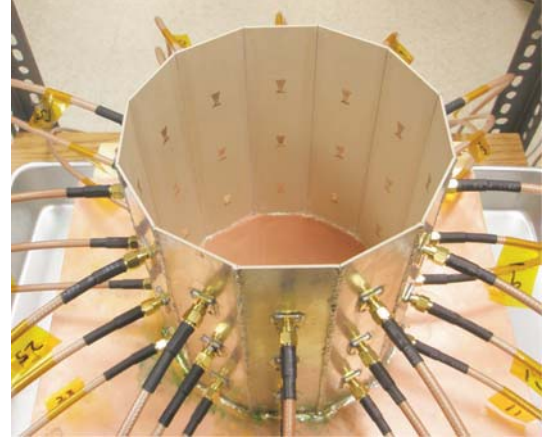


FIGURE 3: Imaging cavity. Twelve panels with three bow-tie antennas each are solder together and to a conducting plate.

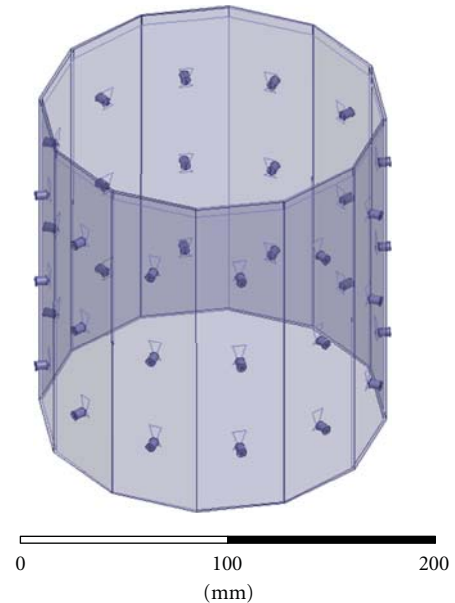


FIGURE 4: HFSS CAD model of the imaging cavity. Twelve panels contain three bow-tie antennas each. The bottom of the cavity is PEC, it is filled with the coupling fluid up to the visible line, and the top surface radiates to air.

the background dyadic Green's function and finding it constitutes part (2) of the characterization problem mentioned above. For convenience we use the lossy free-space dyadic Green's function and give some numerical and experimental justification for this. Fully modeling the multiple scattering between the breast and the imaging structure in the forward solver is not trivial and we discuss it in The Appendix.

We validate our methods with a combination of simulation and experiment. We first present the formalism of [12] in the context of cavity problems. We then explain our experimental setup, which consists of a cylindrical imaging cavity with printed antennas, solid-state switching matrix, and water/oil coupling medium. The HFSS numerical model

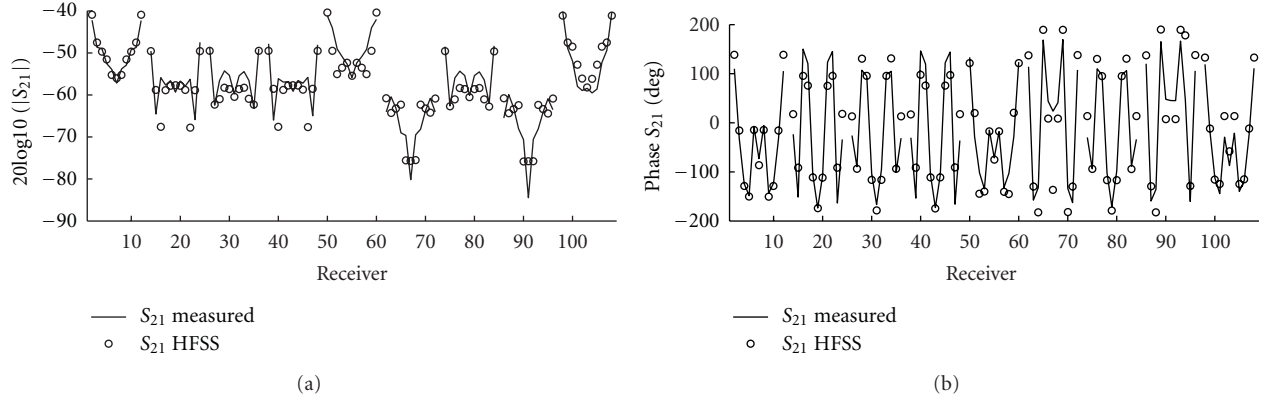


FIGURE 5: Measured and simulated magnitude and phase of incident S_{21} between each of the three transmitting antennas and all receivers. Solid: measured. Dots: HFSS. The groupings from left to right are the eleven receivers of each level (middle, top, and bottom), repeated for the three transmitters (middle, top, and bottom), plotted counterclockwise when viewed from above for a given receiver level. For example, data 38 : 48 are middle receivers and top transmitter. The magnitude and phase agree best for transmitters and receivers on the same level (i.e., data 1 : 11, 50 : 60, and 98 : 108).

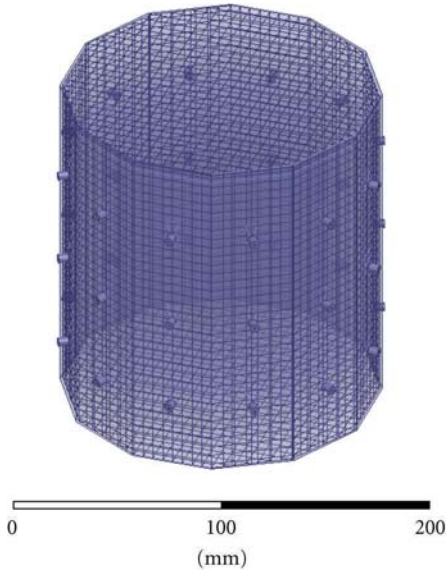


FIGURE 6: HFSS CAD model of the imaging cavity with mesh of unassigned sheets to constrain the adapting meshing of HFSS for field interpolation. Sheets are spaced every 5 mm in each direction.

is presented and the simulation results are compared to those of experiment. We form 3D images of the relative permittivity and conductivity using both HFSS synthetic data and experimental data for simple targets. We also present findings on the sensitivity of image reconstructions to the accuracy of modeling the background electrical properties.

Future work includes continuing the validation of our methodology, experimentally imaging more realistic breast phantoms, designing a hemispherical imaging cavity, investigating practical solutions to modeling the breast-cavity scattering interactions, and developing a clinical imaging system.

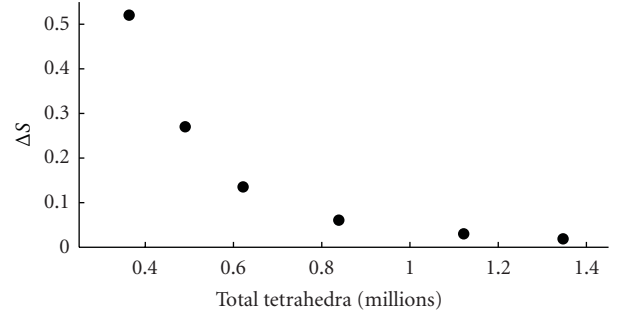


FIGURE 7: HFSS convergence with number of tetrahedra for each adaptive meshing step.

2. Formulation with Source Characterization

2.1. Traditional Volume Integral Equations. The electric field volume integral equation (VIE) for an inhomogeneous distribution of permittivity and conductivity is given by

$$\mathbf{E}(\mathbf{r}) = \mathbf{E}_{\text{inc}}(\mathbf{r}) + k_o^2 \int \overline{\mathbf{G}}(\mathbf{r}, \mathbf{r}') \cdot \left(\delta\epsilon(\mathbf{r}') + \frac{i\delta\sigma(\mathbf{r}')}{\epsilon_b\omega} \right) \mathbf{E}(\mathbf{r}') dV', \quad (1)$$

where $\mathbf{E}(\mathbf{r})$ and $\mathbf{E}_{\text{inc}}(\mathbf{r})$ are the total and incident fields, respectively, and \mathbf{r} is the position vector. The lossless background wave number is given by $k_o^2 = \omega^2\mu_o\epsilon_b$, where the background permittivity is $\epsilon_b = \epsilon_o\epsilon_{rb}$ with relative permittivity ϵ_{rb} . The object contrast functions are defined:

$$\begin{aligned} \epsilon_b\delta\epsilon(\mathbf{r}) &= \epsilon(\mathbf{r}) - \epsilon_b, \\ \delta\sigma(\mathbf{r}) &= \sigma(\mathbf{r}) - \sigma_b, \end{aligned} \quad (2)$$

where σ_b is the background conductivity. The quantity $\delta\epsilon(\mathbf{r})$ is unitless and $\delta\sigma(\mathbf{r})$ is an absolute measure of conductivity with units of Siemens per meter and $\overline{\mathbf{G}}(\mathbf{r}, \mathbf{r}')$ is the background dyadic Green's function.

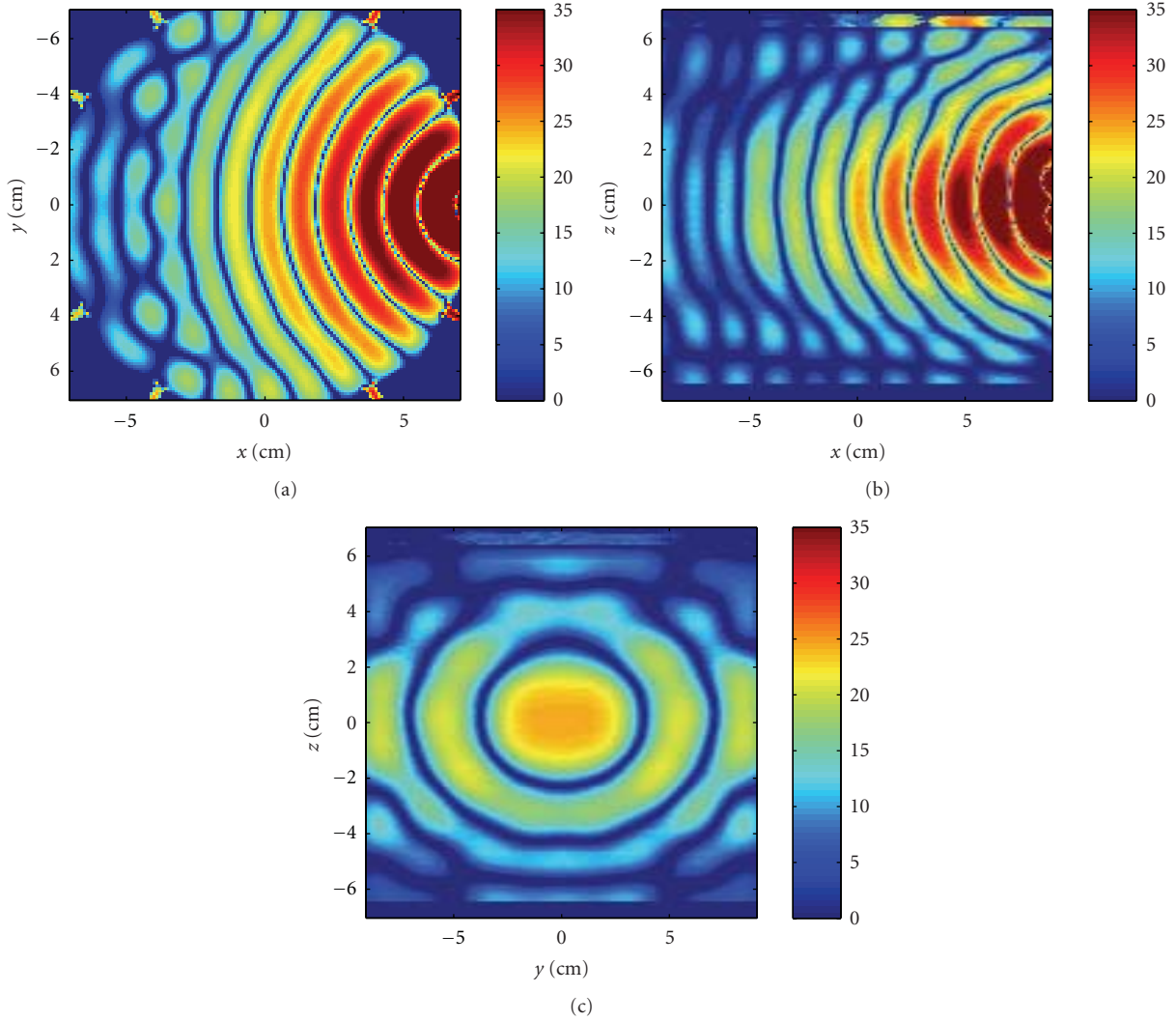


FIGURE 8: Crosscuts through the center of the cavity of the z -component of the incident electric field due to the middle transmitter. The scale is $20\log_{10}(|\text{Re}\{E_{z,\text{inc}}\}|)$ of the unnormalized field. (a) Horizontal x - y , and (b) vertical x - z , and (c) vertical y - z planes.

Defining the scattered field as

$$\mathbf{E}_{\text{sca}}(\mathbf{r}) = \mathbf{E}(\mathbf{r}) - \mathbf{E}_{\text{inc}}(\mathbf{r}) \quad (3)$$

and restricting the observation point \mathbf{r} to points outside the object region in (1), we can write the VIE for the scattered field concisely as

$$\mathbf{E}_{\text{sca}}(\mathbf{r}) = \int \overline{\mathbf{G}}(\mathbf{r}, \mathbf{r}') \cdot \mathbf{O}(\mathbf{r}') \mathbf{E}(\mathbf{r}') dV', \quad (4)$$

where we define the following object function:

$$\mathbf{O}(\mathbf{r}) = k_0^2 \left(\delta\epsilon(\mathbf{r}) + i \frac{\delta\sigma(\mathbf{r})}{\epsilon_b \omega} \right). \quad (5)$$

In the context of inverse scattering, (1) represents the solution to the wave equation in the object domain, while (4) relates the material contrasts to scattered field measurements taken outside the object domain. Depending on the inversion algorithm, these two equations are used in combination to

recover both the contrasts and the total fields. Traditionally, (1) and (4) are used as they are to develop inverse scattering algorithms.

2.2. Integral Equations for Cavity S-Parameter Measurements.

In a previous work [12], we showed that it is possible to transform (1) and (4) so that they are consistent with an S-parameter-based measurement system. We showed that the resulting equations were valid for both free-space and cavity-like geometries and went on to validate the free-space case with an inverse scattering experiment [13]. Here, we will summarize the results for a cavity geometry.

Consider the cavity depicted in Figure 1. An object to be imaged is placed in the middle of the cavity. The cavity is filled with a background material having a permittivity and conductivity of ϵ_b and σ_b , respectively. The cavity is lined with radiating apertures, which could be antennas. Each aperture has its own feeding transmission line and S-parameter reference plane.

We define the normalized incident and total fields throughout the cavity due to a transmitting aperture as

$$\begin{aligned} \mathbf{e}_{\text{inc}}(\mathbf{r}) &= \frac{\mathbf{E}_{\text{inc}}(\mathbf{r})}{a_o}, \\ \mathbf{e}(\mathbf{r}) &= \frac{\mathbf{E}(\mathbf{r})}{a_o}, \end{aligned} \quad (6)$$

where a_o is the transmit voltage measured with respect to the S-parameter reference plane. The normalized incident field captures all background multiple scattering not present between the object and the cavity.

Let transmitting apertures be indexed with i and those receiving indexed with j . We can write (1) in terms of the normalized incident and total fields produced by a transmitter by dividing both sides by $a_{o,i}$:

$$\mathbf{e}_i(\mathbf{r}) = \mathbf{e}_{\text{inc},i}(\mathbf{r}) + \int \bar{\mathbf{G}}(\mathbf{r}, \mathbf{r}') \cdot \mathbf{O}(\mathbf{r}') \mathbf{e}_i(\mathbf{r}') dV'. \quad (7)$$

This is the integral equation we will use to represent the forward scattering solution. The normalized total field is the field solution in the object domain and, with the appropriate dyadic Green's function for the cavity, includes the scattering interactions between the object and the cavity.

In [12] we showed how to transform the scattered field volume integral equation given by (4) into one that predicts S-parameters. This new integral operator allows us to directly compare model predictions to measurements in the inversion algorithm. The two-port scattered field S-parameter, $S_{ji,\text{sca}}$, measured between the transmission line reference planes of two apertures in the presence of an object is given by

$$S_{ji,\text{sca}} = \int \mathbf{g}_j(\mathbf{r}') \cdot \mathbf{O}(\mathbf{r}') \mathbf{e}_i(\mathbf{r}') dV', \quad (8)$$

where $\mathbf{e}_i(\mathbf{r})$ is the normalized total object field produced by the transmitter and $\mathbf{g}_j(\mathbf{r})$ is the vector Green's function kernel for the receiver. It was also shown in [12] by reciprocity that $\mathbf{g}_j(\mathbf{r})$ is related to the normalized incident field of the receiver as

$$\mathbf{g}_j(\mathbf{r}) = -\frac{Z_o^j}{2i\omega\mu} \mathbf{e}_{\text{inc},j}(\mathbf{r}), \quad (9)$$

where ω is the operating frequency in radians, μ is the background permeability, and Z_o^j is the characteristic impedance of the receiver transmission line.

Equations (7) and (8) are the integral equations we will use for the inverse scattering algorithm. They consistently link the electric field volume integral equations to an S-parameter measurement system. We need only to determine the normalized incident fields in the object domain and the background dyadic Green's function; no other step is required to characterize the system, except to calibrate the transmission line reference planes.

Lastly, in experiment, we never measure scattered field S-parameters directly but obtain them by subtracting the S-parameters for the total and incident fields:

$$S_{ji,\text{sca}} = S_{ji,\text{tot}} - S_{ji,\text{inc}}, \quad (10)$$

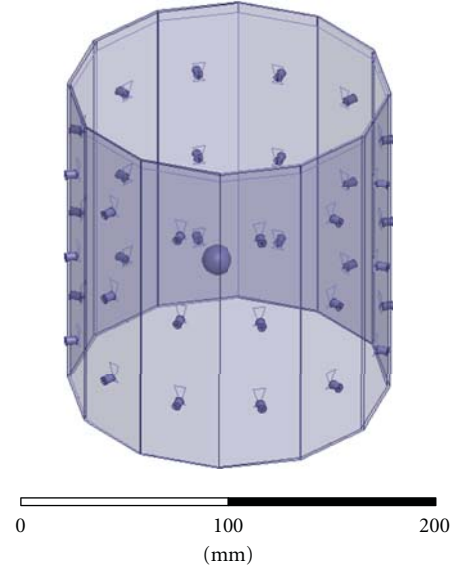


FIGURE 9: HFSS model of a simple sphere used to generate synthetic scattered field S-parameters.

where $S_{ji,\text{inc}}$ is measured in the absence of the object and $S_{ji,\text{tot}}$ is measured in the presence of the object.

2.3. Determining $\mathbf{e}_{\text{inc}}(\mathbf{r})$ and $\bar{\mathbf{G}}(\mathbf{r}, \mathbf{r}')$. The normalized incident field is required in both (7) and (9) and is required for every aperture. We can either measure it experimentally or estimate it with simulation. Experimentally mapping the fields requires proper probe calibration and has the added complication in a cavity that the probe-wall interactions cannot be neglected. An alternative approach, the one we adopt for this paper, is to estimate the normalized incident field with simulation. This can be done provided that we have a computer aided design (CAD) model that accurately represents the cavity. It is also possible in simulation to model the feeding transmission lines and line voltages in order to assign an S-parameter reference plane that is identical to the reference plane used by a vector network analyzer for the physical measurement. We will show how we use Ansoft HFSS to accomplish this.

As stated in the introduction, determining the background dyadic Green's function is nontrivial, especially for arbitrary cavity geometries. Despite this, for the immediate investigation, we use the free-space dyadic Green's function under the condition that the background medium is extremely lossy. Though not strictly correct, this approximation is convenient provided the multiple scattering throughout the cavity is limited by the background loss. It also allows us, for the time being, to retain use of an FFT-based volumetric forward solver. We give examples later evaluating this assertion. There are several approaches for determining or approximating the background dyadic Green's function for arbitrary geometries, which we discuss in The Appendix and leave for future work.

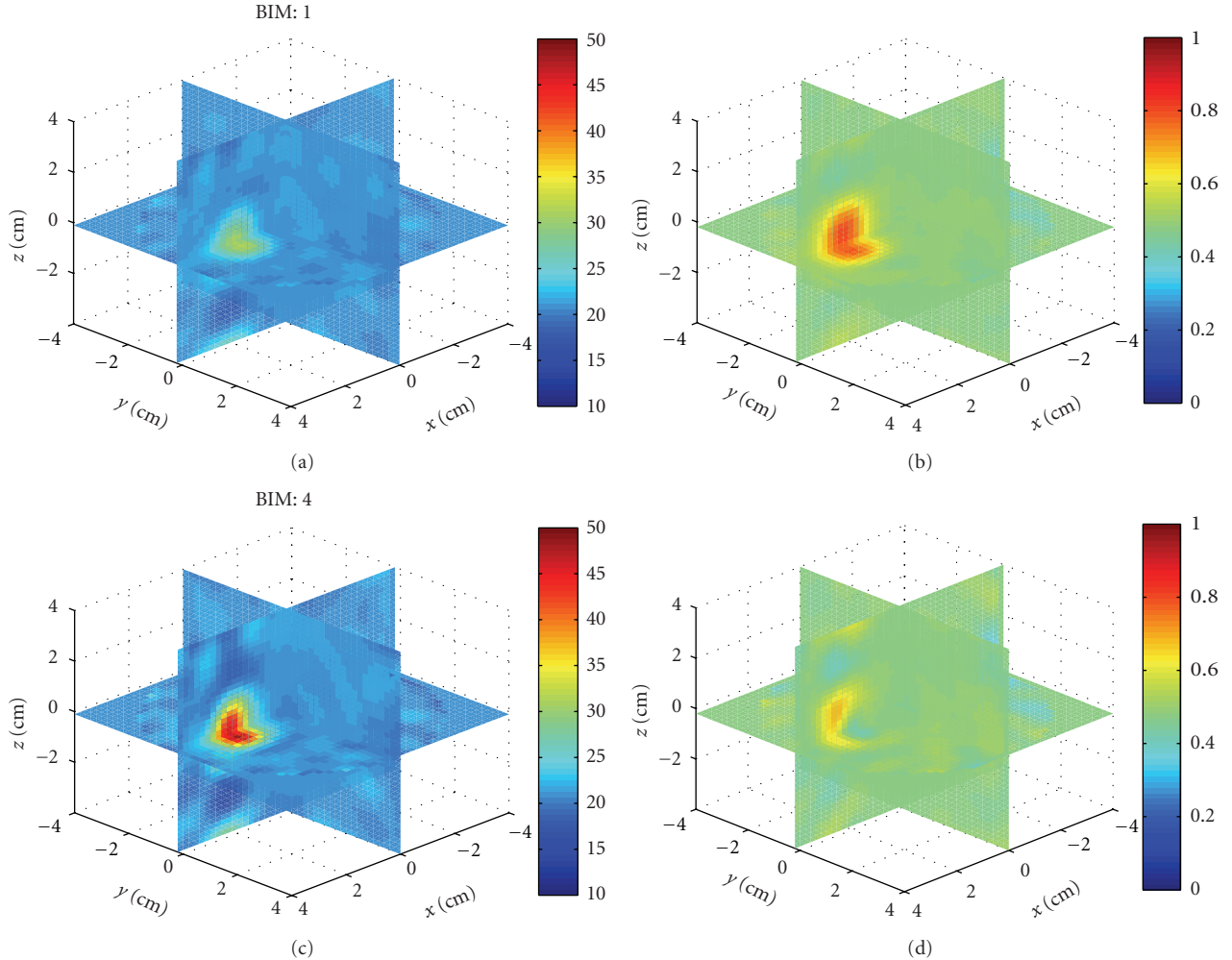


FIGURE 10: Reconstructions of a single sphere $(\epsilon_r, \sigma) = (40, 1)$ located at $(x, y, z) = (0, 0, 2)$ cm of Example 1. (a) and (c) and (b) and (d) Relative permittivity and conductivity, respectively. (a) and (b) is the Born approximation. (c) and (d) is BIM iteration 4. Here, iterations help retrieve the relative permittivity in (c), but the Born approximation yielded better conductivity in (b).

3. Born Iterative Method

The imaging algorithm we use is the Born iterative method (BIM) [16–19]. The BIM successively linearizes the nonlinear problem by alternating estimates of the contrasts and the object fields according to the following algorithm.

- (1) Assume the object fields are the incident fields (Born approximation).
- (2) Given the measured scattered field data, estimate the contrasts with the current object fields by minimizing a suitable cost function.
- (3) Run the forward solver with current contrasts. Store the updated object field.
- (4) Repeat step 2 until convergence.

This algorithm and its implementation are described in detail in our previous work [13], where we successfully formed images of dielectric constant for plastic objects in a free-space experiment. This was done using the same BIM

and the integral equations for S -parameters given above using antennas characterized with HFSS.

We use the multivariate covariance-based cost function of [15]. The Gaussian interpretation of this cost function allows us to experimentally justify the values we use to regularize it by our *a priori* knowledge of the experimental noise and range of contrast values. For the forward solver, because we use the lossy free-space dyadic Green's function to model the internal scattering, we use the BCGFFT [20–22], which we have validated with analytic solutions. In the examples that follow, we found that 4 BIM iterations were repeatedly sufficient for the data residual and object to converge.

4. Breast Imaging System Prototype

The breast imaging system prototype we built is shown in Figure 2. The imaging structure is a cavity, shown in Figure 3, that was created by soldering twelve vertical panels of microwave substrate together and soldering the collection to a conducting base. Opposite panels are separated by 15 cm,

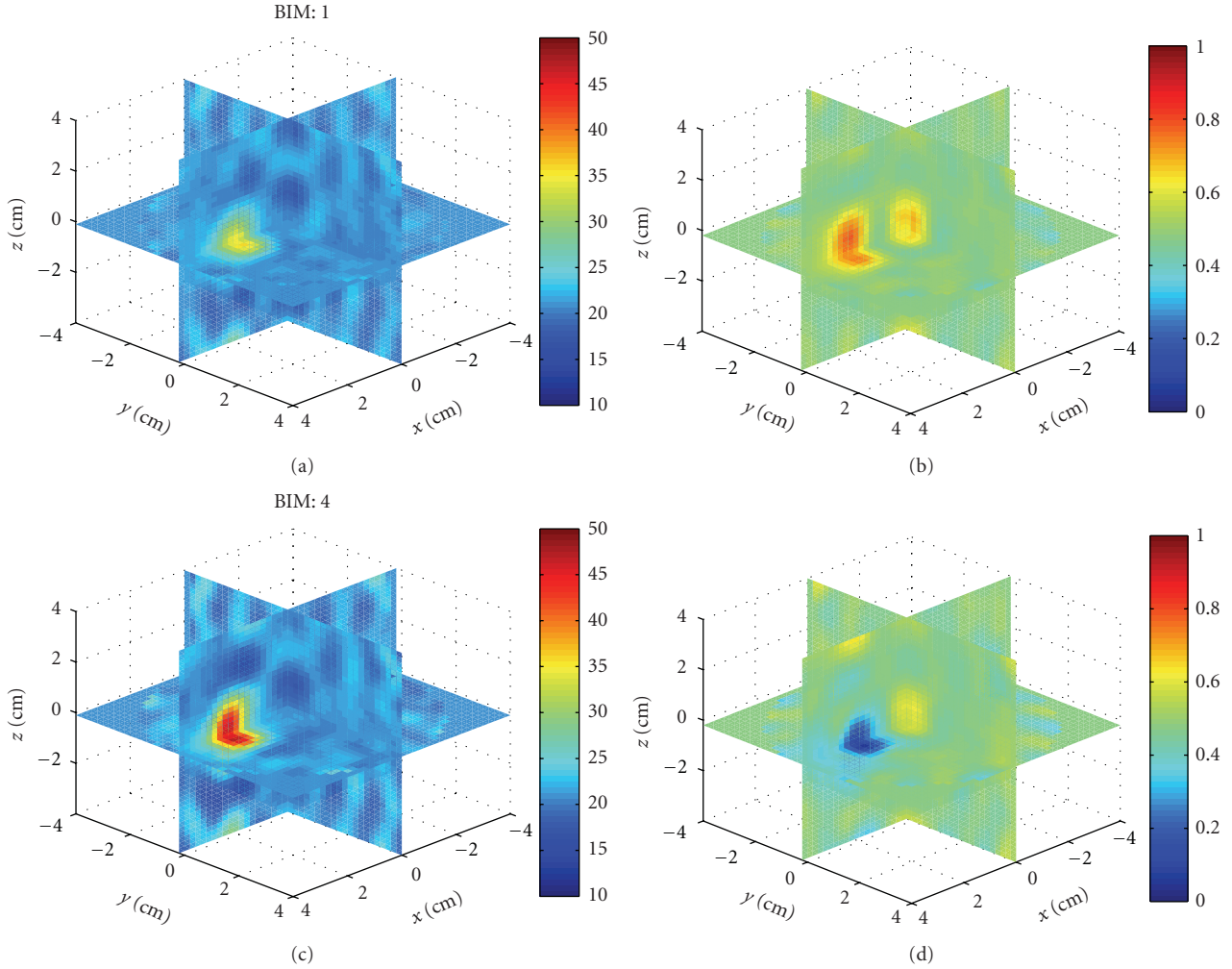


FIGURE 11: Reconstructions of a single sphere $(\epsilon_r, \sigma) = (40, 0)$ located at $(x, y, z) = (0, 0, 2)$ cm of Example 1. Born iterations helped retrieve the relative permittivity in (c) and are essential in recovering the conductivity in (d).

and the cavity is 17 cm long. Three antennas are printed on each panel for a total of 36 antennas. In the prototype, the three antennas of one panel are used as transmitters, while all other antennas are receivers. The transmit antennas are switched with a Dowkey SP6T electromechanical switch. The receivers are connected through an SP33T solid-state switching matrix that was designed and assembled in-house. 2-port S-parameter measurements were taken with an Agilent PNA-5230A vector network analyzer (VNA) at 2.75 GHz between each transmitter and any one receiver. This frequency was chosen as a compromise between resolution and switch performance, which rolls off above 3 GHz. A rotator was mounted above the cavity and aligned in the center of the cavity. Test objects are suspended with fishline and rotated to provide multiple transmitter views.

4.1. Liquid Coupling Medium. We expect breast tissue to have a relative permittivity between 10 and 60 [23]. Without a matching medium, much of the incident power would be reflected at the breast/air interface reducing the sensitivity of the system [24]. Also, the contrast ratio between the object

and the background would be too high for the BIM inverse scattering algorithm to converge.

The matching medium we use is an oil/water emulsion developed in a previous work [25]. This fluid is designed to balance the high permittivity and high conductivity of water with the low permittivity and low conductivity of oil, in order to achieve a fluid with moderate permittivity while limiting loss as much as possible. We are also able to tune the microwave properties of this emulsion by adjusting the oil/water ratio. We aimed for a relative permittivity value around 20, which brings the maximum permittivity contrast to about 3:1. The fluid mixture we used was 65%/35% oil/water.

The electrical properties of the fluid were measured using the Agilent 85070E slim form dielectric probe. The measured properties at 2.75 GHz were $(\epsilon_r, \sigma) = (19, 0.34)$. Relative permittivity is unitless; the units of conductivity used throughout the paper are Siemens/m. When using this value in the numerical model (presented below) the magnitude of cross-cavity S_{21} required some adjustment when compared to the measurements. We obtained the best

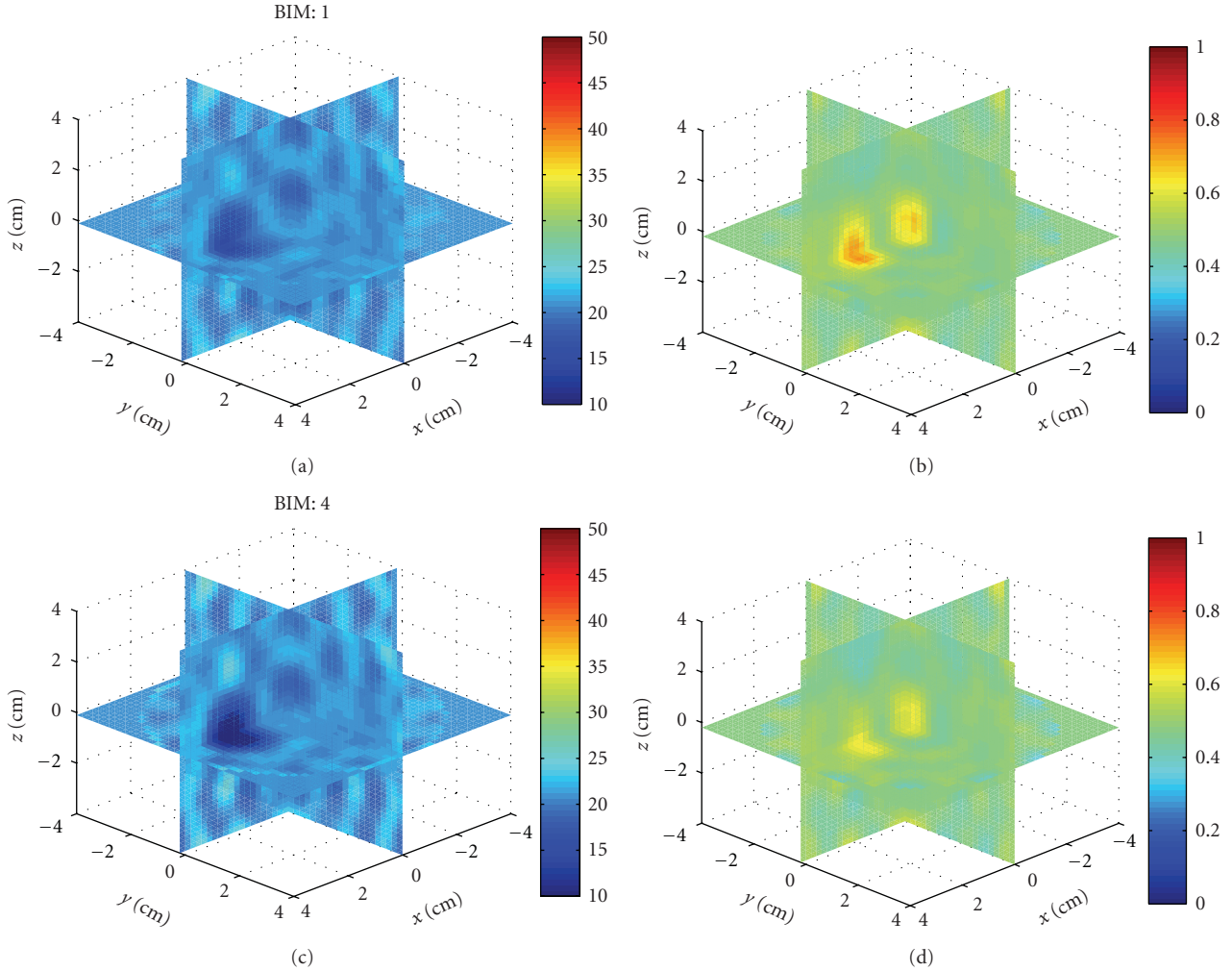


FIGURE 12: Reconstructions of a single sphere $(\epsilon_r, \sigma) = (10, 1)$ located at $(x, y, z) = (0, 0, 2 \text{ cm})$ of Example 1. Born iterations helped the recovery of the low permittivity in (c), but at the expense of the correct conductivity value which was better with the Born approximation in (b).

model agreement for $(\epsilon_r, \sigma) = (21, 0.475)$, which are the values we use throughout the paper. We suspect that the probe area may be too small to accurately measure the bulk properties of the mixture, but the fluid otherwise appears homogeneous for propagation at 2.75 GHz. We are still investigating this effect.

When taking data, we fill the cavity with the coupling fluid to a height that is 0.5 cm below the top edge. This fluid height is accounted for in the numerical model. Any fluid displacement from adding or removing test objects is compensated in order to keep the height constant. We have also found the emulsion to be stable over the course of measurements, which we confirmed by comparing transmission measurements before and after we take data for imaging.

4.2. Antenna Design. The antennas are bow-tie patch antennas, similar to the antennas in [6, 26]. They are of single frequency and vertical polarization. The bow-tie antenna was chosen to give more degrees of freedom to help

impedance match the antenna to the coupling fluid. The vertical polarization was chosen for best illumination of the object and other antennas in the cylindrical geometry. The substrate material is Rogers RO3210, with 50 mil thickness and reported dielectric constant of 10.2. The antennas were originally designed to operate at 2.8 GHz in the cavity filled with a fluid with $(\epsilon_r, \sigma) = (24, 0.34)$; however, after iterating, we found best performance at 2.75 GHz in a fluid of $(\epsilon_r, \sigma) = (21, 0.475)$.

4.3. System Parameters. In determining the system noise and isolation requirements, the minimum expected signal determines the required noise level, and the maximum relative magnitude between signals on adjacent channels determines the required switch path isolation. From previous numerical studies of cavity-like breast imaging with similar emulsion properties [27], we expect the scattered field S_{21} magnitude of small inclusions to be in the range from -100 to -50 dB, and so the relative signal strength between adjacent antennas could differ by as much as -50 dB. This

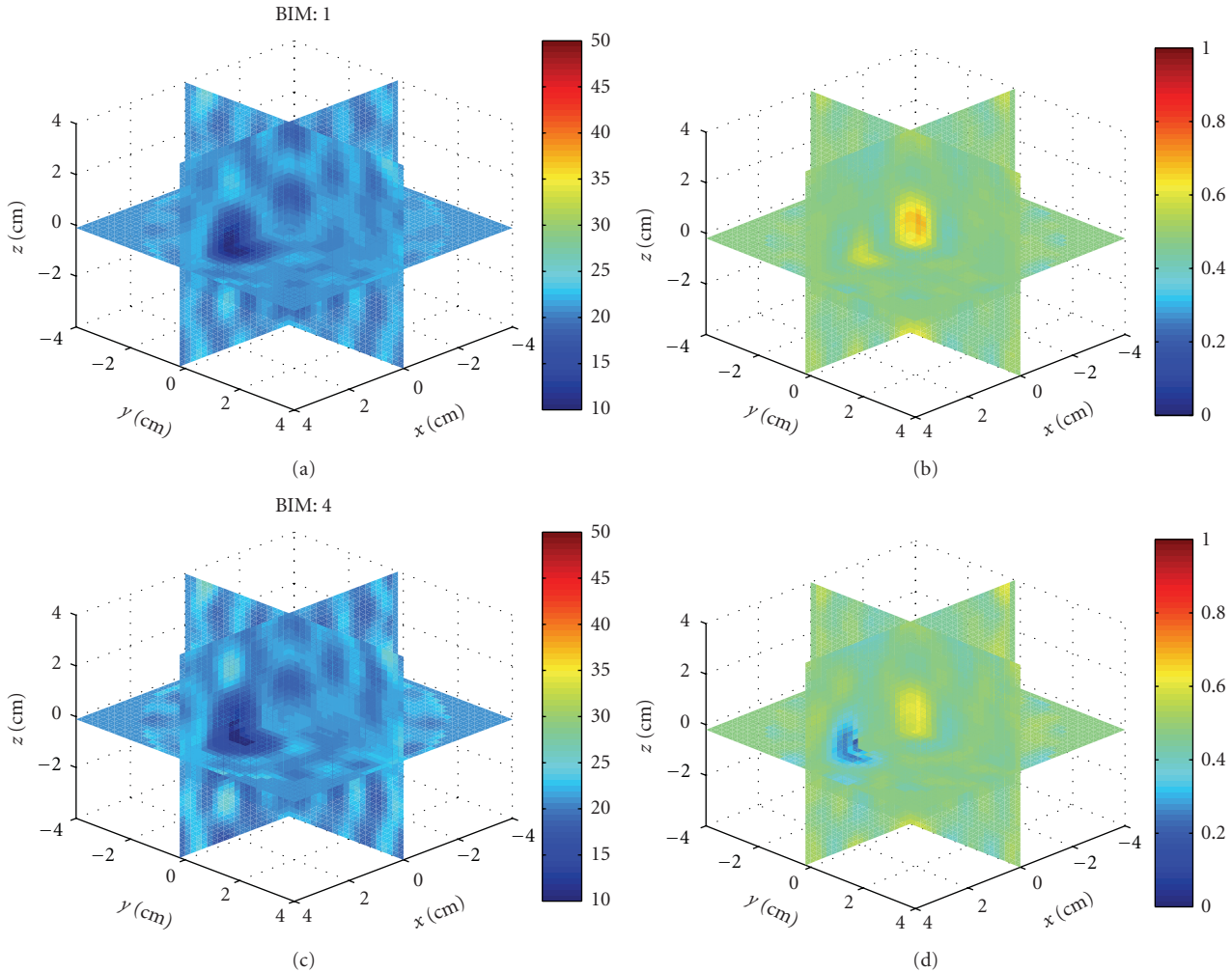


FIGURE 13: Reconstructions of a single sphere $(\epsilon_r, \sigma) = (40, 0)$ located at $(x, y, z) = (0, 0, 2 \text{ cm})$ of Example 1. Born iterations helped bring out the proper conductivity value in (d).

means that the noise of our system must be less than -100 dB , which is achievable by our VNA with averaging and an IF bandwidth of 100 kHz or less. Also, the switching matrix paths must be isolated by at least -50 dB .

4.4. Switching Matrix. The receivers were connected through a SP33T solid-state switching matrix that was designed and assembled in-house. The matrix consists of two custom SP16T solid-state switching matrices and a cascaded pair of Minicircuits SPDT switches. Each SP16T switch is composed of two layers of SP4T Hittite HMC241QS16 nonreflective switches, which are buffered at the output by a third layer consisting of a single SPDT Hittite HMC284MS8GE on each path. The buffer layer was added to increase interpath isolation. The switch is controlled with an embedded digital board and computer parallel port. The operating band of the switching matrix is between $0.1\text{--}3 \text{ GHz}$. The overall loss of a path through the SP33T matrix is no worse than 8 dB across the band. We measured the switch path isolation to be better than -55 dB between $1\text{--}3 \text{ GHz}$, which meets the criteria above.

By separating the transmitter and receiver switching, the isolation between these two operation modes is dictated by the network analyzer and the cables. In more realistic systems, where the antennas are dual mode and so object rotation is not necessary, the isolation requirements are more stringent, because the transmit amplitude will be orders of magnitude larger than the scattered field.

4.5. VNA Calibration. Two-port VNA calibrations were accomplished between each transmitter and each receiver. The S -parameter reference planes were calibrated to the points where the cables connect to the antenna. These reference planes are identical to those in the HFSS CAD model (presented below). While calibrating, we left the unused ports open with the rationale that the one-way switch isolation of -55 dB provided sufficient matching to the open ports. Short-open-load measurements for a 1-port calibration were taken for each antenna. Next, we measured the through path between the transmitter and each receiver using a connector. In software, we combined the 1-port and through measurements to accomplish a 2-port

short-open-load-through (SOLT) calibration with arbitrary through between each transmitter and receiver for a total of 99 separate 2-port calibrations. The calibration for a particular transmitter/receiver pair is recalled in the VNA before taking data.

5. Numerical Model

We use Ansoft HFSS to numerically model the cavity, similar to [27]. We use it several ways. First, we model the feeding transmission lines in order to assign S -parameter reference planes that are identical in both simulation and experiment. Second, we estimate the normalized incident fields due to the transmitters throughout the cavity for use in (7) and (9), where the normalized incident fields now include all background multiple scattering not present between the object and the cavity. Also, we use the model to generate synthetic scattered field S -parameters of numerical targets in order to study the performance of the inverse scattering algorithm given the source geometry and system parameters.

Figure 4 shows the HFSS CAD model of the 12-sided cavity. The model includes the panel thickness and dielectric constant, bottom conductor, probe feed, coupling fluid properties, and height of the fluid. Same as in the experiment, the cavity is filled to a height that is 0.5 cm below the top (seen as the line below the top edge of the cavity). The remaining 0.5 cm is air with a radiating boundary condition. The outer boundary of the cavity is PEC.

Next we compare measured and simulated incident S -parameters in order to access the accuracy of the model. Figure 5 shows the magnitude and phase, respectively, of the measured and simulated incident S -parameters between each transmitter and all receivers. The magnitude and phase agree best when the receivers are on the same level as the transmitter. In this case, the magnitude agrees generally to within 3 dB, for all three levels, and the phase agrees to within 30 degrees, which is approximately $\lambda/10$, a common metric for many microwave systems. For measurements between antenna levels in Figure 5, the agreement is not as good in magnitude, but the phase error remains similar to the previous cases. This also shows that the one-way path loss across the cavity is approximately -50 dB, so we expect any multiple scattering to be localized. This partially justifies our approximation of the cavity dyadic Green's function with the lossy free-space dyadic Green's function.

When computing the incident fields, the center of the cavity was meshed with a coarse Cartesian grid of sparse unassigned sheets, shown in Figure 6. Sheets are spaced every 5 mm in the x , y , and z directions. The spacing is approximately $\lambda/5$ at 2.75 GHz in the fluid with relative permittivity of 21. We have found that this helps constrain the adaptive meshing of HFSS when we obtain the incident fields by interpolating the FEM mesh onto a fine Cartesian grid, [12].

When simulating the structure, with or without scattering targets, we use a convergence criterion of $\Delta S = 0.02$ which is reached in 7 adaptive meshing iterations. A typical simulation completed with approximately 1.4 million tetrahedra using 23.5 GBytes of RAM and swap

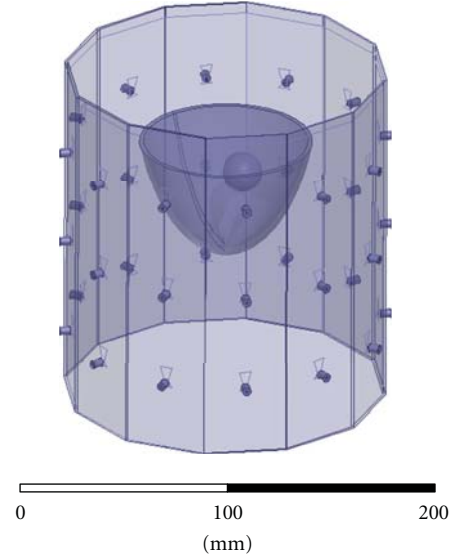


FIGURE 14: HFSS CAD numerical breast phantom of Example 2. The inclusion is 2 cm in diameter with relative permittivity and conductivity contrasts of 2 : 1. The skin layer is 2 mm thick.

space to obtain a full 36×36 S -matrix. Simulations took approximately 25 hours on a dual E5504 Intel Xeon (2x Quad Core) desktop with 24 GBytes of RAM. Figure 7 shows a typical convergence rate as a function of tetrahedra.

We obtained the incident fields for only the three transmitters. The incident fields for the receivers were obtained through rotation, where we assume the 12 panels of the experimental cavity are identical. The incident fields were sampled on a $17 \text{ cm} \times 17 \text{ cm} \times 18 \text{ cm}$ grid with 1 mm spacing, which is $\lambda/24$ at 2.75 GHz in a fluid with relative permittivity 21. In simulation, the average transmit power was 1 Watt, so, from transmission line analysis, the line voltage is given by

$$a_o = \sqrt{2P_{ave}Z_o} = \sqrt{2Z_o}, \quad (11)$$

which is used in (6). The phase of a_o is zero because the S -parameter reference planes of the HFSS model and the experimental cavity were identical.

Figure 8 shows three crosscuts of the z -component of the incident electric field through the center of the cavity for the center transmitter in a fluid of relative permittivity of 21 and conductivity 0.475 at 2.75 GHz. The coordinate origin is at the center of the cavity, and the transmitter is located on the positive x axis. The effects of the cavity on the incident field are seen in Figure 7, where the fields are guided by the walls of the cavity; the coaxial feeds are also visible; the fluid-air interface is visible in Figures 8(b) and 8(c).

6. Image Reconstructions

6.1. Synthetic Data. We first test the BIM and numerical characterization using synthetic data from HFSS. This is to assess the performance of the algorithm and source geometry under near ideal circumstances. We simulated the

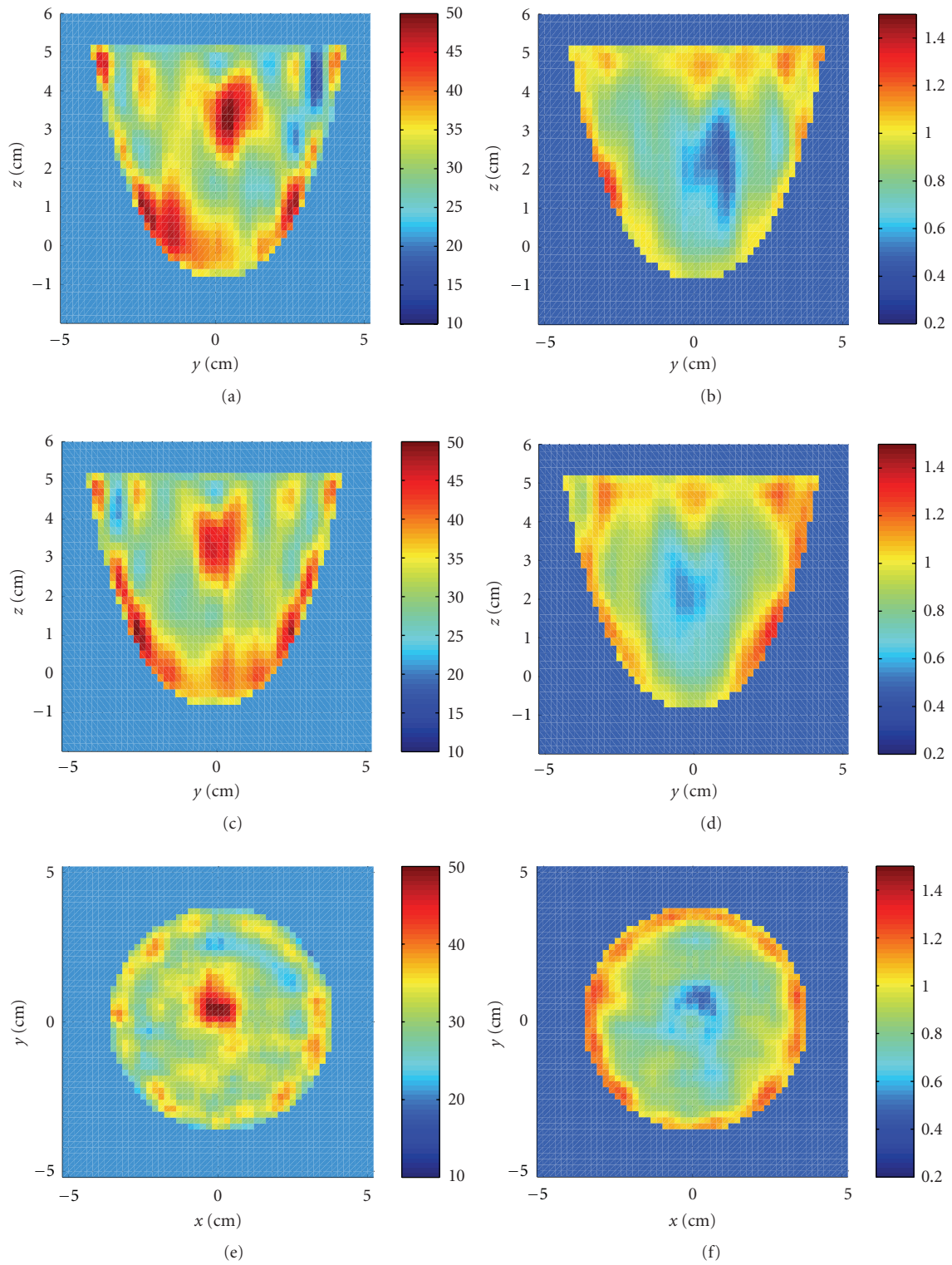


FIGURE 15: Reconstructions of the HFSS numerical breast phantom in Example 2 after four iterations. (a), (c), and (e) and (b), (d), and (f) Relative permittivity and conductivity, respectively. (a) and (b), (c) and (d), and (e) and (f) Cuts at $x = 0$ cm, $y = 0$ cm, and $z = 3$ cm. The relative permittivity of the inclusion is recovered, but both images contain many artifacts.

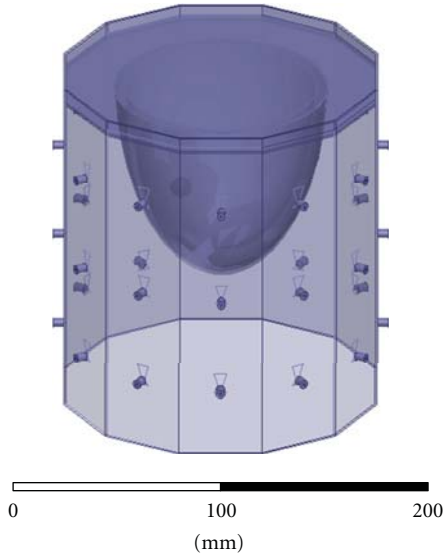


FIGURE 16: HFSS CAD numerical breast phantom with skin layer, fat layer, glandular tissue, and chest wall of Example 3. The inclusion is 1 cm in diameter with relative permittivity and conductivity contrasts of 2 : 1.

scattered field S -parameters of simple numerical objects and use these data as measurements in the inversion algorithm. HFSS scattered field data includes any multiple scattering between the object and the cavity. The background medium had a relative permittivity of 21 and a conductivity of 0.475 Siemens/m. The incident fields were computed with these background parameters and used in volume integral equations.

Example 1. We first used HFSS to simulate the scattered field S -parameters for a single 1.5 cm diameter sphere located at $(x, y, z) = (0, 0, 2 \text{ cm})$ with four combinations of relative permittivity and conductivity: (40, 1), (40, 0), (10, 1), and (10, 0). The HFSS model is shown in Figure 9. Figures 10, 11, 12, and 13 show images of the first and fourth BIM iterations for each object. As shown, in some cases, the BIM steps were essential in recovering the correct property values of the sphere; in other cases, the relative permittivity was improved at the expense of the conductivity value. These images show that the source geometry and numerical characterization are adequate for the retrieval of some object property combinations, but not others. This fact, together with the visible artifacts, suggests that the images could be improved with a denser source geometry.

Example 2. Next we imaged a more anatomical numerical breast phantom. The numerical phantom is shown in Figure 14. The breast is 9 cm at the widest point and 6 cm deep. The outer layer is a 2 mm thick skin layer, and the inclusion is 2 cm in diameter. The dielectric properties of the skin layer, glandular tissue, and inclusion, respectively, are $(\epsilon_r, \sigma) = \{(45, 1.59), (21, 0.475), \text{ and } (42, 0.8)\}$, which were obtained from [28]. We assume we know the volume region of the breast, so we mask that volume excluding all other

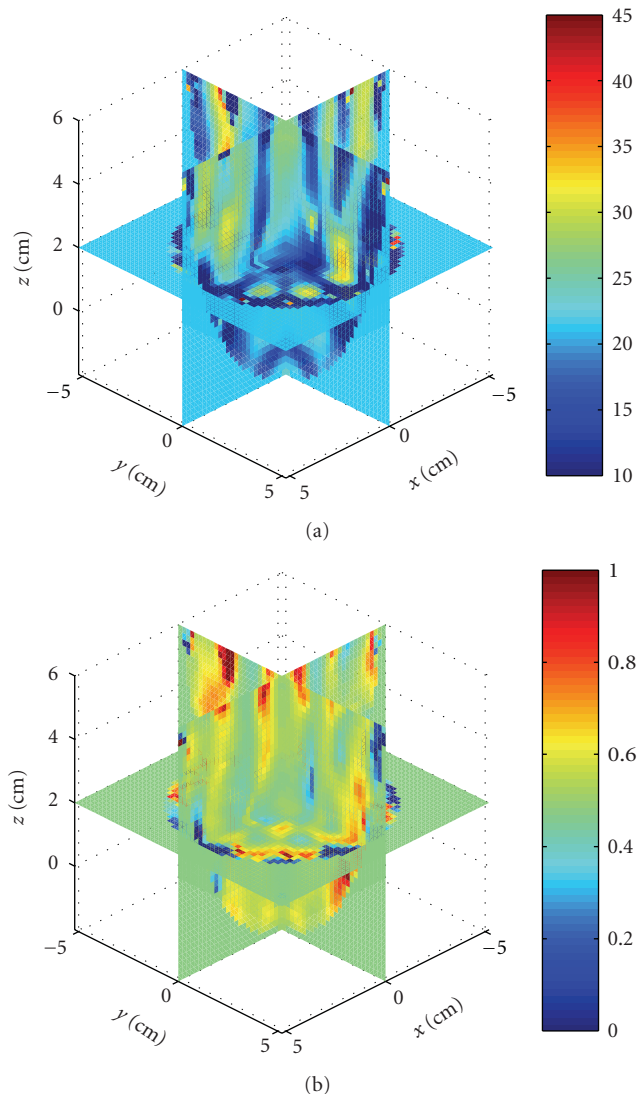


FIGURE 17: Reconstructions of the HFSS numerical breast phantom, which includes the chest wall of Example 3. (a) and (b) Relative permittivity and conductivity, respectively. The object could not be reconstructed.

points during inversion. Figure 15 shows the reconstructed relative permittivity and conductivity after 4 iterations for three cuts. The relative permittivity of the inclusion is recovered, but the conductivity of the inclusion is not recovered. The skin layer is also visible in the conductivity images. Both sets of images suffer from artifacts, which is due to the sparse spatial sampling of the antennas and indicates that the images can be improved with more angular views.

Example 3. To push the algorithm, we imaged a phantom that included a skin layer, fat layer, glandular tissue, chest wall, and inclusion, with relative permittivity and conductivity, respectively, of (45, 1.6), (5.1, 0.16), (21, 0.475), (52, 2.0), and (40, 1.0). The HFSS model is shown in Figure 16. The reconstructions are shown in Figure 17. In this case the algorithm failed to recover the contrasts. This suggests that

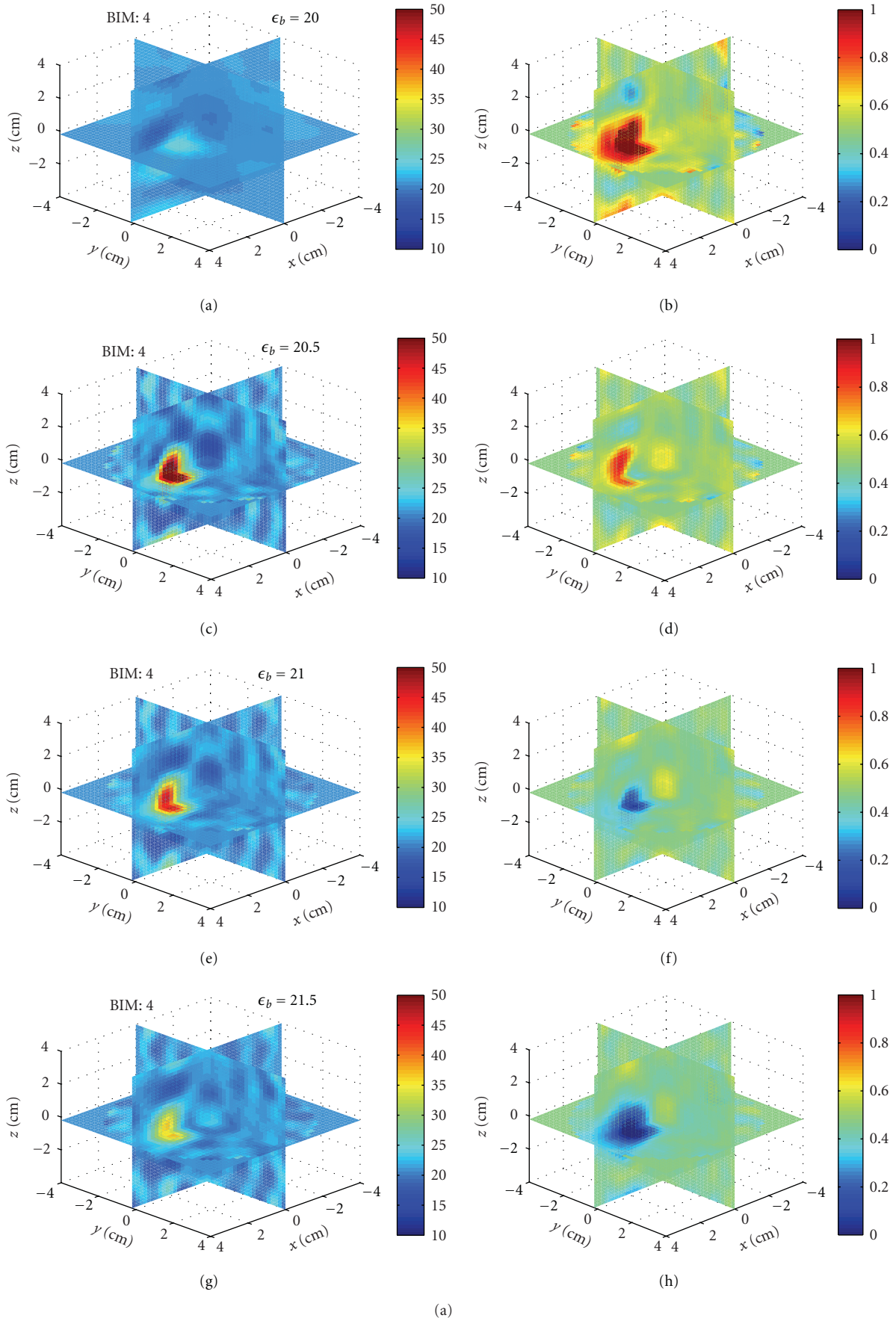


FIGURE 18: Continued.

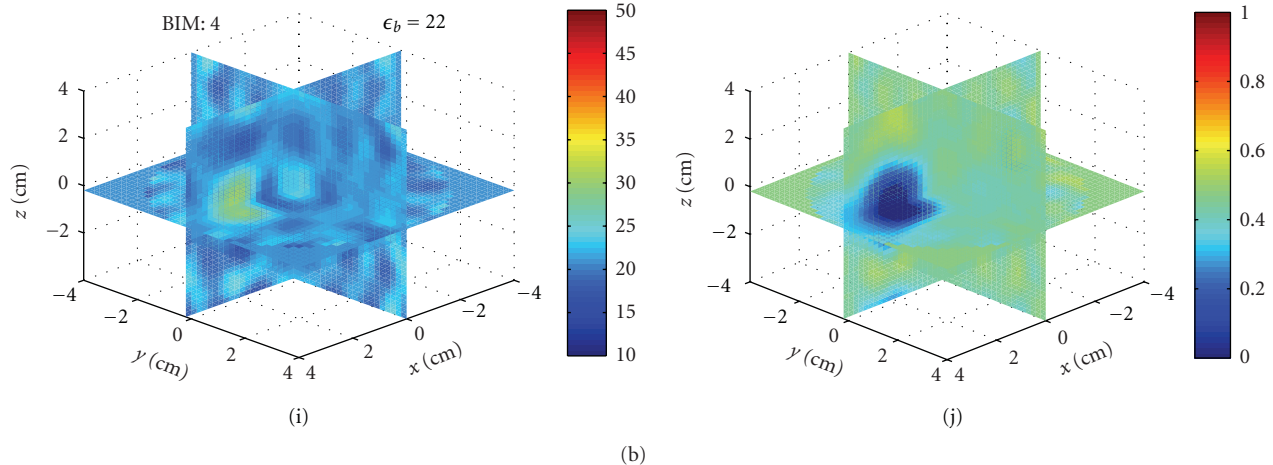


FIGURE 18: Sensitivity of image reconstructions to background permittivity for Example 4. (a), (c), (e), (g), and (i) and (b), (d), (f), (h), and (j) Relative permittivity and conductivity, respectively. The scattered field data was generated in HFSS in a background of (21, 0.475). The reconstructions are done with assumed background relative permittivities of 20, 20.5, 21, 21.5, 22 for (a) and (b), (c) and (d), (e) and (f), (g) and (h) and (i) and (j), respectively. The recovered contrasts of the sphere oscillate about the background.

(1) the object is too different from the background for the BIM to converge, (2) object-cavity interactions are too strong to use the free-space dyadic Green's function, or (3) images cannot be constructed if the chest wall is not modeled, meaning that it is necessary to model the chest wall for the incident fields and the dyadic Green's function.

Example 4. Finally, we studied the effects of different background permittivities when forming images. This represents a case in experiment where the measurements are taken in a fluid with some set of properties, but the fluid properties we use in the model are slightly off. We formed images using HFSS scattered field data of the sphere with $(\epsilon_r, \sigma) = (40, 0)$ in a background of $(\epsilon_b, \sigma) = (21, 0.475)$, but where we use incident fields from five different background permittivities: {20, 20.5, 21 (again), 21.5, 22} and the same conductivity.

Figure 18 shows 3D crosscuts at the fourth BIM iteration for all five backgrounds. Figures 18(e) and 18(f) are the correct images. Notice that an error in the background permittivity of 1, or 5%, is enough for the reconstructed object contrast to oscillate, demonstrating that reconstructions are very sensitive to our knowledge of the background properties.

6.2. Experimental Data. At this time, only simple plastic objects have been imaged with the experimental system; however, future work includes imaging more realistic breast phantoms. Among the test objects, we show the results here for several acrylic spheres. The objects were suspended from a platform and rotated to 12 positions in 30 degree increments. Scattered field S-parameter measurements from each position were combined to yield a full 36×36 S-parameter matrix, which was used in the inverse scattering algorithm.

Experiment 1. We imaged a single acrylic sphere, shown in Figure 19. The diameter of the sphere was 2.54 cm, with

properties $(\epsilon_r, \sigma) = (2.7, 0)$. The sphere was located at approximately $(x, y, z) = (1.5 \text{ cm}, 1.5 \text{ cm}, 0)$. Figure 20 shows the reconstructions after 4 iterations of the x - y plane. The inversion domain is masked so that only a cylindrical region containing the rotated object is imaged. We also imaged two acrylic spheres, shown in Figure 19. Figure 21 shows the reconstructions after 4 iterations. In both cases, the relative permittivity is recovered quite well, and the conductivity contrast is correctly valued but the shape is incorrect. There are also many artifacts present. Given that the imaging algorithm could recover the single sphere using HFSS data, we can attribute these discrepancies to differences between the experiment and the model, such as knowledge in the coupling medium properties, substrate properties, VNA calibration, cavity size measurements, or object motion.

Experiment 2. Finally, while the primary discussions in this paper concern a cavity having antennas that operate at 2.75 GHz, we also built a lower frequency cavity where the antennas operate at 915 MHz. This cavity was numerically characterized using the same methods, but the background fluid properties were $(\epsilon_r, \sigma) = (23, 0.1)$. Figure 22 shows the cavity with three acrylic spheres. Two spheres are located in the x - y plane, while the third is positioned at approximately $(x, y, z) = (4 \text{ cm}, -3 \text{ cm}, 5 \text{ cm})$. We imaged the relative permittivity and conductivity, and the results after 4 iterations are shown in Figure 23. The shape and properties of the two in-plane spheres are well recovered. The third sphere is also detected but cut off at the upper left of the imaging domain. Artifacts are also present, but this example better demonstrates that the numerical characterization, BIM, and free-space Green's function are capable of recovering objects in this cavity and source geometry. It should be noted that images formed with data at 915 MHz are less susceptible to modeling errors because the cavity and objects are electrically smaller, but the resolution is reduced.

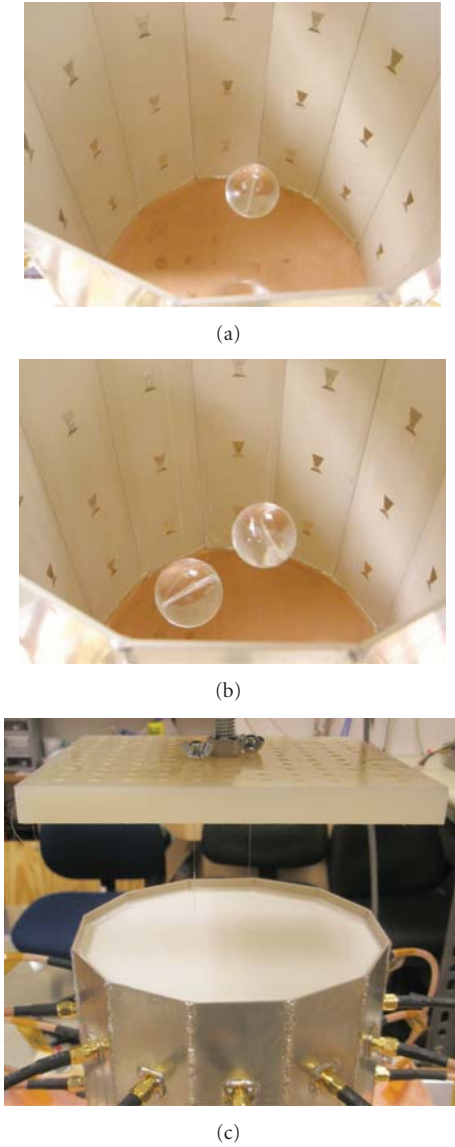


FIGURE 19: Test objects and coupling fluid for Experiment 1. (a) Single suspended acrylic sphere. (b) Two acrylic spheres. (c) Cavity filled with the coupling medium. Objects are suspended and rotated from the nylon platform.

6.3. *Discussion.* Overall, the imaging algorithm, numerical characterization, and experiment worked with some success, and there are several areas for continued investigation.

First, Examples 1 and 2, and also Experiments 1 and 2, validate the technique described in this paper showing that the numerical characterization of the cavity incident fields and the use of the vector Green’s function formulation linking the incident fields to the inverse scattering algorithm can be used to successfully form images in a cavity geometry. Examples 1 and 2 demonstrate the consistency of the method using synthetic scattered field S-parameter data. Experiments 1 and 2 show that the characterization and experiment agreed enough for the BIM to recover the location and permittivity of the test objects. More realistic phantoms

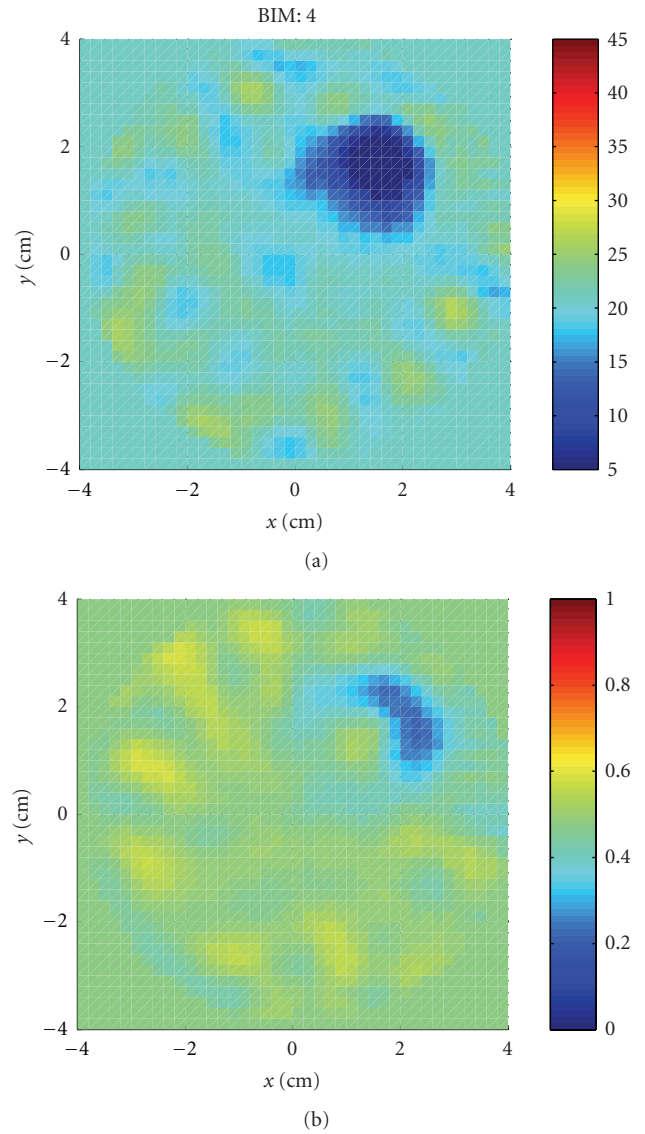


FIGURE 20: Reconstructions of the single acrylic sphere of Experiment 1 shown in Figure 19(a). (a): Relative permittivity. (b): Conductivity. The permittivity is recovered well but the shape in the conductivity is not.

and lower contrast phantoms will help further confirm the methodology.

Second, in Example 1, although some permittivity and conductivity combinations of the sphere were recovered, others were not. Given that the data was synthetic, this points to inherent imaging ambiguities in the simultaneous retrieval of both permittivity and conductivity in the inverse scattering problem. Possible solutions are increasing the number of unique data, or including prior information about the relations between permittivity and conductivity in tissue.

Third, the success of the algorithm in Example 2 in recovering the partial breast phantom suggests that our use of the lossy free-space dyadic Green’s function in the forward solver of the BIM did not grossly affect image reconstruction

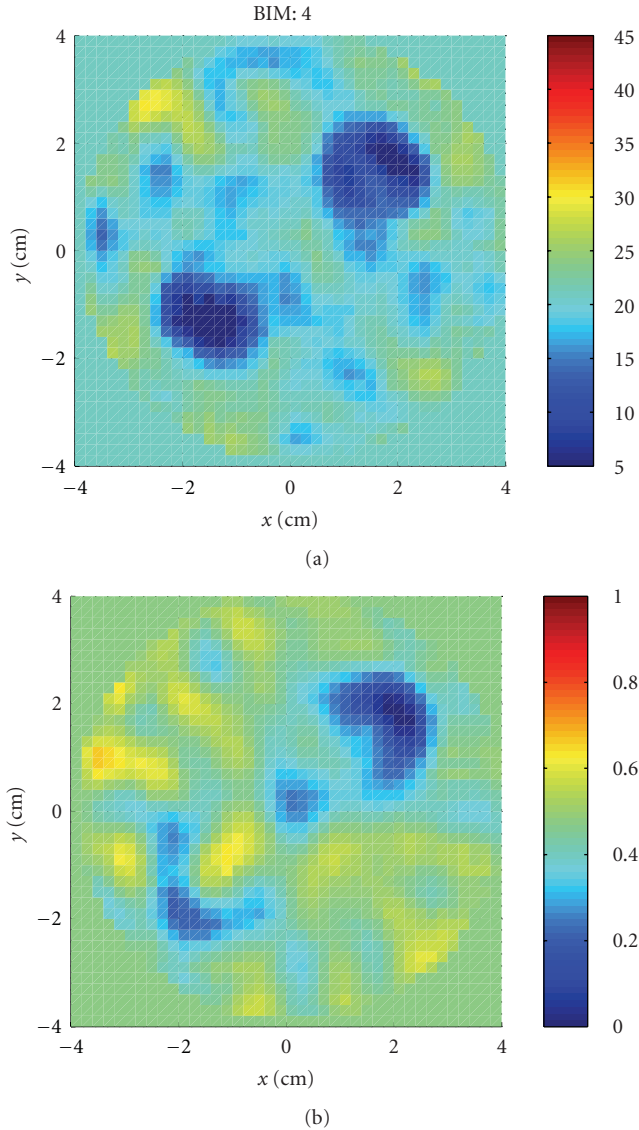


FIGURE 21: Reconstructions of the two acrylic spheres of Experiment 1 shown in Figure 19(b). (a) Relative permittivity. (b) Conductivity. The permittivity is again recovered well but the shape in the conductivity is not.

in this case. This is keeping in mind that the synthetic scattered field S -parameter data did include any multiple scattering between the phantom and the cavity.

Fourth, in light of the successful reconstruction of the simple phantom in Example 2, the failure of the algorithm to recover the more complete breast phantom in Example 3 points to the need to model the chest wall. This can be done by including it in the incident field computations but it may also be necessary in estimating the cavity dyadic Green's function. This is an area to be investigated.

Lastly, Example 4 shows that we must know the background relative permittivity to within 5% of the actual or else risk incorrectly estimating whether the contrasts are higher or lower than the background. An equivalent error can arise from a correct background permittivity but incorrectly



FIGURE 22: Second cavity with antennas designed to operate at 915 MHz of Experiment 2. Three acrylic sphere are suspended (one visible). Cavity is filled with fluid for imaging.

measuring the dimensions of the cavity. We suspect that the very high recovered conductivity values in both Experiments 1 and 2 may be due in part to these types of systematic errors. This demonstrates the difficulty in achieving the necessary consistency between the model, experiment, characterization, and imaging algorithm to accurately form microwave breast images of diagnostic quality.

7. Conclusion

We demonstrated the use of a numerical characterization technique for a breast imaging system prototype. We used HFSS to numerically estimate the incident fields of the antennas in a cavity geometry and formally linked them to an S -parameter-based inverse scattering algorithm and experimental setup. The imaging algorithm was the Born Iterative Method and recovered both numerical and experimental test objects with some success. Future work includes further validation of our methodology, imaging realistic breast phantoms, investigating practical solutions to modeling breast-cavity scattering interactions, image quality assessments with and without numerical characterization, and developing a hemispherical cavity and clinical imaging system.

Appendix

Determining the Background Dyadic Green's Function

We list the following approaches for obtaining the background dyadic Green's function as work for future investigation.

Analytical Dyadic Green's Function. There exist analytical solutions of the dyadic Green's function for some simple cavity geometries, such as cubes or cylinders, [29], which might approximately model certain cavity-based imaging setups. These solutions, however, will likely not include finer details such as antenna plating, connectors, substrate material, or open-ended cavities, such as those used for breast imaging. Analytic solutions though lend themselves to the possibility of retaining some convolution structure in the VIE so fast forward solvers can be used (e.g., fast half space solutions

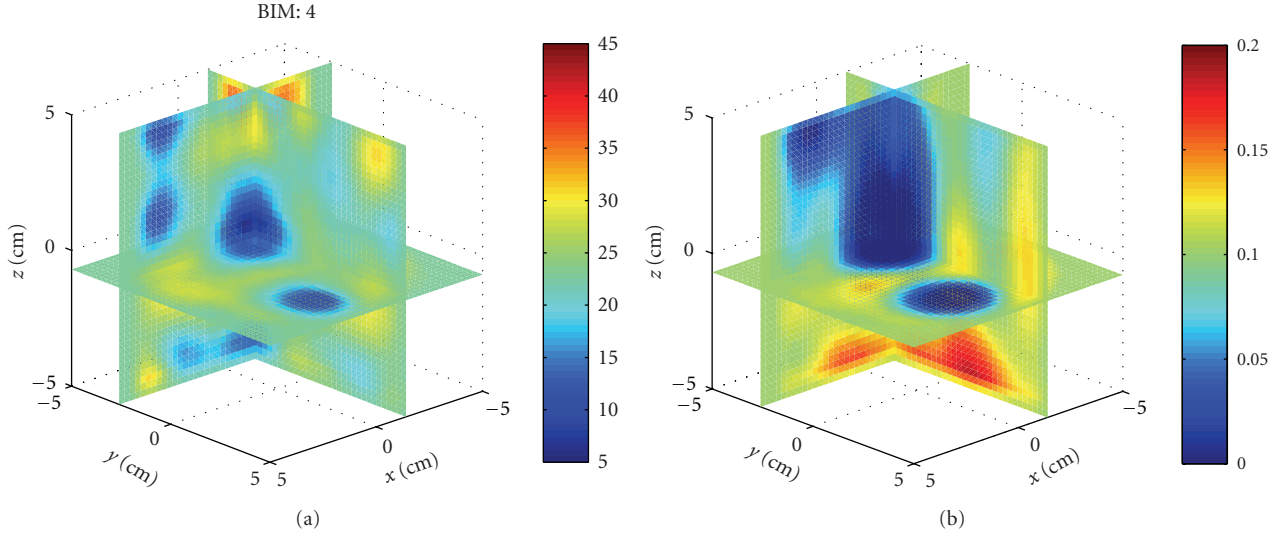


FIGURE 23: Reconstruction of the relative permittivity and conductivity of three acrylic spheres using a cavity operating at 915 MHz from Experiment 2. The two spheres in plane are well recovered and the third detected at the upper left of the image.

[30], applied to multisided cavities). Determining the dyadic Green's function analytically becomes a formidable task as the geometry complicates, where simulation may be better suited.

Full Numeric Simulation. The most complete solution is to fully simulate the object and cavity using a numeric simulator, which will capture all the multiple scattering between the object and the cavity. However, unlike a dyadic Green's function, which only needs to be found once for a particular geometry and the values of which are only needed on the interior of the object domain, this method must simulate the cavity structure outside the object domain in every instance of the simulation. When used in an inverse scattering algorithm, which might compute the domain VIE for each source, frequency, and iteration, then repeatedly simulating the cavity structure adds to the already high computational burden. In addition, one must choose a proper simulation technique to handle both antenna surfaces and inhomogeneous media.

Numerical Dyadic Green's Function. If analytical solutions are not accurate enough, then one must determine the dyadic Green's function numerically. This requires simulating three orthogonal dipoles in turn at every point in the object domain and recording the response at every other point in the domain. The dyadic Green's function is symmetric, so half of the combinations are redundant, and while the convolution nature of the VIE is destroyed, some computational speed-up is possible for symmetric operators. This technique, however, requires accurate modeling around the dipole singularity, which can be difficult. In the case of PEC structures, the technique in [31] computes the dyadic Green's function by finding an array of image dipoles outside the cavity, which avoids the complications from the singularity. The main advantage of determining the dyadic Green's function numerically is that, once found, we no longer need to simulate the cavity structure and can turn our attention to optimizing the computation of the dyadic Green's function.

Approximate Solutions. If the background loss is sufficiently high, so that the resonances of the cavity are damped, then we can approximate the dyadic Green's function. This can be done by adopting an analytical solution (e.g., free-space or cavity) or by, for instance, developing a perturbation method. Adopting the free-space dyadic Green's function (or a perturbation on it) also allows us to retain the convolution structure of the VIE- and FFT-based forward solvers, which may be more beneficial to the inverse scattering algorithm than modeling higher-order multiple scattering.

Acknowledgments

The authors would like to thank Steven Clarkson for help with data collection. They would also like to thank the Basic Radiological Sciences Ultrasound Group for the use of the positioning equipment and useful discussions. This research was supported in part by the Department of Defense, Breast Cancer Research Program, Predoctoral Traineeship Award no. BC073270, DoD/BCRP award no. BC095397, the National Institute of Health T32 EB005172, and by the National Science Foundation award no. 0756338.

References

- [1] P. M. Meaney, M. W. Fanning, D. Li, S. P. Poplack, and K. D. Paulsen, "A clinical prototype for active microwave imaging of the breast," *IEEE Transactions on Microwave Theory and Techniques*, vol. 48, no. 1, pp. 1841–1853, 2000.
- [2] T. Rubk, P. M. Meaney, P. Meincke, and K. D. Paulsen, "Non-linear microwave imaging for breast-cancer screening using Gauss-Newton's method and the CGLS inversion algorithm," *IEEE Transactions on Antennas and Propagation*, vol. 55, no. 8, pp. 2320–2331, 2007.
- [3] C. Gilmore, P. Mojabi, A. Zakaria et al., "A wideband microwave tomography system with a novel frequency selection procedure," *IEEE Transactions on Biomedical Engineering*, vol. 57, no. 4, pp. 894–904, 2010.

- [4] T. Rubk, O. S. Kim, and P. Meincke, "Computational validation of a 3-D microwave imaging system for breast-cancer screening," *IEEE Transactions on Antennas and Propagation*, vol. 57, no. 7, pp. 2105–2115, 2009.
- [5] M. Klemm, I. J. Craddock, J. A. Leendertz, A. Preece, and R. Benjamin, "Radar-based breast cancer detection using a hemispherical antenna array—experimental results," *IEEE Transactions on Antennas and Propagation*, vol. 57, no. 6, pp. 1692–1704, 2009.
- [6] J. P. Stang, W. T. Joines, Q. H. Liu et al., "A tapered microstrip patch antenna array for use in breast cancer screening," in *Proceedings of the IEEE International Symposium on Antennas and Propagation and USNC/URSI National Radio Science Meeting (APSURSI '09)*, North Charleston, SC, USA, June 2009.
- [7] C. Yu, M. Yuan, J. Stang et al., "Active microwave imaging II: 3-D system prototype and image reconstruction from experimental data," *IEEE Transactions on Microwave Theory and Techniques*, vol. 56, no. 4, pp. 991–1000, 2008.
- [8] M. Ostadrahimi, P. Mojabi, C. Gilmore et al., "Analysis of incident field modeling and incident/scattered field calibration techniques in microwave tomography," *IEEE Antennas and Wireless Propagation Letters*, vol. 10, pp. 900–903, 2011.
- [9] S. M. Aguilar, M. A. Al-Joumayly, S. C. Hagness, and N. Behdad, "Design of a miniaturized dual-band patch antenna as an array element for microwave breast imaging," in *Proceedings of the IEEE International Symposium on Antennas and Propagation and USNC/URSI National Radio Science Meeting (APSURSI '10)*, Toronto, Canada, July 2010.
- [10] M. Klemm, C. Fumeaux, D. Baumann, and I. J. Craddock, "Time-domain simulations of a 31-antenna array for breast cancer imaging," in *Proceedings of the IEEE International Symposium on Antennas and Propagation and USNC/URSI National Radio Science Meeting (APSURSI '11)*, pp. 710–713, Spokane, Wash, USA, July 2011.
- [11] E. A. Attardo, A. Borsic, P. M. Meaney, and G. Vecchi, "Finite element modeling for microwave tomography," in *Proceedings of the IEEE International Symposium on Antennas and Propagation and USNC/URSI National Radio Science Meeting (APSURSI '11)*, pp. 703–706, Spokane, Wash, USA, July 2011.
- [12] M. Haynes and M. Moghaddam, "Vector green's function for S-parameter measurements of the electromagnetic volume integral equation," in *Proceedings of the IEEE International Symposium on Antennas and Propagation and USNC/URSI National Radio Science Meeting (APSURSI '11)*, pp. 1100–1103, Spokane, Wash, USA, July 2011.
- [13] M. Haynes, S. Clarkson, and M. Moghaddam, "Electromagnetic inverse scattering algorithm and experiment using absolute source characterization," in *Proceedings of the IEEE International Symposium on Antennas and Propagation and USNC/URSI National Radio Science Meeting (APSURSI '11)*, pp. 2545–2548, Spokane, Wash, USA, July 2011.
- [14] M. Haynes and M. Moghaddam, "Large-domain, low-contrast acoustic inverse scattering for ultrasound breast imaging," *IEEE Transactions on Biomedical Engineering*, vol. 57, no. 11, Article ID 5510108, pp. 2712–2722, 2010.
- [15] A. Tarantola, *Inverse Problem Theory*, SIAM, Philadelphia, Pa, USA, 2005.
- [16] W. C. Chew, *Waves and Fields in Inhomogeneous Media*, IEEE, New York, NY, USA, 1995.
- [17] W. C. Chew and Y. M. Wang, "Reconstruction of two-dimensional permittivity distribution using the distorted Born iterative method," *IEEE Transactions on Medical Imaging*, vol. 9, no. 2, pp. 218–225, 1990.
- [18] M. Moghaddam and W. C. Chew, "Nonlinear two-dimensional velocity profile inversion using time domain data," *IEEE Transactions on Geoscience and Remote Sensing*, vol. 30, no. 1, pp. 147–156, 1992.
- [19] L. Fenghua, Q. H. Liu, and L.-P. Song, "Three-dimensional reconstruction of objects buried in layered media using Born and distorted Born iterative methods," *IEEE Geoscience and Remote Sensing Letters*, vol. 1, no. 2, pp. 107–111, 2004.
- [20] H. Gan and W. C. Chew, "Discrete BCG-FFT algorithm for solving 3D inhomogeneous scatterer problems," *Journal of Electromagnetic Waves and Applications*, vol. 9, no. 10, pp. 1339–1357, 1995.
- [21] Z. Q. Zhang and Q. H. Liu, "Three-dimensional weak-form conjugate- and biconjugate-gradient FFT methods for volume integral equations," *Microwave and Optical Technology Letters*, vol. 29, no. 5, pp. 350–356, 2001.
- [22] P. Zwamborn and P. M. van den Berg, "The three dimensional weak form of the conjugate gradient FFT method for solving scattering problems," *IEEE Transactions on Microwave Theory and Techniques*, vol. 40, no. 9, pp. 1757–1766, 1992.
- [23] M. Lazebnik, L. McCartney, D. Popovic et al., "A large-scale study of the ultrawideband microwave dielectric properties of normal breast tissue obtained from reduction surgeries," *Physics in Medicine and Biology*, vol. 52, no. 10, pp. 2637–2656, 2007.
- [24] P. M. Meaney, S. A. Pendergrass, M. W. Fanning, D. Li, and K. D. Paulsen, "Importance of using a reduced contrast coupling medium in 2D microwave breast imaging," *Journal of Electromagnetic Waves and Applications*, vol. 17, no. 2, pp. 333–355, 2003.
- [25] J. Stang, L. van Nieuwstadt, C. Ward et al., "Customizable liquid matching media for clinical microwave breast imaging," *Physics in Medicine and Biology*. In preparation.
- [26] J. P. Stang and W. T. Joines, "Tapered microstrip patch antenna array for microwave breast imaging," in *IEEE/MTT-S International Microwave Symposium Digest*, July 2008.
- [27] J. Stang, *A 3D active microwave imaging system for breast cancer screening*, Ph.D. dissertation, Department of Electrical and Computer Engineering Duke University, Durham, NC, USA, 2008.
- [28] M. Lazebnik, E. L. Madsen, G. R. Frank, and S. C. Hagness, "Tissue-mimicking phantom materials for narrowband and ultrawideband microwave applications," *Physics in Medicine and Biology*, vol. 50, no. 18, pp. 4245–4258, 2005.
- [29] C.-T. Tai, *Dyadic Green's Functions in Electromagnetic Theory*, IEEE, New York, NY, USA, 1994.
- [30] X. Millard and Q. H. Liu, "A fast volume integral equation solver for electromagnetic scattering from large inhomogeneous objects in planarly layered media," *IEEE Transactions on Antennas and Propagation*, vol. 51, no. 9, pp. 2393–2401, 2003.
- [31] F. D. Q. Pereira, P. V. Castejón, D. C. Rebenaque, J. P. García, and A. A. Melcón, "Numerical evaluation of the green's functions for cylindrical enclosures by a new spatial images method," in *IEEE Transactions on Microwave Theory and Techniques*, vol. 53, pp. 94–104, January 2005.

Research Article

Measurement and Analysis of Microwave Frequency Signals Transmitted through the Breast

Jeremie Bourqui, John Garrett, and Elise Fear

Department of Electrical and Computer Engineering, Schulich School of Engineering, University of Calgary, Calgary, AB, Canada T2N 1N4

Correspondence should be addressed to Jeremie Bourqui, bourquij@ucalgary.ca

Received 2 September 2011; Accepted 6 December 2011

Academic Editor: Paul Meaney

Copyright © 2012 Jeremie Bourqui et al. This is an open access article distributed under the Creative Commons Attribution License, which permits unrestricted use, distribution, and reproduction in any medium, provided the original work is properly cited.

Microwave approaches to breast imaging include the measurement of signals transmitted through and reflected from the breast. Prototype systems typically feature sensors separated from the breast, resulting in measurements that include the effects of the environment and system. To gain insight into transmission of microwave signals through the breast, a system that places sensors in direct contact with the breast is proposed. The system also includes a lossy immersion medium that enables measurement of the signal passing through the breast while significantly attenuating signals traveling along other paths. Collecting measurements at different separations between sensors also provides the opportunity to estimate the average electrical properties of the breast tissues. After validation through simulations and measurements, a study of 10 volunteers was performed. Results indicate symmetry between the right and left breast and demonstrate differences in attenuation, maximum frequency for reliable measurement, and average properties that likely relate to variations in breast composition.

1. Introduction

Microwave approaches have been proposed as complementary methods for breast imaging, providing images related to the electromagnetic properties of tissues in the breast. Significant variations in the properties of healthy tissues are expected, leading to challenges in both measurement of microwave signals and creation of meaningful images. A recent study analyzed measurements of 354 samples of healthy breast tissues that had been surgically excised [1]. Results indicated that permittivity and conductivity increased with decreasing proportion of adipose tissues in the samples. Specifically, fatty tissues are expected to exhibit low permittivity and conductivity at microwave frequencies, while the properties of glandular tissues are expected to be several times greater. A second study analyzed properties of malignant tissues, suggesting significant differences in the properties of these tissues when compared to fatty tissues and a much less dramatic difference (on the order of 10%) when comparing malignant and glandular tissue properties [2]. The composition of the breast also varies from patient

to patient. For example, women may have primarily fatty tissues in the breast or dense breasts that consist primarily of glandular tissues. The combination of breast composition and electromagnetic properties of breast tissues suggests that microwave imaging involves detecting small changes in a complex environment. Further more, challenges related to microwave imaging and measurement are also anticipated to vary with breast composition, as lower attenuation of signals and high contrast between healthy and malignant tissues are expected for fatty breasts.

In order to gain insight into the challenges related to measurement and imaging, simulation models based on breast MR scans of patients have been developed [3]. These models provide realistic breast shapes and spatial distributions of tissues. In attempt to accurately represent tissues properties, dielectric properties models that are based on the measurement study are incorporated [4]. To enhance the match between simulated and measured data, models of the antennas and aspects of the system (e.g., immersion liquid) are also included. Simulations of the breast models and sensors performed with numerical techniques such as

the finite difference time domain (FDTD) method provide insight into reflected and transmitted signals expected in measurement. For example, a recent study compared measurements of volunteers and simulations of patient-specific models, showing good agreement between the dominant reflections [5]. However, differences between simulations and measurements of later-time reflections were evident, and transmitted signals were not measured. Transmitted signals are of particular interest in light of another recent study of the properties of breast tissues, which suggests differences between *in vivo* and *ex vivo* measurements [6]. If differences between reported measurements and actual tissue properties exist, then simulation models may not accurately predict signals transmitted through the breast. This information is a valuable tool for specifying requirements for measurement systems, such as dynamic range and frequency band.

Several prototype systems have been designed for microwave breast imaging and include collection of transmitted signals. For example, one system for microwave tomography has an array of antennas positioned at distance from the breast and placed in a lossy immersion liquid [7]. This system is designed to operate from 500 MHz to 3 GHz. A second example, a multistatic radar system, has antennas arranged on a hemisphere [8]. A dielectric insert and layer of immersion liquid are used to separate the antennas from the breast. The bandwidth for this system is in the range from 4 to 10 GHz [9]. Although both systems collect transmitted data, the signals are expected to be influenced by the external environment rather than predominantly effected by the breast. Different immersion liquids are also expected to have different effects on the transmitted signals that are related to the electromagnetic properties of the liquids. In addition, both systems have been designed for a specific frequency band of operation and do not permit the assessment of transmission over a very wide frequency band including lower frequencies.

Therefore, there is a need to assess the upper frequency limit at which signals transmitted through the breast may be reliably measured and also to gain insight into intra- and inter-patient differences in this maximum frequency. In this paper, we report a system designed to measure signals transmitted through the breast at frequencies in the range of 1–10 GHz. The sensors are in direct contact with the breast and a lossy immersion liquid is employed to attenuate alternative paths that the signals may travel. Measurement of transmitted signals with known separations between sensors and without significant path in the coupling medium also provides the opportunity to assess the average properties of breast tissues. Reflection-based measurements contain too much ambiguity to make an assessment of average properties practical (using a limited number of sensor locations). We further note that this system is not designed explicitly for imaging, although estimation of average properties of breast tissues would be helpful for microwave imaging algorithms. After validation of the system, a study of 10 volunteers is performed in order to gain insight into the changes in attenuation and maximum frequency of operation that occur for different patients and within the same patient. We report a simple technique to estimate the average permittivity and conductivity of the tissues from transmission measurements



FIGURE 1: Cassiopeia antenna.

and apply this technique to the measurements collected from patients.

2. Methods

In this section, the system to measure microwave signal transmission through the human breast and approach to average property estimation are described. The electrical conductivity of breast tissues is expected to vary significantly between patients, which translates to variations in signal attenuation. Cases, in which very high attenuation occurs, (e.g., predominantly glandular tissues) are expected to lead to measurement challenges due to extremely weak transmitted signals. These challenges have to be addressed by careful design of two aspects of the measurement system. First, the overall dynamic range needs to be as high as possible. Secondly, there are multiple paths that the signals may take; the signals that travel through the breast are of interest, while the signals that travel around the breast are not. Therefore, the system must facilitate detection of signals traveling through the breast only. The sensor design and system configuration implemented to achieve these goals are described in Section 2.1. The system also provides an opportunity to gain additional information through estimating average properties of the breast tissues. A simple approach to roughly estimating the average properties is discussed in Section 2.2.

2.1. Sensor and System. The Cassiopeia antenna (Figure 1) [10] is the sensor used to both transmit and receive signals. This antenna is designed to come into contact with the breast skin and to operate in a lossy immersion liquid. The antenna is essentially a balanced antipodal Vivaldi antenna (BAVA) with a director included in the aperture, similar to the antenna reported in [11]. The key differences are a modified feed structure and the use of higher permittivity materials to confine fields to the antenna such that the sensor is relatively insensitive to the immersion liquid. The details of the antenna and feed design, along with initial simulation and measurement results with the Cassiopeia placed in air and glycerin, are found in [10]. For this study, the antenna is placed in a 2% saline solution in order to attenuate signals that travel along paths outside of the breast. As shown in

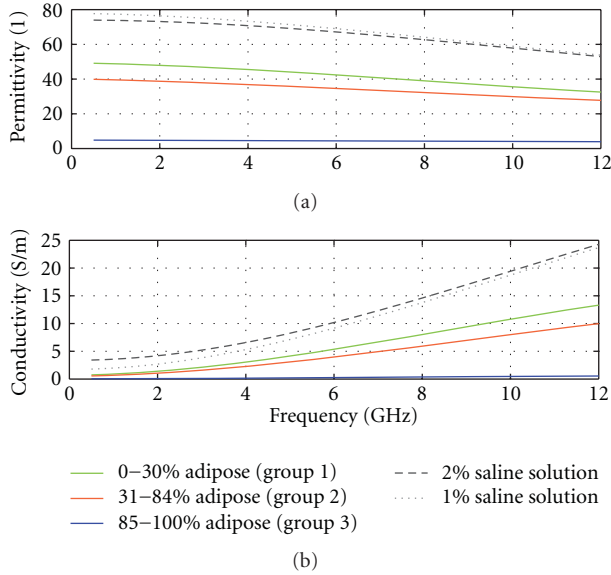


FIGURE 2: Relative permittivity and conductivity of the 3 breast tissue groups, as well as 1% and 2% saline solutions.

Figure 2, the 2% saline exhibits conductivity well above the expected conductivity of breast tissues, which significantly attenuates signals traveling along these unwanted paths.

To collect transmission measurements, two sensors are placed on opposite sides of the tank (or breast) (Figure 3). The sensors are placed 37 mm below the top of the tank in order to completely immerse the sensors in the saline. The two sensors are aligned, and each sensor is mounted on a sliding arm, as shown in Figures 3 and 4. The separation distance can be manually adjusted between 140 mm and 10 mm using a knurled wheel; digital callipers are attached to both sides so that precise separation distances can be recorded. This configuration permits the antennas to be positioned such that contact is made with the breast skin. Modifying the separation distance may easily be accomplished with high accuracy; several measurements at different separation distances are typically collected. The antennas are connected to a vector network analyzer (PNA N5242A, Agilent Technologies, Palo Alto, CA, USA). To maximize sensitivity, measurements are performed with an intermediate frequency (IF) bandwidth of 10 Hz and a port power level of 10 dBm. These settings produce a comfortable 120 dB dynamic range at the antenna ports without need for additional averaging. A total of 401 points are recorded over a 1-to-10 GHz bandwidth. The total sweep time is 36 seconds.

The performance of the sensor in saline and the ability of the sensors to measure transmitted signals are assessed. First, measured and simulated reflection coefficients over a broad-frequency band are inspected. Simulations are also performed to evaluate the integrity of the radiated field distribution in breast tissues. The breast model examined consists of a 2 mm thick skin layer filled with homogeneous breast tissue representing fat (tissue group 3 which represents median properties of samples containing 0–30% fat in [4]). The dimensions of the breast model are detailed in [11].



FIGURE 3: View of the measurement tank with the two sensors (Cassiopeia antenna) attached to movable arms.

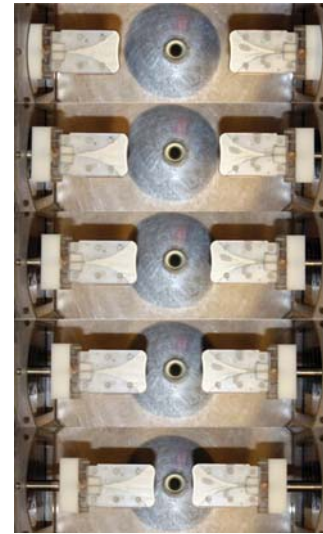


FIGURE 4: View of the sensors set at different separation distances.

An FDTD simulation tool (SEMCAD X, SPEAG, Zurich) is used to perform the simulations with parameters similar to those reported in [10]. Dispersive model parameters published in [4, 12, 13] are used to model the 2% saline, skin, and tissue group 3, respectively. Validation of the radiated fields through measurements is challenging, so transmitted signals are measured through breast models representing low and high loss scenarios. The hemispherical, low-loss breast model is described in [14] and shown in Figure 5. This model has a diameter of 100 mm and is made of a solid dielectric material with relative permittivity of 15 and loss tangent supposedly less than 0.002 (Eccostock HiK, Emerson, and Cuming Microwave Products, Randolph, MA, USA). The high-loss breast model has the same dimensions, however, consists of a thin rubber membrane filled with a 1% saline solution. The conductivity of 1% saline is greater than the conductivities reported for the three breast tissue groups in [4] but below the 2% saline, thus very weak transmission is expected.

Figure 6 shows the user interface used for work with human participants. It consists of a bed on which the volunteers lie in a prone position. The bed includes an opening where the breast extends into the measurement tank placed underneath. The PNA is located under the bed directly behind the measurement tank. Several measurements are



FIGURE 5: View of the low-loss breast model in the measurement tank. Picture was taken without the 2% saline for better clarity.

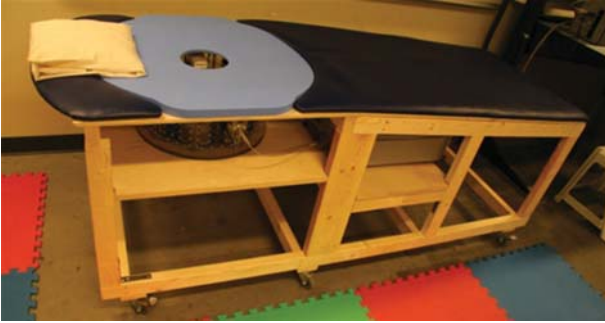


FIGURE 6: Measurement system integrated in the user interface.

collected from each volunteer (more details on the volunteer study are provided in Section 4). The antennas are placed in contact with the breast, and an initial measurement is collected. The antenna separation is modified, and a new set of measurements is obtained. This process is repeated several times, resulting in a set of transmission coefficients collected with different separation distances between the antennas. Note that the full scattering coefficient matrix (S_{11} , S_{21} , S_{12} , and S_{22}) is recorded for each measurement.

2.2. Property Estimation. A simple method to estimate the average electrical properties of the breast tissues is introduced. The method takes advantage of the differences between transmission coefficients recorded at two different separations between the antennas, however, involves several assumptions. First, it is assumed that the contact between the skin and the sensor remains unchanged after repositioning one of the sensors. Secondly, the change in response due to cable movement is considered negligible. These assumptions are believed to be reasonable based on the stability of the reflection coefficients (S_{11} and S_{22}) observed between measurements. Third, it is assumed that the inner structure of the breast is the same for two measurements collected at different separations (i.e., the two paths have the same average properties). Therefore, the difference between the transmitted signals is assumed to be solely related to the change in transmission length induced by reducing the

separation between the sensors. To relate the change in transmission coefficient to the average electrical properties of the breast tissues, we further assume a uniform plane wave model to describe the propagation from the transmitting to receiving antenna. This implicitly ignores any effects of multipath in the breast tissues. The electric field in the tissues is approximated as:

$$E^+(z) = E_0 \cdot e^{-\alpha \cdot z} \cdot e^{-j \cdot \beta \cdot z}, \quad (1)$$

where α is the attenuation constant, and β is the phase constant. These constants are then approximated using a pair of transmission measurements along with a correction for radial spreading of the signal:

$$\alpha(f) = \frac{-\log\left(\frac{|S_{21}(f)|_1}{|S_{21}(f)|_2}\right)(D_1/D_2)}{D_1 - D_2}, \quad (2)$$

$$\beta(f) = -\frac{\theta_1(f) - \theta_2(f)}{D_1 - D_2},$$

where D_i is the separation distance at which the measurements has been taken, $|S_{21}(f)|_i$ is the magnitude of the transmission coefficient and, $\theta(f)_i$ is the phase of the transmission coefficient. Subscripts 1 and 2 refer to the two measurements used for the calculations. Note that D_1 must be greater than D_2 .

After the attenuation and phase constant are retrieved, the corresponding permittivity and conductivity are calculated using (3):

$$\epsilon_r(f) = \frac{\beta(f)^2 - \alpha(f)^2}{(2\pi f)^2 \mu_0 \epsilon_0}, \quad (3)$$

$$\sigma(f) = \frac{2\alpha(f)\beta(f)}{2\pi f \mu_0},$$

where ϵ_0 and μ_0 are the permittivity and permeability of vacuum.

3. Validation

The measurement system is validated by first examining the behaviour of a single sensor, then through collecting transmission data. More specifically, the ability to adequately measure transmitted signals over the entire frequency band of interest and the feasibility of the property estimation method are explored.

3.1. Sensor and System Performance. Figure 7 presents the reflection coefficient (S_{11}) for each of the sensors measured in the 2% saline solution. For the sake of completeness, the simulated result is also shown. The value of S_{11} is below -10 dB over the frequency range of interest, indicating that most of the power is radiated or absorbed by the antenna but not reflected back to the source. Discrepancies between the responses of the two sensors as well as the simulations and measurements are observed. These discrepancies can be mostly attributed to the sensitive construction process of the

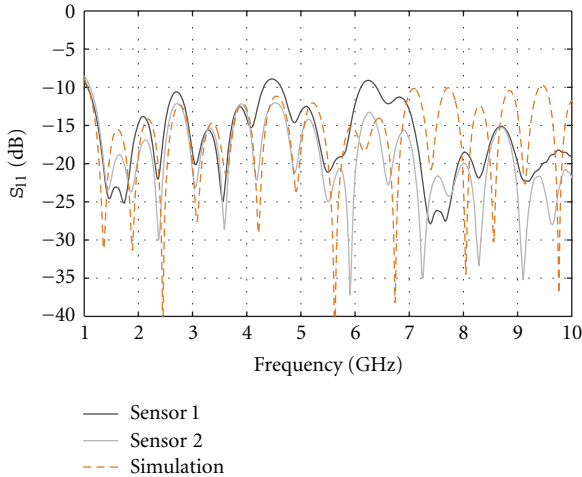


FIGURE 7: Reflection coefficient measured for both sensors when immersed in 2% saline. Simulated counterpart is in dashed line.

Cassiopeia. As described in [10], this sensor is composed of several metallic and plastic pieces which have to be machined and assembled. In addition, a cement material is poured into the sensor aperture which needs to fill tight spaces. Between machining variation of plastic material and the difficulty in controlling the cement filling process, construction discrepancy between sensors is to be expected. We also note that the discrepancy between simulated and measured response increases for the second half of the frequency band, and this is due to inexact material properties used in simulation. Specifically, the sensor utilizes Eccostock HiK materials for which models of the dielectric properties over the entire frequency band of interest are not available.

Figure 7 suggests that, as per the results presented in [10], the Cassiopeia can reasonably operate in conductive media. However in a high-permittivity liquid, such as the 2% saline, the antenna starts to behave as a leaky wave structure, especially at lower frequencies (below 3 GHz). This is illustrated in Figure 8, which presents the simulated radiation behaviour when the antenna contacts the breast model, as in [9], consisting of a skin layer filled with a material representing low-loss tissues. At 2 GHz, the structure radiates in the vertical direction and the intensity of radiation in the breast tissues is quite low, considering that the breast tissues are considerably less lossy than the immersion medium. This behaviour is the result of the antenna becoming a leaky wave structure in high-permittivity media. At higher frequencies (4, 6, 8 GHz), the leaky wave effect is significantly reduced as the field is more confined in the antenna structure. Based on this simulated result, significantly lower transmission measurements are expected in the lower-frequency band.

Figure 9 presents the measured and simulated transmission coefficient obtained with the low-loss breast model. At the lower frequencies, a very low transmission magnitude is noted, as expected from Figure 8. However, the transmission level appears to stabilize at 4 GHz and above. We note that, at the higher frequencies, the simulated data predict a stronger transmission than observed in practice. Again, differences in the Eccostock HiK material properties between

measurements and simulations are the main source of this disagreement, especially the conductivity which, in practice, significantly increases with frequency. Nevertheless, the main observation is that the measurement system demonstrates the ability to measure transmitted signals over the frequency band of interest.

The transmission coefficients measured through the high-loss breast model are presented in Figure 10 and demonstrate the ability of our measurement system to measure very weak transmitted signals. More precisely, one may observe that the transmission coefficient measured, while the breast model presented is easily distinguished from the measurement taken at the same sensor separation without the breast present until both signals reach the noise floor. In other words, this result suggests that these weak recorded signals actually propagate into the breast model and not in the immersion medium or the tank structure.

3.2. Property Estimation. In order to validate the property estimation technique, measurements with the tank containing only a 1% saline immersion medium are used. This lower-loss medium was chosen instead of the 2% saline in order to measure signals over a wider-frequency bandwidth. The transmission measurements for several distances are shown in Figure 11(a), while the calculated permittivity and conductivity, using the two shortest separation distances along with (2) and (3), are shown in Figures 11(b) and 11(c). One can observe that the estimation is not very accurate below 3 GHz. At these frequencies, the poor radiation behaviour of the antenna, translated in a very low coupling efficiency, contributes to the error in results. However, above 3 GHz, the calculated values are very close to the theoretical ones, confirming that the assumptions made to simplify estimation of average properties are valid for this simple case.

In summary, the results presented in this section demonstrate that the Cassiopeia antenna, immersed in 2% saline, exhibits low S_{11} over a very wide band, and that radiated field behaviour improves with frequency (related to leaky wave behaviour at lower frequencies). The work with two sensors demonstrates that the system is capable of detecting signals transmitted through objects with low and high loss characteristics over the entire frequency range of interest. The approach to estimating average properties is verified for a simple scenario, showing that reasonable estimates are obtained from 3 to 10 GHz.

4. Volunteer Study

To gain insight into the maximum frequency at which signals transmitted through the breast may be detected, a study of 10 volunteers has been performed. The description of the study is followed by presentation of the measured data. Finally, the average property estimation is applied to the measured data, providing mixed results.

4.1. Recruitment and Protocol. This study has been approved by the Conjoint Health Research Ethics Board (CHREB) of the University of Calgary, (ID 23244). The volunteers were

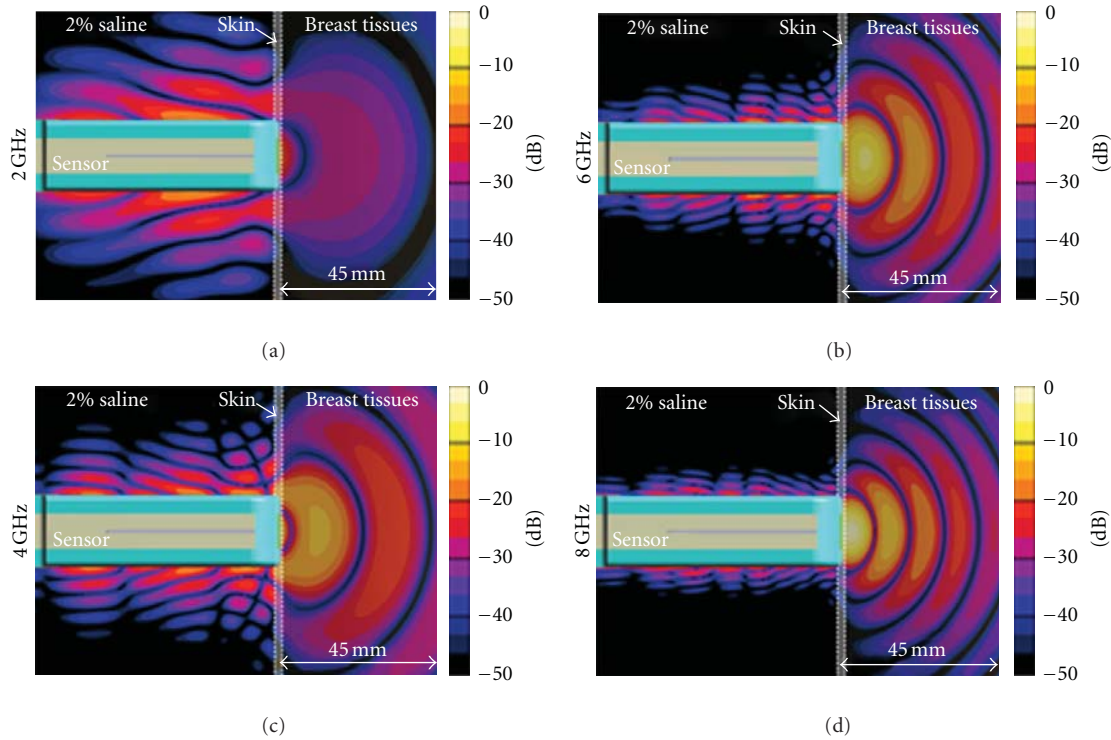


FIGURE 8: Electric field radiated by the antenna in realistic breast tissues while immersed in 2% saline. All field intensities are normalised to identical input power. The side-on view is shown (i.e., the cross-section through the cylindrical breast model is along its long axis).

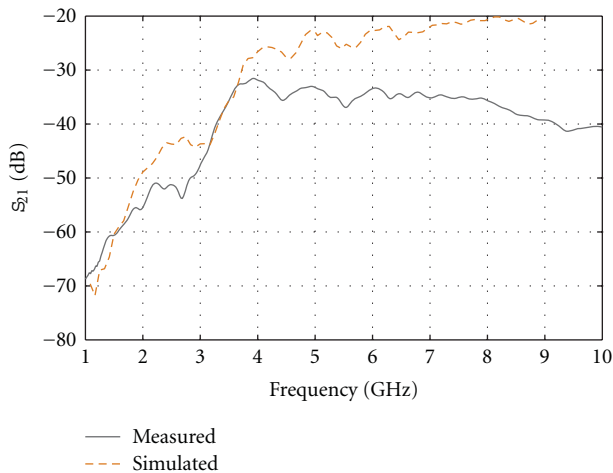


FIGURE 9: Measured and simulated transmission through the low-loss breast model (100 mm diameter).

recruited through billboard posters and by word of mouth. To ensure good contact with the sensors, the breasts must extend far enough into the measurement tank. Therefore, one of the criteria for participation in the study was a minimum “C” cup size. The age of the volunteers was recorded; however, no additional information on breast tissue composition was available (e.g., X-ray mammograms or other breast imaging results). The volunteers are referred to by their ages.

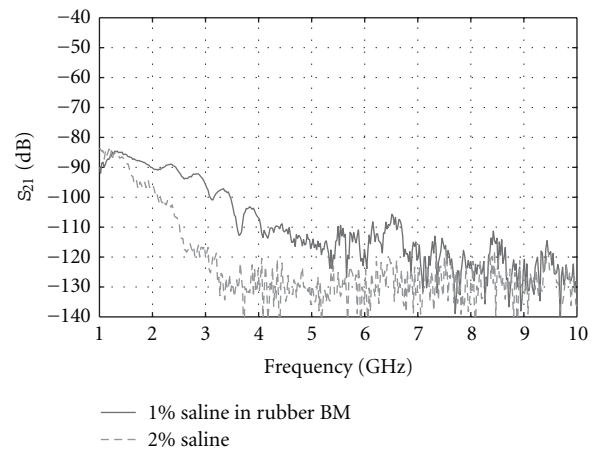


FIGURE 10: Transmission measurement through a rubber membrane containing a 1% saline solution (“high-loss breast model”) and with 2% saline filling the region between the two sensors positioned with the same separation distance (100 mm).

Measurements took place in a research laboratory with a registered nurse helping the volunteers to be positioned on the machine. A research engineer controlled the data acquisition (from behind a privacy screen), while the nurse adjusted the separation distance between the sensors. The left and right breasts were examined and a total of four measurements were taken for each breast. First, the sensors were positioned to contact the breast skin and an initial

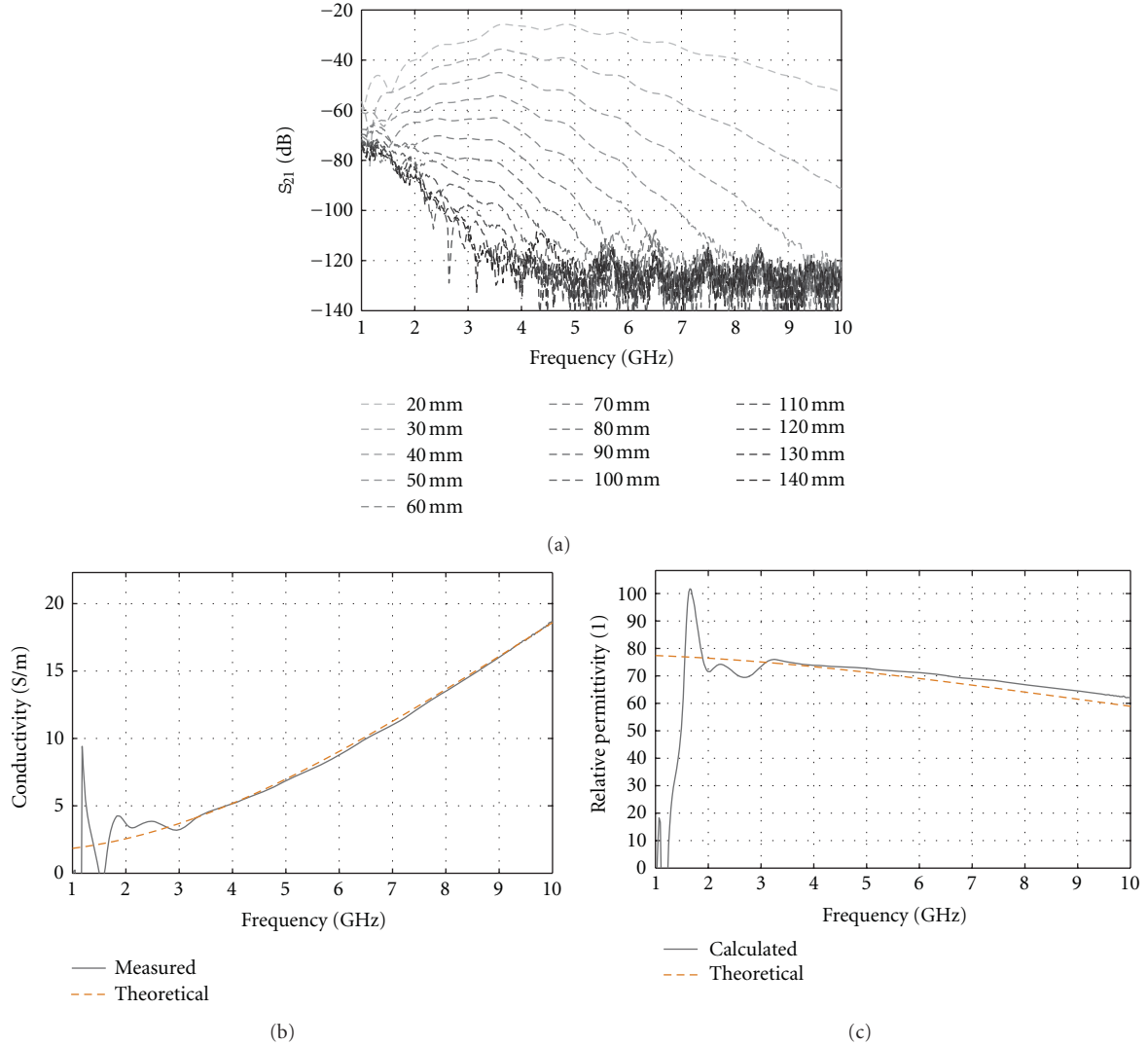


FIGURE 11: Measurement (a) taken with different separation distances of the sensors and the tank containing only a 1% immersion liquid. Conductivity (b) and relative permittivity (c) calculated using (2) and (3) and compared with theoretical values based on [12].

measurement was recorded. Then, one of the sensors was moved 5 mm toward the breast and a second measurement was recorded. The third measurement was recorded after moving the second sensor 5 mm closer to the breast. Finally, the first sensor was brought another 5 mm closer before the fourth measurement was recorded. Therefore, a total of 4 measurements (each at a different separation distance) was taken for each breast. This procedure was successfully realized for all of our volunteers without any discomfort reported.

4.2. Measured Results. Volunteers between 21 to 65 years of age participated in our study. As expected, we have observed considerable variation in signal attenuation due to variation in breast tissues between individuals. For example, in the case of a 35-year-old individual (Figure 12), signals were recorded for the entire frequency band of interest. While for a 55-year-old volunteer (Figure 13), the transmission is weaker, and no significant signals are recorded after

4 GHz. We note that results for each patient typically exhibit similar characteristics, namely, increased transmission with decreased separation between sensors as well as decreased transmission with frequency.

In order to compare the attenuation level between each case, the last frequency point for which the transmitted signal achieves a 20 dB signal-to-noise ratio (SNR) is used as metric. For this specific measurement system, the 20 dB SNR translates to a transmission coefficient level of -100 dB. This point is referred to the “maximum frequency”, and the observed values are plotted in Figure 14(a). The maximum frequency is determined for the shortest separation distance between sensors that permits this measurement to be collected. The corresponding separation distances are also given in Figure 14(b). Figure 14(c) investigates the relation between separation and maximum frequency, showing no correlation. This confirms that the variations in maximum frequency are related to differences in breast tissue composition among our volunteers.

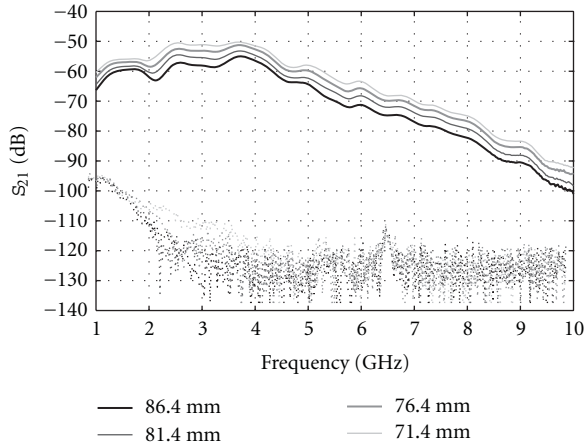


FIGURE 12: Transmission magnitude for the 35-year-old volunteer, left breast with different separation distances between the sensors. The dashed curves correspond to the transmission measured for the same distances but without the breast present.

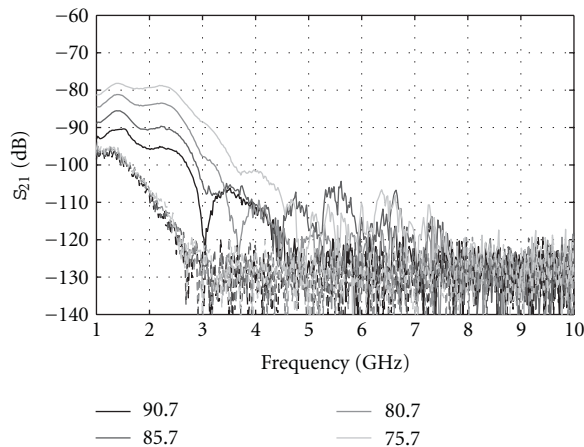


FIGURE 13: Transmission magnitude for the 55-year-old volunteer, left breast with different separation distances between the sensors. The dashed curves correspond to the transmission measured for the same distances but without the breast present.

Figure 14(a) shows that, while the maximum frequency for the patients varies between 3.5 to 10 GHz (measurement limit), a certain symmetry between the left and right breasts for individual patients is observed. Only the 21- and 55-year-old volunteers show larger differences between breasts. However, in the case of the 55-year-old individual, the separation distances (Figure 14(b)) are quite different. When maximum frequencies for similar distances are compared, better symmetry is observed. This suggests that the variation seen in the maximum frequency for the 55-year-old volunteer is due to difference in separation distances. It is also observed that the separation distances for our 62-year-old volunteer are significantly different between the left and right breast; however, good symmetry in the maximum frequency is still noted. This volunteer had previous surgery on her left breast, so perhaps changes in tissue properties (e.g., scar tissue) result in similar maximum frequencies at different separation distances.

While not sufficient for generating statistics, the measurements do suggest the possibilities of using signals up to 10 GHz to image breast tissues, depending on breast composition. At the same time, the measured transmission levels are specific to our system. Sensors with higher gain and measurement equipment with better dynamic range would increase the overall sensitivity. On the other hand, it was practically observed that a slight decrease of the transmission path length can significantly increase the signal intensity, which makes moderate breast compression an appealing option. For example, in Figure 13, more than 10 dB in transmission is gained with a 10 mm decrease of separation between sensors.

4.3. Property Estimates. For each patient, the property estimation technique is applied to the 6 combinations of data available from the 4 measured transmission coefficients; the results are averaged to produce a single estimate. This averaging is performed to limit the effect of possible outliers in the measured data. The accuracy of the result is difficult to assess since the ground truth remains unknown. However, based on the observed attenuation, preliminary estimates of tissue properties and/or breast composition can be hypothesized.

For example, volunteers 35, 36, 43(a), and 65 years of age have maximum frequency for transmission reaching 10 GHz with a significant separation distance between sensors. This suggests that these patients have predominantly fatty breast tissues (tissue group 3). The estimated properties for these volunteers' breasts are shown in Figure 15, converging toward the group 3 model as hypothesized.

For breasts that likely have more significant glandular tissue composition (i.e., lower maximum frequencies), the average property estimation is unfortunately not as successful. For example, the permittivity estimates show significant variations with frequency, and the permittivity curve usually does not follow the expected Cole-Cole model shape. The conductivity usually behaves close to expected; however, some results show unexpectedly high conductivities or conductivity that decreases with frequency. To illustrate these observations, estimated properties for our 30-year-old volunteer are shown in Figure 16. Several factors may be the source of these behaviors. First, heterogeneous breasts are very likely to generate multipath, as signals may travel through fatty tissue or glandular tissue, hence arriving at different times at the sensor. This multipath makes our simple propagation model inadequate. Secondly, our estimation technique assumes that the breast tissues deform homogeneously. This means that the changes in the transmission coefficient are related to the entire breast and not local volumes. It is known that the elastic modulus values are not consistent across different tissue types [15], which means that different tissues deform differently. As a result, the change in transmission can arise from local deformation, instead of the assumed homogeneous deformation. Therefore, alternative techniques to estimate average properties are required for breasts that are not predominantly fatty.

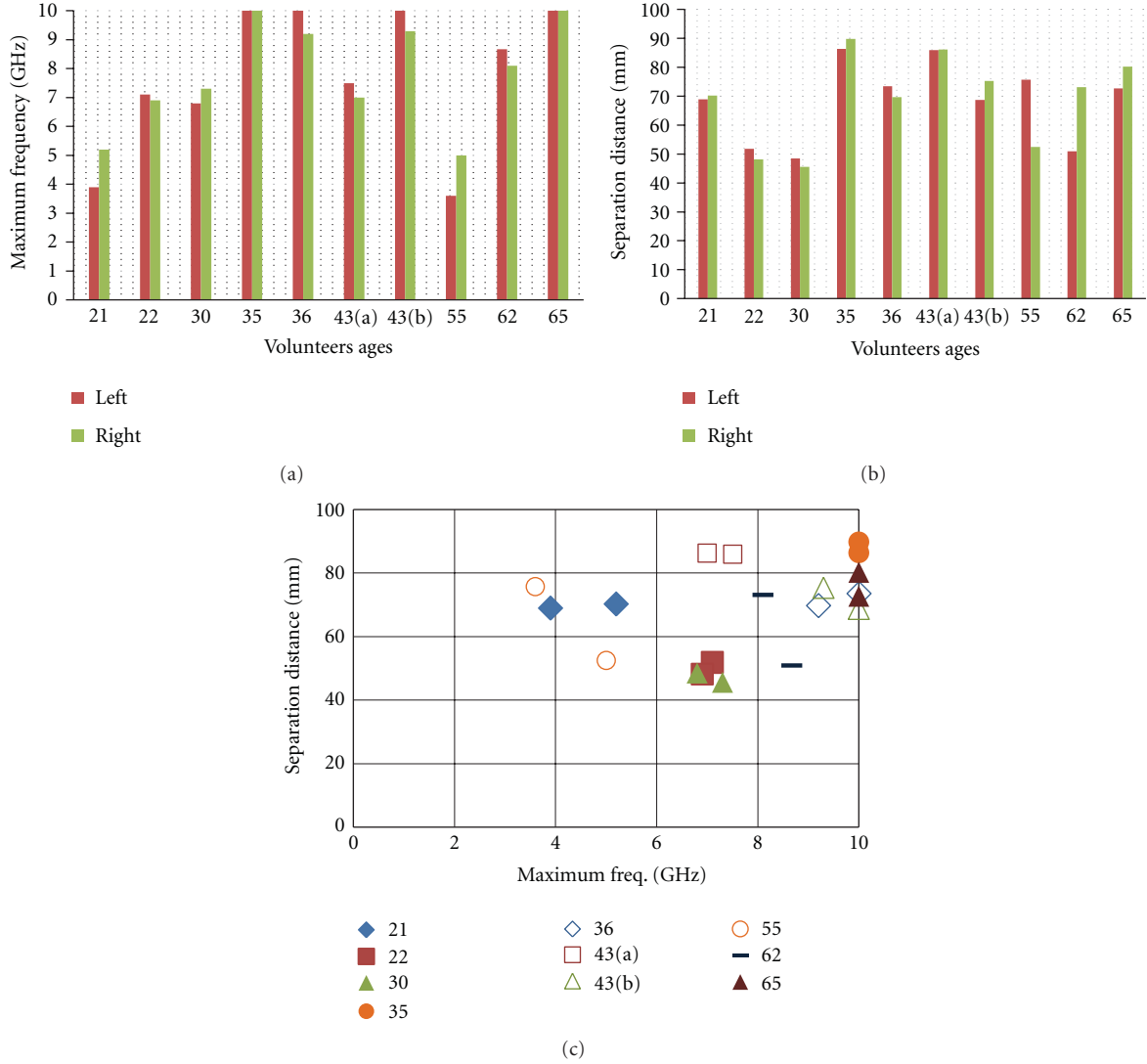


FIGURE 14: Measurement results: (a) maximum frequency and (b) separation distances in function of volunteer ages. (c) separation distance as a function of maximum frequency for each volunteer breast.

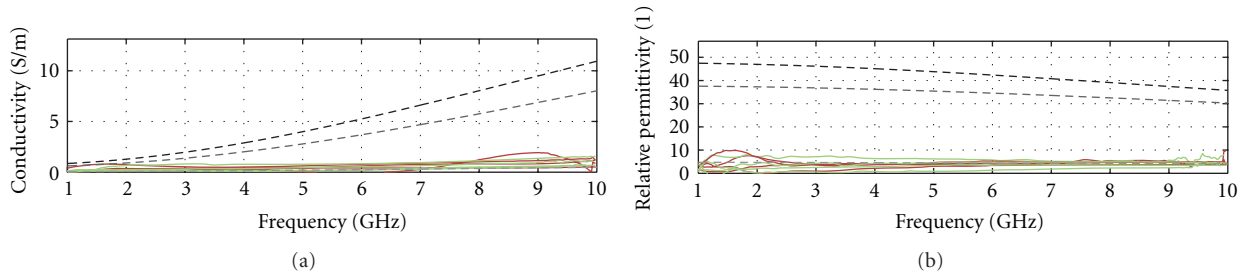


FIGURE 15: Estimation of breast tissue electrical properties (conductivity in (a) and permittivity in (b)) for the 35-, 36-, 43(a)- and 65-year-old volunteers. Groups 1, 2, and 3 refer to the glandular, transition, and fatty categories of tissues defined in [1].

5. Conclusion

The prototype system reported in this paper is designed specifically to measure transmitted signals through the breast. Antennas designed to contact the breast during microwave measurement are adapted to measure transmitted signals. Two antennas are placed on opposite sides of the

breast, while immersed in saline. Through operation in a lossy medium, signals traveling along alternate paths are attenuated, such that the signal traveling directly through the breast is expected to have a predominant effect on the measurement. As the system is aimed at determining appropriate frequencies of operation, it operates over a wide

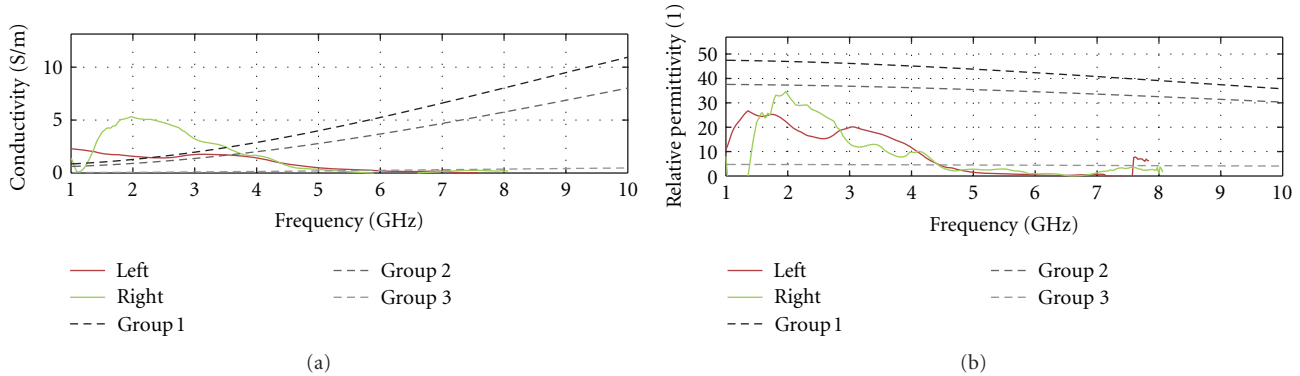


FIGURE 16: Estimation of breast tissues electrical properties (conductivity in (a) and permittivity in (b)) for the 30-year-old volunteer. Groups 1, 2, and 3 refer to the tissue categories defined in [1].

band (1–10 GHz). Therefore, the bandwidth and approach to measurement differ from previously reported prototype systems aimed at microwave imaging (e.g., [7, 8]). In particular, the system is designed to enable transmission measurements through the entire breast over a frequency range from 1 to 10 GHz. We note that microwave tomography systems also involve measurement of signals transmitted through the breast (as well as a lossy immersion liquid); however, a maximum measurement frequency of 3 GHz has been used in work with patients. Therefore, the system reported in this paper permits exploration of transmitted signals over a higher-frequency band.

The system is deployed in a study of 10 volunteers with unknown breast composition. For each volunteer, four measurements are collected per breast, with separation between sensors adjusted for each measurement. The maximum frequency at which transmitted signals are reliably measured is noted, and significant variation in this frequency is observed for the 10 volunteers. There is, however, similarity between the maximum frequencies observed for the right and left breasts. In addition, the results of our measurements suggest that the use of frequencies up to 10 GHz is realistic. However, for denser breasts, this upper limit is likely considerably reduced. In such cases, the image reconstruction scheme (whether tomographic or radar-based) could be adapted to use only the relevant frequency band. As a result, the image resolution would likely be patient-dependant in the same way as image contrast depends on breast density with X-ray mammography. It was also practically observed that the use of moderate compression and sensors that contact the breast significantly improves SNR. Therefore, results of this study suggest that the data collected with this system provide unique insights into microwave measurements of the breast.

Finally, an approach to estimating the average properties of breast tissues has been introduced, and reasonable results are obtained for volunteers with suspected primarily fatty breasts. This method is based on several assumptions that do not appear to hold for volunteers that are suspected to have greater glandular tissue content. Therefore, future work includes developing average property estimation techniques that are effective for a wider range of breast compositions. In addition, a new waveguide like UWB sensor is being

developed to avoid leakage into the surrounding saline medium and which improves the coupling efficiency with the breast tissues, especially at lower frequencies. For further investigation, a second study is planned that also includes clinical breast imaging in order to give insight into the breast composition and aid in interpreting results.

References

- [1] M. Lazebnik, L. McCartney, D. Popovic et al., “A large-scale study of the ultrawideband microwave dielectric properties of normal breast tissue obtained from reduction surgeries,” *Physics in Medicine and Biology*, vol. 52, no. 10, pp. 2637–2656, 2007.
- [2] M. Lazebnik, D. Popovic, L. McCartney et al., “A large-scale study of the ultrawideband microwave dielectric properties of normal, benign and malignant breast tissues obtained from cancer surgeries,” *Physics in Medicine and Biology*, vol. 52, no. 20, pp. 6093–6115, 2007.
- [3] E. Zastrow, S. K. Davis, M. Lazebnik, F. Kelcz, B. D. V. Veen, and S. C. Hagness, “Development of anatomically realistic numerical breast phantoms with accurate dielectric properties for modeling microwave interactions with the human breast,” *IEEE Transactions on Biomedical Engineering*, vol. 55, no. 12, pp. 2792–2800, 2008.
- [4] M. Lazebnik, M. Okoniewski, J. H. Booske, and S. C. Hagness, “Highly accurate debye models for normal and malignant breast tissue dielectric properties at microwave frequencies,” *IEEE Microwave and Wireless Components Letters*, vol. 17, no. 12, pp. 822–824, 2007.
- [5] J. Sill, J. Bourqui, T. Williams, and E. Fear, “Tissue sensing adaptive radar for breast cancer detection: comparison of measured and simulated patient data,” in *IEEE International Symposium on Antennas and Propagation and CNC/USNC/URSI Radio Science Meeting*, Toronto, Canada, 2010.
- [6] R. J. Halter, T. Zhou, P. M. Meaney et al., “The correlation of in vivo and ex vivo tissue dielectric properties to validate electromagnetic breast imaging: initial clinical experience,” *Physiological Measurement*, vol. 30, no. 6, pp. S121–S136, 2009.
- [7] D. Li, P. M. Meaney, T. Raynolds, S. A. Pendergrass, M. W. Fanning, and K. D. Paulsen, “Parallel-detection microwave spectroscopy system for breast imaging,” *Review of Scientific Instruments*, vol. 75, no. 7, pp. 2305–2313, 2004.

- [8] M. Klemm, J. A. Leendertz, D. Gibbins, I. J. Craddock, A. Preece, and R. Benjamin, "Microwave radar-based differential breast cancer imaging: imaging in homogeneous breast phantoms and low contrast scenarios," *IEEE Transactions on Antennas and Propagation*, vol. 58, no. 7, Article ID 5452974, pp. 2337–2344, 2010.
- [9] D. Gibbins, M. Klemm, I. J. Craddock, J. A. Leendertz, A. Preece, and R. Benjamin, "A comparison of a wide-slot and a stacked patch antenna for the purpose of breast cancer detection," *IEEE Transactions on Antennas and Propagation*, vol. 58, no. 3, pp. 665–674, 2010.
- [10] J. Bourqui, E. C. Fear, and M. Okoniewski, "Versatile ultrawideband sensor for near-field microwave imaging," in *the 4th European Conference on Antennas and Propagation (EuCAP'10)*, Barcelona, Spain, April 2010.
- [11] J. Bourqui, M. Okoniewski, and E. C. Fear, "Balanced antipodal vivaldi antenna with dielectric director for near-field microwave imaging," *IEEE Transactions on Antennas and Propagation*, vol. 58, no. 7, pp. 2318–2326, 2010.
- [12] J. Hilland, "Simple sensor system for measuring the dielectric properties of saline solutions," *Measurement Science and Technology*, vol. 8, no. 8, pp. 901–910, 1997.
- [13] S. Gabriel, R. W. Lau, and C. Gabriel, "The dielectric properties of biological tissues: III. Parametric models for the dielectric spectrum of tissues," *Physics in Medicine and Biology*, vol. 41, no. 11, pp. 2271–2293, 1996.
- [14] T. C. Williams, J. Bourqui, T. R. Cameron, M. Okoniewski, and E. C. Fear, "Laser surface estimation for microwave breast imaging systems," *IEEE Transactions on Biomedical Engineering*, vol. 58, no. 5, pp. 1193–1199, 2011.
- [15] A. Gefen and B. Dilmoney, "Mechanics of the normal woman's breast," *Technology and Health Care*, vol. 15, no. 4, pp. 259–271, 2007.